Masahiro Yamashita
Hiroshi Okamoto *Editors*

Material Designs and New Physical Properties in MX- and MMX-Chain Compounds

Springer

Material Designs and New Physical Properties in MX- and MMX-Chain Compounds

Masahiro Yamashita • Hiroshi Okamoto
Editors

Material Designs and New Physical Properties in MX- and MMX-Chain Compounds

Springer

Editors
Masahiro Yamashita
Departement of Chemistry
Tohoku University
Sendai
Japan

Hiroshi Okamoto
Kashiwa
Japan

ISBN 978-3-7091-1316-5 ISBN 978-3-7091-1317-2 (eBook)
DOI 10.1007/978-3-7091-1317-2
Springer Wien Heidelberg New York Dordrecht London

Library of Congress Control Number: 2012953272

Printed on acid-free paper

Springer is part of Springer Science+Business Media (www.springer.com)

Preface

Material Designs and New Physical Properties in MX- and MMX-Chain Compounds

The history of quasi-one-dimensional halogen-bridged Pt complexes began at the end of the nineteenth century when Wolffram reported a Cl-bridged complex, $Pt(etn)_4Cl_3 \cdot 2H_2O$ (etn=ethylamine), which is called Wolffram's red salt because of its lustrous red color. This complex was considered to be a Pt^{III} complex, but it has been shown that it is actually a Pt^{II}–Pt^{IV} mixed valence complex $[Pt(etn)_2][PtCl_2(etn)_4]Cl_4 \cdot 4H_2O$. Since then, many Pt complexes as well as Pd complexes have been synthesized. In 1981, $Ni(chxn)_2Br_3$ (chxn=1R,2R-diaminocyclohexane) was synthesized. X-ray structure analysis revealed that it was not a Ni^{II}–Ni^{IV} complex, but a Ni^{III} complex. Theoretically, these compounds are thought to be extended Peierls–Hubbard systems, where the electron–phonon interaction (S), the transfer integral (T), and the on-site and nearest-neighbor Coulomb repulsion energies (U and V, respectively) strongly compete with each other. The electronic states of these complexes depend mainly on the competition between U and S. When S is larger than U, M(II)–M(IV) mixed valence states or charge density wave states (CDW), where the bridging halide ions are displaced from the midpoints between two neighboring metal ions, (represented as $–X–M^{II}–X–M^{IV}–X–$), are stabilized. On the other hand, when U is larger than S, an M(III) average valence or Mott–Hubbard (MH) state, where the bridging halide ions are located at the midpoint between two neighboring metal ions (represented as $–X^{III}–X–M^{III}–X–$), becomes stable. These Pt, Pd, and Ni complexes show very interesting chemical and physical properties, such as intense and dichroic charge transfer bands, progressive overtones in resonance Raman spectra, midgap absorptions attributed to solotons and polarons, and gigantic third-order nonlinear optical susceptibilities, and have applications in field effect transistor (FET) devices.

In the 1980s, a new type of complex composed of binuclear metal complexes and bridging halogens, represented as –M–M–X–M–M–X–, was reported. They

have a variety of electronic states and undergo various phase transitions by temperature, pressure, as well as photo irradiation.

In this book, we describe these complexes, including experimental results and theoretical treatments.

Masahiro Yamashita
(Tohoku University)

Hiroshi Okamoto
(University of Tokyo)

Contents

Part II MMX-Chain Compounds

Contributors

Hiroaki Iguchi Department of Chemistry, Graduate School of Science, Tohoku University, Sendai, Japan

Kaoru Iwano Institute of Materials Structure Science, High Energy Accelerator Research Organization (KEK), Tsukuba, Japan

Hideo Kishida Department of Applied Physics, Nagoya University, Nagoya, Japan

Hiroyuki Matsuzaki Department of Advanced Materials Science, Faculty of Frontier Sciences, University of Tokyo, Chiba, Japan

Research Institute of Instrumentation Frontier, National Institute of Advanced Industrial Science and Technology (AIST), Ibaraki, Japan

Minoru Mitsumi Department of Material Science, Graduate School of Material Science, University of Hyogo, Hyogo, Japan

Arao Nakamura JST CREST, Tokyo, Japan

Hiroshi Okamoto Department of Advanced Materials Science, Faculty of Frontier Sciences, University of Tokyo, Chiba, Japan

Department of Advanced Materials Science, Graduate School of Frontier Sciences, University of Tokyo, Kashiwa, Japan

Shinya Takaishi Department of Chemistry, Graduate School of Science, Tohoku University, Sendai, Japan

Masahiro Yamashita Department of Chemistry, Graduate School of Science, Tohoku University, Sendai, Japan

Kenji Yonemitsu Department of Physics, Chuo University, Tokyo, Japan

Department of Functional Molecular Science, Graduate University for Advanced Studies, Okazaki, Japan

JST, CREST, Tokyo, Japan

Chapter 1
General Introduction

S. Takaishi and M. Yamashita

1.1 Quasi-one-Dimensional Halogen-Bridged Metal Complexes

For a long time, quasi-one-dimensional (Q1D) halogen-bridged metal complexes have attracted much attention of chemists and physicists because of significant physical properties based on their Q1D electronic structures such as intense and dichroic charge transfer (CT) bands [1–3], progressive overtones in the resonance Raman spectra [4–7], midgap absorptions attributable to solitons and polarons [8–10], gigantic third-order nonlinear optical susceptibilities [11, 12], spin-Peierls transitions [13], thermochromism in the organic media [14], insertion of 1D chains into artificial peptides [15], current oscillation phenomena [16], and field effect carrier doping [17].

Q1D halogen-bridged metal complexes have chain structure of group 10 metals (M = Ni, Pd, Pt) bridged by halide ions (X = Cl, Br, I), in which d_z^2 orbital of M and p_z orbital of X overlap forming 1D electronic system (Fig. 1.1). They are classified into two types. One has the infinite chain structure of alternating stacking of M and X, such as –M–X–M–X–, so-called MX chains. The other has infinite chain structure of alternating stacking of M–M dimer unit of paddle-wheel structure and X, such as –M–M–X–M–M–X–, so-called MMX chains.

1.2 History of MX-Chains

History of MX-chains began at the end of the nineteenth century since Wolffram reported Cl-bridged Pt complex $[Pt(etn)_4Cl]Cl_2{\cdot}2H_2O$ (etn = aminoethane, Fig. 1.2) [18]. This complex is called Wolffram's red salt because of its lustrous

S. Takaishi (✉) • M. Yamashita
Department of Chemistry, Graduate School of Science, Tohoku University,
6-3 Aramaki-Aza-Aoba, Aoba-Ku, Sendai 980-8578, Japan
e-mail: takaishi@mail.tains.tohoku.ac.jp

M. Yamashita and H. Okamoto (eds.), *Material Designs and New Physical Properties in MX- and MMX-Chain Compounds*, DOI 10.1007/978-3-7091-1317-2_1,

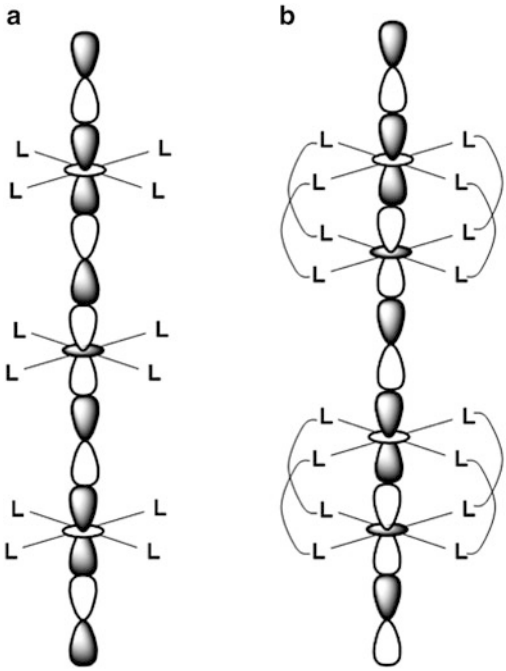

Fig. 1.1 Schematic chain structure of (**a**) MX- and (**b**) MMX-chains

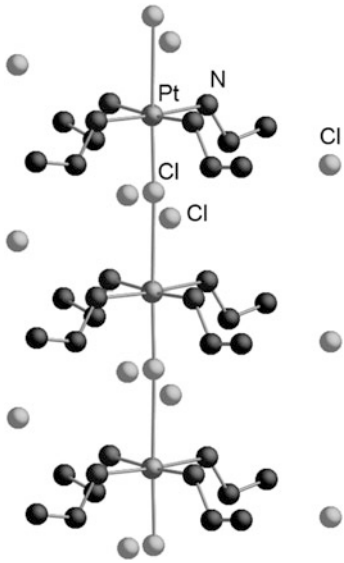

Fig. 1.2 Crystal structure of Wolffram red salt $[Pt(etn)_4Cl]Cl_2{\cdot}2H_2O$

red color. This complex used to be thought of as a Pt^{3+} complex, but it has been shown by X-ray crystal structure analysis that this complex is alternatively stacked by square planer $[Pt^{2+}(etn)_4]^{2+}$ and octahedral $[Pt^{4+}(etn)_4Cl_2]^{2+}$ [19]. Tsuchida et al.

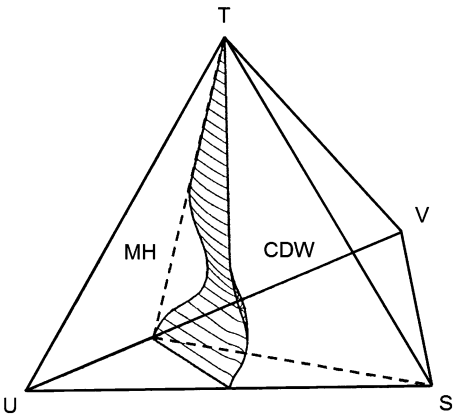

Fig. 1.3 Phase diagram of MX-chains

have studied optical properties of this complex in the 1950s and shown that the origin of the color is due to the intervalence charge transfer (IVCT) transition from Pt^{2+} to Pt^{4+} species [20, 21]. Kida et al. developed derivatives of the complexes in the 1960s [22]. These compounds were spotlighted as model compounds of 1D Peierls–Hubbard theory in the 1980s [23–25], and their physical properties had been extensively studied. In this period, many derivatives had been also developed by changing metal ions (M = Pt, Pd), in-plane ligand (L = alkylamine, ethylenediamine (en), 1*R*,2*R*-diaminocyclohexane (chxn) etc.), and bridging halides (Cl, Br, I).

Yamashita et al. reported the first Ni-based complex $[Ni(chxn)_2Br]Br_2$ in 1981 [26]. At that time, this complex was thought to be a Ni^{2+}–Ni^{4+} mixed-valence state, but it has been clarified that this complex is in averaged-valence state by means of X-ray crystal structure analysis [27]. In the Ni complexes, many attractive physical properties have been reported such as gigantic third-order nonlinear optical susceptibility [11, 12], spin-Peierls transition [13], etc.

1.3 Electronic State of MX-Chains

The electronic states of MX chains are interpreted by extended Peierls–Hubbard model considering electron–lattice interaction (*S*), transfer integral between neighbor orbital (*T*), on-site coulomb repulsion (*U*), and intersite coulomb repulsion (*V*) (Fig. 1.3) [23–25]. Actually, the energy of their electronic states is often explained by the competition between *S* and *U* for clarity.

When M = Ni, *U* is the dominant factor because of the small $3d_z^2$ orbital, resulting in a uniform oxidation state of $Ni^{3+}(d^7)$. This electronic state is called average valence (AV) or Mott–Hubbard (MH) state. When M = Pd and Pt, on the other hand, *S* is larger than *U* because of the larger $4d_z^2$ or $5d_z^2$ orbital, resulting $M^{2+}(d^8)$ and $M^{4+}(d^6)$ mixed-valence state. This electronic state is called charge-

density-wave (CDW) state. The bridging halide ion is close to M^{4+} ion, inducing the twofold periodicity.

1.4 MX-Chains as a Mixed-Valence Complex

Mixed-valence complexes have been extensively studied. Such a system is interesting not only in solid state chemistry but also in solution chemistry. A binuclear Ru^{2+}–Ru^{3+} mixed valence complex, Creutz–Taube ion: $[(NH_3)_5Ru^{2+}(pz)Ru^{3+}(NH_3)_5]^{5+}$ (pz = pyrazine) [28, 29], and its analogues have been enormously studied from the viewpoint of photoinduced electron transfer [30–32]. The MX-chains have been also attractive targets as 1D extended Creutz–Taube like complexes.

Robin and Day have classified the mixed-valence system into three categories [33]. This classification is often used in mixed-valence systems. Here we briefly introduce this classification.

Class I: This comprises compounds in which the different oxidation states are associated with very different environments. The energy required to transfer an electron between the two is large. Thus, there is essentially no interaction between the different oxidation states, and no special properties associated with the mixed valency.

Class II: These compounds also have different environments for the different oxidation states, but the sites are now sufficiently similar that electron transfer requires only a small energy. These compounds are semiconductors and have optical absorptions resulting from the kind of intervalence transition in visible near infrared regions.

Class III: These compounds have all atoms in an identical, fractional oxidation state with electrons delocalized between them. This category can be divided into two subclasses: In Class IIIA the electron delocalization occurs within a finite cluster; Class IIIB is where the electrons are delocalized throughout the solid.

When the MX-chains are classified according to Robin–Day's classification, Pt and Pd complexes are classified into class II, Ni complexes are classified into class IIIA category. It should be noted that we describe the electronic structure of the CDW complexes as $-X\cdots M^{2+}\cdots X-M^{4+}-X\cdots$ in this article for clarity. More strictly, however, this state should be noted as $-X\cdots M^{3-\rho}\cdots X-M^{3+\rho}-X\cdots$, where ρ is the degree of valence disproportionation or CDW amplitude ($0<\rho<1$).

1.5 MMX Chains

Q1D dinuclear halogen-bridged complexes, those are abbreviated as MMX-chains, have also got attracted for several decades. They have larger degrees of freedom in the electrons in the MMX chains compared to those in the MX chains, and that cause a larger variety of electronic states. On the basis of theoretical calculations

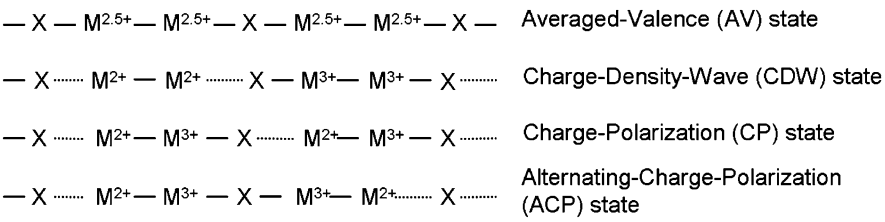

Fig. 1.4 Schematic representations of four possible electronic states in MMX-chain system

and experimental data, the electronic states of the MMX chains can be classified into the following four states as shown in Fig. 1.4. The electronic states are also known to be strongly correlated to the position of the bridging halide ions. Except AV state, the bridging halide ions are displaced from the midpoint between neighboring metal ions and slightly approach to M^{3+} ion. It should be noted that the represented oxidation number in Fig. 1.4 is formal oxidation number. Strictly, 3+ and 2+ should be represented as $(2.5 + \rho)+$ and $(2.5-\rho)+$ $(0 \leq \rho \leq 0.5)$, respectively, because those are in Robin–Day's class II category.

So far, two types of MMX chain compounds have been reported. One is $[M_2(dta)_4I]$ series (M = Pt and Ni; dta = $C_nH_{2n+1}CS_2^-$, n = 1–4), which form neutral chains [34–36]. Another is $R_4[Pt_2(pop)_4X]\cdot nH_2O$ (R = alkylammonium ions, alkyldiammonium ions, or alkali metal ions: X = Cl, Br or I), which form anionic chains [37–40]. Because platinum ions usually have a larger hybridization with iodides than chloride and bromides, iodide-bridged compounds are expected to stabilize the various oxidation states and, as a result, cause the various phase transitions.

References

1. Clark RJH, Kurmoo M (1980) Inorg Chem 19:3522
2. Tanaka M, Kurita S, Kojima T, Yamada Y (1984) Chem Phys 91:257
3. Wada Y, Mitani T, Yamashita M, Koda T (1985) J Phys Soc Jpn 54:3143
4. Clark RJH, Franks ML, Trumble WR (1976) Chem Phys Lett 41:287
5. Clark RJH, Kurmoo M, Mountney DN, Toftlund H (1982) J Chem Soc Dalton Trans 1982:1851
6. Clark RJH (1990) Chem Soc Rev 19:107
7. Clark RJH (1983) Adv Infrared Raman Spectrosc 11:95
8. Okamoto H, Kaga Y, Shimizu Y, Oka Y, Iwasa Y, Mitani T, Yamashita M (1998) Phys Rev Lett 80:861
9. Tanino H, Kobayashi K (1983) J Phys Soc Jpn 52:1446
10. Okamoto H, Yamashita M (2023) Bull Chem Soc Jpn 1998:71
11. Iwasa Y, Funatsu E, Hasegawa T, Koda T, Yamashita M (1991) Appl Phys Lett 59:2219
12. Kishida H, Matsuzaki H, Okamoto H, Manabe T, Yamahsita M, Taguchi T, Tokura Y (2000) Nature 405:929

13. Takaishi S, Tobu Y, Kitagawa H, Goto A, Shimizu T, Okubo T, Mitani T, Ikeda R (2004) J Am Chem Soc 126:1614
14. Kimizuka N, Lee SH, Kunitake T (2000) Angew Chem Int Ed 39:389
15. Tanaka K, Kaneko K, Shionoya M (2007) Dalton Trans 2007:5369
16. Kishida H, Ito T, Nakamura A, Takaishi S, Yamashita M (2009) J Appl Phys 106:016106
17. Takaishi S, Yamashita M, Matsuzaki H, Okamoto H, Tanaka H, Kuroda S, Goto A, Shimizu T, Takenobu T, Iwasa Y (2008) Chem Euro J 14:472
18. Wolffram H (1900) Dissertation, Königberg
19. Craven BM, Hall D (1961) Acta Cryst 14:475
20. Yamada S, Tsuchida R (1956) Bull Chem Soc Jpn 29:421
21. Yamada S, Tsuchida R (1956) Bull Chem Soc Jpn 29:894
22. Kida S (1804) Bull Chem Soc Jpn 1965:38
23. Nasu K (1984) J Phys Soc Jpn 52:3865
24. Webber-Milbrodt SM, Gammel JT, Bishop AR, Lor EY Jr (1992) Phys Rev B 45:6435
25. Iwano K, Nasu K (1992) J Phys Soc Jpn 61:1380
26. Yamashita M, Nonaka Y, Kida S, Hamaue Y, Aoki R (1981) Inorg Chim Acta 52:43
27. Toriumi K, Wada Y, Mitani T, Bandow S, Yamashita M, Fujii Y (1989) J Am Chem Soc 111:2341
28. Creutz C, Taube H (1969) J Am Chem Soc 91:3988
29. Creutz C, Taube H (1973) J Am Chem Soc 95:1086
30. Richardson DE, Taube H (1984) Coord Chem Rev 60:107
31. Poppe J, Moscherosch M, Kaim W (1993) Inorg Chem 32:2640
32. Yokogawa D, Sato H, Nakao Y, Sakaki S (1966) Inorg Chem 2007:46
33. Robin MB, Day P (1967) Adv Inorg Radiochem 10:247
34. Bellitto C, Flamini A, Gastaldi L, Scaramuzza L (1983) Inorg Chem 22:444
35. Mitsumi M, Murase T, Kishida H, Yoshinari T, Ozawa Y, Toriumi K, Sonoyama T, Kitagawa H, Mitani T (2001) J Am Chem Soc 123:11179
36. Mitsumi M, Yoshida Y, Kohyama A, Kitagawa Y, Ozawa Y, Kobayashi M, Toriumi K, Tadokoro M, Ikeda N, Okumura M, Kurmoo M (2009) Inorg Chem 48:6680
37. Che CM, Herbstein FH, Schaefer WP, Marsh RE, Gray HB (1983) J Am Chem Soc 105:4604
38. Kurmoo M, Clark RJH (1985) Inorg Chem 24:4420
39. Clark RJH, Kurmoo M, Dawes HM, Hursthouse MB (1986) Inorg Chem 25:409
40. Matsuzaki H, Matsuoka T, Kishida H, Takizawa K, Miyasaka H, Sugiura K-, Yamashita M, Okamoto H (2003) Phys Rev Lett 90:046401

Part I
MX-Chain Compounds

Chapter 2
Structures and Optical Properties of Pt and Pd Compounds with Charge-Density-Waves

Hiroshi Okamoto and Hiroyuki Matsuzaki

2.1 Introduction

Dynamics of excitons and photocarriers in one-dimensional (1D) semiconductors have been attracting much attention from both theoretical and experimental point of views. In 1D electronic systems, it is known that the excitonic effect is remarkably enhanced due to the singularity of the 1D Coulomb potential. The effect of the electron–lattice (e–l) interaction is also important in 1D electronic systems as exemplified by the Peierls transition. It was theoretically expected that a free exciton (FE) is easily relaxed to a self-trapped exciton (STE) via lattice relaxations, since there is no barrier between an FE and an STE in 1D systems [1]. In 1D half-filled electronic systems, it is known that the e–l interaction sometimes plays a significant role on their electronic structures and charge dynamics. A typical example of such an e–l coupled system is *trans*-polyacetylene (*trans*-(CH_x)), in which the dimerization or equivalently the bond alternation occurs via the Peierls mechanism [2]. In *trans*-$(CH)_x$, it is known that charge and/or spin carriers are stabilized as solitons [3, 4] or polarons under the influence of the e–l interaction, which exhibit characteristic midgap absorptions. Thus, clarifying the nature of solitons and polarons as well as of excitons is essential for understanding optical and transport properties of the 1D e–l coupled systems. In general, conjugated polymers including $(CH)_x$ cannot be obtained as single crystals and

H. Okamoto (✉)
Department of Advanced Materials Science, Faculty of Frontier Sciences, University of Tokyo, 5-1-5 Kashiwanoha, Kashiwa, Chiba 277-8561, Japan
e-mail: okamotoh@k.u-tokyo.ac.jp

H. Matsuzaki
Department of Advanced Materials Science, Faculty of Frontier Sciences, University of Tokyo, 5-1-5 Kashiwanoha, Kashiwa, Chiba 277-8561, Japan

Research Institute of Instrumentation Frontier, National Institute of Advanced Industrial Science and Technology (AIST), Tsukuba Central 5, 1-1-1 Higashi, Tsukuba, Ibaraki 305-8565, Japan

M. Yamashita and H. Okamoto (eds.), *Material Designs and New Physical Properties in MX- and MMX-Chain Compounds*, DOI 10.1007/978-3-7091-1317-2_2,

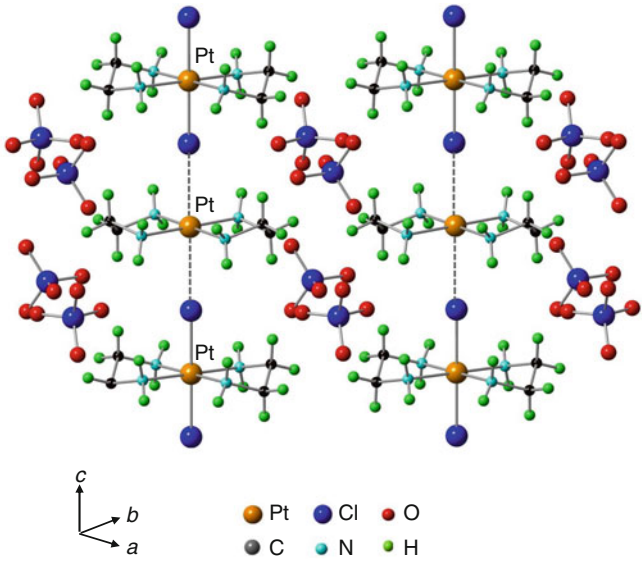

Fig. 2.1 Structure of $[Pt(en)_2][Pt(en)_2Cl_2](ClO_4)_4$

their electronic states are not so controllable. Therefore, it is difficult to perform systematic studies of excitons, solitons, and polarons in those systems.

Subsequently, halogen(X)-bridged transition metal(M) compounds (or equivalently MX-chain compounds) have provided a unique opportunity to study the nature of excitons, solitons, and polarons [5]. A great advantage of this category of materials is that their electronic structures can be widely controlled and a variety of materials can be obtained as single crystals. As a result, a number of studies concerning excitons, solitons, and polarons have been reported so far in MX-chain compounds [6–52].

MX-chain compounds are represented as $[MA_2][MA_2X_2]Y_4$ (or simply $\{MA_2X\}Y_2$), where A and Y are the ligand and the counter anion, respectively. The crystal structure of $[Pt(en)_2][Pt(en)_2Cl_2](ClO_4)_4$ (en = ethylenediamine) is shown in Fig. 2.1 as a typical example of MX-chain compounds. As shown in the figure, the $[MA_2]$ moieties are bridged by the halogen ions (X) and the hydrogen (H)-bonds between the amino groups of the ligands (A) and the counter anions (Y) support the MX chains. In the compounds with M = Pt and Pd, M(II) and M(IV) mixed-valence state, or equivalently, the commensurate charge-density-wave (CDW) state is stabilized due to the strong e–l interaction, while in the compounds with M = Ni, Ni(III) mono-valence state, or equivalently, the Mott–Hubbard (MH) state appears [53–55]. As detailed in Chap. 4, a Pd(III) MH compound has also been recently synthesized.

In the Pt and Pd compounds, amplitudes of CDW can be controlled by the replacements of metals (M = Pt and Pd), bridging halogens (X = Cl, Br, and I), ligand molecules (A = ethylenediamine (en), ethylamine, diaminocyclohexane (chxn), etc.) and counter anions ($Y = ClO_4$, BF_4, Cl, Br, I, etc.) surrounding the MX chains [28, 32]. In addition, the nondegenerate CDW states can be obtained in

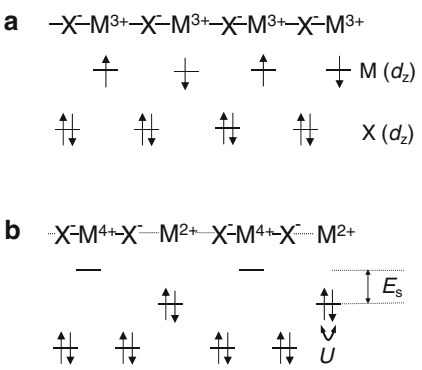

Fig. 2.2 Schematic electronic structure of the MX chain. (**a**) The mono-valence (Mott–Hubbard) state and (**b**) the mixed-valence (CDW) state

the heterometal compounds in which Pt and Pd ions arrange alternatively [26, 52]. Such a controllability of CDW in MX-chain compounds allows us to make an advanced study of dynamics of excitons, solitons, and polarons.

In this chapter, firstly, we review how the CDW ground state can be controlled by the choice of constituent elements (M, X, A, and Y). Secondly, we summarize the fundamental optical properties of the CDW compounds, focusing on the optical absorption and photoluminescence (PL) properties, which are dominated by the transition to the lowest charge-transfer (CT) exciton and the emission from the self-trapped exciton (STE), respectively. After that, we detail nature of solitons and polarons investigated by the photoinduced absorption (PA) spectroscopy. From the comparison of PL properties from STEs and PA spectra due to solitons and polarons, we discuss the relaxation dynamics of photoexcited states in MX-chain compounds in the CDW phase.

2.2 Control of CDW Ground States [5, 32]

In MX-chain compounds, 1D electronic state of an MX chain consists of d_{z^2} orbitals of M and p_z orbitals of X. The ground state is the mono-valence M(III) state or the mixed-valence M(II) and M(IV) state (or equivalently the commensurate CDW state) as shown in Figs. 2.2a, b, respectively. In Pt and Pd compounds, the mono-valence state is usually unstable due to the site-diagonal-type e–l interaction overcoming the on-site Coulomb repulsion energy U on the metal site [8, 9]. In Ni compounds, the mono-valence state is stabilized due to the large U on the Ni sites, so that their electronic structure is considered to be the Mott–Hubbard (MH) insulator state [53, 54]. More precisely, the Ni compounds belong to the CT insulators in which the transition from the halogen p valence band to the Ni 3d upper Hubbard band corresponds to the optical gap [55]. CDW states are never stabilized in the Ni compounds. In this section, we show that CDW states (amplitudes of CDW, degeneracy of CDW, and optical gap energies) in Pt and Pd compounds can be widely controlled by the choice of constituent elements in MX-chain compounds.

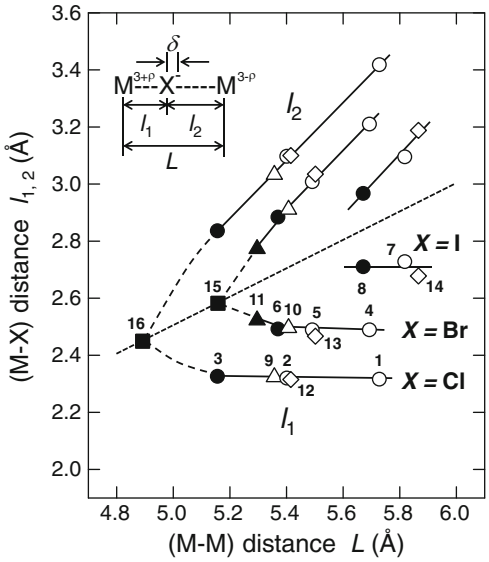

Fig. 2.3 Correlation between the M–M distance (L) and the M–X distance (l_1 and l_2). The material for each number is listed in Table 2.1. Data of the homometal compounds are represented by *circles* for M = Pt, *triangles* for M = Pd, and *squares* for M = Ni. Data of the heterometal compounds with M = Pt and Pd are represented by *diamonds*. *Open* and *filled marks* indicate the compounds with Y = ClO_4 and Y = halogen, respectively. (Reprinted figure with permission from [5])

2.2.1 Control of CDW Amplitudes

By replacing metals (M = Pt or Pd) and bridging halogens (X = Cl, Br, or I), the Coulomb repulsion energy (U) on the metal site and the transfer energy (t) between the nearest-neighbor two metal sites can be considerably changed. It is because the expanses of d_{z^2} orbitals of M and p_z orbitals of X are different among the respective metal ions (M) and bridging halogen ions (X) [13, 32]. As a result, we can obtain a variety of compounds having different bridging halogen displacements δ from the midpoint between the neighboring two M ions (see the inset of Fig. 2.3). The systematic structural studies revealed that δ is closely correlated to the metal to metal (M–M) distance L, which is strongly dependent on the choice of the ligand (A) and the counter anion (Y) and also on the strength of the H-bond between A and Y [32].

In Table 2.1, the M–M distance L, the metal to halogen (M–X) distance l_1 and l_2 ($l_1 < l_2$), the halogen displacement δ ($l_2 - l_1 = 2\delta$), and the distortion parameter d ($d = 2\delta/L$) are listed for various MX-chain compounds. In Fig. 2.3, the values of l_1 and l_2 are plotted as a function of L. The dotted line indicates $l_1 = l_2 = L/2$, which is a hypothetical line for no bridging halogen displacements ($\delta = 0$). The Ni compounds having the MH states are located on this line. The deviation of l_1 and l_2 from the dotted line corresponds to a magnitude of δ. The most significant feature in Fig. 2.3 is that the data points fall on almost the same lines according to the choice of bridging halogen (X) ions (Cl^-, Br^- or I^-), while M, A, and Y are replaced. It indicates the strong correlation between δ and L.

Table 2.1 The M–M distance L, the M–X distance l_1 and l_2 ($l_1 < l_2$), the bridging halogen displacement δ ($=(l_2 - l_1)/2$), the distortion parameter d ($=2\delta/L$), the CT-exciton energy E_{CT}, and the photoluminescence energy E_{Im} for various MX-chain compounds

		L (Å)	I_1 (Å)	I_2 (Å)	δ (Å)	d	E_{CT} (eV)	E_{Im} (eV)
1.	$[Pt(chxn)_2][Pt(chxn)_2Cl_2](ClO_4)_4$	5.730	2.314	3.416	0.511	0.190	3.20	1.49
2.	$[Pt(en)_2][Pt(en)_2Cl_2](ClO_4)_4$	5.403	2.318	3.095	0.3885	0.144	2.73	1.17
3.	$[Pt(chxn)_2][Pt(chxn)_2Cl_2]Cl_4$	5.158	2.324	2.834	0.255	0.099	1.99	0.90
4.	$[Pt(en)_2][Pt(en)_2Br_2](ClO_4)_4$-I	5.493	2.487	3.006	0.2595	0.094	1.98	0.78
5.	$[Pt(en)_2][Pt(en)_2Br_2](ClO_4)_4$-II	5.695	2.487	3.208	0.3605	0.1266	2.40	1.11
6.	$[Pt(chxn)_2][Pt(chxn)_2Br_2]Br_4$	5.372	2.490	2.882	0.196	0.073	1.40	0.68
7.	$[Pt(en)_2][Pt(en)_2I_2](ClO_4)_4$	5.820	2.726	3.093	0.1835	0.063	1.38	0.60
8.	$[Pt(chxn)_2][Pt(chxn)_2I_2]I_4$	5.673	2.708	2.965	0.2564	0.0453	0.94	–
9.	$[Pd(en)_2][Pt(en)_2Cl_2](ClO_4)_4$	5.357	2.324	3.003	0.3545	0.130	2.05	0.86
10.	$[Pd(en)_2][Pd(en)_2Br_2](ClO_4)_4$	5.407	2.911	2.496	0.2075	0.075	1.13	0.40
11.	$[Pd(chxn)_2][Pd(chxn)_2Br_2]Br_4$	5.296	2.523	2.773	0.125	0.047	0.75	–
12.	$[Pd(en)_2][Pt(en)_2Cl_2](ClO_4)_4$	5.415	2.315	3.100	0.3925	0.145	3.22	1.65
13.	$[Pd(en)_2][Pt(en)_2Br_2](ClO_4)_4$	5.502	2.467	3.035	0.284	0.103	2.59	1.54
14.	$[Pd(en)_2][Pt(en)_2I_2](ClO_4)_4$	5.866	2.678	3.188	0.255	0.087	2.28	1.12
15.	$[Ni(chxn)_2Cl_2]Cl_2$	4.894	2.447		0	0	1.83	–
16.	$[Ni(chxn)_2Br_2]Br_2$	5.160	2.580		0	0	1.28	–

Parameter values are taken from [5] and references therein

Typical MX-chain compounds have ClO_4^- for the counteranion (Y). The data of those compounds are shown by open marks in Fig. 2.3. The data of the compounds with halogen ions for Y are plotted by solid marks in the same figure. By changing the counteranion from ClO_4^- to halogen ions, the H-bonds between the amino groups of the ligands and the counteranions are strengthened. As a result, the M–M distance L is considerably decreased. Such a feature was ascertained by the infrared (IR) and X-ray measurements [28, 32, 56]. As shown in Fig. 2.3, the lengths L in the compounds with Y = halogen (solid marks) are relatively smaller than those of the compounds with Y = ClO_4 (open marks).

The position of the bridging halogen (X) ion between the neighboring two M ions, or the M–X distance l_1 and l_2, depends strongly on the choice of X. As seen in Fig. 2.3, the shorter M–X distance l_1 is almost constant in Pt or Pd compounds having the same X ions, even when L is considerably changed. The constant values of l_1 ($\sim$2.33 Å for X = Cl and $\sim$2.50 Å for X = Br, 2.68 $\sim$ 2.73 Å for X = I) are close to the sum of the ionic radii of the bridging halogen ions (Cl^-: 1.81 Å, Br^-: 1.96 Å and I^-: 2.16 Å [57, 58]) and the metal (Pd^{4+}: 0.62 Å and Pt^{4+}: 0.63 Å [59]). Starting from the M^{3+}–X^- regular chain structure, the deviation of l_1 from the dotted line ($L/2$) corresponds to the amplitude of the halogen displacements δ. Therefore, the decrease of L induces the decrease of the longer M–X distance l_2, and then induces the decrease of δ. Thus, we can consider that the decrease of L suppresses effectively the e–l interaction. At the same time, the decrease of L leads to the increase of transfer energy (t) between the neighboring M ions, making the electronic state more delocalized and also decreasing δ, that is, the CDW

amplitude. The increase of l_1 (the deviation from the constant value of l_1) in [Pd(chxn)$_2$Br]Br$_2$ (No. 11 in Fig. 2.3) located near the CDW-MH phase boundary is attributable to such an increase of t [28].

2.2.2 Control of CDW Degeneracy

MX compounds have the doubly degenerate CDW ground states, which are expressed as follows.

$$-X^- - M^{4+} - X^- - M^{2+} - X^- - M^{4+} - X^- - M^{2+} - X^- -$$
$$-X^- - M^{2+} - X^- - M^{4+} - X^- - M^{2+} - X^- - M^{4+} - X^- -$$

This degeneracy of CDW can also be modified by the choice of constituent elements.

In the CDW compounds with halogen for the counteranion (Y), a direction of each halogen displacement is two-dimensionally ordered in the *bc* plane [28, 32], as shown below.

$$-X^- - M^{4+} - X^- - M^{2+} - X^- - M^{4+} - X^- - M^{2+} - X^- -$$
$$-X^- - M^{4+} - X^- - M^{2+} - X^- - M^{4+} - X^- - M^{2+} - X^- -$$
$$-X^- - M^{4+} - X^- - M^{2+} - X^- - M^{4+} - X^- - M^{2+} - X^- -$$

This is not due to the overlapping of the electronic states between the neighboring MX chains but due to the interchain coupling through the tight network of the H-bonds between the aminogroups of the ligands (A) and the counter halogen ions (Y). Thus, although the electronic states are still one-dimensional, a 2D ordering of CDW is formed.

Degeneracy of CDW states can be excluded more clearly by the metal alternation method. By substituting a half of Pt ions with Pd ions in M = Pt compounds, we can obtain the heterometal compounds in which Pt and Pd ions are arranged alternatively [26]. In those compounds, the 1D electronic state consists of the 4d orbitals of Pd and the 5d orbitals of Pt. As the energy level of the former is lower than the latter, the CDW state is formed by Pd^{2+} ions and Pt^{4+} ions, as shown below.

$$-X^- - Pt^{4+} - X^- - Pd^{2+} - X^- - Pt^{4+} - X^- - Pd^{2+} - X^- -$$

In this type of the heterometal compounds, CDW states are nondegenerate. The lattice parameters, L, l_1 and l_2 for the heterometal compounds were also plotted in Fig. 2.3 by diamonds. The deviation of the data points from those of the homometal

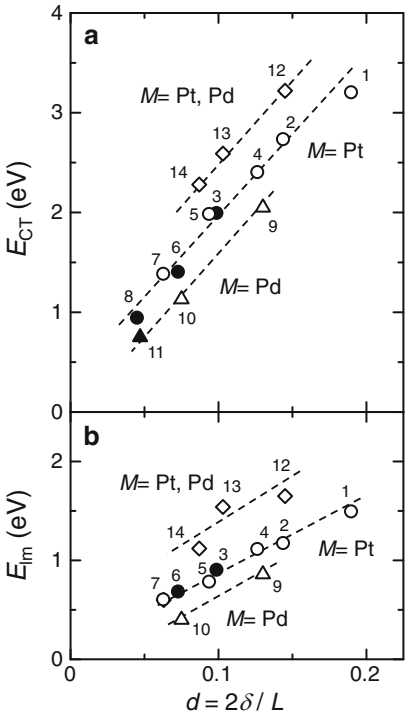

Fig. 2.4 Energies of (**a**) CT-exciton absorption peaks (E_{CT}) and (**b**) STE luminescence peaks (E_{lm}) as a function of the distortion parameter d. The material for each number is listed in Table 2.1. Data of the Pt compounds are represented by *circles*. Data of the heterometal compounds with M = Pt and Pd are represented by *diamonds*. *Open* and *filled marks* indicate the compounds with Y = ClO_4 and Y = halogen, respectively. (Reprinted figure with permission adapted from [5])

Pt or Pd compounds is very small. It is because L is determined mainly by the choice of the ligand (A), the counter anion (Y), and the bridging halogen ions (X), and l_1 is almost equal to the sum of the ion radii of Pt^{4+} and X^- ions as mentioned above.

It provides serious modifications to relaxation processes of photoexcited states in the MX chains whether CDW is degenerate or nondegenerate; in degenerate CDW states, solitons are the low-energy excitations and play dominant roles on the relaxation processes but in nondegenerate CDW states, formations of solitons are suppressed. Relaxation processes of photoexcited states associated with solitons are discussed in Sect. 2.3.2.

2.2.3 *Control of Optical Gap Energies*

In the MX-chain compounds, the lowest optical transition corresponding to the optical gap is the charge-transfer (CT) exciton transition expressed as (M^{2+}, $M^{4+} \rightarrow M^{3+}$, M^{3+}) [13, 32]. In Table 2.1, the energies of those transitions (E_{CT}) are listed for the various compounds. In Fig. 2.4a, E_{CT} is plotted for Pt and Pd compounds, and the heterometal (M = Pt and Pd) compounds as a function of the distortion parameter

d ($d = 2\delta/L$). E_{CT} is mainly determined by the energy difference E_s between the M^{2+} site and the M^{4+} site shown in Fig. 2.2b. In the compounds having the same metal ions, we can see the linear relation between E_{CT} and d, which indicates that E_s is proportional to the halogen displacement δ.

E_{CT} in Pd compounds is smaller than that in Pt compounds. This trend is related to the magnitude of the on-site Coulomb repulsion energy U. In the localized limit shown in Fig. 2.2a, E_{CT} is proportional to ($E_s - U$). Since U is larger in the Pd compounds than in the Pt compounds, E_{CT} in the former is lower than in the latter. In the heterometal compounds with M = Pt and Pd, E_{CT} is relatively larger than that in the homometal compounds with M = Pt. This is attributable to the energy difference between the 4d orbitals of Pd^{2+} and 5d orbitals of Pt^{2+}, since the energy level of the former is lower than the latter.

From the results of Fig. 2.3 showing the X, A, and Y dependence of δ and the results of Fig. 2.4a showing the M dependence of E_{CT}, we can widely control the magnitudes of E_{CT} by the choice of M, X, A, and Y.

2.3 Nature and Dynamics of Excitons, Solitons, and Polarons

Photogeneration and relaxation of excitons, solitons, and polarons in MX-chain compounds are strongly dependent on the optical gap energies E_{CT} and the bridging halogen displacements δ. In Sect. 2.3.1 we review the PL properties from STEs depending on E_{CT} and δ. In Sect. 2.3.2, we show how photogenerated solitons and polarons can be detected. In Sect. 2.3.3, we discuss the conversion process of an exciton to a spin-soliton pair. In Sect. 2.3.4, we summarize the overall relaxation dynamics of photoexcited states associated with excitons, solitons, and polarons in MX-chain compounds.

2.3.1 Self-Trapped Excitons

In MX-chain compounds, PL from STEs is observed in common. In Fig. 2.5, the PL spectrum of $[Pt(en)_2][Pt(en)_2Cl_2](ClO_4)_4$ at 2 K was shown as a typical example [11]. The PL peak is located at 1.2 eV, showing a large Stokes shift of about 1.5 eV. Such a large Stokes shift comes from the large lattice relaxation energy of the STE, which originates from the dissolution of the bridging halogen displacements as illustrated in Fig. 2.6a. Adiabatic potential energies of an exciton (FE and STE) as a function of the deformation coordinate Q (the displacements of the bridging X ions from their equilibrium positions in the CDW ground state) were also schematically shown in Fig. 2.6b. At the higher energy side of the PL, a series of 17 sharp structures due to Raman scattering bands are observed (Fig. 2.5), which correspond to the symmetric-stretching mode of bridging Cl ions. The appearance of the higher order Raman bands also indicates the strong e–l interaction of this compound.

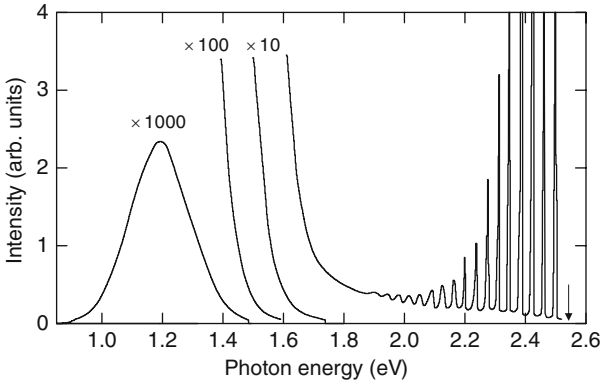

Fig. 2.5 Photoluminescence and Raman bands in $[Pt(en)_2][Pt(en)_2Cl_2](ClO_4)_4$ at 2 K. The excitation photon energy (2.54 eV) is indicated by the *arrow*. (Reprinted figure with permission from [11])

Dynamics of STE was studied by time-resolved PL measurements [60–62]. Figure 2.7 shows the time evolutions of PL at several probe energies in $[Pt(en)_2][Pt(en)_2Br_2](ClO_4)_4$-I. The oscillatory structures were observed and attributed to the wave-packet motion in the potential curve as shown by the arrow in Fig. 2.6b. A similar oscillation was also detected in $[Pt(en)_2][Pt(en)_2Br_2](PF_6)_4$ by using transient absorption technique [63].

Next, we discuss how the PL properties depend on materials. The energies of PL (E_{lm}) for various MX compounds were also listed in Table 2.1 and plotted against the distortion parameter d in Fig. 2.4b [5]. E_{lm} is 40–50 % of E_{CT} for the Pt or Pd compounds and 50–60 % for the heterometal compounds with M = Pt and Pd, showing large Stokes shifts in common. On the other hand, the efficiency of PL is considerably changed by the decrease in gap energy E_{CT}. In Fig. 2.8, the relative intensities of PL for the 2.4-eV excitation measured at 2 K are plotted for various MX compounds [5]. The intensity of PL decreases by more than four orders of magnitude when E_{CT} decreases from 2.7 to 1.4 eV. This result suggests that with decrease of E_{CT}, that is, the halogen distortion δ, the STE becomes unstable. Another feature in Fig. 2.8 is that the PL intensity in the compounds with nondegenerate CDW [the heterometal compounds (diamonds) and the Pt compounds with the 2D ordered CDW (solid circles)] is relatively larger than those of the Pt compounds with 1D CDW. This is related to the fact that nonradiative recombination of photoexcited states via soliton formations is suppressed in nondegenerate CDW compounds. This point is discussed in the following subsections.

2.3.2 *Photogeneration of Solitons and Polarons*

In this section, we review the studies of solitons and polarons in the MX-chain compounds. The most effective method to detect solitons and polarons is a

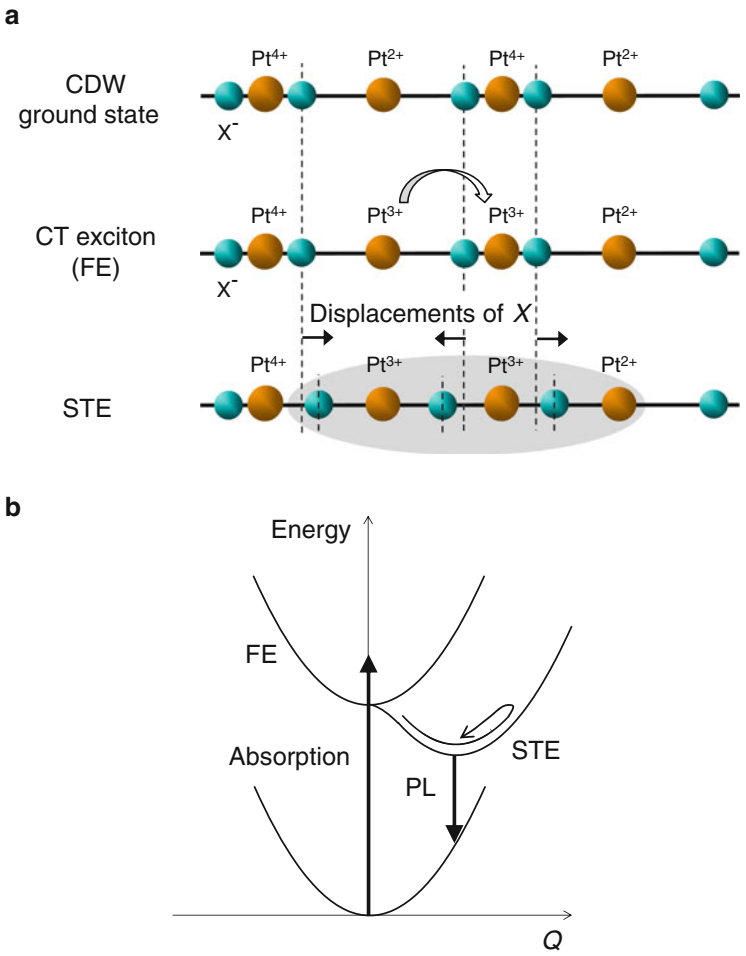

Fig. 2.6 (**a**) Schematic of the CDW ground state, the CT exciton (FE), and the STE. (**b**) Schematic of the adiabatic potential curves of the CT exciton (FE) and the STE as a function of the deformation coordinate (see the text)

photoinduced absorption (PA) spectroscopy, which had been indeed used for the studies of solitons, polarons, and bipolarons in conjugated polymers [2], and a number of important information were obtained. Photoinduced electron spin resonance (PESR) could also detect sensitively photoexcited species with spins. Those measurements were performed on the MX-chain compounds to clarify nature of photogenerated species.

At the beginning of those studies, the Pt–Cl chain compound, $[Pt(en)_2][Pt(en)_2Cl_2](ClO_4)_4$, had been extensively studied. In this compound, however, photoinduced gap states were very stable and not mobile so that they never decayed at low temperatures once they were photogenerated. Therefore, it was difficult to

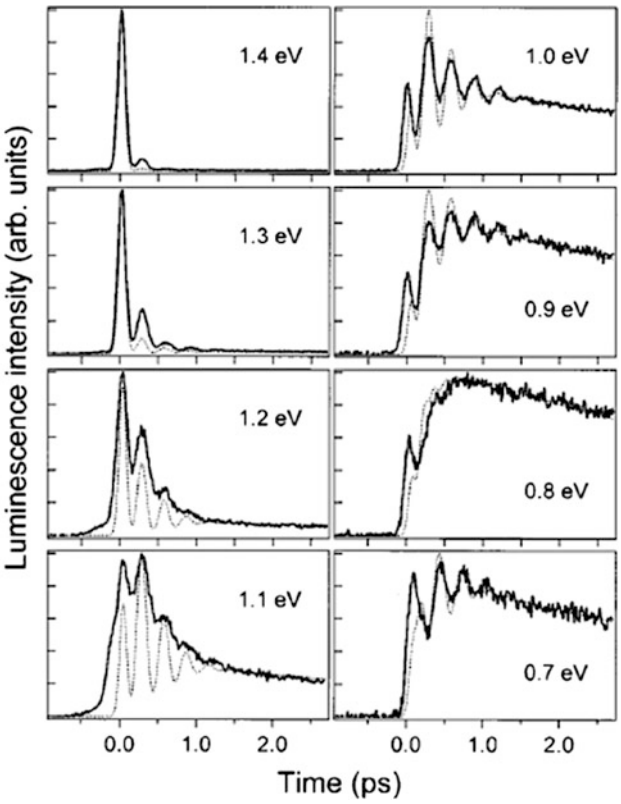

Fig. 2.7 Time evolutions of the luminescence intensity in $[Pt(en)_2][Pt(en)_2Br_2](ClO_4)_4$-I. The experimental results are shown by *solid lines*. *Dotted lines* shown the simulations (see [61]). (Reprinted figure with permission from [61]. Copyright (1999) by the American Physical Society)

investigate nature and dynamical aspects of the gap states in that compound. To solve this problem, Pt–Br and Pt–I chain compounds were subsequently studied, in which photoinduced gap states are mobile and their dynamical aspects could be clarified. Here, we introduce the comparative studies of the homometal compound, $[Pt(en)_2][Pt(en)_2Br_2](ClO_4)_4$-II, and the heterometal compound, $[Pd(en)_2][Pt(en)_2Br_2](ClO_4)_4$, using PA and PESR measurements [52]. As mentioned in Sect. 2.2.2, the CDW ground states are degenerate in the former and nondegenerate in the latter, so that solitons are stabilized only in the former. Such a difference in the two compounds enables us to obtain a clear evidence for the photogeneration of solitons. In $[Pt(en)_2][Pt(en)_2Br_2](ClO_4)_4$, two monoclinic polymorphisms with the space group $P2_1/m$ and $C2/m$ were obtained [10, 11] and labeled as I and II, respectively, as already used. Hereafter, $[Pt(en)_2][Pt(en)_2Br_2](ClO_4)_4$-II and $[Pd(en)_2][Pt(en)_2Br_2](ClO_4)_4$ are abbreviated as Pt–Br–Pt-II and Pd–Br–Pt, respectively.

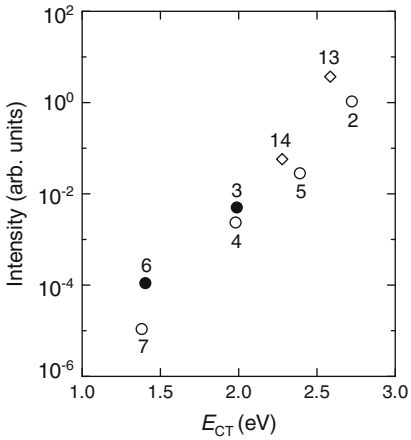

Fig. 2.8 Normalized integrated intensities of the luminescence as a function of E_{CT} in the MX chain compounds. The material for each number is listed in Table 2.1. Luminescence is measured at 2 K with the excitation photon energy of 2.4 eV. Data of the Pt compounds are represented by *circles*. Data of the heterometal compounds with M = Pt and Pd are represented by *diamonds*. *Open* and *filled marks* indicate the compounds with Y = ClO_4 and Y = halogen, respectively. (Reprinted figure with permission from [5])

Figure 2.9a shows the PA spectrum $\Delta\alpha$ (photoinduced change of $\alpha = kl$) of [Pt$(en)_2$][Pt$(en)_2Br_2$]$(ClO_4)_4$-II single crystal with the excitation of 3.2 eV at 77 K. Here, k and l are the absorption coefficient and the sample thickness, respectively. Polarization of both the irradiation light (E_{ex}) and the transmission light (E) is parallel to the chain axis b. In Fig. 2.9a, the polarized absorption spectrum for $E//b$ was also shown by the broken line. The arrow indicates the optical gap energy E_{CT}. A midgap absorption band labeled as **α** at 1.55 eV and a weak shoulder structure labeled as **β** at 1.79 eV were observed in as-grown samples. These absorption bands were enhanced by light irradiations. In addition, a weak PA band labeled as **γ** was observed at 0.7 eV. To discriminate the observed PA bands, time characteristics of three structures were investigated. The results showed that bands **α** and **β** exhibited the same decay characteristics, while band **γ** decays in a different manner compared with **α** and **β**. These results suggest that optically excited states include two different photoproducts associated with **α**, **β**, and with the lower energy band **γ**.

The absorption and PA spectra in the heterometal compound, Pt–Br–Pd, were shown in Fig. 2.9b. They were considerably different from the spectra in Pt–Br–Pt-II. In the absorption spectrum below the optical gap energy E_{CT}, there were no prominent structures. By the 3.2 eV excitation, two PA bands appeared, which were labeled as $\mathbf{a_1}$ and $\mathbf{a_2}$. $\mathbf{a_1}$ and $\mathbf{a_2}$ were found to show the same decay characteristics, suggesting that they are related to the same excited species.

To deduce the generation process of the photoproducts, excitation profiles of PA bands (**α** and **γ** in Pt–Br–Pt-II, and $\mathbf{a_1}$ in Pt–Br–Pd) were measured. The results are shown in Fig. 2.10 by circles for band **α**, triangles for band **γ** in Pt–Br–Pt-II, and the

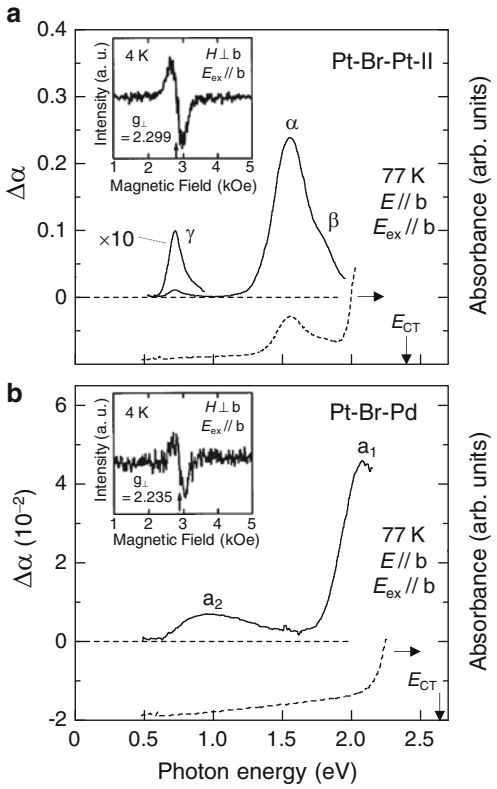

Fig. 2.9 PA spectra with the excitation of 3.2 eV and polarized absorption spectrum (*broken line*) measured at 77 K of (**a**) Pt–Br–Pt-II and (**b**) Pt–Br–Pd. Both the excitation lights (E_{ex}) and the transmission lights (E) are polarized parallel to the b axis. Insets show PESR spectra (derivative of absorption) at 4 K for the excitation of 3.1 eV. (Reprinted figure from [52])

inverted triangles for band $\mathbf{a_1}$ in Pt–Br–Pd. The thin solid line is the absorption spectra (ε_2) due to the CT excitons obtained from the polarized reflectivity spectra and their peaks correspond to E_{CT}. As seen, in Pt–Br–Pt-II, CT excitons do not contribute to the generation of band $\boldsymbol{\gamma}$, but contribute to band $\boldsymbol{\alpha}$. Band $\boldsymbol{\gamma}$ in Pt–Br–Pt-II and band $\mathbf{a_1}$ in Pt–Br–Pd were generated only for the excitation energies higher than E_{CT}.

PESR measurements were also performed to investigate whether the photoproducts have spins ($S = 1/2$) or not. In Pt–Br–Pt-II, an ESR signal was observed in an as-grown single crystal. The ESR signal was enhanced by the photoirradiations. The inset in Fig. 2.9a showed the increased component (the PESR signal) for the 3.1 eV excitation. The excitation profile of the integrated intensities of PESR signals was shown by solid squares in Fig. 2.10a. Paramagnetic spins were produced by the 2.5-eV excitation. The same excitation did not generate band $\boldsymbol{\gamma}$ but enhances bands $\boldsymbol{\alpha}$ and $\boldsymbol{\beta}$ so that the PESR signals in Pt–Br–Pt-II should be related to bands $\boldsymbol{\alpha}$ and $\boldsymbol{\beta}$. In those measurements, it could not be determined whether band $\boldsymbol{\gamma}$ is related to a spin ($S = 1/2$) or not.

In Pt–Br–Pd, on the other hand, no ESR signal was detected in an as-grown single crystal. The PESR signal by the 3.1 eV excitation was shown in the inset of Fig. 2.9b and the excitation profile of the integrated intensities of PESR signals was

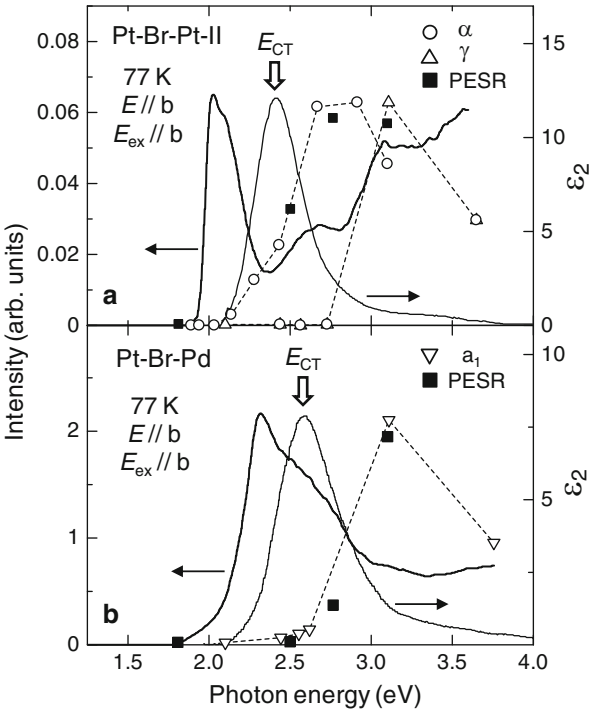

Fig. 2.10 Excitation profiles for the intensities of the PA bands (*open marks*), the PESR (*solid squares*), and the luminescence (*thick solid lines*) at 77 K in (**a**) Pt–Br–Pt-II and (**b**) Pt–Br–Pd. *Thin solid lines* show the imaginary part of the dielectric constants ε_2. (Reprinted figure from [52])

shown by solid squares in Fig. 2.10b. The PESR signals were observed only by the excitations above 2.7 eV. Such a behavior is in agreement with the excitation profile of the PA band $\mathbf{a_1}$, so that $\mathbf{a_1}$ is associated with a spin ($S = 1/2$).

Since these PA bands were observed in the gap region, it is natural to consider that they are attributable to spin-solitons (S^0), charged-solitons (S^+, S^-), or polarons (P^+, P^-) [10, 16, 21]. Figure 2.11 shows the localized energy levels of spin-solitons (S^0), charged-solitons (S^- and S^+), and polarons (P^- and P^+) in the case that the transfer energy t between the neighboring metal ions is equal to zero [21]. From this simplified picture, we can understand that S^0, P^+, and P^- have spin $S = 1/2$, and S^+ and S^- have no spin, while S^+, S^-, P^+, and P^- have a charge. The more realistic electronic structures of these gap states with a finite t are presented schematically in Fig. 2.12. Several groups reported theoretical absorption spectra of the gap states obtained based upon the 1D extended Peierls–Hubbard model [27, 33–35, 47]. Their spectral features are essentially the same; two absorption bands arise for a polaron, and one midgap band arises for either a spin- or charged-soliton.

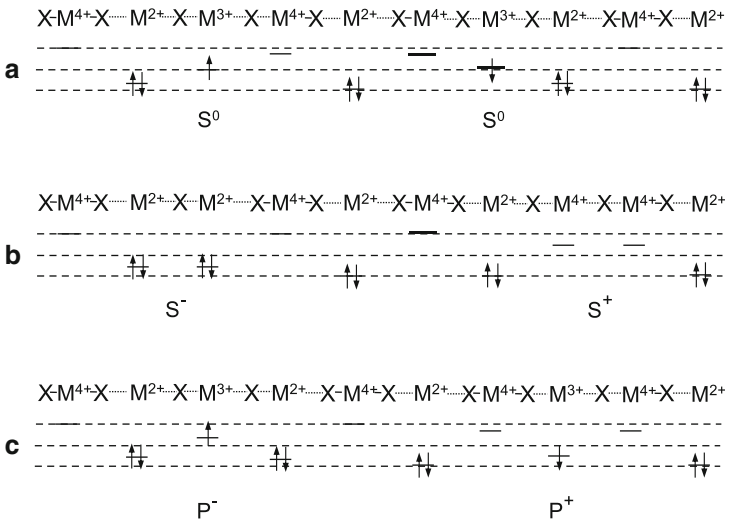

Fig. 2.11 Localized energy levels of (**a**) spin-solitons (S^0), (**b**) charged-solitons (S^-, S^+), and (**c**) polarons (P^-, P^+) (Reprinted figure with permission from [5])

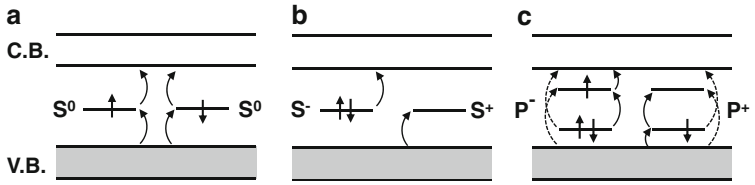

Fig. 2.12 Schematic electronic structures: (**a**) spin-solitons (S^0), (**b**) charged-solitons (S^-, S^+), and (**c**) polarons (P^-, P^+) (Reprinted figure with permission from [5])

In Fig. 2.12, the solid arrows indicate the possible optical transitions. For a polaron, it was theoretically revealed that oscillator strengths of the transitions indicated by broken arrows are extremely weak.

Taking into account the theoretical expectations shown in Fig. 2.12, a doublet structure $\mathbf{a_1}$ and $\mathbf{a_2}$ related to spins ($S = 1/2$) in Pt–Br–Pd could be assigned to polarons. It should be noted that in Pt–Br–Pd, electron polarons exist on the Pt sites and hole polarons on the Pd sites and therefore, the electron–hole asymmetry exists. In this case, PA energies for a positively charged polaron and a negatively charged one will be different from each other due to the difference in the magnitude of U on the metal sites. Thus the large spectral width of band $\mathbf{a_2}$ was attributed to the superposition of the two transitions slightly split due to the electron–hole asymmetry.

In Pt–Br–Pt-II, bands $\boldsymbol{\alpha}$, $\boldsymbol{\beta}$ and band $\boldsymbol{\gamma}$ have different origins as mentioned above. The important information is that PA bands $\boldsymbol{\alpha}$ and $\boldsymbol{\beta}$ were not detected in Pt–Br–Pd. Pt–Br–Pd has the nondegenerate CDW state, so that solitons should not be stabilized. These results suggested that bands $\boldsymbol{\alpha}$ and $\boldsymbol{\beta}$ could be attributed to

solitons. Considering that bands **α** and **β** are associated with spins, solitons responsible for **α** and **β** should be spin-solitons. A simple model shown in Fig. 2.12 expects that a single midgap absorption arises for a spin-soliton. However, the observed PA consists of a doublet structure **α** and **β** and is located at the higher energy than $E_{CT}/2$. These experimental features could be explained by the theoretical studies; Iwano et al. showed that the absorption band of a spin-soliton is split under the presence of quantum lattice fluctuations [33] and its energy is higher than $E_{CT}/2$ due to the effect of on-site Coulomb repulsion U [51]. Thus, PA bands **α** and **β** were reasonably assigned to spin-solitons.

The energy of band **γ** is small, being about $0.3 \times E_{CT}$, so that band **γ** was assigned to the lower energy transition of polarons, which correspond to $\mathbf{a_2}$ band in Pt–Br–Pd. In fact, the lower energy transitions of polarons are observed at around $0.37 \times E_{CT}$ in Pr–Br–Pd. In another Pt–Br chain compound, $[Pt(chxn)_2][Pt(chxn)_2Br_2]Br_4$ (chxn = cyclohexanediamine), the similar low energy PA band was also observed at $0.35 \times E_{CT}$ (not shown) [37]. Moreover, the excitation profile of polarons (band $\mathbf{a_1}$) in Pt–Br–Pd is similar to that of band **γ**, as shown in Fig. 2.10. This also supports the assignment of band **γ** to the lower energy transition of polarons. The higher energy transition of polarons could not be identified in these studies. It was considered to be obscured by the strong PA band **β**.

2.3.3 Conversion of an Exciton to a Spin-Soliton Pair

In this section, we discuss the relaxation dynamics of photoexcited states in MX-chain compounds associated with excitons, solitons, and polarons. As mentioned above, two relaxation processes are considered to exist; radiative decay (PL) from STE and nonradiative decay via conversions to soliton or polaron pairs and their recombination. In order to clarify the interrelation of these two processes, excitation profiles of PL were measured and compared to those of PA signals in Pt–Br–Pt-II and Pt–Br–Pd, which were shown in Fig. 2.10 [5, 52].

The excitation profiles of PL from STE were shown by thick solid lines in Fig. 2.10. In Pt–Br–Pt-II, the intensity of PL begins to increase from the absorption edge at about 1.9 eV and then decreases sharply at around E_{CT}. Such a sharp decrease of PL corresponds to the increase of the generation efficiency of spin-soliton pairs. This suggests that a conversion from an exciton to a spin-soliton pair occurs. This interpretation was supported by the fact that in Pt–Br–Pd the PL intensity did not decrease for the excitations with the energy of E_{CT} and that the relative PL intensity in Pt–Br–Pd is more than one order of magnitude larger than that in Pt–Br–Pt-II (see Figs. 2.8 and 2.10).

Dynamical aspects of the exciton to spin-soliton conversion were also investigated by the time-resolved PL measurements. In Fig. 2.13, the time-integrated PL spectra due to STEs at 10 K were shown by solid lines, and time characteristics of PL were shown in the insets. PL dynamics were reproduced by a single exponential decay, as shown by the broken lines. The decay time τ is ∼220 ps in Pt–Br–Pt-II and ∼390 ps in Pt–Br–Pd. Those values are at least one order of

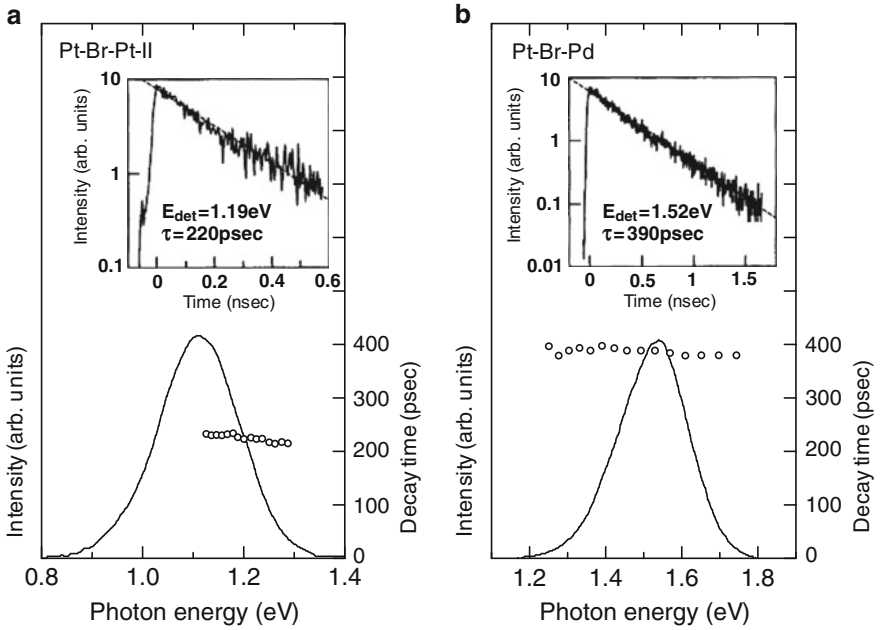

Fig. 2.13 Photoluminescence spectra (*solid lines*) and photoluminescence decay time τ (*circles*) at 10 K for the excitation energy of 3.2 eV in (**a**) Pt–Br–Pt-II and (**b**) Pt–Br–Pd. Both the excitation lights (E_{ex}) and the emission lights (E) are polarized parallel to the b axis. Insets show the time characteristics of photoluminescence for the detection energies of 1.19 eV in Pt–Br–Pt-II and 1.52 eV in Pt–Br–Pd. *Broken lines* show single exponential decays. (Reprinted figure from [52])

magnitude smaller than the radiative life time τ_r of STEs (4–6 ns) [20, 48], which was estimated from the oscillator strength of the CT-exciton transition in typical Pt compounds. This indicated that annihilations of STEs were dominated by nonradiative processes.

Figure 2.14 showed the temperature dependence of the decay time τ of PL in Pt–Br–Pt-II and Pt–Br–Pd, which was well reproduced by using the following formula as shown by the broken lines in Fig. 2.14.

$$\tau = \left[{\tau_0}^{-1} + {\tau_a}^{-1}\exp(-\Delta/kT)\right]^{-1} \tag{2.1}$$

The used parameter values were $\tau_0 = 225$ ps, $\tau_a = 115$ ps, and $\Delta = 9.5$ meV in Pt–Br–Pt-II, and $\tau_0 = 385$ ps, $\tau_a = 38$ ps, and $\Delta = 34$ meV in Pt–Br–Pd. The smaller values of τ (or Δ and τ_0) in Pt–Br–Pt-II compared to Pt–Br–Pd was considered due to the conversion from STEs to soliton pairs.

The theoretical studies based upon the 1D extended Peierls–Hubbard model provided detailed potential energy surfaces of the excited states for homometal CDW compounds, which were detailed in [22, 23, 51] and also in Chap. 8. The inset of Fig. 2.14 showed the cross section of the first and the second lowest potential surfaces as a function of intersoliton distance l_0. The higher potential surface

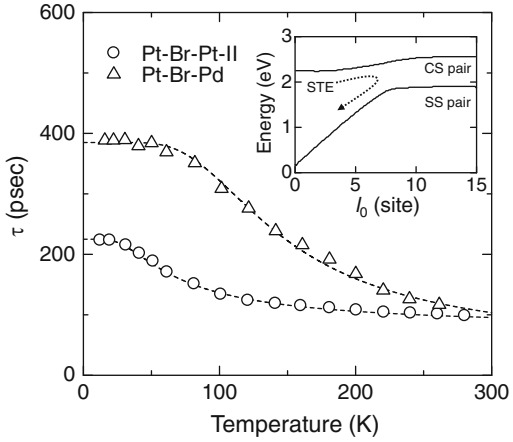

Fig. 2.14 Temperature dependence of the luminescence decay time τ. The detection energies are 1.19 eV in Pt–Br–Pt-II and 1.52 eV in Pt–Br–Pd. The inset shows the cross-section of the calculated potential energy surfaces (taken from [51]). SS and CS show a spin-soliton pair and a charged-soliton pair, respectively. (Reprinted figure from [52])

includes the STE and the charged-soliton pair and the lower surface includes the spin-soliton pair and is connected to the CDW ground state. With the parameters appropriate for MX-chain compounds, a spin-soliton pair is always the lowest energy excitation, although the energy difference between a spin-soliton pair and an STE is not so large [51].

According to more detailed theoretical analyses, a conversion from the STE to the spin-soliton pair was possible. These expectations were in good agreement with the experimental results of Pt–Br–Pt-II discussed above. In Pt–Br–Pt-II, it is reasonable to consider that Δ is a potential barrier between the STE and the spin-soliton pair and τ_0^{-1} is a tunneling rate through the barrier. We can imagine in the inset of Fig. 2.14 that such a barrier exists when the conversion from the STE to the spin-soliton pair occurs at large values of l_0, e.g., larger than 8. In Pt–Br–Pd, the energy of potential surfaces is expected to increase sharply with increasing l_0 compared with that in Pt–Br–Pt-II (the inset of Fig. 2.14), so that the spin-soliton pair cannot be dissociated. This situation is analogous to bipolarons in nondegenerate conjugated polymers. In this case, the depth of the potential well around the STE should be increased. As a result, Δ was enhanced and τ_0^{-1} was decreased in Pt–Br–Pd relative to those values in Pt–Br–Pt-II. Thus, it is expected that the main relaxation path of STEs in Pt–Br–Pd is also the nonradiative recombination process through the solitonic states, which is essentially the same as that indicated by the arrows in the inset of Fig. 2.14 except for the slope of potential surfaces.

It is important to comment on the comparison of solitons in MX-chain compounds with those in *trans*-$(CH)_x$, in which nature of spin-solitons had also been extensively studied. In *trans*-$(CH)_x$, however, a conversion of an electron-hole

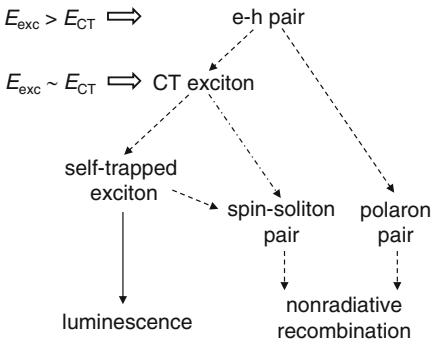

Fig. 2.15 Schematic diagram of the relaxation process of the photoexcited state in Pt–Br–Pt-II (Reprinted figure with permission from [5])

pair (the singlet B_u state) to a spin-soliton pair is essentially forbidden within the noninteracting electron model, due to the charge configuration symmetry in the bond ordered wave (BOW) ground state [64, 65]. Additional interactions (i.e., a second nearest-neighbor hopping [64]) which break the charge configuration symmetry, permit the conversion of the electron-hole pair to a spin-soliton pair. On the other hand, the MX-chain compounds are not charge configuration symmetric from the nature of CDW, so that photogeneration of spin-solitons is possible to occur. Moreover, in contrast to *trans*-$(CH)_x$, the excitonic effect is important in MX-chain compounds. Thus, the generation process of spin-solitons from the photoexcited states in MX-chain compounds is considerably different from that in *trans*-$(CH)_x$.

2.3.4 Overall Dynamics of Photoexcited States

The relaxation process of photoexcited states in Pt–Br–Pt-II was summarized in Fig. 2.15. Polarons are not generated from the CT exciton, since the energy of a polaron pair is much higher than the CT exciton. Polarons can be generated only from the higher energy excited states corresponding probably to the electron-hole continuum. CT excitons are relaxed to STEs. A part of STEs decay by PL, and the other parts are relaxed to spin-soliton pairs and then decay nonradiatively. CT excitons with large excess energies dissociate into spin-soliton pairs before stabilizing as STEs, since the generation efficiency of spin-solitons increases with increase of the excitation photon energy at around E_{CT} as seen in Fig. 2.10. This process is also shown by the dashed–dotted line in Fig. 2.15.

As mentioned in Sect. 2.2.2, Pt and Pd compounds having halogen ions as the counter anions show the 2D-ordered CDW states. In a typical example of such compounds, $[Pt(chxn)_2][Pt(chxn)_2Br_2]Br_4$, it was also demonstrated that photogenerations of solitons were suppressed [37] and only the photogeneration of polarons was observed. In general, in the compounds having 2D-ordered CDW states, PL intensities were relatively larger than that in the 1D CDW compounds as seen in Fig. 2.8, consistent with the result of the hetero-metal compound, Pt–Br–Pd.

When the bridging halogen displacement δ and the optical gap energy E_{CT} decrease and a compound approaches to the CDW-MH phase boundary, photoresponses are largely changed from those discussed here. A photoexcited state in the CDW ground state, that is, a M^{3+} pair is converted to a M^{3+} domain over several tens M^{3+} sites [66, 67]. In this case, the lowest photoexcited state of a M^{3+} pair cannot be regarded as an excitonic state, but the photoresponses should be regarded as a photoinduced phase transition from CDW to MH state. Such photoinduced CDW to MH transitions were indeed observed in $[Pd(chxn)_2][Pd(chxn)_2Br_2]Br_4$ and $[Pt(chxn)_2][Pt(chxn)_2I_2]I_4$ [66, 67]. In the latter compound, the photoinduced CDW to metal transition was also found in the case of strong photoexcitations. Photoinduced phase transitions in those MX-chain compounds are discussed in Chap. 5 in detail.

2.4 Summary

In this chapter, we reviewed the tunability of the CDW states in MX-chain compounds. By substituting the metals (M = Pt, Pd, and Ni), the bridging halogens (X = Cl, Br, and I), and the ligand molecules and the counter anions surrounding MX chains, the amplitude of CDW, the degeneracy of CDW, and the optical gap energy could be widely controlled. On the basis of such controls of the CDW states, nature of photoexcited states, i.e., excitons, solitons, and polarons, was investigated. From the comparative studies of the degenerate and nondegenerate CDW compounds using photoluminescence, photoinduced absorption, and photoinduced electron spin resonance measurements, the photoinduced gap states were clearly characterized as spin-solitons and polarons. By comparing the excitation profiles of the photoinduced absorption signals due to spin-solitons and the photoluminescence from self-trapped excitons, it was demonstrated that the luminescence process competes with the dissociation to spin-soliton pairs and the subsequent nonradiative decay. The detailed analyses of the temperature dependence of the photoluminescence decay time revealed that a conversion from a self-trapped exciton to a spin-soliton pair occurs through a finite potential barrier, the magnitude of which depends on the degeneracy of CDW. Such an exciton to a spin-soliton pair conversion could be explained by the theoretical simulations based upon the 1D-extended Peierls–Hubbard model. Thus, a spin-soliton pair is the lowest energy excitation, so that it plays dominant roles on the relaxation process of photoexcited states in MX-chain compounds having CDW ground states.

On the basis of these fundamental studies on the CDW states, a great deal of efforts for designs and syntheses of new MX-chain compounds and explorations of new phenomena have been made. As a result, a variety of novel physical properties such as gigantic nonlinear optical responses and ultrafast-photoinduced phase transitions have been discovered. The details of them are reviewed in the following several chapters from both experimental and theoretical points of view.

References

1. Whitfield G, Shaw PB (1976) Phys Rev B 14:3346
2. For a review, see Heeger AJ, Kivelson S, Schrieffer JR (1988) Rev Mod Phys 60: 781
3. Su WP, Schrieffer JR, Heeger AJ (1979) Phys Rev Lett 42:1698
4. Su WP, Schrieffer JR, Heeger AJ (1980) Phys Rev B22:2099
5. Okamoto H, Yamashita M (1998) Bull Chem Soc Jpn 71:2023
6. Tanino H, Kobayashi K (1983) J Phys Soc Jpn 52:1446
7. Nasu K (1984) J Phys Soc Jpn 52:3865
8. Nasu K (1984) J Phys Soc Jpn 53:302
9. Nasu K (1984) J Phys Soc Jpn 53:427
10. Ichinose S (1984) Solid State Commun 50:137
11. Tanaka M, Kurita S, Okada Y, Kojima T, Yamada Y (1985) Chem Phys 96:343
12. Tanino H, Koshizuka N, Kobayashi K, Yamashita M, Hoh K (1985) J Phys Soc Jpn 54:483
13. Wada Y, Mitani T, Yamashita M, Koda T (1985) J Phys Soc Jpn 54:3143
14. Matsushita N, Kojima N, Ban T, Tsujikawa I (1987) J Phys Soc Jpn 56:3808
15. Kuroda N, Sakai M, Nishina Y, Tanaka M, Kurita S (1987) Phys Rev Lett 58:2212
16. Onodera Y (1987) J Phys Soc Jpn 56:250
17. Kurita S, Haruki M, Miyagawa K (1988) J Phys Soc Jpn 57:1789
18. Haruki M, Kurita S (1988) Phys Rev B39:5706
19. Wada Y, Era K, Yamashita M (1988) Solid State Commun 67:953
20. Tanino H, Ruhle W, Takahashi K (1988) Phys Rev B38:12716
21. Baeriswyl D, Bishop AR (1988) J Phys C 21:339
22. Mishima A, Nasu K (1989) Phys Rev B39:5758
23. Mishima A, Nasu K (1989) Phys Rev B39:5763
24. Matsushita N, Kojima N, Watanabe N, Tsujikawa I (1989) Solid State Commun 71:253
25. Donohoe RJ, Ekberg SA, Tait CD, Swanson BI (1989) Solid State Commun 71:49
26. Wada Y, Mitani T, Toriumi K, Yamashita M (1989) J Phys Soc Jpn 58:3013
27. Tagawa Y, Suzuki N (1990) J Phys Soc Jpn 59:4074
28. Okamoto H, Toriumi K, Mitani T, Yamashita M (1990) Phys Rev B42:10381
29. Wada Y, Yamashita M (1990) Phys Rev B42:7398
30. Kuroda N, Sakai M, Suezawa M, Nishina Y, Sumino K (1990) J Phys Soc Jpn 59:3049
31. Okamoto H, Okaniwa K, Mitani T, Toriumi K, Yamashita M (1991) Solid State Commun 77:465
32. Okamoto H, Mitani T, Toriumi K, Yamashita M (1992) Mater Sci Eng B13:L9
33. Iwano K, Nasu K (1992) J Phys Soc Jpn 61:1380
34. Gammel JT, Saxena A, Batistic I, Bishop AR, Phillpot SR (1992) Phys Rev B45:6408
35. Webber-Milbrodt SM, Gammel JT, Bishop AR, Lor EY Jr (1992) Phys Rev B45:6435
36. Donohoe RJ, Worl LA, Arrington CA, Bulou A, Swanson BI (1992) Phys Rev B45:13185
37. Okamoto H, Mitani T, Toriumi K, Yamashita M (1992) Phys Rev Lett 69:2248
38. Sakai M, Kuroda N, Suezawa M, Nishina Y, Sumino K, Yamashita M (1992) J Phys Soc Jpn 61:1326
39. Okamoto H, Toriumi K, Mitani T, Yamashita M (1992) Mol Cryst Liq Cryst 218:247
40. Okamoto H, Mitani T (1993) Prog Theor Phys Suppl 113:191
41. Okamoto H, Mitani T, Toriumi K, Yamashita M (1993) Synth Met 55:524
42. Kuroda N, Ito M, Nishina Y, Kawamori A, Kodera Y, Matsukawa T (1993) Phys Rev B48:4245
43. Kuroda N, Ito M, Nishina Y, Yamashita M (1993) J Phys Soc Jpn 62:2237
44. Ooi H, Yamashita M, Kobayashi T (1993) Solid State Commun 86:789
45. Ooi H, Yoshizawa M, Yamashita M, Kobayashi T (1993) Chem Phys Lett 210:237
46. Tagawa Y, Suzuki N (1995) J Phys Soc Jpn 64:1800
47. Tagawa Y, Suzuki N (1995) J Phys Soc Jpn 64:2212
48. Wada Y, Lemmer U, Gobel EO, Yamashita M, Toriumi K (1995) Phys Rev B52:8276

49. Okamoto H, Oka Y, Mitani T, Yamashita M (1997) Phys Rev B55:6330
50. Okamoto H (1997) In: Nasu K (ed) Relaxations of excited states and photoinduced structural phase transitions. Springer, Berlin, p 92
51. Iwano K (1997) J Phys Soc Jpn 66:1088
52. Okamoto H, Kaga Y, Shimada Y, Oka Y, Iwasa Y, Mitani T, Yamashita M (1998) Phys Rev Lett 80:861
53. Toriumi K, Wada Y, Mitani T, Bandow S, Yamashita M, Fujii Y (1989) J Am Chem Soc 111:2341
54. Toriumi K, Okamoto H, Mitani T, Bandow S, Yamashita M, Wada Y, Fujii Y, Clark RJH, Michael DJ, Edward AJ, Watkin D, Kurmoo M, Day P (1990) Mol Cryst Liq Cryst 181:333
55. Okamoto H, Shimada Y, Oka Y, Chainani A, Mitani T, Toriumi K, Inoue K, Manabe T, Yamashita M (1996) Phys Rev B54:8438
56. Okaniwa K, Okamoto H, Mitani T, Toriumi K, Yamashita M (1991) J Phys Soc Jpn 60:997
57. Pauling L (1960) The nature of the chemical bond, 3rd edn. Cornell University Press, New York
58. Muller O, Roy R (1974) The major ternary structural families. Springer, New York
59. Lide DR, Lide Jr (1998) Handbook of chemistry and physics, 79th edn. CRC press, Boca Raton, FL
60. Tomimoto S, Nansei H, Saito S, Suemoto T, Sakata K, Takeda J, Kurita S (1998) Phys Rev Lett 81:417
61. Tomimoto S, Saito S, Suemoto T, Sakata K, Takeda J, Kurita S (1999) Phys Rev B60:7961
62. Matsuoka T, Suemoto T, Takeda J, Kurita S (2003) Phys Rev Lett 91:247402
63. Dexheimer SL, Van Pelt AD, Brozik JA, Swanson BI (2000) Phys Rev Lett 84:4425
64. Kivelson S, Wu W-K (1986) Phys Rev B 34:5423
65. Takimoto J, Sasai M (1989) Phys Rev B 39:8511
66. Matsuzaki H, Yamashita M, Okamoto H (2006) J Phys Soc Jpn 75:123701
67. Kimura K, Matsuzaki H, Takaishi S, Yamashita M, Okamoto H (2009) Phys Rev B 79:075116

Chapter 3
Ni(III) Mott–Hubbard Compounds

S. Takaishi and M. Yamashita

3.1 Introduction

For a long time, MX-chain compounds have been extensively studied since Wolffram reported Cl-bridged Pt complex in 1900. To date, more than 300 compounds were reported by combining metal ions (M = Ni, Pd, Pt), bridging halogens (X = Cl, Br, I) in plane ligands (L = ethylenediamine(en), 1*R*,2*R*-diaminocyclohexane(chxn), etc.), and counteranions (ClO_4^-, BF_4^-, X^-, etc.). However, the number of Ni compounds is very few compared to Pd or Pt compounds. The first Ni complex was reported by Yamashita et al. in 1981. Although there had been much controversy about the electronic state of these compounds, it has been clarified that this complex is in averaged valence state by means of X-ray crystal structure analysis [1]. In the Ni complexes, many attractive physical properties have been reported such as gigantic third-order nonlinear optical susceptibility [2], spin-Peierls transition [3], etc. In this chapter, we introduce structure, physical properties, and recent progresses in the Ni complexes.

3.2 Crystal Structure

Figure 3.1 shows a crystal structure of the Ni^{III} complex $[Ni(chxn)_2Br]Br_2$ [1]. $Ni(chxn)_2$ moieties are bridged by Br ions, forming a –Ni–Br–Ni–Br– linear chain along *b*-axis. The crystal structure of this compound is isomorphic to the corresponding Pd and Pt compounds $[M(chxn)_2X]X_2$ (M = Pd and Pt; X = Cl, Br, and I). There is significant difference in the position of the bridging halide ions

S. Takaishi (✉) • M. Yamashita
Department of Chemistry, Graduate School of Science, Tohoku University,
6-3 Aramaki-Aza-Aoba, Aoba-Ku, Sendai 980-8578, Japan
e-mail: takaishi@mail.tains.tohoku.ac.jp

M. Yamashita and H. Okamoto (eds.), *Material Designs and New Physical Properties in MX- and MMX-Chain Compounds*, DOI 10.1007/978-3-7091-1317-2_3,

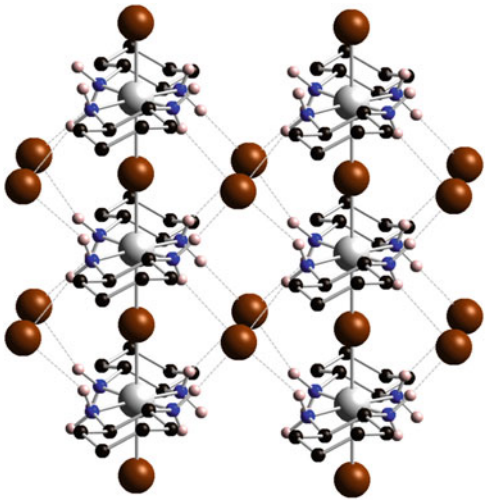

Fig. 3.1 Crystal structure of $[Ni(chxn)_2Br]Br_2$. *Gray*: Ni, *Brown*: Br, *Black*: C, *Blue*: N, *Pink*: H

between the Ni and the Pd and Pt ions. In the Ni complexes, bridging Br^- ions are located at the midpoints between neighboring Ni ions, whereas they are displaced from the midpoint in Pd or Pt compounds and are disordered [4]. This indicates that the Ni ions are in a trivalent Ni^{III} Mott–Hubbard (MH) state. There are hydrogen bonds between the amino protons and counteranions, forming a 2D hydrogen-bond-network. Ni–Ni distances along the 1D chain are 5.161(2) Å.

3.3 Magnetic Properties

Figure 3.2 shows the temperature dependence of the magnetic susceptibility of $[Ni(chxn)_2Br]Br_2$ measured as a single crystal [3]. Curie-like behavior was observed at low temperatures, whereas nearly no temperature dependence was observed at higher temperatures. The small amount of spin concentration showing Curie-like behavior (≈0.4 %) was attributed to some paramagnetic impurities or spins at the chain end. The weak temperature dependence of the susceptibility at high temperature region was interpreted to be due to an $S = 1/2$ Heisenberg chain with strong antiferromagnetic (AF) interactions. Such temperature dependence of susceptibilities can be understood via the Bonner–Fisher theory [5]. Recently, Eggert, Affleck, and Takahashi (EAT) have proposed a theory that explains more accurately the susceptibilities, which slightly differ from Bonner–Fisher behavior at low temperatures [6]. The result of EAT theory for $T < 0.2\ J/k_B$ is given by the following equation:

$$\chi(T) = \frac{N{g^2}{\mu_B}^2}{2J\pi^2}\left\{1 + \frac{1}{2\ln(15.4J/k_BT)}\right\}, \tag{3.1}$$

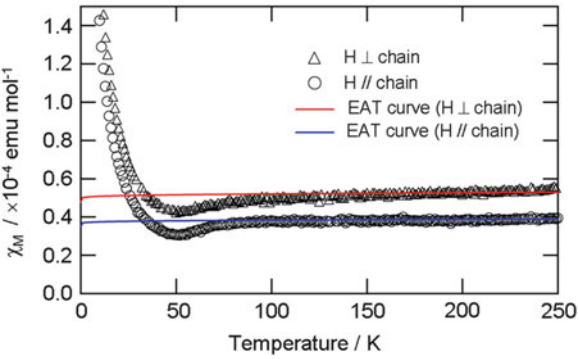

Fig. 3.2 Magnetic susceptibilities observed in a single crystal of $[NiBr(chxn)_2]Br_2$ with a magnetic field (1 T) parallel and perpendicular to the 1D chain. *Red* and *blue lines* show theoretical susceptibilities proposed by Eggerd–Affleck–Takahashi (EAT) with $J = 2{,}000$ K

where N is the Avogadro's number, g is the Lande's factor, and k_B is the Boltzmann constant. In this equation, J is defined as $H = 2J\Sigma S_i \cdot S_{i+1}$. The exchange interaction was estimated to be $J/k_B = 2{,}000 \pm 500$ K by fitting the present data above 130 K in Eq. (3.1). The magnetic susceptibility slightly decreased below 100 K. This suggests that some phase transition to a nonmagnetic state, such as CDW $(-\mathrm{Br}\cdots\mathrm{Ni^{II}}\cdots\mathrm{Br}-\mathrm{Ni^{IV}}-\mathrm{Br}\cdots)$ or spin-Peierls states $(\cdots\mathrm{Br}\cdots\mathrm{Ni^{III}}-\mathrm{Br}-\mathrm{Ni^{III}}\cdots\mathrm{Br}\cdots)$, occurs.

We measured the temperature dependence of the nuclear quadrupole resonance (NQR) signals of the bridging Br ions because the NQR is a quite sensitive probe for detecting subtle changes in the electron distribution around NQR nuclei.

We observed a single resonance line for ^{81}Br at 300 K (137.079 ± 0.005 MHz) and a pair of lines at 130.874 ± 0.01 and 147.786 ± 0.01 MHz at 3.8 K. We assigned these resonance signals to ^{81}Br nuclei on the basis of the corresponding ^{79}Br lines at 164.091 ± 0.005 MHz (300 K) and at 156.656 ± 0.01 and 176.904 ± 0.01 MHz (3.8 K), which are in agreement with the reported isotope frequency ratio (^{79}Br/^{81}Br = 1.1969) [7]. These resonance frequencies were assigned to bridging Br^- ions and not to counter Br^- ions since ^{79} Br NQR frequencies in compounds with Ni–Br covalent bonds have been observed in nearly the same frequency range, e.g., 126.26 MHz for $NiBr_2[P(C_3H_7)_3]_2$ and 126.53 MHz for $NiBr_2[P(C_4H_9)_3]_2$ [8], whereas the resonance lines for ionic Ni–Br bonds are usually at frequencies of one order of magnitude lower than those for the present complex [9].

Figure 3.3 shows a temperature dependence of the ^{81}Br NQR frequencies for the bridging Br^- ions in $[Ni(chxn)_2Br]Br_2$. A single ^{81}Br NQR peak was observed at room temperature, which is consistent with the X-ray results, where all of the bridging Br^- sites are equivalent at room temperature. The resonance frequency gradually decreased with an increase in the temperature above 130 K due to averaging of the electric field gradient (EFG) at Br nuclei by lattice vibrations. The temperature dependence of the NQR frequency ($\nu(T)$) can be described by the harmonic oscillator model for lattice vibrations [10, 11]:

$$\nu(T) = \nu_0 \left[1 - A \coth\left(\frac{\hbar\omega}{2kT}\right)\right] \tag{3.2}$$

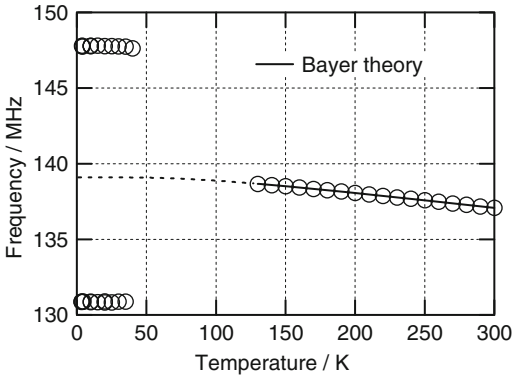

Fig. 3.3 Temperature dependences of ^{81}Br NQR frequencies observed in $[Ni(chxn)_2Br]Br_2$. *Dotted line* is an extrapolation to 0 K according to the Bayer theory

where ν_0, A, and ω are the resonance frequency for the static lattice, a coefficient that depends on modes of lattice vibrations, and the averaged vibration frequency, respectively. The observed data were fitted with Eq. (3.2), and the extrapolated frequency to 0 K ($\nu(0)$) was determined to be 139.1 ± 0.2 MHz.

Upon cooling, the NQR signal disappeared around 130 K, and two lines at 130.87 and 147.78 MHz appeared again below ca. 40 K. The loss of resonance signals between 40 and 130 K is thought to be spectrum broadening due to fluctuation in the EFG upon phase transition. Since the averaged frequency of these two lines is almost the same as the extrapolated frequency from the high-temperature side, the NQR signals below 40 K are split into one of the high-temperature signal. Two resonance lines with a large frequency separation of 16.9 MHz at low temperatures indicate the presence of two nonequivalent Br^- sites, suggesting that a change in the electronic state in $[Ni(chxn)_2Br]Br_2$ takes place between 40 and 130 K.

Here we discuss the possible electronic structures of $[Ni(chxn)_2Br]Br_2$. In an averaged valence MH state, the environments of all Ni or bridging Br^- sites should be equivalent, resulting in a single Br NQR line. In a CDW state, the bridging Br^- ions are displaced, but the sites are equivalent. However, there are two nonequivalent Ni sites, and hence, this state affords a single Br NQR line. In the spin-Peierls state, which is characterized by the displacement of the Ni sites, two nonequivalent bridging Br^- sites are formed in agreement with the two Br NQR lines. The splitting of NQR signals indicates that a spin-Peierls transition occurs in $[Ni(chxn)_2Br]Br_2$ in the range of 40–130 K. This explanation is consistent with the decrease in the magnetic susceptibility observed below 100 K. As shown in Fig. 3.2, χ deviated isotropically from the EAT curve below 100 K clearly. This decrease in χ is due to spin cancelation caused by the transition into a spin-Peierls state.

The charge distribution in the Ni–Br bond can be evaluated by applying the Townes–Dailey approximation: [12, 13]

$$\left|e^2Qq\right| = (1-i)(1-s)\left|e^2Qq_{\text{atom}}\right| \tag{3.3}$$

where e^2Qq, e^2Qq_{atom}, i, and s are the observed coupling constants, given twice the observed resonance frequency ($2h\nu$) by assuming an axially symmetric EFG, the coupling constant for atomic ^{81}Br given by 643.032 MHz [14], the degree of ionicity of the Ni–Br bond, and the s-character of the bonding orbital in Br^- ions, respectively. The s-character, which is the contribution of the s-orbital in the sp-hybrid orbital of Br^- ions, was assumed to be 0.15 by Dailey and Townes [12, 13] in cases when the halide ion is bonded to atoms that are 0.25 more electropositive than the halide ion. Thus, partial electron-transfer values (i) from Ni to Br in comparison with the value (0.0) for a neutral Br atom were approximated to be 0.491 (high-temperature phase) and 0.521 and 0.459 (low-temperature phase). The high-temperature phase $\nu(0)$ was used to determine e^2Qq ($\approx 2\nu(0)$). The differences between the i values in the high- and low-temperature phases (0.03) are comparable to those for $[MBr_6]^{2-}$ containing M–Br bonds (i = 0.37 [15], 0.38 [16], and 0.39 [17] determined in octahedral complex ions where M = $Pd^{4+}(4d^6)$, $Pt^{4+}(5d^6)$, and $Re^{4+}(5d^3)$, respectively), suggesting that a marked change in the population of the electrons of Br atoms takes place during the spin-Peierls transition in the present complex.

3.4 Optical Properties

Figure 3.4 shows the polarized optical conductivity spectrum ($E//b$) for $[Ni(chxn)_2Br]Br_2$ obtained by using the Kramers–Kronig transformation of the reflectivity spectrum, which corresponds to the absorption spectrum [18]. A sharp and intense absorption band was observed at 1.3 eV. Intense absorption spectra have also been observed for Pd and Pt complexes, which were assigned to charge transfer (CT) excitation from the fully occupied d_{z^2} orbital of the M^{II} site to the unoccupied d_{z^2} orbital of the nearest neighbor M^{IV} site. In the case of $[Ni(chxn)_2Br]Br_2$, on the other hand, the origin of the absorption band ought to be different from the Pd or Pt cases because the ground state of Ni compounds is a Ni^{III} MH state.

Okamoto et al. have determined the band structure of $[Ni(chxn)_2Br]Br_2$ by using X-ray photoelectron (XPS), Auger electron (AES), and optical conductivity spectroscopies [19]. From XPS and AES, the U value was estimated to be ca. 5.5 eV [$U = E_{2p}(XPS) - 2E_{valence}(XPS) - E_k(AES)$]. In the optical conductivity spectra, an intense CT band was observed at 1.3 eV. Although there has been controversy in assigning the intense absorption band, it has been concluded that this band is a bridging ligand (p_z band of Br^-) to metal (UH d_{z^2} band of Ni) charge transfer (LMCT) band, meaning that this compound is not an MH insulator but a CT insulator (Fig. 3.5).

Photoluminescence is a powerful probe for investigating the electronic structure of excited states and their dynamics. Although photoluminescence, i.e., relaxation processes, of Peierls-distorted (mixed valence) MX chains have been extensively studied [20], the processes in $[Ni(chxn)_2Br]Br_2$ are not well understood. We have studied the luminescence properties of the MX-chain system $[Ni(chxn)_2Br]Br_2$ [21].

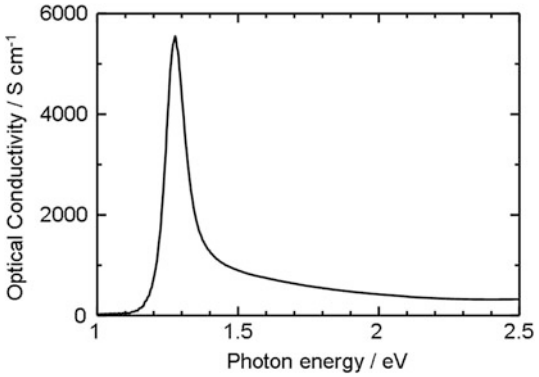

Fig. 3.4 Optical conductivity spectrum of $[Ni(chxn)_2Br]Br_2$. Inset shows proposed band structure determined by XPS and optical conductivity spectra

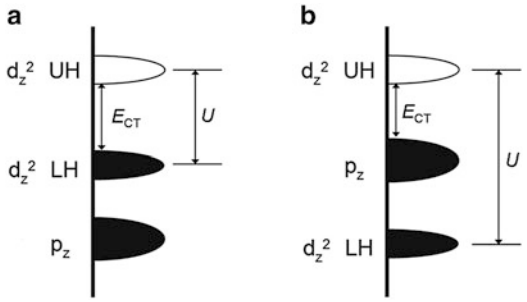

Fig. 3.5 Band structures of (**a**) MH and (**b**) CT insulators

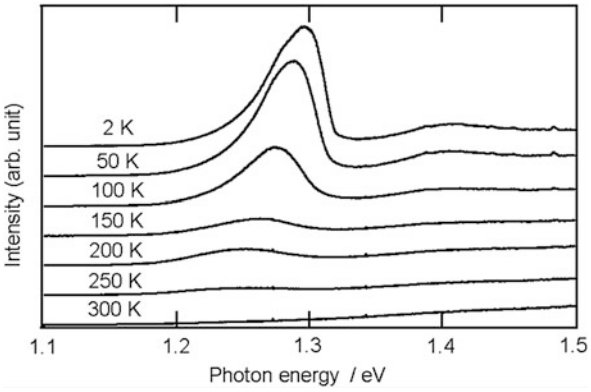

Fig. 3.6 Luminescence spectra of $[Ni(chxn)_2Br]Br_2$

Figure 3.6 shows the temperature dependence of luminescence spectra with excitation energy $E_{ex} = 1.96$ eV. Large and small broad peaks were observed at 1.3 and 1.4 eV, respectively. Intense bands in the optical conductivity spectrum at 1.3 eV have been assigned to LMCT transitions (Br^-, $Ni^{3+} \rightarrow Br^0$, Ni^{2+}) [19]. Therefore, the luminescence peak observed at 1.3 eV was attributed to the relaxation of an LMCT exciton state (Br^0, $Ni^{2+} \rightarrow Br^-$, Ni^{3+}). This luminescence exhibited little or no Stokes shift, showing that the LMCT exciton does not easily

relax into a self-trapped state. This is in contrast to the relaxation process for the CT exciton state ($M^{3+}, M^{3+} \rightarrow M^{4+}, M^{2+}$) in Peierls-distorted Pd and Pt MX chains. Pt and Pd MX chains show large Stokes shifts due to the strong electron–lattice interaction because bridging halide ions X^- are quite sensitive to the charge of M ions. On the other hand, in the case of $[Ni(chxn)_2Br]Br_2$, because the bridging bromine, which is neutral (Br^0) when the LMCT occurs, is insensitive to the charge of the Ni ions, it showed almost no Stokes shift, indicating that the electron–lattice interaction (S) of this system is small or suppressed. More detailed studies have been recently made on the time dependence of the photoluminescence [22] as well as theoretical research [23, 24].

The peaks at 1.3 and 1.4 eV gradually disappeared with an increase in the temperature. This shows that the deactivation process changes from luminescence to thermal relaxation. The peak at 1.3 eV slightly shifted to a lower energy with an increase in the temperature. We attributed the shift to an increase in the Ni–Br distance with an increase in the temperature, resulting in a decrease in the separation of Br^- $4p_z$ and Ni^{3+} $3d_{z^2}$ orbitals.

References

1. Toriumi K, Wada Y, Mitani T, Bandow S, Yamashita M, Fujii Y (1989) J Am Chem Soc 111:2341
2. Kishida H, Matsuzaki H, Okamoro H, Manabe T, Yamashita M, Taguchi Y, Tokura Y (2000) Nature 405:929
3. Takaishi S, Tobu Y, Kitagawa H, Goto A, Shimizu T, Okubo T, Mitani T, Ikeda R (2004) J Am Chem Soc 126:1614
4. Hazell A (1991) Acta Cryst C 47:962
5. Bonner JC, Fisher ME (1964) Phys Rev 135:A640
6. Eggert S, Affleck I, Takahashi M (1994) Phys Rev Lett 73:332
7. Dehmelt HG, Kruger H (1951) Z Physik 129:401
8. Smith PW, Stoessiger R (1971) J Chem Soc D 7:279
9. Nuclear Quadrupole Resonance Spectra Data Base, Japan Association for International Chemical Information, Apr 2003
10. Bayer H (1951) Z Physik 130:227
11. Kushida T, Benedek GB, Bloembergen N (1956) Phys Rev 104:1364
12. Townes CH, Dailey BP (1949) J Chem Phys 17:782
13. Dailey BP, Townes CH (1955) J Chem Phys 23:118
14. King JG, Jaccarino V (1954) Phys Rev 94:1610
15. Ito K, Nakamura D, Kurita Y, Ito K, Kubo M (1961) J Am Chem Soc 83:4526
16. Nakamura D, Kurita Y, Ito K, Kubo M (1960) J Am Chem Soc 82:5783
17. Ikeda R, Nakamura D, Kubo M (1965) J Phys Chem 69:2101
18. Okamoto H, Toriumi K, Mitani T, Yamashita M (1990) Phys Rev B 42:10381
19. Okamoto H, Shimada Y, Oka Y, Chainani A, Takahashi T, Kitagawa H, Mitani T, Toriumi K, Inoue K, Manabe T, Yamashita M (1996) Phys Rev B 54:8438
20. Tanino H, Kobayashi K (1983) J Phys Soc Jpn 52:1446
21. Takaishi S, Kitagawa H, Ikeda R (2002) Mol Cryst Liq Cryst 379:279
22. Takahashi Y, Suemoto T (2004) Phys Rev B 70:081101
23. Iwano K, Ono M, Okamoto H (2002) Phys Rev B 66:235103
24. Iwano K (2006) Phys Rev B 73:035108

Chapter 4
Pd(III) Mott–Hubbard Compounds

S. Takaishi and M. Yamashita

4.1 Introduction

In spite of long history of MX-chain complexes, all Pt or Pd compounds are in CDW state, without exception. We have recently succeeded in realizing Pd(III) MH state by two methods, that is, one is the chemical pressure via long alkyl chains introduced as counteranions, $[Pd(en)_2Br](C_n\text{-}Y)_2{\cdot}H_2O$, and the other is the partial substitution with Ni(III) ions, $[Ni_{1-x}Pd_x(chxn)_2Br]Br_2$. In both systems, it has been revealed that Pd(III) MH state was realized by the chemical pressure acting in the systems.

4.2 Realization of Pd(III) MH State by Means of Fastener Effect Acting Between Alkyl Chains [1]

4.2.1 Crystal Structure of $[Pd(en)_2Br](C_5\text{-}Y)_2{\cdot}H_2O$

Crystal structures of $[Pd(en)_2Br](C_5\text{-}Y)_2{\cdot}H_2O$ (en = ethylendiamine, C_5-Y = dipentylsulfosuccinate) at 259 and 162 K are shown in Fig. 4.1a, b, respectively. At both temperatures, the crystal structures were nearly the same. However, there was a remarkable difference in the periodicity at the two temperatures. At 259 K, the lattice parameters *a* and *b* were as twice as those at 162 K. At 259 K, the Pd (1)–Br bond lengths were 2.512(3) and 2.497(3) Å, whereas the Pd(2)–Br bond lengths were 2.783(3) and 2.777(3) Å. Since a Pd(II)–Br bond length is usually longer than a Pd(IV)–Br one, Pd(1) and Pd(2) were assigned to Pd(IV) and Pd(II),

S. Takaishi (✉) • M. Yamashita
Department of Chemistry, Graduate School of Science, Tohoku University,
6-3 Aramaki-Aza-Aoba, Aoba-Ku, Sendai 980-8578, Japan
e-mail: takaishi@mail.tains.tohoku.ac.jp

M. Yamashita and H. Okamoto (eds.), *Material Designs and New Physical Properties in MX- and MMX-Chain Compounds*, DOI 10.1007/978-3-7091-1317-2_4,

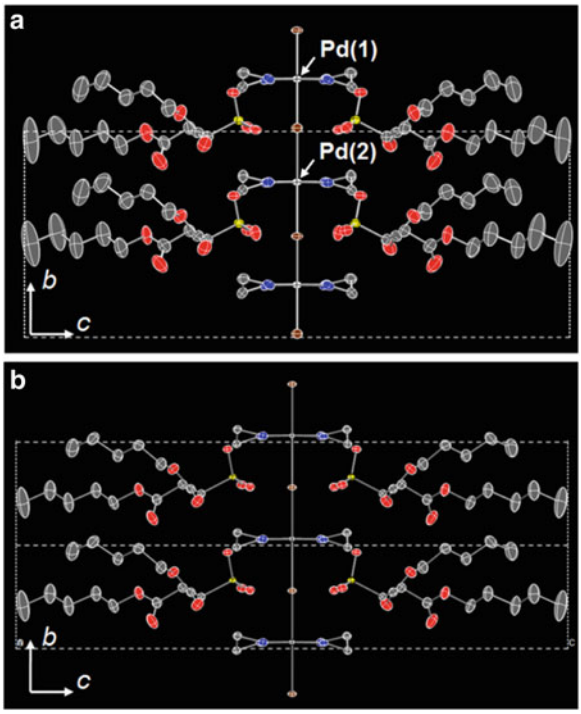

Fig. 4.1 ORTEP drawings of $[Pd(en)_2Br](C_5\text{-}Y)_2{\cdot}H_2O$ at (**a**) 259 K and (**b**) 162 K. Water molecules and hydrogen atoms are omitted for clarity. *White*: Pd, *Brown*: Br, *Blue*: N, *Yellow*: S, *Red*: O, *Gray*: C

respectively. Therefore, this indicates that $[Pd(en)_2Br](C_5\text{-}Y)_2{\cdot}H_2O$ is in a 3D-ordered CDW state $(\cdots Pd(II)\cdots Br - Pd(IV) - Br\cdots Pd(II)\cdots)$ at this temperature. At 162 K, on the other hand, the twofold periodicity disappeared, and all of the Pd ions became equivalent. The Pd–Br bond lengths were 2.613(1) and 2.604 (1) Å, which are intermediate between Pd(II)–Br and Pd(IV)–Br bond lengths, suggesting that the complex is in an MH state [–Pd(III)–Br–Pd(III)–Br–Pd(III)–] at 162 K.

The temperature dependence of the average neighboring $Pd\cdots Pd$ distance along the chain is shown in Fig. 4.2. The average $Pd\cdots Pd$ distance in $[Pd(en)_2Br](C_5\text{-}Y)_2{\cdot}H_2O$ at 293 K was 5.31 Å. This distance is longer than that in $[Pd(chxn)_2Br]Br_2$, which has the shortest $Pd\cdots Pd$ distance so far reported and is in a CDW state [2]. Upon cooling, this distance decreased by approximately 2 % and became 5.21 Å at 110 K, while that of $[Pd(chxn)_2Br]Br_2$ showed almost no temperature dependence. The large temperature dependence in the present complex is considered to be due to suppression of the thermal motion of the alkyl chains. In addition, we found a discontinuity in the $Pd\cdots Pd$ distance with a small hysteresis at 205 K, indicating the first-order phase transition occurs at this temperature.

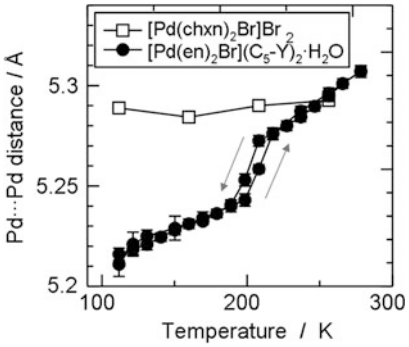

Fig. 4.2 Temperature dependence of averaged Pd···Pd distance in $[Pd(en)_2Br](C_5\text{-}Y)_2{\cdot}H_2O$ upon the cooling and heating processes, together with that of $[Pd(chxn)_2Br]Br_2$

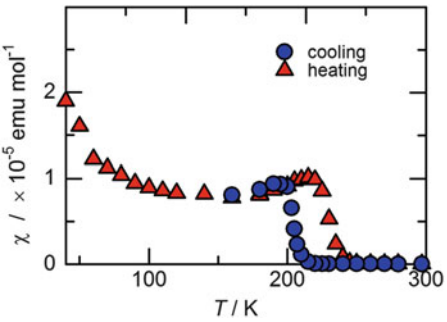

Fig. 4.3 Temperature dependence of spin susceptibility (χ) in $[Pd(en)_2Br](C_5\text{-}Y)_2{\cdot}H_2O$

4.2.2 Electron Spin Resonance Spectroscopy

Electron spin resonance (ESR) spectroscopy is a powerful tool to determine the electronic state of the MX-chain compounds because CDW and MH states should show diamagnetic and paramagnetic (antiferromagnetic) behaviors, respectively. Figure 4.3 shows the temperature dependence of the spin susceptibility (χ) obtained by integrating the first derivative of the ESR signal twice. Around room temperature, quite weak ESR signals on the order of 10^{-8} emu mol^{-1} were observed. This result is in agreement with the structural data, which shows that this complex is in a diamagnetic CDW state at room temperature. On the other hand, χ below 200 K was on the order of 10^{-5} emu mol^{-1}. This could be explained by paramagnetic behavior coupled with a strong antiferromagnetic interaction, which is characteristic of complexes in an MH state. The Curie ($1/T$) contribution below 100 K, which was 0.14 % of the spin concentration, is probably due to the existence of an odd number of Pd(III) ions ($S = 1/2$) in the domains or short chains. A clear discontinuity in χ was observed at ca. 205 $\pm$ 5 K and 230 $\pm$ 5 K in the cooling and heating processes, respectively. We concluded that the discontinuity corresponded to the first order phase transition between CDW and MH states.

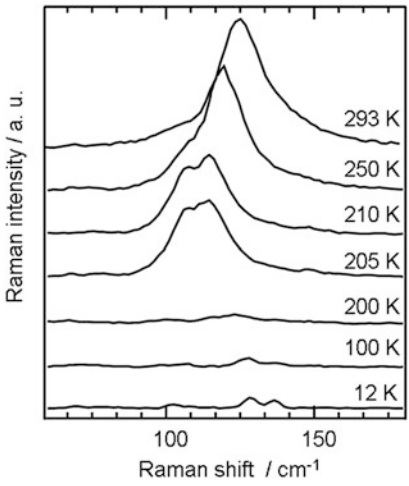

Fig. 4.4 Temperature dependence of Raman spectra of $[Pd(en)_2Br](C_5\text{-}Y)_2 \cdot H_2O$

4.2.3 Raman and Optical Conductivity Spectra

It is known that the Br–Pd–Br symmetrical stretching mode ν(Br–Pd–Br) in Raman spectrum is allowed in the CDW state and forbidden in the MH state [3]. Thus, Raman spectroscopy is a good probe to determine the electronic states of the MX-chain compounds. Figure 4.4 shows the temperature dependence of the Raman spectra. In the high temperature (HT), an intense Raman peak was observed at ca. 130 cm^{-1}, which was assigned to ν(Br–Pd–Br). On the other hand, the peak disappeared in the low temperature (LT) spectra. This result clearly indicates that this complex undergoes the phase transition from CDW to MH states.

Figure 4.5 shows the temperature dependence of the optical conductivity spectra and the peak energies (E_{opt}). A clear discontinuity in E_{opt} was observed at 206 ± 2 K. This temperature is similar to those obtained from the crystal structure analysis, ESR, and Raman spectroscopies. In the HT spectra, the peak energy decreased from 0.86 eV (290 K) to 0.66 eV (210 K). On the other hand, the peak energy barely changed with a change in the temperature in the LT spectra. This can be understood by considering the origin of the electronic transition. In the CDW state, the lowest electronic transition is an IVCT transition from the Pd(II) d_{z^2} to Pd (IV) d_{z^2} species. In this case, the CT energy (E_{opt}) can be evaluated as $2S–U$ if V and t are ignored [4, 5]. In the MH state, on the other hand, the lowest electronic transition is CT transition from averaged Pd(III)–Pd(III) state to disproportioned Pd (II)–Pd(IV) (or Pd(IV)–Pd(II)) state. The CT energy is evaluated to be U. Because almost no temperature dependence was observed in the LT spectra and there was a large temperature dependence of the CT energy in the HT spectra, S, not U, decreases as the Pd $\cdots$ Pd distance becomes shorter.

From the crystal structures, spin susceptibility, optical conductivity spectra, and Raman spectra, we concluded that the first-order phase transition between CDW

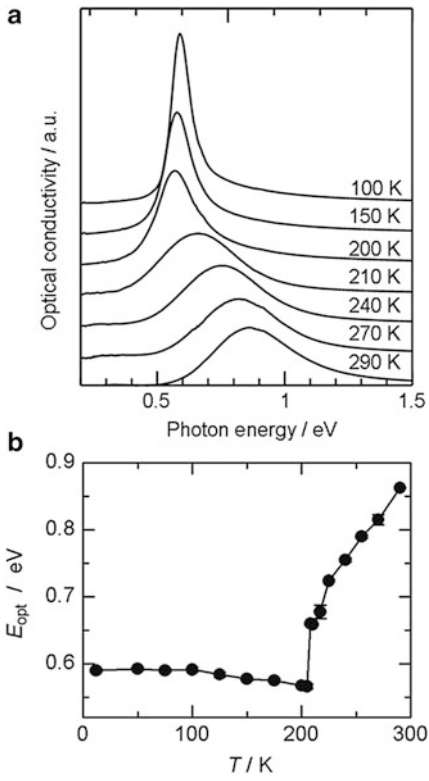

Fig. 4.5 Temperature dependence of (**a**) optical conductivity spectra and (**b**) their peak energy

and MH states occurs at 206 ± 2 K. This phase transition was also confirmed using heat capacity measurements ($\Delta H = 1.554 \pm 0.011$ kJ mol^{-1}, $\Delta S = 7.48 \pm 0.05$ J K^{-1} mol^{-1}).

4.2.4 Alkyl Chain Length Dependency

In order to clarify the origin of the phase transition, we synthesized a series of Pd–Br complexes $[Pd(en)_2Br](C_n\text{-}Y)_2{\cdot}H_2O$ (n = 4, 5, 6, 7, 8, 9, and 12) with different alkyl chain lengths. We determined the nearest neighbor Pd ··· Pd distance of these complexes from powder X-ray diffraction (PXRD) patterns. Increasing the alkyl chain length caused the Pd ··· Pd distance to decrease dramatically even at room temperature, as shown in Fig. 4.6, suggesting that the attractive force between the alkyl chains of the counterions becomes stronger with an increase in the alkyl chain length. In other words, the attractive force acting between the alkyl chains is the origin of the chemical pressure.

Figure 4.7 shows Raman spectra of the series of Pd–Br complexes at room temperature. An intense Raman peak attributed to ν(Br–Pd–Br) was observed for the complexes with short alkyl chains ($n \leq 8$), whereas it was not observed for the

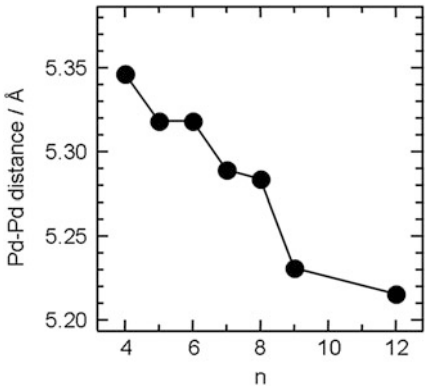

Fig. 4.6 The nearest neighbor Pd · · · Pd distance as a function of alkyl chain length

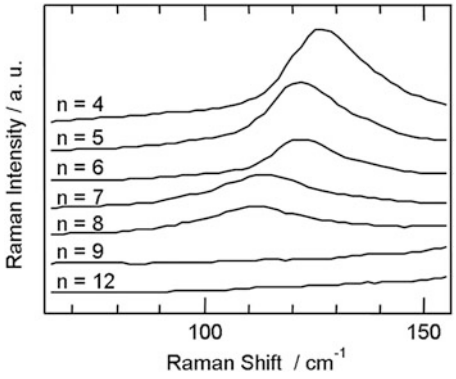

Fig. 4.7 Raman spectra of a series of $[Pd(en)_2Br](C_5\text{-}Y)_2{\cdot}H_2O$ ($4 \leq n \leq 12$) at room temperature

compounds with longer alkyl chains ($n \geq 9$). As mentioned above, this stretching mode is allowed in the CDW state but forbidden in the MH state. Therefore, the compounds with short ($n \leq 8$) and long ($n \geq 9$) alkyl chains have CDW and MH states, respectively, at room temperature.

We measured the temperature dependence of the Raman spectra and determined the T_c for the series of Pd–Br compounds. Figure 4.8 shows the phase diagram of these compounds. With an increase in the alkyl chain length, T_c steadily increased.

4.3 Stabilization of the Pd(III) MH State in Ni–Pd Mixed Metal Complexes, $[Ni_{1-x}Pd_x(chxn)_2Br]Br_2$

We have tried another approach to decrease metal–metal distance, that is, partial substitution with smaller Ni ions, $[Ni_{1-x}Pd_x(chxn)_2Br]Br_2$. These complexes were firstly synthesized by Yamashita et al. in 1997, [6, 7] and their electronic states have

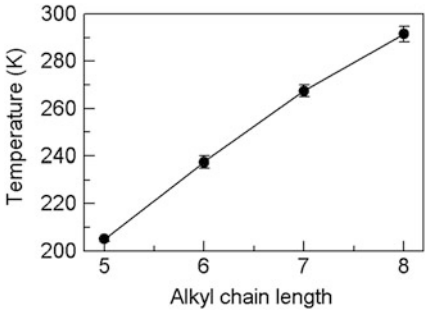

Fig. 4.8 Phase diagram of $[Pd(en)_2Br](C_n\text{-}Y)\cdot H_2O$

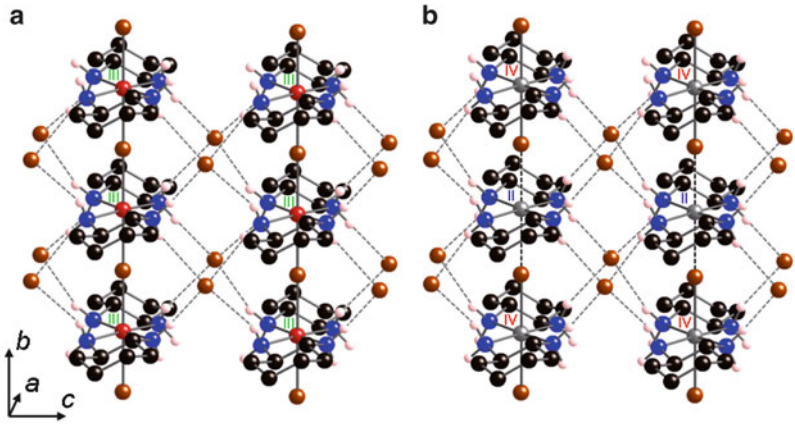

Fig. 4.9 Crystal structures of (**a**) $[Ni(chxn)_2Br]Br_2$ and (**b**) $[Pd(chxn)_2Br]Br_2$

been extensively studied by optical [8] and ESR [9] spectroscopies, X-ray diffuse scattering [10], scanning tunneling microscopy [11], etc. In this section, we introduce their structure and physical properties.

4.3.1 Structure and Electronic States of $[M(chxn)_2Br]Br_2$ (M = Ni, Pd)

A crystal structure of $[Ni(chxn)_2Br]Br_2$ is shown in Fig. 4.9a [12]. In this structure, the Ni(III) ions and Br^- ions alternate with equivalent Ni–Br distances, and the four N atoms of the two chxn ligands coordinating to each Ni(III) ion in the equatorial positions producing a strong ligand field. Each Ni–Br–Ni 1D chain is hydrogen bridged between the amino-protons of chxn and counter Br ions along the chains, as well as over the chains, forming two-dimensional hydrogen-bond networks.

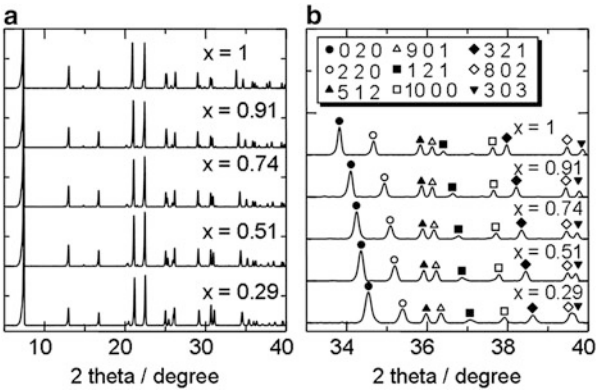

Fig. 4.10 (**a**) XRPD patterns of $[Ni_{1-x}Pd_x(chxn)_2Br]Br_2$ with selected x values. (**b**) Magnification of (**a**) in the range of $33° \leq 2\theta \leq 40°$. Inset indicates Miller index of each peak

The resultant electronic configuration of the Ni(III) ion in the nearly D_{4h} symmetry is $(e_g)^4(b_{2g})^2(a_{1g})^1(b_{1g})^0$ with one unpaired electron in the d_{z^2} orbital. Unpaired electrons in the Ni d_{z^2} orbitals form a 1D antiferromagnetic spin ($S = 1/2$) chain. Large p–d hybridization between the Br p_z orbital and the Ni d_{z^2} orbital leads to a large antiferromagnetic exchange interaction parameter J/k_B ($= -2{,}000$ K [13], $-3{,}600$ K [14], or $-2{,}700 \pm 500$ K [9]).

The Pd(II)–Pd(IV) mixed valence complex $[Pd(chxn)_2Br]Br_2$ is isomorphous to $[Ni(chxn)_2Br]Br_2$ (space group $= I222$) except for the positions of the bridging Br^- ions (Fig. 4.9b) [2]. In the Pd MX chain, the bridging Br^- ions are displaced from the midpoints between two neighboring Pd ions due to a large S and a relatively small U between the 4d electrons, stabilizing a Peierls-distorted CDW state, with alternating Pd(II) and Pd(IV) ions even at room temperature. Therefore, the Pd complex has a diamagnetic ground state.

4.3.2 *Crystal Structure of $[Ni_{1-x}Pd_x(chxn)_2Br]Br_2$*

Figure 4.10 shows PXRD patterns of a few $[Ni_{1-x}Pd_x(chxn)_2Br]Br_2$ complexes at room temperature [15]. All of the compounds showed similar PXRD patterns, and they could be fitted with the space group of $I222$, showing that the crystal structures of each compound are isomorphous. The PXRD patterns shifted gradually with an increase in x, indicating that the unit cell parameters continuously changed and that there was no phase separation. Figure 4.11 shows the unit cell parameters of a series of $[Ni_{1-x}Pd_x(chxn)_2Br]Br_2$ as a function of x. The unit cell length of the a and b axes increased with an increase in x, which is consistent with the finding that the valence orbitals of Pd (4d) are spatially wider more than those of Ni (3d). On the other hand, the length of c axis decreased with an increase in x. This is explained as follows: Since the 1D chain made by –M–X–M–X– covalent bonds runs along the b axis, its length should be directly affected by the substitution. In fact, the unit cell length increased in this direction with an increase in x. On the other hand, the 1D

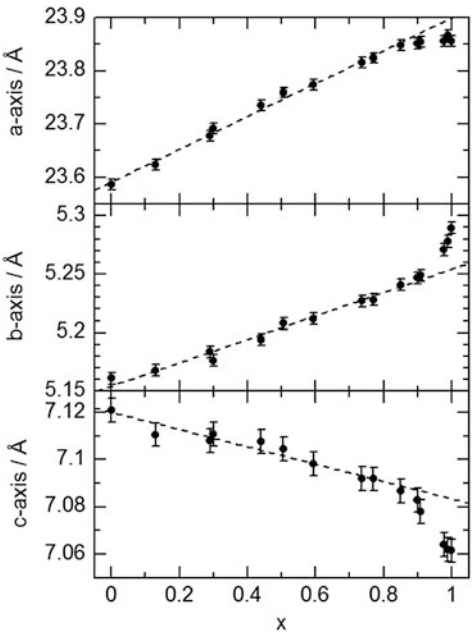

Fig. 4.11 Unit cell parameters of $[Ni_{1-x}Pd_x(chxn)_2Br]Br_2$ as a function of x. *Dashed lines* show fitted data

chains are connected to each other via hydrogen bonds $(N-H\cdots Br\cdots H-N)$ along the c axis. Therefore, in order to maintain the hydrogen bonding, the length of the c axis decreased with an increase in x instead.

The unit cell length in each direction obeys a linear relationship when $x < 0.9$, whereas it deviates from the line when $x > 0.9$, especially in the case of the b and c axes. The x dependence of the unit cell length of the b axis (//1D chain) could be influenced by the electronic state of the compound. When the compound is in the MH state, the unit cell length of the b axis should be simply twice the linear summation of the Ni(III)–Br and Pd(III)–Br bond lengths as follows:

$$b = 2\{(1-x)d(\mathrm{Ni(III)}\cdots\mathrm{Br}) + xd(\mathrm{Pd(III)}\cdots\mathrm{Br})\},$$

where $d(\mathrm{Ni(III)}\cdots\mathrm{Br})$ and $d(\mathrm{Pd(III)}\cdots\mathrm{Br})$ indicate Ni(III)–Br and Pd(III)–Br bond lengths, respectively.

On the other hand, in the CDW state, the oxidation states of Ni and Pd ions are supposed to be Ni(II) and Pd(IV), respectively, because Ni ion cannot have the oxidation state of Ni(IV) due to the higher oxidation potential from Ni(III) to Ni (IV) than that from Br^- to Br^0. Therefore, b axis should be expressed as follows:

$$b = 2\{(1-x)d(\mathrm{Ni(II)}\cdots\mathrm{Br}) + (x-0.5)d(\mathrm{Pd(II)}\cdots\mathrm{Br}) + 0.5d(\mathrm{Pd(IV)}\cdots\mathrm{Br})\},$$

where $d(\mathrm{Ni(II)}\cdots\mathrm{Br})$, $d(\mathrm{Pd(II)}\cdots\mathrm{Br})$, and $d(\mathrm{Pd(II)}\cdots\mathrm{Br})$ indicate Ni(II)–Br, Pd (II)–Br, and Pd(IV)–Br bond lengths, respectively.

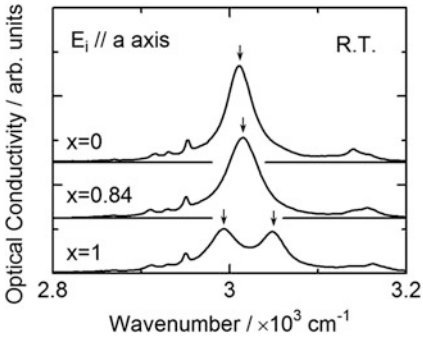

Fig. 4.12 Optical conductivity spectra in the IR region (E_i//c axis). ν(N–H) denotes the N–H stretching mode of chxn ligand

As mentioned above, the length of b axis should obey the different correlation depending on their electronic states. Thus, the deviation from the line when $x > 0.9$ suggests that the electronic state changed at $x = 0.9$.

4.3.3 IR Spectra of $[Ni_{1-x}Pd_x(chxn)_2Br]Br_2$

IR spectra of $[Ni_{1-x}Pd_x(chxn)_2Br]Br_2$ were measured using single crystals [8]. As shown in Fig. 4.12, in spectra of the pure Ni complexes, only a single ν(N–H) peak was observed at around 3,000 cm^{-1}, reflecting the averaged valence [Ni(III)] state. In the spectra of the pure Pd complex, the ν(N–H) peak is split into two peaks due to the formation of the mixed valence [Pd(II) and Pd(IV)] state. In the spectra of the mixed metal chains, splitting was observed when $x > 0.90$. This result indicates that, when $x < 0.90$, the Pd ions are in a Pd(III) MH state, whereas when $x > 0.90$, they are in a Pd(II)–Pd(IV) mixed valence state, or CDW state. Therefore, the Pd ions change from Pd(III) MH to Pd(II)–Pd(IV) mixed valence states at $x \sim 0.9$.

4.3.4 Optical Conductivity Spectra of $[Ni_{1-x}Pd_x(chxn)_2Br]Br_2$

Optical conductivity spectra for $[Ni_{1-x}Pd_x(chxn)_2Br]Br_2$ are shown in Fig. 4.13 [8]. The pure Ni complex ($x = 0$) exhibits a prominent sharp peak (A) at around 1.3 eV. This peak was attributed to the LMCT transition from Br p_z orbitals to the Ni(III) d_{z^2} orbitals. With an increase in x, peak A broadened, and another peak (B) appeared on the lower energy side. When $x > 0.41$, A disappeared, and B became dominant. With a further increase in x, B shifted to lower energy, and when x exceeded 0.9, B disappeared, and a higher energy peak (C) appeared.

There was a discontinuous change in energy between peaks B and C. The energy of C for $0.9 < x < 1$ is almost equal to that of the peak for the pure Pd complex

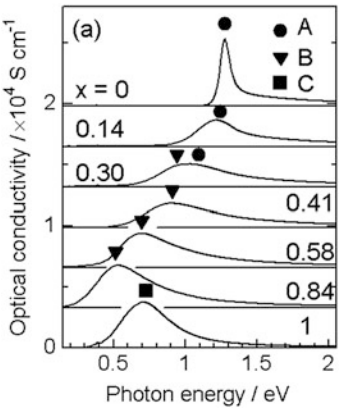

Fig. 4.13 Optical conductivity spectra with the light polarization (E_i)// the *b* axis (chain axis) at room temperature for $[Ni_{1-x}Pd_x(chxn)_2Br]Br_2$

($x = 1$), which has been established to be due to an intervalence charge transfer (IVCT) transition from the occupied Pd(II) $4d_{z^2}$ band to the unoccupied Pd(IV) $4d_{z^2}$ band.

4.3.5 *Local Electronic Structure of $[Ni_{1-x}Pd_x(chxn)_2Br]Br_2$ Measured by Using STM*

Scanning tunneling microscopy (STM) is a powerful tool for studying local electronic structures in these chain complexes. We performed STM measurements on $[Ni_{1-x}Pd_x(chxn)_2Br]Br_2$ in order to clarify the local electronic states [11].

Figure 4.14a shows an STM image of $[Ni(chxn)_2Br]Br_2$ in the range 200×200 Å^2. Bright spots in the image were observed every 5×7 Å^2. The Ni $\cdots$ Ni distances along the *b* (1D chain) and *c* axes were 5.16 and 7.12 Å [12], respectively, meaning that the spots reflect the periodicity of the $[Ni(chxn)_2]$ units in the *bc* plane. In the STM image of $[Pd(chxn)_2Br]Br_2$, on the other hand, bright spots were observed every 10×7 Å^2, as shown in Fig. 4.14b. The Pd $\cdots$ Pd distances along the *b* (1D chains) and *c* axes were 5.29 and 7.07 Å, respectively [2], indicating that these spots reflect the twofold periodicity of the valence structure of the CDW state of $[Pd(chxn)_2Br]Br_2$. The phase of the CDW state is nearly aligned in the *bc* plane, which is consistent with the X-ray diffuse scattering study.

Here we discuss the origin of the bright spots. Figure 4.15 shows band structure of $[Ni(chxn)_2Br]Br_2$ and $[Pd(chxn)_2Br]Br_2$. The valence and conduction bands of $[Ni(chxn)_2Br]Br_2$ are composed of the p_z band of the bridging Br^- ions and the d_{z^2} orbitals of the Ni ions, respectively [16]. On the other hand, the valence and conduction bands of $[Pd(chxn)_2Br]Br_2$ are the d_{z^2} orbitals of the Pd(II) and Pd(IV) ions, respectively. When STM is performed with a positive sample bias, a tunnel

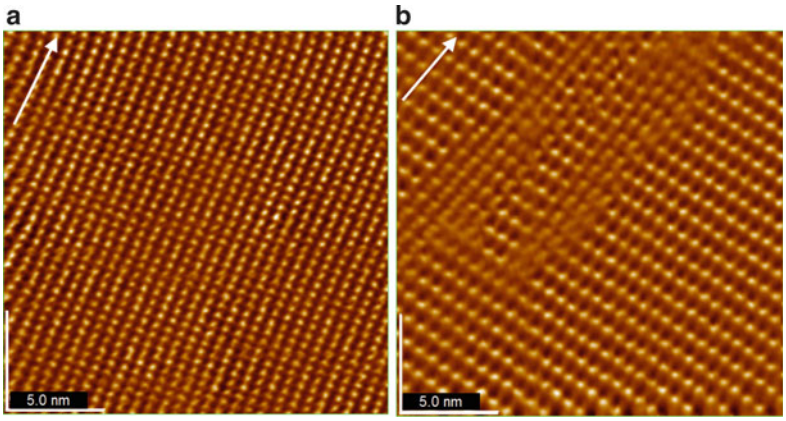

Fig. 4.14 STM images of (**a**) $[Ni(chxn)_2Br]Br_2$ and (**b**) $[Pd(chxn)_2Br]Br_2$ in the *bc* plane (200 × 200 Å). The image was acquired with a sample bias (V_s) of +1.3 V and +1.0 V for Ni and Pd chains, respectively. The *white arrow* shows the 1D chain direction

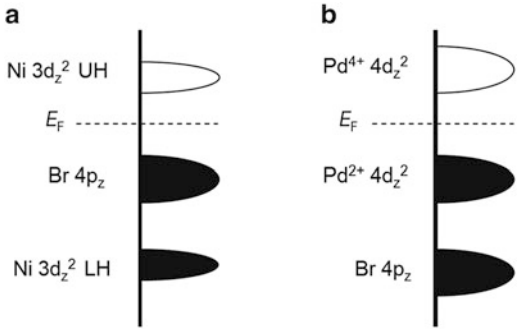

Fig. 4.15 Diagram of the band structure of (**a**) $[Ni(chxn)_2Br]Br_2$ and (**b**) $[Pd(chxn)_2Br]Br_2$

current is observed from the Fermi energy level (E_F) of the tip to the conduction band of the sample. In other words, in the image of $[Ni(chxn)_2Br]Br_2$, a tunnel current from E_F to the UH d_{z^2} band of Ni(III) was observed, whereas that from E_F to the d_{z^2} band of Pd(IV) was observed in the image of $[Pd(chxn)_2Br]Br_2$, which causes the twofold periodicity along the 1D chain observed in the STM image.

Then, we carried out STM measurements on the mixed metal complexes $[Ni_{1-x}Pd_x(chxn)_2Br]Br_2$ to determine their local valence structures. Figure 4.16 shows STM images of the complexes with $x =$ (a) 0.70, (b) 0.80, (c) 0.86, and (d) 0.95 in an area of 200 × 200 Å^2. The image of the $x = 0.70$ complex was similar to that of $[Ni(chxn)_2Br]Br_2$ with almost no twofold periodicity. This result shows that the $x = 0.70$ complex is in a Mott–Hubbard state. In the image of the $x = 0.80$ complex, on the other hand, twofold periodicity was observed in several areas, which we attributed to CDW states.

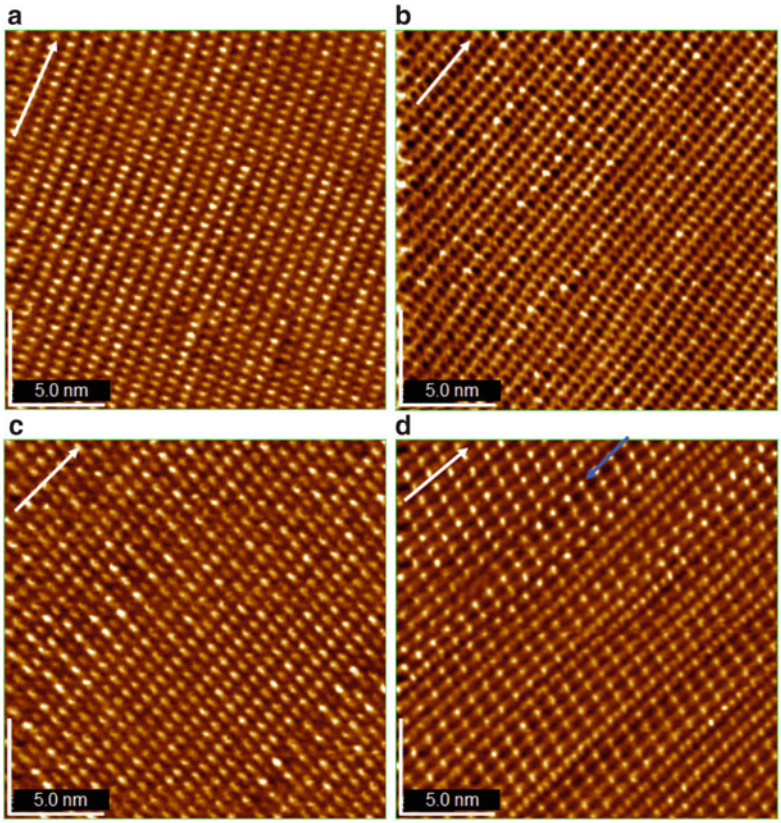

Fig. 4.16 STM images of $[Ni_{1-x}Pd_x(chxn)_2Br]Br_2$ with $x =$ (**a**) 0.70, (**b**) 0.80, (**c**) 0.86, and (**d**) 0.95 in the *bc* plane (200 × 200 Å^2). The sample bias was +1.0 V. The directions of the 1D chains are shown as *white arrows*, and the *blue arrow* shows the 1D chain on which a spin soliton was observed

These CDW states were coherent over approximately ten metal sites along the *b* axis, but almost no coherence was observed along the *c* axis. In the image of the $x = 0.86$ complex, coherence was clearly more propagated than that of the $x = 0.80$ complex. The CDW coherence of the $x = 0.86$ complex spread over approximately 20 metal sites along the b axis, and two or three metal sites along the *c* axis. The image of the $x = 0.95$ complex showed extensive twofold periodicity. Along the *b* axis, for the chains in a CDW state, the twofold periodicity extended over the measured length (ca. 40 metal sites), which shows that the CDW coherence along the chain is longer than 20 nm. Along the *c* axis, on the other hand, the CDW coherence is spread over approximately six or seven sites. We plotted the CDW coherence length as a function of *x* in Fig. 4.17 together with the data obtained by using X-ray diffuse scattering measurements made by Wakabayashi et al. [9]. The CDW coherence determined by using STM is in agreement with the X-ray diffuse scattering results. The CDW coherence propagated with an increase in the value of *x*.

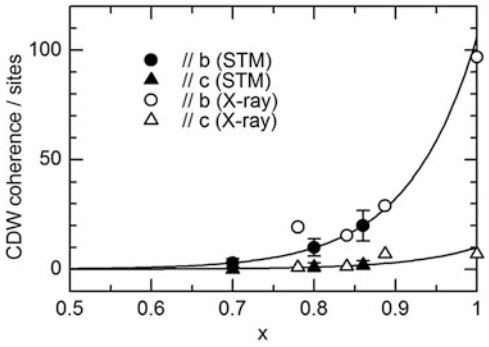

Fig. 4.17 CDW coherence as a function of x. The *filled circle* and *triangle* represent CDW coherence along the chain and c axis, respectively, determined by using STM. The *open circle* and *triangle* represent those determined by using X-ray diffuse scattering measurements. The *solid lines* are guides for the eyes

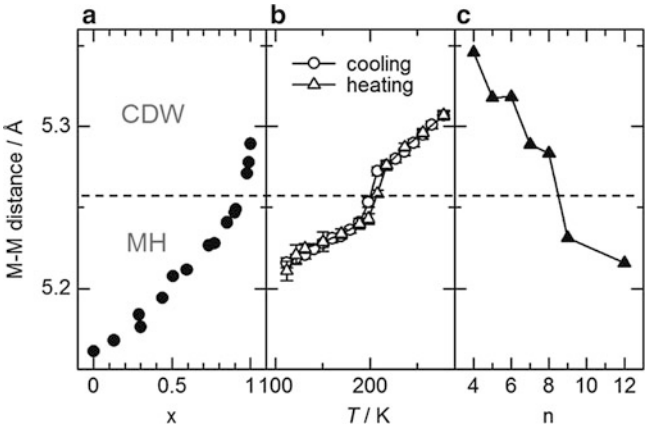

Fig. 4.18 $d(\mathrm{M}\cdots\mathrm{M})$ along the 1D chain as a function of (**a**) x in $[Ni_{1-x}Pd_x(chxn)_2Br]Br_2$ at room temperature, (**b**) temperature of $[Pd(en)_2Br](C_5\text{-}Y)_2{\cdot}H_2O$, and (**c**) n in $[Pd(en)_2Br](C_n\text{-}Y)_2{\cdot}H_2O$ at room temperature

4.4 Comparison of Metal-to-Metal Distance in Both Systems

Finally, we compared the metal-to-metal distance $d(\mathrm{M}\cdots\mathrm{M})$ in the two systems, ($[Pd(en)_2Br](C_n\text{-}Y)_2{\cdot}H_2O$ and $[Ni_{1-x}Pd_x(chxn)_2Br]Br_2$). Figure 4.18 shows the x dependence of $d(\mathrm{M}\cdots\mathrm{M})$ along the 1D chain in $[Ni_{1-x}Pd_x(chxn)_2Br]Br_2$, temperature dependence of $d(\mathrm{M}\cdots\mathrm{M})$ in $[Pd(en)_2Br](C_5\text{-}Y)_2{\cdot}H_2O$, and n dependence of $d(\mathrm{M}\cdots\mathrm{M})$ in $[Pd(en)_2Br](C_n\text{-}Y)_2{\cdot}H_2O$ at room temperature. In all cases, the electronic state changed at an $\mathrm{M}\cdots\mathrm{M}$ distance of ca. 5.26 Å, namely, CDW and MH states are the ground state when $d(\mathrm{Pd}\cdots\mathrm{Pd})$ is longer and shorter than 5.26 Å,

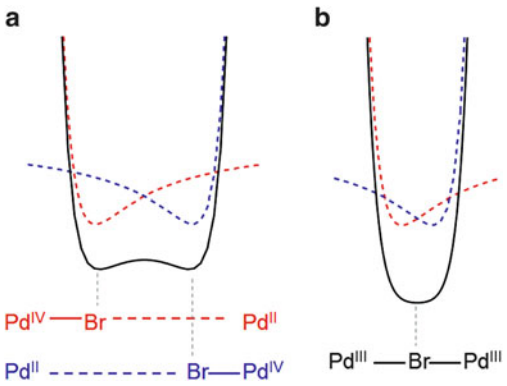

Fig. 4.19 Potential energy curve of the bridging bromide ion in the (**a**) CDW and (**b**) MH states

respectively. This result suggests that a $d(\mathrm{Pd}\cdots\mathrm{Pd})$ of 5.26 Å is the boundary between CDW and MH states.

If the Pd–Br bond is ionic, the potential energy of the bromide ion is given by the Born–Mayer equation. In the $\mathrm{Pd(IV)}-\mathrm{Br}\cdots\mathrm{Pd(II)}$ mixed valence system, this energy forms double minimum potential, which is the sum of the potential curves for $\mathrm{Pd(IV)}-\mathrm{Br}\cdots\mathrm{Pd(II)}$ (red curve) and $\mathrm{Pd(II)}\cdots\mathrm{Br}-\mathrm{Pd(IV)}$ (blue curve), as shown in Fig. 4.19. When $d(\mathrm{Pd}\cdots\mathrm{Pd})$ becomes shorter, the equivalent position of the bromide ions becomes closer to each other, and finally, the double minimum potential becomes a single minimum potential at the midpoint between two neighboring Pd ions, as shown in Fig. 4.19b. In this situation, all of the Pd ions should be equivalent, and the Pd(III) MH state should be stabilized. In the present system, we concluded that the boundary distance between double minimum and single minimum potentials was ca. 5.26 Å.

References

1. Takaishi S, Takamura M, Kajiwara T, Miyasaka H, Yamashita M, Iwata M, Matsuzaki H, Okamoto H, Tanaka H, Kuroda S, Nishikawa H, Oshio H, Kato K, Takata M (2008) J Am Chem Soc 130:12080–12084
2. Hazell A (1991) Acta Cryst C 47:962
3. Yamashita M, Ishii T, Matsuzaka H, Manabe T, Kawashima T, Okamoto H, Kitagawa H, Mitani T, Marumoto K, Kuroda S (1999) Inorg Chem 38:5124–5130
4. Okamoto H, Mitani T, Toriumi K, Yamashita M (1992) Mater Sci Eng B 13:L9
5. Okamoto H, Mitani T (1993) Prog Theor Phys 113:191
6. Manabe T, Yamashita M, Kawashima T, Okamoto H, Kitagawa H, Mitani T, Toriumi K, Miyamae H, Inoue K, Yakushi K (1997) Proc SPIE 3145: 106–115
7. Manabe T, Kawashima T, Yamashita M, Okamoto H, Kitagawa H, Mitani T, Inokuchi M, Yakushi K (1997) Synth Met 86:2233
8. Matsuzaki H, Iwano K, Aizawa T, Ono M, Kishida H, Yamashita M, Okamoto H (2004) Phys Rev B 70:035204
9. Marumoto K, Tanaka H, Kuroda S, Manabe T, Yamashita M (1999) Phys Rev B 60:7699

10. Wakabayashi Y, Wakabayashi N, Yamashita M, Manabe T, Matsushita N (1999) Phys Soc Jpn 68:3948
11. Takaishi S, Miyasaka H, Sugiura K, Yamashita M, Matsuzaki H, Kishida H, Okamoto H, Tanaka H, Marumoto K, Ito H, Kuroda S, Takami T (2004) Angew Chem Int Ed 43:3171
12. Toriumi K, Wada Y, Mitani T, Bandow S, Yamashita M, Fujii Y (1989) J Am Chem Soc 111:2341
13. Takaishi S, Tobu Y, Kitagawa H, Goto A, Shimizu T, Okubo T, Mitani T, Ikeda R (2004) J Am Chem Soc 126:1614
14. Okamoto H, Toriumi K, Mitani T, Yamashita M (1990) Phys Rev B 42:10381
15. Takaishi S, Wu H, Kajiwara T, Brian B, Miyasaka H, Yamashita M (2010) Inorg Chem 49:3694
16. Okamoto H, Shimada Y, Oka Y, Chainani A, Takahashi T, Kitagawa H, Mitani T, Toriumi K, Inoue K, Manabe T, Yamashita M (1996) Phys Rev B 54:8438

Chapter 5
Photoinduced Phase Transitions in MX-Chain Compounds

Hiroyuki Matsuzaki and Hiroshi Okamoto

5.1 Introduction

The control of phase transitions and related macroscopic properties in solids by photoexcitation, which is called "photoinduced phase transition (PIPT)" [1, 2], is now attracting considerable attention as a novel mechanism for photoswitching of optical, transport, and magnetic properties. Several characteristic PIPTs such as neutral (N) and ionic (I) transitions [3–10], insulator to metal transitions [11–25], and diamagnetic to paramagnetic or ferromagnetic transitions [26–39] have been indeed demonstrated thus far. In some of these PIPTs, the photoinduced phases are fairly unstable and their lifetimes are very short, being of picosecond (ps) or sub-ps order. Such ultrafast responses of PIPTs make us expect the generation of a new field involving both basic science and device applications.

From a scientific point of view, the ultrafast nonequilibrium dynamics of PIPTs in solids will be an important subject. By a photoexcitation, charge ordering (CO) and lattice distortions stabilizing CO as well as spin orderings can be dynamically melted or reconstructed as a result of competitive interplays among charge, spin, and lattice degrees of freedom in both photoexcited states and ground states. Generally speaking, PIPTs show a wide variety of dynamics depending on materials and the time scales of their dynamics change over a wide range from seconds to femtoseconds (fs). Such a variety of PIPT dynamics originates from the

H. Matsuzaki (✉)
Faculty of Frontier Sciences, Department of Advanced Materials Science, University of Tokyo, 5-1-5 Kashiwanoha, Kashiwa, Chiba 277-8561, Japan

Research Institute of Instrumentation Frontier, National Institute of Advanced Industrial Science and Technology (AIST), Tsukuba Central 5, 1-1-1 Higashi, Tsukuba, Ibaraki 305-8565, Japan
e-mail: hiroyuki-matsuzaki@aist.go.jp

H. Okamoto (✉)
Faculty of Frontier Sciences, Department of Advanced Materials Science, University of Tokyo, 5-1-5 Kashiwanoha, Kashiwa, Chiba 277-8561, Japan
e-mail: okamotoh@k.u-tokyo.ac.jp

M. Yamashita and H. Okamoto (eds.), *Material Designs and New Physical Properties in MX- and MMX-Chain Compounds*, DOI 10.1007/978-3-7091-1317-2_5,

complicated interactions among charge, spin, and lattice degree of freedom and the time scale will be dominated by the magnitudes of the interactions, such as on-site or intersite electron–electron (e–e) Coulomb interaction, spin–spin (s–s) interaction, electron–lattice (e–l) interaction, and spin–lattice (s–l) interaction. By observing the dynamics of each degree of freedom separately by means of ultrafast snapshots, we will be able to characterize the interactions dominating PIPTs, which cannot be accessed in steady-state measurements and then be able to clarify the mechanisms of PIPTs.

From the viewpoint of applications, ultrafast PIPTs are expected to be new mechanisms for Tbit/s-class switching devices. For this purpose, it is important to utilize a purely electronic transition with no structural changes. In this sense, some material systems in which their electronic structures and physical properties are dominated by electron correlations are good targets. Some of such materials indeed show photoinduced changes of electronic states and their recovery within a few picoseconds. These phenomena are expected to be utilized as future all-optical switching devices. Another advantage of PIPTs for applications is that transport, and magnetic properties as well as optical properties can be considerably modulated by photoexcitation. This enables us to construct new switching or memory devices. For the developments of such devices using PIPTs, discriminations of the dynamics of different degrees of freedom are also important.

A key strategy toward realizing such PIPTs is the exploration of 1D systems. Since 1D systems have simple electronic structures as compared with 2D and 3D systems, they will provide good opportunities for us to discuss the mechanism and dynamics of PIPTs in detail. In addition, 1D systems essentially include instabilities inherent to e–l and s–l interactions as well as the e–e interaction, and sometimes produce characteristic phase transitions by lowering temperature or applying pressure. Under the influence of these interactions, a small density of photoexcitations will be able to stimulate instability of electronic states, and then drastic PIPTs may be observed. In this sense, the halogen (X)-bridged transition metal (M) compound (the MX-chain compound) focused on here, which are prototypical 1D systems with strong e–e and e–l interactions, are good targets for realizing characteristic PIPTs.

In this chapter, we review several kinds of PIPTs observed in the MX-chain compound (1) a photoinduced insulator–metal transition in the bromine-bridged nickel-chain compound [23], (2) a photoinduced charge-density-wave (CDW) to Mott–Hubbard phase transitions, and (3) a photoinduced insulator–metal transition in the halogen-bridged palladium-chain [40] and platinum-chain compounds [25].

Here, we will briefly introduce the compounds discussed in this chapter and summarize the concepts of the PIPTs they exhibit. The first example is a photoinduced insulator–metal transition (or a photoinduced Mott transition) in a bromine-bridged nickel chain compound [23], $[Ni(chxn)_2Br]Br_2$ (chxn = cyclohexanediamine), which consists of nickel (Ni^{3+})-bromine (Br^-) chains [41]. The crystal and electronic structures of this compound are detailed in Chap. 4. This compound has an unpaired electron in the 3d orbital of each Ni site forming a half-filled 1D electronic state. It is, however, not a metal due to the large Coulomb repulsion (U) among 3d electrons of Ni overcoming the electron transfer energy. Electrons are

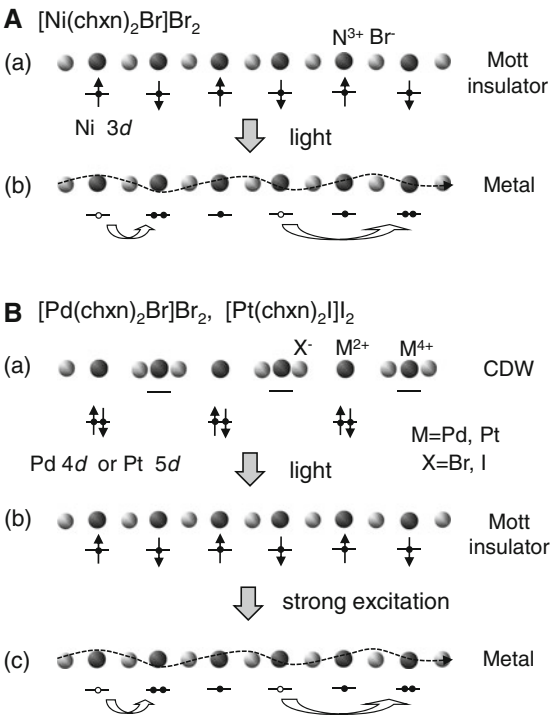

Fig. 5.1 Schematic illustrations of electronic structures and PIPTs in (**A**): $[Ni(chxn)_2Br]Br_2$, (**B**): $[Pd(chxn)_2Br]Br_2$ and $[Pt(chxn)_2I]I_2$. In Fig. (**A**) and (**B**), (a) and (b) show the electronic structures before and after photoexcitation, respectively

localized on each Ni site as schematically shown in Fig. 5.1A(a), and then this compound becomes a 1D Mott insulator [42, 43]. When this compound is irradiated with lights, the electrons are excited to other sites as shown in Fig. 5.1A(b). This corresponds to a photogeneration of electron and hole carriers. A number of carriers may change a Mott insulator to a metallic state. In Sect. 5.3, we will show that a photoinduced insulator–metal transition (or equivalently a photoinduced Mott transition) indeed occurs in an ultrafast time scale in the bromine-bridged Ni compound [23].

The second example is a PIPT from a CDW state to a Mott–Hubbard (MH) state in a bromine-bridged palladium compound $\left[Pd(chxn)_2Br\right]Br_2$ [40]. The crystal and electronic structures of the halogen-bridged Pd and Pt compounds are detailed in Chap. 4. In Pd and Pt compounds, the mono-valence state $(\cdots X^- - M^{3+} - X^- - M^{3+} - X^- \cdots)$ or MH state is usually unstable due to strong site-diagonal e–l interaction, and instead the mixed-valence state $(\cdots X^- - M^{4+} - X^- - M^{2+} - X^- - M^{4+} - X^- - M^{2+} \cdots)$ or CDW state with a dimeric displacement of the bridging X ions is stabilized. The most notable feature of the PdBr-chain compound is its proximity to the CDW–MH phase boundary [44, 45]. It has been reported that the CDW phase is changed to the MH phase by substituting about 16 % of Pd with Ni [46, 47]. This result makes us expect that Pd^{3+} species photogenerated via the charge-transfer (CT) transition $(Pd^{2+},\ Pd^{4+}) \rightarrow (Pd^{3+},\ Pd^{3+})$ render the surrounding CDW unstable, leading to a phase transformation from CDW to MH [48] as shown in Fig. 5.1B(a, b). In the PdBr-chain compound, such a PIPT is indeed observed.

The last example is the PIPT of the iodine-bridged platinum compound $\left[\mathrm{Pt(chxn)_2I}\right]\mathrm{I_2}$ [25]. This compound is also located close to the CDW–MH phase boundary [44, 45]. In this compound, the electron transfer energy between the neighboring M ions is larger than that in the PdBr-chain compound mentioned above. Therefore, we can expect that the CDW–MH transition is more continuous [49] and the transition efficiency is enhanced as compared to the PdBr-chain compound. It was indeed demonstrated that the photoinduced CDW–MH transition occurs with high efficiency leading to a complete phase conversion in the PtI-chain compound. For a strong photoexcitation, the low-energy spectral weight is increased, which is discussed in terms of the MH insulator to metal transition. The dynamics and mechanism of PIPTs observed in PdBr-chain compound and PtI-chain compound is elucidated in Sect. 5.4 by means of femtosecond pump–probe reflection spectroscopy. In Sect. 5.5, we give the summary of this chapter.

5.2 Experimental Methods

5.2.1 Femtosecond Pump–Probe Reflection Spectroscopy

In this chapter, we discuss the ultrafast dynamics of PIPTs in MX-chain compounds investigated on the basis of the results of femtosecond (fs) pump–probe (PP) reflection spectroscopy. Here, we briefly explain the experimental method. The experimental setup of fs PP reflection spectroscopy is schematically illustrated in Fig. 5.2. As a light source of the fs PP reflection spectroscopy, a Ti: sapphire (Al_2O_3) regenerative amplifier system operating at 1 kHz was employed. The fundamental output from the amplifier (800 nm: 1.55 eV) with a pulse width of 130 fs was divided into two beams by a beam splitter. In most of the experiments described in this chapter, one beam was used for a pump light, and the other for the excitation of an optical parametric amplifier (OPA) system from which probe lights ranging from 0.1 to 2.5 eV were obtained. When it is necessary to change the photon energy of the pump light, the fundamental beam for the pump light from the amplifier is introduced to another OPA system from which we can obtain tunable pump lights ranging from 0.5 to 2.5 eV.

In the fs PP measurements, the probe beam was focused at around the center of the excitation area on the sample surface. The reflected beam was detected by a Si, an InGaAs, or a HgCdTe photodetector. A suitable detector was selected depending on the measured energy range. A part of the probe beam is split before it is delivered to the sample and detected by another photodetector as shown in Fig. 5.2. The output signals (sample signal and the reference signal) of two photodetectors were analyzed with three boxcar integrators and an analogue processor to get a photoinduced reflectivity change. To adjust the delay time (t_d) of the probe light with respect to the pump light, the optical-pass length of pump light was changed by a computer-controlled stepping motor. The time resolution of the apparatus is about 180 fs.

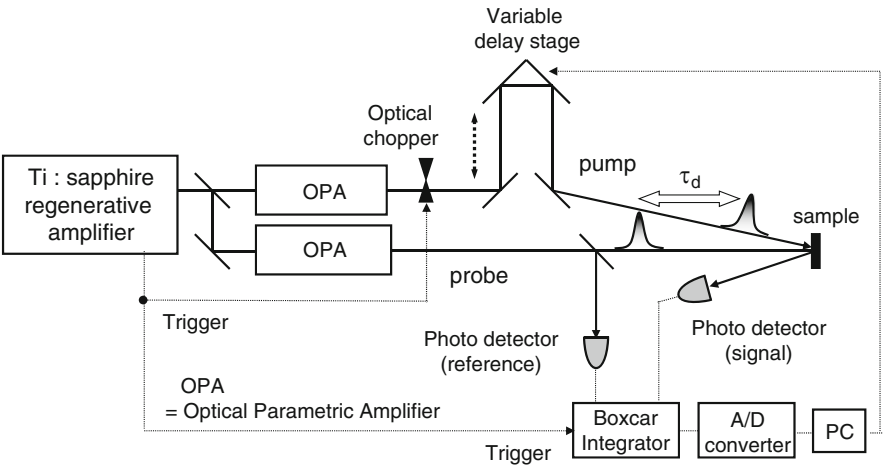

Fig. 5.2 Schematic of experimental setup for femtosecond pump–probe reflection measurement

5.3 Photoinduced Phase Transition in Mott-Insulator State of Halogen-Bridged Nickel-Chain Compound

Since the discovery of high-T_C superconductivity, doping-induced insulator (I)–metal (M) transitions or filling-control Mott transitions in 3d transition-metal compounds have been attracting much attention. In most undoped 3d transition-metal oxides, electrons are localized on atomic sites due to the large on-site Coulomb repulsion energy U, forming antiferromagnetic insulators (Mott insulators). Their electronic and magnetic properties can, however, be modified to a large extent by chemical doping [50–52]. The high-T_C superconductivity that emerges in the hole- or electron-doped layer-structured cuprates is the most drastic example. Photoexcitation is another effective method to create carriers in materials [53]. In this section, we describe the photoinduced I–M transition of the bromine-bridged Ni-chain compound, $\left[\mathrm{Ni(chxn)_2Br}\right]\mathrm{Br_2}$, which is a prototypical 1D Mott insulator. Photocarrier doping by using a 130-femtosecond laser pulse on the Ni chain induces a marked change of the electronic structure. When the photoexcitation density exceeds 0.1 per Ni site, a Drude-like high-reflection band emerges in the IR region, indicating the formation of a metallic state. Ultrafast dynamics of the photoinduced metallic state will be discussed on the basis of the results of temporal and doping-density dependence of the reflectivity spectra.

Before the detailed discussion on the photoinduced I–M transition in the Ni–Br chain compound, we will review the studies of the filling-control Mott transition in the 2D cuprates, as a prototypical example of the I–M transition in strongly correlated electron systems. In a typical undoped cuprate, La_2CuO_4, the crystal structure of which is shown in Fig. 5.3a, hole carries can be introduced to the CuO plane (the *ab* plane) by substituting La^{3+} ions with Sr^{2+} ions [50, 54]. As the

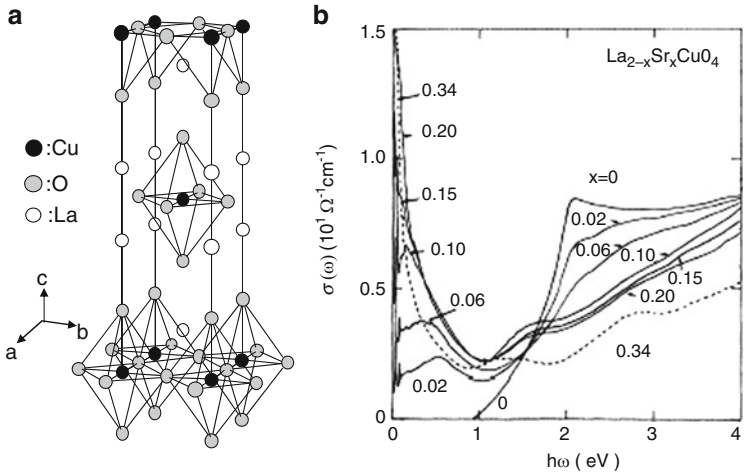

Fig. 5.3 (**a**) Crystal structure of the 2D cuprate, La_2CuO_4. (**b**) Optical conductivity $\sigma(\omega)$ spectrum of $La_{2-x}Sr_xCuO_4$ with various hole carrier concentrations (x) [54]

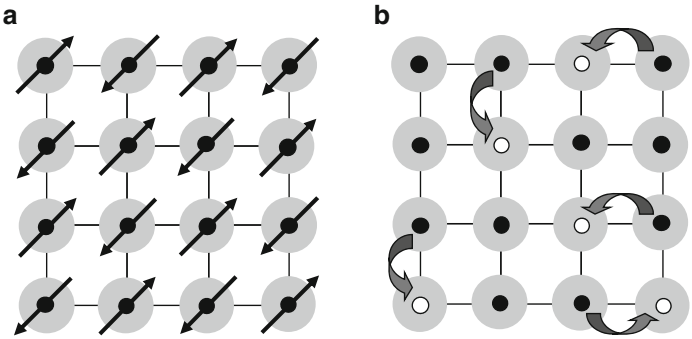

Fig. 5.4 (**a**) Schematics of localized 3d electrons (*filled circles*) and antiferromagnetic spin order (*arrows*) in 2D Mott insulator. (**b**) Conducting (metallic) state realized by the introduction of holes

hole-carrier concentration (x) in $La_{2-x}Sr_xCuO_4$ is increased, the transition from Mott insulator to metal occurs at around $x = 0.05$. This I–M transition is schematically illustrated in Fig. 5.4. Figure 5.4a shows the schematic of the electronic state of the Mott insulator, in which 3d electrons are localized in each Cu^{2+} ion due to the large on-site Coulomb repulsion energy U between the 3d electrons. The arrows indicate the antiferromagnetic spin arrangement. Figure 5.4b shows the holes-doping regime. When the holes (the open circles) are introduced by the doping, the electrons can move to other sites as indicated by the arrows due to the presence of the electron vacancies. In this case, a finite density of state is produced near the Fermi level within the optical gap and then the I–M transition occurs. As well known, $La_{2-x}Sr_xCuO_4$ ($0.06 < x < 0.25$) exhibits superconductivity at low temperatures. In another 2D cuprate, Nd_2CuO_4, a similar I–M

transition and superconductivity at low temperature is observed by substituting Nd by Ce through the electron-carrier doping [55]. In these materials, the I–M transitions and the collapse of the gap are clearly reflected by the optical conductivity spectra in the near-IR to visible region. Figure 5.3b shows the doping concentration (x) dependence of the optical conductivity (σ) spectra in $La_{2-x}Sr_xCuO_4$, which are obtained by the Kramers–Kronig (KK) analyses of the reflectivity spectra [54]. The parent compound (La_2CuO_4) has a clear peak at around 2 eV corresponding to the charge-transfer (CT) gap. With increasing x, the spectral weight of the CT-gap transition is transferred into the intragap region. Such a huge spectral change over a wide energy region is the ubiquitous feature of the Mott transition in the 2D cuprate and also other strongly correlated electron systems of 3d transition-metal oxides [50]. Our purpose is to trigger a similar Mott transition by a photocarrier doping in the Ni-chain compound.

5.3.1 *Ultrafast Photoinduced Transition from Mott Insulator to Metal in Bromine-Bridged Nickel-Chain Compound*

The polarized reflectivity spectrum of the Ni–Br chain compound is presented in Fig. 5.5a. A sharp peak at around 1.3 eV is due to the CT-gap transition. The transient reflectivity (TR) spectra observed at the delay time t_d after the photoexcitation are presented by the dots and lines. The excitation photon energy is 1.55 eV just above the CT gap. The intensity of the irradiated light was 3.6 mJ/cm^2. Under this condition, the average excitation density x_{ph} of the absorbed photon is 0.5 per Ni site within the absorption depth (460 Å), as estimated by taking account of the reflection loss (30 %) and the unit cell volume (8.68×10^{-21} cm^3). Immediately following the photoexcitation ($t_d = 0.1$ ps), the reflectivity in the mid-IR region considerably increases, being reminiscent of the Drude-like metallic response, while the reflectivity around the CT band decreases due to photoinduced bleaching. The magnitude of the transient reflectivity R' at $t_d = 0.1$ ps reaches about 70 % at the lowest photon energy of the probe light (0.12 eV), where the change of reflectivity ($\Delta R/R = (R' - R)/R$) is as large as 260 % of the original reflectivity R. The optical conductivity σ spectrum was obtained by performing the KK analyses of the original reflectivity spectrum and the transient ones, which are shown in Fig. 5.5b. As seen in the figure, the σ at $t_d = 0.1$ ps monotonically increases with lowering the probe photon energy to 0.12 eV, suggesting the closing of the optical gap. Such a noticeable photoinduced feature is observed only for the probe light polarization (E) parallel to the Ni–Br chain ($E//b$) and not for $E \perp b$ at all, indicating the photogeneration of a quasi-1D metallic state.

To clarify the photoinduced change of the electronic state in more detail, the excitation density x_{ph} dependence of the TR has been investigated. Spectra of the TR and σ at $t_d = 0.1$ ps for various x_{ph} are shown in Fig. 5.6. For the weak

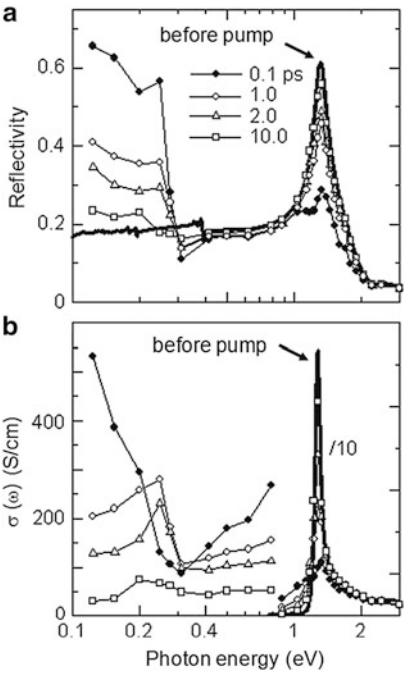

Fig. 5.5 (**a**) Polarized reflectivity spectra in $[Ni(chxn)_2Br]Br_2$ before and at the delay time t_d after the photoexcitation at room temperature. The excitation energy is 1.55 eV and the excitation density x_{ph} is 0.5 photon/Ni site. Polarizations of both the pump and probe lights are parallel to the chain axis *b*. (**b**) Optical conductivity $\sigma(\omega)$ spectra obtained by the Kramers–Kronig analyses of the reflectivity data in (**a**)

excitation of $x_{ph} < 0.012$, a midgap absorption is observed at 0.4–0.5 eV in the σ spectrum as depicted in Fig. 5.6. With increase of x_{ph}, the low-energy part of σ below 0.2 eV remarkably grows, and for $x_{ph} > 0.1$, the optical gap seems to disappear.

To investigate the time evolution of the photoinduced I–M transition (Mott transition), it is useful to examine the transfer of the spectral weight from the CT-gap region to the inner-gap one. The spectral weight can be quantitatively analyzed in terms of the effective number of electrons $N_{eff}(\omega)$ defined as follows [50, 54].

$$N_{\mathrm{eff}}(\omega) = \frac{2m_0}{\pi e^2 N} \int_0^{\omega} \frac{\sigma(\omega')}{4\pi} d\omega' \tag{5.1}$$

Here, m_0 is the free electron mass and N the number of Ni atoms per unit volume. $N_{eff}(\omega)$ is the measure for the kinetic energy of electrons on an energy scale of $\hbar\omega$. Since the lower energy bound of the measured photoinduced signals is 0.12 eV, the photoinduced change in N_{eff} (ΔN_{eff}) was calculated by using σ from 0.12 eV to $\hbar\omega$. The results for various x_{ph} at $t_d = 0.1$ ps are presented in Fig. 5.7. $\Delta N_{eff}(\omega)$ monotonically increases with $\hbar\omega$ up to 1 eV, reflecting the accumulation of the spectral weight below 1 eV. Then, it abruptly drops almost to zero at 1.3 eV due to the bleaching around the CT band, signaling that the spectral weight of the CT-gap transition is transferred to the inner-gap region by the photocarrier doping. The values of ΔN_{eff} above 1.5 eV for $x_{ph} = 0.12$ and $x_{ph} = 0.5$ are negative as seen in

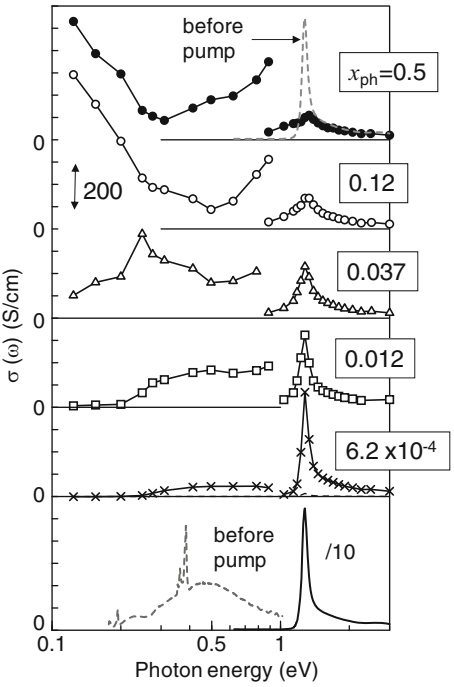

Fig. 5.6 The $\sigma(\omega)$ spectra of $[Ni(chxn)_2Br]Br_2$ before photoexcitation (*solid line* in *bottom panel* and *broken line* in *top panel*) and immediately after the photoexcitation (t_d =0.1 ps). The *gray broken line* in the *bottom panel* shows the polarized absorption spectrum before the photoexcitation (given in arbitrary units), which was directly measured using the transmission configuration

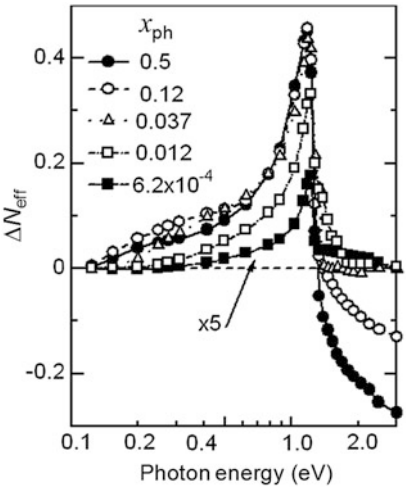

Fig. 5.7 Photoinduced changes of the effective number of electrons N_{eff} (ω) [ΔN_{eff} (ω)] at t_d = 0.1 ps for various x_{ph} in $[Ni(chxn)_2Br]Br_2$

Fig. 5.7. With increase of x_{ph} from 0.12 to 0.5, the photoinduced bleaching observed around the CT band is enhanced, while the spectral intensity in the IR region decreases slightly as seen in Fig. 5.7. These results suggest that the negative values of ΔN_{eff} above 1.5 eV for $x_{ph} > 0.1$ (especially for $x_{ph} = 0.5$) may be attributable to the miscount of the spectral weight in the IR region below the lower energy bound (0.12 eV) of the measured spectral range.

Here, let us comment on the validity of the KK analyses on the TR spectra. When applying the KK analyses on the TR spectra, there are two important effects to be considered [56, 59] (1) carrier concentration changes depending on the distance from the sample surface and (2) absorption depths of the probe light l_r and the pump light l_p are different. It is, therefore, necessary to check carefully the validity of the analyses. In the experimental results of the Ni–Br chain compound, the spectral shape of the TR due to the midgap absorption observed for $x_{ph} < 0.012$ is almost unchanged and, therefore, will not be considerably affected by those two effects. However, it is reasonable to consider that the absolute values of the TR and σ are somewhat underestimated, since $l_r > l_p$ (= 460 Å). To evaluate the two effects on the Drude-like reflection band observed for $x_{ph} > 0.1$, we postulated a metallic state expressed by a simple Drude model with the thickness l_t (200–2,000 Å) on the surface of the Ni–Br chain compound and simulated the R and σ spectra. The result of the simulation demonstrates that for $l_t > 1{,}000$ Å, spectral shape and absolute value of R and σ are independent of l_t. In the Ni–Br chain compound, the thickness of photoinduced metallic state (region with carrier concentration > 0.1) exceeds 1,000 Å for $x_{ph} > 0.2$. So we can consider that the Drude-like reflection band observed for $x_{ph} > 0.2$ will not be considerably influenced by the two effects. For the intermediate excitation density ($0.02 < x_{ph} < 0.2$), it might be necessary to take account of some errors in the analysis. Nevertheless, the observed systematic changes of ΔN_{eff} (ω) and the approximate holding of the sum rule over the wide range of x_{ph} ensure that the analysis using the KK analyses presented here reflects well the photoinduced changes of the electronic state.

In Fig. 5.8a, ΔN_{eff} (1 eV) and ΔN_{eff} (0.2 eV) at $t_d = 0.1$ ps are plotted as a function of x_{ph}. ΔN_{eff} (1.0 eV), which represents the total spectral weight transferred from the CT band to the inner-gap region, saturates for $x_{ph} > 0.04$. In contrast, ΔN_{eff} (0.2 eV), i.e., the spectral weight accumulated in the lower energy region between 0.12 and 0.2 eV, increases almost linearly with x_{ph} up to $x_{ph} = 0.1$. The steady increase of ΔN_{eff} (0.2 eV) for $x_{ph} > 0.04$ is attributable to the growth of the Drude weight. Let us compare the x_{ph} dependence of ΔN_{eff} with the chemical-doping-density (x) dependence of N_{eff} in the 2D cuprates previously reported, which is shown in Fig. 5.8b [50, 54]. In Fig. 5.8b, the solid and open circles show the x dependence of N_{eff} at 1.5 eV and that for the Drude component in the IR region, respectively. The observed clear resemblance of the x_{ph} dependence of ΔN_{eff} in the Ni–Br chain compound with the x dependence of N_{eff} in the 2D cuprate demonstrates that the Mott transition is driven by the photocarrier doping in the Ni–Br chain compound.

A remarkable aspect of the photoinduced Mott transition is the influence of the electron–hole asymmetry on the transient optical spectra. Being distinct from the chemical doping case, photoexcitation generates both electrons and holes in

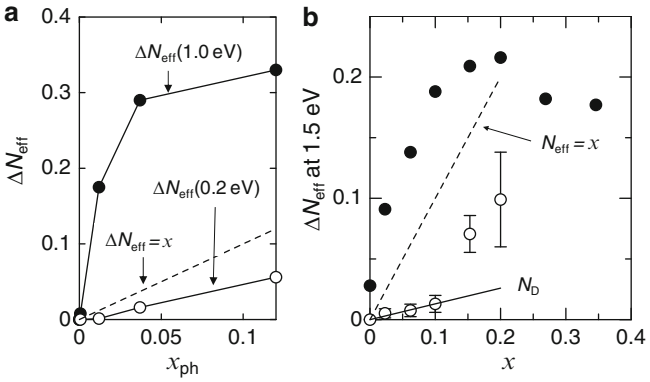

Fig. 5.8 (**a**) Photoinduced changes of the effective number of electrons ΔN_{eff} (1.0 eV) and ΔN_{eff} (0.2 eV) at $t_d = 0.1$ ps as functions of excitation photon density x_{ph} in $[Ni(chxn)_2Br]Br_2$. (**b**) The effective number of electrons as a function of the chemical-doping concentration x for $La_{2-x}Sr_xCuO_4$ [54]. N_{eff} and N_D are the total spectral weight in the IR region and the Drude component, respectively

materials. In the Ni–Br chain compound, it has been clarified from the measurement of the DC conductivity [60] and the Seebeck coefficient (H Okamoto, unpublished result) that a small number of electron carriers exists in an as-grown sample. A weak midgap absorption due to such carriers or small polarons is indeed observed in the σ spectrum ($E//b$) as shown by the broken line in Fig. 5.6. The photoinduced absorption observed for small x_{ph} ($= 6.2 \times 10^{-4}$) resembles this midgap absorption in spectral shape and energy position. This resemblance suggests that electron-type carriers are responsible for the photoinduced midgap absorption. The hole-type carriers with the Br p-character may be strongly localized by the strong electron–lattice interaction and hence make the least contribution to the spectral weight of the midgap absorption. When the metallic state is formed for $x_{ph} > 0.1$, however, there should be no distinction between electrons and holes for the strongly d–p hybridized state near the Fermi level.

5.3.2 *Relaxation Dynamics of the Photoinduced Metallic State*

The ultrashort lifetime of the photogenerated metallic state is another important aspect of the present photoinduced Mott transition. Figure 5.9a, b show the temporal characteristics of ΔR at 0.12 eV and $-\Delta R$ at 1.39 eV, respectively. Both two characteristics are almost the same with each other. In Fig. 5.9a, we also show the temporal evolutions of ΔN_{eff} (0.5 eV) for $x_{ph} = 0.012$ and $x_{ph} = 0.5$ by the open circles. ΔR (0.12 eV) and ΔN_{eff} (0.5 eV) are also in good agreement with each other. Therefore, the time characteristics of ΔR can be considered to reflect those of ΔN_{eff}

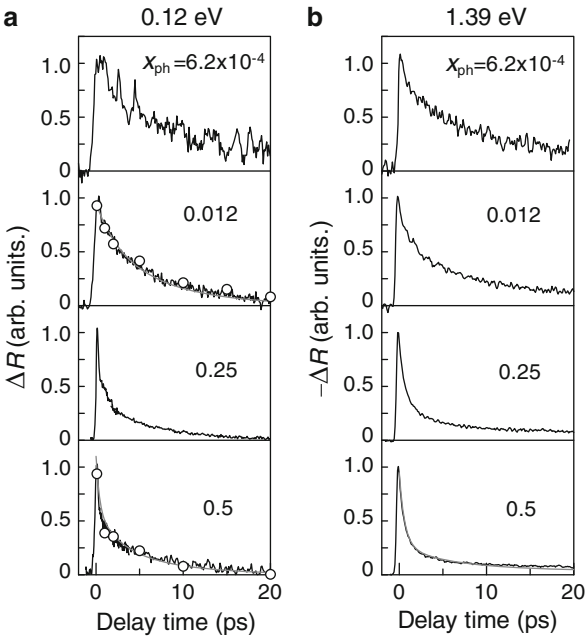

Fig. 5.9 Temporal profiles of ΔR measured (**a**) at 0.12 eV and (**b**) at 1.39 eV for various excitation photon density x_{ph} in $[Ni(chxn)_2Br]Br_2$. Temporal profiles of ΔN_{eff} (0.5 eV) for $x_{ph} = 0.5$ and 0.012 are also shown by the *open circles*

(0.5 eV). The time characteristics of ΔR (0.12 eV) can be well reproduced by the sum of the three exponential functions whose time constants τ_d (weights) are 3 ps (40 %), 8 ps (50 %), and $\gg$500 ps (10 %) for $x_{ph} = 0.012$ and 0.5 ps (60 %), 3 ps (15 %), and 8 ps (25 %) for $x_{ph} = 0.5$. The component with $\tau_d \gg 500$ ps for $x_{ph} = 0.012$ is attributable to some long-lived-trapped carriers. The ultrafast decay component with $\tau_d = 0.5$ ps is dominant for $x_{ph} = 0.5$, while such an ultrafast decay was not detected for $x_{ph} = 0.012$. Therefore, it is likely that the ultrafast decay is characteristic of the photogenerated metallic states.

The decay dynamics of the photoexcited state in Mott insulators has also been studied on the 2D cuprates (La_2CuO_4, Nd_2CuO_4, and $Sr_2CuO_2Cl_2$) [20, 21, 61, 62] and 1D cuprate (Sr_2CuO_3) [63], and 1D organic CT complex [(BEDT-TTF)-(F_2TCNQ), BEDT-TTF = bis(ethylenedithio)tetrathiafulvalene, F_2TCNQ = difluorotetracyanoquinodimethane] [18]. In La_2CuO_4, Nd_2CuO_4 and (BEDT-TTF)-(F_2TCNQ), in which photoinduced I–M transitions were demonstrated, decay time τ of metallic states was revealed to be shorter than 40 fs in the 2D cuprates and shorter than 200 fs in (BEDT-TTF)-(F_2TCNQ). These values of τ are significantly shorter than that in conventional semiconductors. The electron–electron scattering with emission of spin-excitations or spinons is considered as a possible mechanism for the ultrafast relaxation in the Mott insulators [20, 21, 61–63]. In the present bromine-bridged Ni-chain compound, enhancement of similar electron–electron scattering in the quasi-1D metallic state may play a major role in the increase of the recombination rate of photocarriers.

5.4 Photoinduced Phase Transition in CDW State of Halogen-Bridged Palladium-Chain and Platinum-Chain Compounds

In this section, we report another typical example of PIPTs in MX-chain compounds, that is, the photoinduced transition from the CDW state to the Mott–Hubbard state observed in the bromine-bridged Pd compound. In this photoinduced transition, the valences of Pd ions are changed just after the photoirradiation. Subsequently, the bridging halogen displacements are released, giving rise to the generation of coherent oscillations of bridging halogen ions. In the iodine-bridged platinum compound with more itinerant electronic states, the CDW ground state can be converted not only to the Mott–Hubbard state but also to the metallic state by strong photoexcitations. Dynamical aspects of these transitions are discussed in detail.

5.4.1 Ultrafast Photoinduced Transition from Charge-Density-Wave State to Mott–Hubbard State in Bromine-Bridged Palladium-Chain Compound

In this subsection, we discuss the CDW to MH transition, in $[Pd(chxn)_2Br]Br_2$, which is located near the CDW to MH phase boundary (see Chap. 4). Figure 5.10a shows the polarized reflectivity spectrum of $[Pd(chxn)_2Br]Br_2$ with the CDW state for the light polarization (E_i) oriented parallel to the chain axis b (i.e., $E_i//b$). The reflectivity spectrum of $[Pd_{0.84}Ni_{0.16}(chxn)_2Br]Br_2$ in the MH state is also shown for comparison [47], and the corresponding σ spectra obtained by the Kramers–Kronig transformation (KKT) of the R spectra are shown in Fig. 5.10b. The broad peak at ca. 0.7 eV in $[Pd(chxn)_2Br]Br_2$ is due to the charge-transfer (CT) transition, $(Pd^{2+}, Pd^{4+}) \rightarrow (Pd^{3+}, Pd^{3+})$ (see Fig. 5.10b). The σ spectrum for $\left[Pd_{0.84}Ni_{0.16}(chxn)_2Br\right]Br_2$ exhibits a peak structure at ca. 0.55 eV attributable to the Mott-gap transition, $(Pd^{3+}, Pd^{3+}) \rightarrow (Pd^{2+}, Pd^{4+})$ (Fig. 5.10b) [47]. Considering the Ni concentration, we call in the following these two compounds, $[Pd(chxn)_2Br]Br_2$ and $[Pd_{0.84}Ni_{0.16}(chxn)_2Br]Br_2$, as $x = 0$ and $x = 0.16$ compounds, respectively. Figure 5.10e shows the transient reflectivity change (ΔR) for $E_i//b$ using the 1.55-eV pump with polarization parallel to b. The averaged excitation photon density x_{ph} within the absorption depth (450 Å) is 0.025 photon (ph.)/Pd. Here, x_{ph} was evaluated from the absorption coefficient (2.23×10^5 cm^{-1}) and the reflection loss (61 %) of the pump light. Immediately after the photoexcitation ($t_d = 0.25$ ps), the reflectivity at 0.8–2 eV decreases and the reflectivity below 0.8 eV increased. The spectral shape of the transient ΔR is similar to the differential spectrum, i.e., $\Delta R = R(x = 0.16)–R(x = 0)$ in Fig. 5.10c, indicating that the MH state is generated by the photoexcitation in a CDW background.

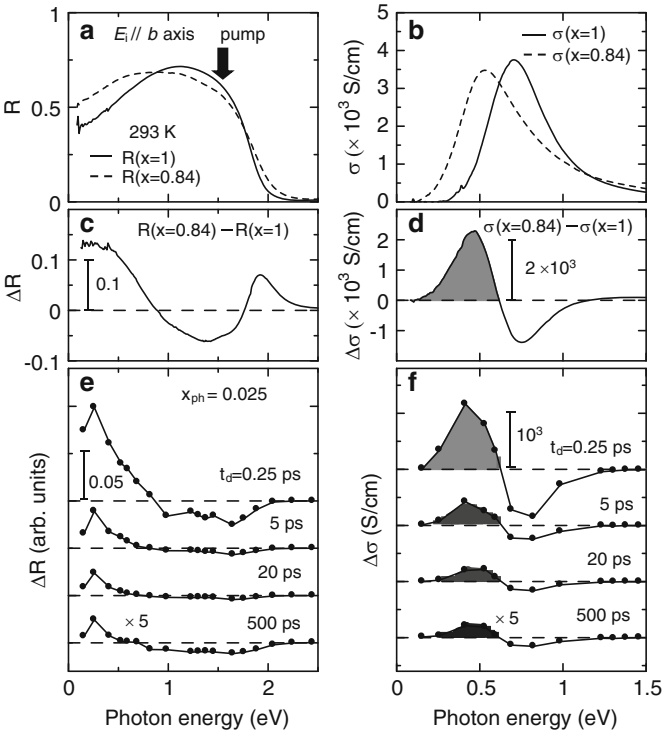

Fig. 5.10 (**a**, **b**) Polarized reflectivity (R) and optical conductivity (σ) spectra with $E_i//b$ for $[Pd(chxn)_2Br]Br_2$ ($x = 1$) (*solid line*) and $[Ni_{0.16}Pd_{0.84}(chxn)_2Br]Br_2$ ($x = 0.84$) (*dashed line*) at room temperature. (**c**, **d**) Differential reflectivity (ΔR) and optical conductivity ($\Delta\sigma$) spectra between $[Ni_{0.16}Pd_{0.84}(chxn)_2Br]Br_2$ ($x = 0.84$) and $[Pd(chxn)_2Br]Br_2$ ($x = 1$). (**e**, **f**) Photoinduced reflectivity change (ΔR) and optical conductivity change ($\Delta\sigma$) in $[Pd(chxn)_2Br]Br_2$ ($x = 1$) at various delay times (t_d) after photoexcitation (*dots*). *Solid lines* are guides to the eye. The pump energy is 1.55 eV [indicated by an *arrow* in (**a**)]. The excitation density (x_{ph}) is 0.025 photon/Pd. The polarizations of the pump and probe lights are parallel to b

To evaluate the photoconversion efficiency, we calculated photoinduced change ($\Delta\sigma$) spectra by KKT analysis of the $R + \Delta R$ spectra. As shown Fig. 5.10f, $\Delta\sigma$ also coincides well with the differential spectrum (i.e., $\Delta\sigma = \sigma(x = 0.84) - \sigma(x = 1)$ in Fig. 5.10d). The spectral shape of the photoinduced $\Delta\sigma$ spectrum appears to be almost independent of t_d up to 500 ps. By comparing the integrated intensity of the induced absorption in the photoinduced $\Delta\sigma$ (the gray area in Fig. 5.10f) with that of differential spectrum (the gray area of $\sigma(x = 0.84) - \sigma(x = 1)$ in Fig. 5.10d), a efficiency (ϕ) of the CDW to MH conversion was evaluated to be 55 % at $t_d = 0.25$ ps for $x_{ph} = 0.025$ ph./Pd. From these values it can be deduced that an MH domain produced by one photon consists of 22 Pd sites. The high efficiency of the CDW–MH conversion can be attributed to the near-degeneracy of the CDW and MH states.

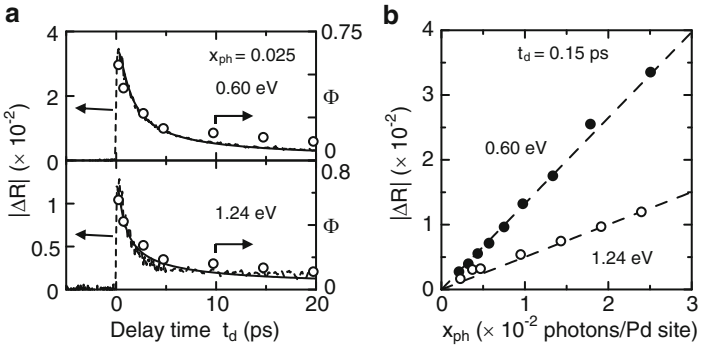

Fig. 5.11 (**a**) Time profiles of ΔR(0.60 eV) and ΔR(1.24 eV) for $x_{ph} = 0.025$ (*dashed lines*). The time profile of ϕ is also shown (*open circles*). *Solid lines* are fitting curves (see text). (**b**) Excitation-density dependence of ΔR(0.60 eV) and ΔR(1.24 eV) for $t_d = 0{:}15$ ps (*dots*). *Dashed lines* are guides for the eye

To obtain information about the nature of the photogenerated MH state, we also measured ΔR spectra under a resonant excitation of the CT transition (0.7 eV) (not shown). The spectral shape and its time dependence for the 0.7-eV pump were found to be almost the same as those for the 1.55-eV excitation. Previous electroreflectance [64] and photoconductivity [45] measurements for MX-chain compounds in the CDW phase revealed that the excited state produced by resonant excitation is an excitonic CT state. Therefore, it is natural to consider that the MH domain consisting of ca. 20 Pd sites ($\cdots - Pd^{3+} - Pd^{3+} \cdots\cdots Pd^{3+} - Pd^{3+} - \cdots$) is also generated by pumping at 1.55 eV from an excitonic (or local) CT state ($\cdots - Pd^{2+} - Pd^{3+} - Pd^{3+} - Pd^{4+} - \cdots$) via multiple CT processes.

Next, let us discuss the dynamical aspects of the photoinduced transition. Figure 5.11a shows the time profile of ϕ (open circles) together with those of the transient reflectivity change ($|\Delta R|$) at 0.60 and 1.24 eV (the dashed line). As two profiles are in very close agreement with each other, the profiles of $|\Delta R|$ at these two energies are considered to be suitable for use as a measure for the photogeneration and decay of the MH domains. The initial responses of ΔR(0.60 eV) and ΔR (1.24 eV) are presented by open circles in Fig. 5.12a(i), b(i), respectively. ΔR (0.60 eV) increases immediately upon photoexcitation, while ΔR(1.24 eV) decreases. This behavior is well reproduced by the temporal profile of the step response calculated by the convolution assuming a Gaussian pulse response function with a width of 180 fs (solid line). This indicates that the formation of the 1D MH domain occurs much faster than the time resolution of the present observations. Immediately after the initial rise, a coherent oscillation is observed up to 3 ps [see Fig. 5.12a(ii), b(ii)], which will be discussed later.

The time profiles of ΔR (Fig. 5.11a) excluding the oscillation can be reproduced well by

$$\Delta R(t) = A \cdot \mathrm{erf}\left\{\left(\frac{t}{\tau}\right)^{-n}\right\} \tag{5.2}$$

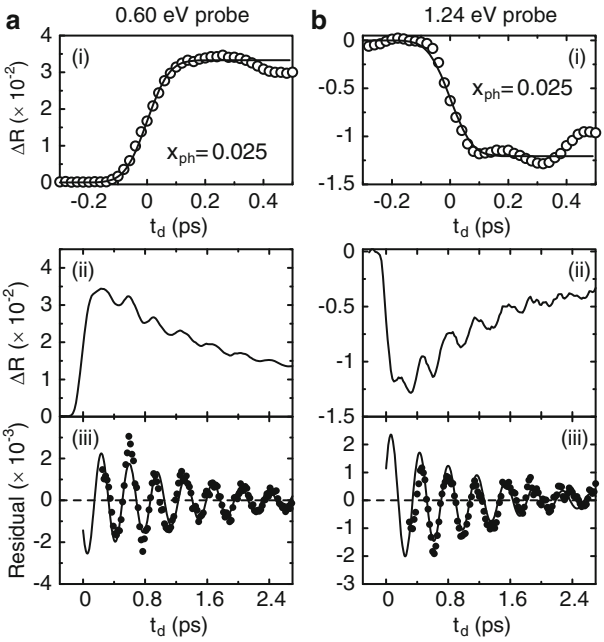

Fig. 5.12 (**a**, **b**) (i) Initial ΔR response for $x_{ph} = 0.025$ (*open circles*) with probe photon energies of (**a**) 0.60 eV and (**b**) 1.24 eV. *Solid lines* denote fitting curves. (ii) Time profiles of ΔR within 3 ps. (iii) Oscillatory components obtained by subtracting background rise and decay from time profiles shown in (ii) (*dots*) (see text). *Solid lines* denote the time profiles of a damped oscillator

where erf is the error function. The calculated response with parameters for $\tau = 0.85$ ps and $n = 0.8$ for ΔR(0.60 eV) and $\tau = 0.42$ ps and $n = 0.61$ for ΔR (1.24 eV) are shown as solid lines in Fig. 5.11a. Equation (5.2) describes the geminate recombination of a pair of excited species diffusing along a 1D chain [65], and is consistent with the linear relationships between ($|\Delta R|$) and x_{ph} (Fig. 5.11b). The parameter τ is related to the diffusion constant (D) and the initial distance between two photogenerated species (l_o) by $\tau = l_o^2/4D$.

For an infinite chain, n is 0.5. The evaluated values of n (>0.5) indicate that the decay rate of the excited species is larger than in an infinite case, possibly due to the spatial confinement of the motion of the excited species, which increases the encounter rate [66]. A plausible candidate for the excited species is the pair of domain walls (DWs) between the original CDW state and the photogenerated MH state (i.e., the CDW–MH DWs). When the MH and CDW states are degenerate, a finite 1D MH domain corresponds to a pair of CDW–MH DWs, similar to the case of DWs in the neutral (N)-ionic (I) transition system [67]. Strictly, the energy of the MH state is slightly higher than that of the CDW state, so that an MH domain will be confined.

The coherent oscillations observed in the ΔR response [Fig. 5.12a(ii), b(ii)] provide important information about the charge and lattice dynamics of the present photoinduced CDW to MH transition. By subtracting the background rise and decay from the ΔR response, we extracted the oscillatory component and plotted

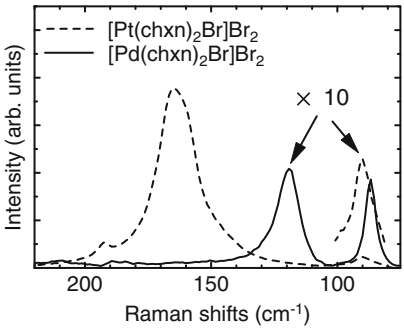

Fig. 5.13 Polarized Raman scattering spectra obtained under excitation of 1.96 eV for $[Pd(chxn)_2Br]Br_2$ (*solid line*) and $[Pt(chxn)_2Br]Br_2$ (*dashed line*). The intensity of excitation is the same for both compounds

by dots in Fig. 5.12a(iii), b(iii). The data were analyzed assuming a damped oscillator given by the following formula.

$$\Delta R_{\mathrm{osc}} = \mathrm{A}_0 \cos(\omega_0 t - \theta_0) \exp(-t/\tau_0) \tag{5.3}$$

Here, where ω_0 is the oscillation frequency, τ_0 is the decay time, and θ_0 is the initial phase. The simulated results (solid lines) reproduce well the experimental results. The evaluated frequency ω_0 (the period T_0) of the oscillation does not depend on the probe energy ($\omega_0 = 90$ cm^{-1}, $T_0 = 0.36$ ps). The decay time τ_0 of the oscillation is 1.4 ps (1.2 ps) for 0.6 eV (1.24 eV). The initial phase θ_0 at 1.24 eV is small (ca. $\pi/6$), indicating that the oscillator is of a cosine type, and shifts by π at 0.60 eV, which corresponds to the sign reversal of ΔR_{osc}. Such a change in the sign of ΔR_{osc} is in agreement with that in ΔR response (Fig. 5.10e), suggesting that the coherent oscillation is associated with the CDW–MH conversion. A possible origin of the oscillation is the symmetric Pd–Br stretching mode in the photogenerated MH domains, since the CDW–MH conversion should be accompanied by release of the bridging-Br displacements.

The polarized Raman spectrum with the backscattering configuration for $[Pd(chxn)_2Br]Br_2$ is shown in Fig. 5.13, together with that for $[Pt(chxn)_2Br]Br_2$ which has larger bridging-Br displacements. The polarizations of the incident and scattering lights are both parallel to the PdBr chains. The band is observed at ca. 85 cm^{-1} in both compounds with the comparable intensities, indicating that this peak is not related to an M–Br stretching mode but probably to a mode associated with the ligand molecules. The band at 120 cm^{-1} (165 cm^{-1}) in $\left[Pd(chxn)_2Br\right]Br_2$($[Pt(chxn)_2Br]Br_2$) can be assigned to the symmetric Pd–Br (Pt–Br) stretching mode. The intensity decrease and the lower frequency shift of the Raman band in $[Pd(chxn)_2Br]Br_2$ are due to the decrease of the bridging-Br displacements and the resultant softening of the mode, respectively. In $[Pd(chxn)_2Br]Br_2$, the frequency of the coherent oscillation (90 cm^{-1}) is lower than that of the Raman band (120 cm^{-1}), consistent with the relative weakness of Pd^{3+}–Br^- bond in the photoinduced MH-like domains compared to the original Pd^{4+}–Br^- bond in the CDW state. Here, it should be noted that in the photogenerated MH domains, the Br ion is not located at the precise midpoint between neighboring Pd ions. Otherwise, the frequency of the oscillation in the ΔR

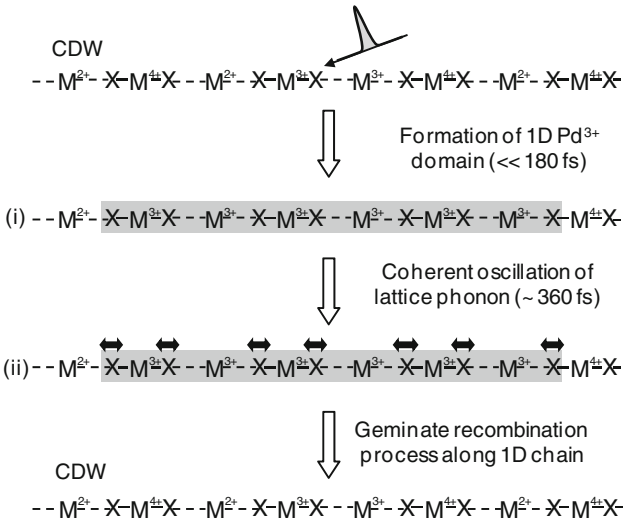

Fig. 5.14 Schematic of proposed CDW–MH conversion process

response should be double the frequency of the Pd–Br stretching mode. This suggests that some charge modulation $(-\mathrm{Pd}^{3+\rho} - \mathrm{Pd}^{3-\rho} - \mathrm{Pd}^{3+\rho} - \mathrm{Pd}^{3-\rho} -)$ $(0 < \rho \ll 1)$ remains even in the MH domains, which is likely related to the constrained finite size of the MH domains (ca. 20 Pd sites).

On the basis of the results presented above, the dynamics for the photoinduced CDW-to-MH transition can be interpreted in the scheme shown in Fig. 5.14. Upon excitation, a CT excited state is photogenerated, and a confined 1D MH domain composed of ca. 20 Pd sites subsequently emerges (i). As this process is a sequence of CT processes, the transition will complete on the time scale of the transfer energy T. For a typical value of T for the MX chains, 0.7 eV [68, 69], the time scale is 6 fs, which is much faster than the time resolution (180 fs). Therefore, the formation process of the confined 1D MH domain could not be resolved by the present pump–probe measurements. In the formation process of a 1D MH domain, the bridging-Br displacements persist as shown in Fig. 5.14(i), since the period of the Pd–Br stretching mode (360 fs) is much longer than the time scale of the transfer energy T. The important finding is that the initial formation of a 1D MH domain is purely electronic, driven through the effect of the intersite Coulomb repulsion V. Namely, a photogenerated $\mathrm{Pd}^{3+} - \mathrm{Pd}^{3+}$ pair decreases the energy gain due to V in the background CDW state and then destabilizes the neighboring Pd^{2+} and Pd^{4+} sites. A large-size MH-like Pd^{3+} domain can be realized without the release of the Br displacements, indicating that V is essential for stabilization of the CDW state. In $\left[\mathrm{Pd(chxn)_2Br}\right]\mathrm{Br_2}$, the effect of e–l interaction is suppressed compared with other Pd compounds owing to the shorter Pd–Pd distance resulting from the chemical pressure of the strong 2D hydrogen-bond network [44, 70]. The suppression of e–l interaction is considered to be the reason why the MH domain can be produced

easily without the release of the Br displacements. The relaxation of the Br displacements (ii) occurs after the formation of the 1D MH domain, accompanied by the coherent oscillation, which modulates the energy of the $4d_{z^2}$ orbital and, therefore, the Mott-gap transition in the 1D MH domain. As a result, the coherent oscillation is detected in the ΔR response. The photogenerated MH domains subsequently return to the ground state via the 1D random walk of DW pairs, which was reproduced by the error function.

5.4.2 *Ultrafast Photoinduced Transitions in Charge Density Wave, Mott Insulator, and Metallic Phases in Iodine-Bridged Platinum-Chain Compound*

In the Ni–Br chain compound with the MH-type ground state, the photoinduced transition to metal occurs as discussed in Sect. 5.3. On the other hand, in the Pd–Br chain compound near the CDW and MH phase boundary, the photoinduced CDW to MH transition is driven. Therefore, it is natural to expect that a CDW to metal transition can be induced by the photoirradiation on a CDW compound near the CDW and MH phase boundary. In $\left[\mathrm{Pd(chxn)_2Br}\right]\mathrm{Br_2}$ discussed above, however, such a CDW to metal transition cannot be induced even by the strong photoexcitation. To realize a photoinduced CDW to metal transition, a compound having more itinerant electronic states is appropriate. From these considerations, we selected [Pt$(\mathrm{chxn})_2\mathrm{I}]\mathrm{I_2}$. In this compound, the 1D electronic state is composed of 5d orbital of Pt and 5p orbital of I, so that the itinerancy should be enhanced compared to $\left[\mathrm{Pd(chxn)_2Br}\right]\mathrm{Br_2}$ with 1D electronic state composed of 4d orbital of Pd and 4p orbital of Br.

Figure 5.15a shows the reflectivity spectrum of $\left[\mathrm{Pt(chxn)_2I}\right]\mathrm{I_2}$ with the light polarization (E) parallel to the chain axis b ($E//b$). The imaginary part of dielectric constant ε_2 [solid line in panel (b)] was obtained by using the KKT of the reflectivity spectrum. The broad peak at 0.95 eV is due to the CT transition ($\mathrm{Pt^{2+}}$, $\mathrm{Pt^{4+}}$) $\rightarrow$ ($\mathrm{Pt^{3+}}$, $\mathrm{Pt^{3+}}$). In Fig. 5.15c, e, photoinduced reflectivity changes (ΔR) spectra for ($E//b$) with the polarization of the pump light ($E_{ex}//b$) are presented for three excitation densities (x_{ph}). x_{ph} is the averaged photon (ph) density of the pump light absorbed within the absorption depth (ca. 300 Å). The delay time t_d of the probe light relative to the pump light is 0.16 and 1.7 ps. Errors of ΔR are smaller than 10^{-3} (10^{-4}) in the mid-IR (near-IR) region. At $t_d = 0.16$ ps, the reflectivity increases below 1 eV. For $x_{ph} = 0.005$ and 0.02 ph/Pt, ΔR has a peak at ca. 0.4 eV, while for $x_{ph} = 0.05$ ph/Pt, ΔR has no peak but monotonically increases with decrease in energy. At $t_d = 1.7$ ps, ΔR has a peak at ca. 0.4 eV in common. The results demonstrate that there is a metastable-photoinduced phase characterized by the reflection peak at ca. 0.4 eV.

To get information of the photoinduced phase, the photoinduced change in ε_2 ($\Delta\varepsilon_2$) (Fig. 5.15d, f) was obtained by KKT of $R + \Delta R$. At $t_d = 0.16$ ps, ε_2 decreases at ca. 0.95 eV in common. For $x_{ph} = 0.005$ and 0.02 ph/Pt, ε_2 rather

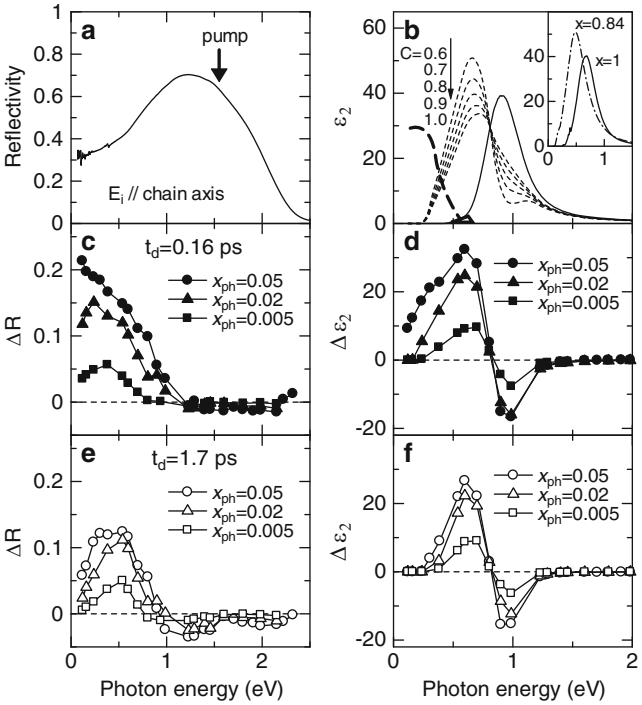

Fig. 5.15 (**a**, **b**) Polarized reflectivity (R) and ε_2 spectra along the chain (*solid lines*) in $[Pt(chxn)_2I]I_2$. *Thin broken lines* in (**b**) show the ε_2 spectra of the MH state for various C values. The *thick broken line* shows the ε_2 spectrum for the photoinduced metallic state (see text). The inset in (**b**) shows the ε_2 spectra of $[Ni_{1-x}Pd_x(chxn)_2Br]Br_2$. (**c**)–(**f**) Photoinduced changes in R (ΔR) and ε_2 ($\Delta\varepsilon_2$) for three excitation densities at $t_d = 0.16$ and 1.7 ps

increases at ca. 0.6 eV. Such spectral changes are very similar to those observed in the CDW–MH transition of the PdBr-chain compound, which is discussed in Sect. 5.4.1. This indicates that the similar transition occurs in the PtI-chain compound. For $x_{ph} = 0.05$ ph/Pt, ε_2 has a large spectral weight below 0.2 eV, suggesting a formation of a metallic state. At $t_d = 1.7$ ps (Fig. 5.15f), the spectral shape of ε_2 is equal to that for $x_{ph} = 0.005$ and 0.02 ph/Pt at $t_d = 0.16$ ps. This indicates that the metallic state quickly returns to the MH state.

Here we evaluate the conversion efficiency ϕ of the CDW to MH transition. In Fig. 5.16, the magnitude of $\Delta\varepsilon_2$ at 0.6 eV, $\Delta\varepsilon_2$(0.6 eV), characterizing the amount of the MH state is plotted by solid circles for three x_{ph} values. The excitation density dependence of ΔR at 0.54 eV, ΔR (0.54 eV), is also shown by open circles, which coincides with that of $\Delta\varepsilon_2$ (0.6 eV). Therefore, we use ΔR (0.54 eV) as a measure for the amount of the MH state. ΔR (0.54 eV) is proportional to x_{ph} for the low excitation density (the broken line in Fig. 5.16). It starts to deviate from the linear relation at $x_{ph} \sim 0.006$ ph/Pt and tends to saturate for $x_{ph} > 0.015$ ph/Pt. Such saturation is attributable to the space filling of the photogenerated species [7, 38, 71]. Assuming

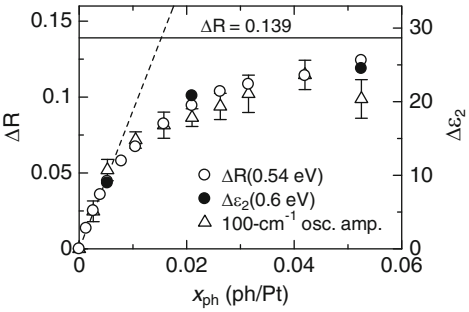

Fig. 5.16 Excitation-density dependence of ΔR (0.54 eV) and ε_2 (0.6 eV) at $t_d = 1.7$ ps and the amplitude of the coherent oscillation (100 cm^{-1}) on ΔR (0.69 eV) in arbitrary unit. The *dashed line* shows a linear relation

the space filling of the photoinduced MH states and the saturation density of $x_{ph} = 0.015$ ph/Pt, the size of the photoinduced MH domain is evaluated to be 70 Pt sites/ph. In $[Pd(chxn)_2Br]Br_2$, ΔR is proportional to x_{ph} at least up to 0.025 ph/Pd which is about four times as large as 0.006 ph/Pt and ϕ (ca. 20 Pd sites/ph) is about 1/3.5 of 70 Pt sites/ph in the PtI compound [40]. These results are fairly consistent with each other. Using the value of ϕ and the linear relation between ΔR and x_{ph}, we can evaluate the ΔR value for the complete CDW to MH conversion to be 0.139, which was shown by the solid line in Fig. 5.16. From this line, the ratio C of the photoinduced MH state relative to the original CDW state for $x_{ph} = 0.05$ is estimated to be 0.9.

Now, we can deduce the ε_2 spectrum for the MH state using the evaluated C value. Thin broken lines in Fig. 5.15b show the spectra of $\varepsilon_2(\text{CDW}) + \Delta\varepsilon_2(0.05)/C$ with $C = 0.6$–1.0, which give the hypothetical spectra of the MH phase. Here, ε_2(CDW) is the original spectrum and $\Delta\varepsilon_2$ (0.05) is $\Delta\varepsilon_2$ at $t_d = 1.7$ ps for $x_{ph} = 0.05$ ph/Pt. In the inset of Fig. 5.15b, the ε_2 spectrum of $\left[Ni_{0.16}Pd_{0.84}(chxn)_2Br\right]Br_2$ in the MH phase is presented together with that of $[Pd(chxn)_2Br]Br_2$ in the CDW phase [47]. The former provides a single peak with a Lorentzian shape. Therefore, it is reasonable to consider that the C values of 0.6–0.8 giving the split or distorted spectra are not valid and the appropriate C value is 0.9–1.0. This is also consistent with the C value (0.9) estimated from the excitation density dependence.

To clarify the nature of the metallic state produced just after the photoirradiation for $x_{ph} = 0.05$ ph/Pt, we normalized the $\Delta\varepsilon_2$ spectra for $x_{ph} = 0.05$ and 0.02 ph/Pt ($t_d = 0.16$ ps) at the absorption peak (0.65 eV) for the MH state and calculated the differential spectrum between them, which is shown by the thick broken line in Fig. 5.15b. The spectrum shows a monotonous increase with decrease in energy, demonstrating the formation of a metallic state. As discussed above, the conversion to the MH state is almost complete for $x_{ph} = 0.05$ ph/Pt. It is therefore natural to consider that the metallic state is produced by the carrier doping to the MH state. Such a carrier doping after the photogenerations of MH domains may be understood possibly by the following processes (1) the residual CDW domains or the boundary between the MH domains has finite charges, acting as additional carriers in the MH state or (2) the MH state is formed by the first half of the pump pulse and the carriers are generated in the MH state by the second half of the pump pulse, while it is difficult to discriminate these two processes.

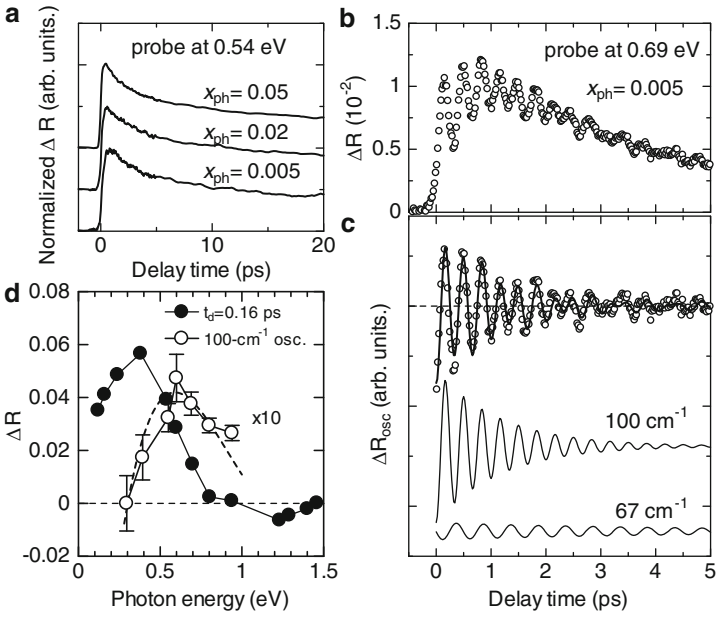

Fig. 5.17 (**a**) Time profiles of normalized ΔR (0.54 eV). (**b**) Time profile of ΔR (0.69 eV) for $x_{ph} = 0.005$. (**c**) Oscillatory components extracted from (**b**) and the fitting curve (*solid line*) which is the sum of the two damped oscillators shown in the lower part. (**d**) Probe-energy dependence of the 100-cm^{-1} oscillation amplitude (*open circles*) and ΔR ($t_d = 0.16$ ps) (*solid circles*) for $x_{ph} = 0.005$ ph/Pt. The *broken line* is the first derivative of ΔR ($t_d = 0.16$ ps)

Let us proceed to the discussion about the dynamics of the PIPT. In Fig. 5.17a, the time profiles of normalized ΔR (0.54 eV) are presented. The signal instantaneously rises, indicating that the MH domain is formed within the temporal resolution (180 fs). The decay time of the MH domain is ca. 20 ps. These features are independent of x_{ph}. Subsequently to the initial rise, the coherent oscillations are observed similarly to the case of the CDW to MH transition in $[Pd(chxn)_2Br]Br_2$. To scrutinize the oscillations, we selected ΔR (0.69 eV) for $x_{ph} = 0.005$ ph/Pt, which is plotted in Fig. 5.17b, and extracted the oscillatory component by subtracting the background rise and decay from ΔR, which is plotted in Fig. 5.17c. The oscillatory component can be reproduced well by the sum of the two damped oscillators,

$$\Delta R_{osc} = \sum_{i}^{2} A_i \cos(\omega_i t - \theta_i) \exp(-t/\tau_i) \tag{5.4}$$

as shown by the solid line. Here, ω_i is the oscillation frequency, τ_i is the decay time, and θ_i is the initial phase. In the fitting procedure, the response function of the measurement system was taken into account as a Gaussian profile. The two

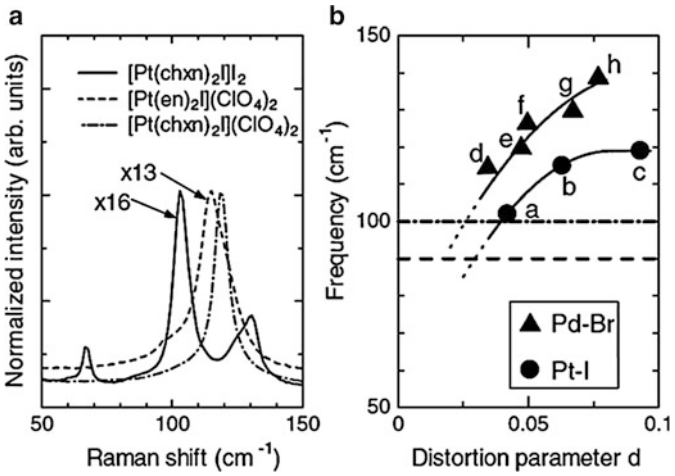

Fig. 5.18 (**a**) Polarized Raman spectra obtained from a 1.96 eV excitation for $[Pt(chxn)_2I]I_2$, $[Pt(en)_2I](ClO_4)_2$, and $[Pt(chxn)_2I](ClO_4)_2$. (**b**) Frequencies of the M–X stretching Raman bands as a function of the distortion parameter *d*; a: $[Pt(chxn)_2I]I_2$, b: $[Pt(en)_2I](ClO_4)_2$, c: $[Pt(chxn)_2I](ClO_4)_2$, d: $[Pd(en)_2Br](C_5\text{-}Y)_2\cdot(H_2O)$, e: $[Pd(chxn)_2Br]Br_2$, f: $[Pd(en)_2Br](C_5\text{-}Y)_2\cdot(H_2O)$, g: $[Pd(en)_2Br](C_4\text{-}Y)_2\cdot(H_2O)$, and h: $[Pd(en)_2Br](ClO_4)_2$ (en = ethylenediamine and Y = sulfosuccinate) (a–c and e–h: 293 K and d: 206 K). The *broken line* and the *dashed dotted line* show the frequency of the coherent oscillation for $[Pd(chxn)_2Br]Br_2$ and $[Pt(chxn)_2I]I_2$, respectively

oscillatory components are also shown in Fig. 5.17c. The evaluated ω_i, τ_i, and θ_i are 100 cm^{-1}, 1.2 ps, and π (cosine type) for the high-frequency component and 67 cm^{-1}, 5 ps and $3/2\pi$ (sine type) for the low-frequency one. The excitation-density dependence of the amplitude for the 100-cm^{-1} oscillation (triangles in Fig. 5.16) is the same as that of the amount of the MH phase characterized by ΔR (0.54 eV) (open circles). In addition, the oscillation is of cosine type. These results suggest that the 100-cm^{-1} oscillation is a displacive-type oscillation associated with the CDW–MH transition. Since this transition should be accompanied by the release of the displacements of the I ions, the oscillation can be assigned to the Pt–I stretching mode in the photogenerated MH domains. As the 67-cm^{-1} oscillation is of sine type, it will be due to an impulsive stimulated Raman process.

To clarify the origin for the coherent oscillation with 100 cm^{-1} in more detail, we refer to the Raman spectra. In Fig. 5.18a, the Raman spectrum of $[Pt(chxn)_2I]I_2$ is presented together with those of other PtI-chain compounds, $[Pt(en)_2I](ClO_4)_2$ and $[Pt(chxn)_2I](ClO_4)_2$. All of the Raman spectra were measured with the back-scattering configurations and with the polarizations of incident and scattering lights parallel to 1D chains. A small peak at 67 and 130 cm^{-1} in $[Pt(chxn)_2I]I_2$ can be assigned to the oscillation of the ligand molecules like the case of $[Pd(chxn)_2Br]Br_2$ [40]. The bands at 100–120 cm^{-1} are due to the symmetric Pt–I stretching mode. In Fig. 5.18b, the frequency of this mode is plotted as a function of the distortion parameter *d* by the solid circles. *d* is defined as $d = 2\delta/L$ (δ is the displacement of the bridging X ions and *L* is the M–M distance). The frequency of the Pd–Br

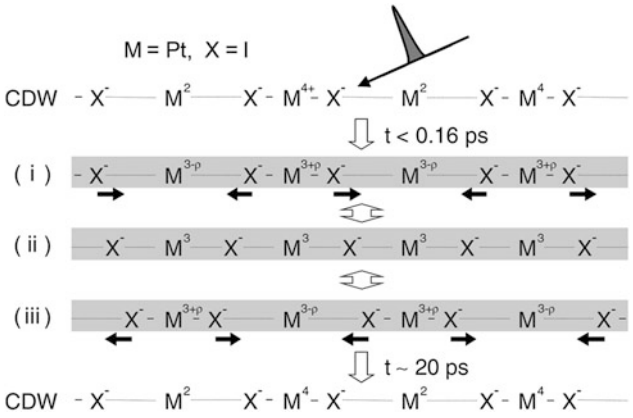

Fig. 5.19 Schematic of the CDW–MH conversion. After the formation of a 1D M^{3+} domain shown in (i), the equilibrium position of X comes on the midpoint between the neighboring M ions as shown in (ii). At the same time, the coherent oscillation of X occurs as (i) → (ii) → (iii) → (ii) → (i). ρ corresponds to the charge modulation associated with the displacements of X

stretching mode in the PdBr chains was also presented by the solid triangles in the same figure. The frequency of each mode sharply decreases with decrease in d. In fact, in $[Pd(chxn)_2Br]Br_2$, the frequency of the coherent oscillation (90 cm^{-1}) within the photogenerated MH domains (broken line in Fig. 5.18b) is much lower than that of the Pd–Br stretching Raman band (120 cm^{-1}: e in Fig. 5.18b) [40]. In $[Pt(chxn)_2I]I_2$, however, the frequency of the coherent oscillation (100 cm^{-1}: dashed–dotted line in Fig. 5.18b) is almost equal to that of the Raman band (102 cm^{-1}) and is larger than that (90 cm^{-1}) in the PdBr chains, although the mass of I is much larger than that of Br.

This contradiction can be explained as follows. Since the size of a photogenerated MH domain is very large (ca. 70 Pt sites) in $[Pt(chxn)_2I]I_2$, the equilibrium position of the bridging I ion should be the midpoint between the neighboring Pt^{3+} ions. In such a case, the frequency of the coherent oscillation on ΔR is double the frequency of the Pt–I stretching vibration. It is because the two electronic states corresponding to phase $= \pi$ and phase $= 0$ of the oscillation, which are illustrated in Fig. 5.19(i), (iii), respectively, are the same with each other [40]. Judging from the relation in Fig. 5.18b, the vibrational frequency for $d = 0$ should be much smaller than 100 cm^{-1} and may be decreased to ca. 50 cm^{-1} in the Pt–I chain. In this case, the frequency of the coherent oscillation on ΔR is ca. 100 cm^{-1} (the double of 50 cm^{-1}) as observed. In $[Pd(chxn)_2Br]Br_2$, in which the size of a MH domain is not so large (ca. 20 Pd sites), the Br ions do not come on the midpoints and therefore the frequency of the coherent oscillation on ΔR is not doubled.

The probe-energy dependence of the 100-cm^{-1}-oscillation amplitude was plotted by open circles in Fig. 5.17d. The spectrum is similar not to ΔR ($t_d = 0.16$ ps) (solid circles) but to the first derivative of ΔR ($t_d = 0.16$ ps) (broken line). It indicates that the gap energy in the MH state is modulated by the Pt–I stretching vibration. This also supports the fact that the coherent Pt–I vibrations are generated over the MH state. The observed doubling of the coherent oscillation frequency is

the direct evidence for the complete release of the bridging halogen displacements, that is, for the complete CDW to MH transition within the photoinduced domains.

From these discussions, the CDW–MH transition dynamics by the weak excitation can be schematically shown as Fig. 5.19. By the photoirradiation, a large 1D MH domain (ca. 70 Pt^{3+} sites) is formed from a CT excited state within the temporal resolution (i). Subsequently, the equilibrium positions of the I ions come on the midpoints between the neighboring Pt ions (ii). At the same time, the coherent vibration of the I ions is generated as (i) → (ii) → (iii) → (ii) → (i) → (ii). The photogenerated MH domain returns to the CDW ground state with ca. 20 ps.

5.5 Summary

In this chapter, we have reviewed the investigations of PIPTs in the three types of MX-chain compounds. Under the influence of the strong electron–electron and electron–lattice interactions, materials exhibit characteristic PIPTs, some of which are driven in an ultrafast (ps or sub ps) time scale.

In Sect. 5.3, a photoswitching from an insulator to a metal in a 1D Mott insulator of the bromine-bridged Ni-chain compound has been detailed. The increase of the excitation density changes the photoproduct from the midgap state to the metallic state. A most significant feature of this PIPT is that the response time is quite fast. The photoinduced metallic state is generated within the temporal resolution ($\ll$180 fs) and recovers to the insulator with a time constant of 0.5 ps. This is the first observation of the photoinduced Mott transition in the strongly correlated electron systems.

In Sect. 5.4, PIPTs in the CDW state of the halogen-bridged palladium-chain compound, $[Pd(chxn)_2Br]Br_2$, and platinum-chain compound, $[Pt(chxn)_2I]I_2$, have been discussed. $[Pd(chxn)_2Br]Br_2$ is located near the CDW–MH phase boundary, and it was demonstrated that the irradiation of a fs laser pulse causes the instantaneous formation of a 1D Mott–Hubbard domain composed of ca. 20 Pd sites without alternation of bridging-Br displacements. This result demonstrates the important role of intersite Coulomb repulsion in the phase transition and in the stabilization of the CDW state. The formation of the MH domain is followed by a coherent oscillation with a period of 360 fs, attributable to the relaxation of the bridging-Br displacements coupled with the charge transfer between neighboring Pd ions. In $[Pt(chxn)_2I]I_2$, which is also located near the CDW–MH phase boundary, the PIPT from the CDW phase to MH phase is found by means of the femtosecond pump–probe reflection spectroscopy. The results have demonstrated the high efficiency of the photoinduced CDW–MH transition in which ca. 70 Pt sites are converted to MH state per photon. Such large conversion efficiency makes possible the complete and transient transition from CDW to MH phase. In the photogenerated MH domains, the bridging I ions come on the midpoints between the neighboring Pt ions. With increase in the excitation density, the low-energy spectral weight of absorption is increased, suggesting that the CDW–MH transition is completed and the transition to the metallic state occurs.

The PIPTs presented here give us typical patterns of PIPTs in 1D electron–electron and electron–lattice coupled systems. The findings of PIPTs will lead to new possibilities for the applications of in MX-chain compound as future optical switching and memory devices.

Acknowledgments The studies reported here were done in collaboration with many researchers; Dr. M. Ono, Dr. A. Maeda, Mr. K. Kimura and Prof. Y. Tokura (University of Tokyo), Prof. M. Yamashita, Prof. S. Takaishi, and Prof. S. Iwai (Tohoku University), Prof. H. Kishida (Nagoya University). We thank all of these collaborators. We also thank Dr. K. Iwano and Prof. K. Nasu (KEK), Prof. K. Yonemitsu (IMS) for valuable discussions.

References

1. Nasu K (ed) (1997) Relaxations of excited states and photoinduced structural phase transitions. Springer, Berlin
2. Nasu K (ed) (2004) Photoinduced phase transitions. World Scientific, Singapore
3. Koshihara S, Tokura Y, Mitani T, Saito G, Koda T (1990) Phys Rev B 42:6853
4. Koshihara S, Takahashi Y, Sakai H, Tokura Y, Luty T (1999) J Phys Chem B 103:2592
5. Suzuki T, Sakamaki T, Tanimura K, Koshihara S, Tokura Y (1999) Phys Rev B 60:6191
6. Iwai S, Tanaka S, Fujinuma K, Kishida H, Okamoto H, Tokura Y (2002) Phys Rev Lett 88:57402
7. Okamoto H, Ishiga Y, Tanaka S, Kishida H, Iwai S, Tokura Y (2004) Phys Rev B 70:165202
8. Tanimura K (2004) Phys Rev B 70:144112
9. Collet E, Cailleau MH, Cointe MB, Cailleau H, Wulff M, Luty T, Koshihara S, Meyer M, Toupet L, Rabiller P, Techert S (2003) Science 300:612
10. Uemura H, Okamoto H (2010) Phys Rev Lett 105:258302
11. Fiebig M, Miyano K, Tomioka Y, Tokura Y (1998) Science 280:1925
12. Ogasawara T, Kimura T, Ishikawa T, Kuwata-Gonokam M, Tokura Y (2001) Phys Rev B 63:113105
13. Okimoto Y, Matsuzaki H, Tomioka Y, Kezsmarki I, Ogasawara T, Matsubara M, Okamoto H, Tokura Y (2007) J Phys Soc Jpn 76:043702
14. Matsubara M, Okimoto Y, Ogasawara T, Tomioka Y, Okamoto H, Tokura Y (2007) Phys Rev Lett 99:207401
15. Matsubara M, Okimoto Y, Ogasawara T, Iwai S, Tomioka Y, Okamoto H, Tokura Y (2008) Phys Rev B 77:094410
16. Matsubara M, Ogasawara T, Tomioka Y, Tobe K, Okamoto H, Tokura Y (2009) J Phys Soc Jpn 78:023707
17. Iwai S, Yamamoto K, Kashiwazaki A, Hiramatsu F, Nakaya H, Kawakami Y, Yakushi K, Okamoto H, Mori H, Nishio Y (2007) Phys Rev Lett 98:097402
18. Okamoto H, Matsuzaki H, Wakabayashi T, Takahashi Y, Hasegawa T (2007) Phys Rev Lett 98:037401
19. Kawakami Y, Iwai S, Fukatsu T, Miura M, Yoneyama N, Sasaki T, Kobayashi N (2009) Phys Rev Lett 103:066403
20. Okamoto H, Miyagoe T, Kobayashi K, Uemura H, Nishioka H, Matsuzaki H, Sawa A, Tokura Y (2010) Phys Rev B 82:060513(R)
21. Okamoto H, Miyagoe T, Kobayashi K, Uemura H, Nishioka H, Matsuzaki H, Sawa A, Tokura Y (2011) Phys Rev B 83:125102
22. Cavalleri A, To'th C, Siders CW, Squier JA, Raksi F, Forget P, Kieffer JC (2001) Phys Rev Lett 87:237401

23. Iwai S, Ono M, Maeda A, Matsuzaki H, Kishida H, Okamoto H, Tokura Y (2003) Phys Rev Lett 91:57401
24. Chollet M, Guerin L, Uchida N, Fukaya S, Shimada H, Ishikawa T, Matsuda K, Hasegawa T, Ota A, Yamochi H, Saito G, Tazaki R, Adachi S, Koshihara S (2005) Science 307:86
25. Kimura K, Matsuzaki H, Takaishi S, Yamashita M, Okamoto H (2009) Phys Rev B 79:075116
26. Hauser A (1991) J Chem Phys 94:2741
27. Sato O, Iyoda T, Fujishima A, Hashimoto K (1996) Science 272:704
28. Ogawa Y, Koshihara S, Koshino K, Ogawa T, Urano C, Takagi H (2000) Phys Rev Lett 84:3181
29. Tayagaki T, Tanaka K (2001) Phys Rev Lett 86:2886
30. Matsuda K, Machida A, Moritomo Y, Nakamura A (1998) Phys Rev B 58:4203
31. Liu XJ, Moritomo Y, Nakamura A, Tanaka H, Kawai T (2001) Phys Rev B 64:100401(R)
32. Kise T, Ogasawara T, Ashida M, Tomioka Y, Tokura Y, Kuwata-Gonokami M (2000) Phys Rev Lett 85:1986
33. Ogasawara T, Matsubara M, Tomioka T, Kuwata-Gonokami M, Okamoto H, Tokura Y (2003) Phys Rev B 68:180407(R)
34. Koshihara S, Tokura Y, Iwasa Y, Koda T (1991) Phys Rev B 43:431
35. Matsuzaki H, Matsuoka T, Kishida H, Takizawa K, Miyasaka H, Sugiura K, Yamashita M, Okamoto H (2003) Phys Rev Lett 90:046401
36. Matsuzaki H, Fujita W, Awaga K, Okamoto H (2003) Phys Rev Lett 91:017403
37. Ogasawara T, Ogushi K, Tomioka Y, Takahashi KS, Okamoto H, Kawasaki M, Tokura Y (2005) Phys Rev Lett 94:087202
38. Okamoto H, Ikegami K, Wakabayashi T, Ishige Y, Togo J, Kishida H, Matsuzaki H (2006) Phys Rev Lett 96:037405
39. Ikegami K, Ono K, Togo J, Wakabayashi T, Ishige Y, Matsuzaki H, Kishida H, Okamoto H (2007) Phys Rev B 76:085106
40. Matsuzaki H, Yamashita M, Okamoto H (2006) J Phys Soc Jpn 75:123701
41. Toriumi K, Wada Y, Mitani T, Bandow S, Yamashita M, Fujii Y (1989) J Am Chem Soc 111:2341
42. Okamoto H, Shimada Y, Oka Y, Chainani A, Takahashi T, Kitagawa H, Mitani T, Toriumi K, Inoue K, Manabe T, Yamashita M (1996) Phys Rev B 54:8438
43. Okamoto H, Toriumi K, Mitani T, Yamashita M (1990) Phys Rev B 42:10381
44. Okamoto H, Mitani T, Toriumi K, Yamashita M (1992) Mater Sci Eng B 13:L9
45. Okamoto H, Yamashita M (1998) Bull Chem Soc Jpn 71:2023
46. Takaishi S, Miyasaka H, Sugiura K, Yamashita M, Matsuzaki H, Kishida H, Okamoto H, Tanaka H, Marumoto K, Ito H, Kuroda S, Takami T (2004) Angew Chem Int Ed 43:3171
47. Matsuzaki H, Iwano K, Aizawa T, Ono M, Kishida H, Yamashita M, Okamoto H (2004) Phys Rev B 70:035204
48. Iwano K (2004) Phys Rev B 70:241102(R)
49. Nasu S (1983) J Phys Soc Jpn 52:3865
50. Imada M, Fujimori A, Tokura Y (1998) Rev Mod Phys 70:1039
51. Tokura Y, Nagaosa N (2000) Science 288:462
52. Millis AJ (1998) Nature 392:147
53. Yu G, Lee CH, Heeger AJ, Herron N, McCarron EM (1991) Phys Rev Lett 67:2581
54. Uchida S, Ido T, Takagi H, Arima T, Tokura Y, Tajima S (1991) Phys Rev B 43:7942
55. Tokura Y, Takagi H, Uchida S (1989) Nature 337:345
56. Nagai M, Shimano R, Kuwata-Gonokami M (2001) Phys Rev Lett 86:5795
57. Nagai M, Kuwata-Gonokami M (2002) J Lumin 100:233
58. Vinet JY, Combescot M, Tanguy C (1984) Solid State Commun 51:171
59. Lietoila A, Gibbons JF (1982) Appl Phys Lett 40:624
60. Okamoto H, Toriumi K, Okaniwa K, Mitani T, Yamashita M (1991) Synth Met 41–43:2791
61. Matsuda K, Hirabayashi I, Kawamoto K, Nabatame T, Tokizaki T, Nakamura A (1994) Phys Rev B 50:4097

62. Ashida M, Taguchi Y, Tokura Y, Clay RT, Mazumdar S, Svirko YP, Kuwata-Gonokami M (2002) Europhys Lett 58:455
63. Ogasawara T, Ashida M, Motoyama N, Eisaki H, Uchida S, Tokura Y, Ghosh H, Shukla A, Mazumdar S, Kuwata-Gonokami M (2000) Phys Rev Lett 85:2204
64. Wada Y, Yamashita M (1989) Phys Rev B 42:7398
65. Zozulenko IV (1990) Solid State Commun 76:1035
66. Sugita A, Yamashita M, Kobayashi Y (2001) J Chem Phys 114:2369
67. Nagaosa N, Takimoto J (1986) J Phys Soc Jpn 55:2745
68. Iwano K, Nasu K (1992) J Phys Soc Jpn 61:1380
69. Iwano K, Nasu K (1993) J Phys Soc Jpn 62:1778
70. Okamoto H, Toriumi K, Mitani T, Yamashita M (1990) Phys Rev B 42:10381
71. Rothberg L, Jedju TM, Etemad S, Baker GL (1987) Phys Rev B 36:7529

Chapter 6
Nonlinear Electrical Conductivity, Current Oscillation and Its Control in Halogen-Bridged Nickel(III) Compounds

Hideo Kishida and Arao Nakamura

6.1 Introduction

Nonlinear conduction is a phenomenon that the electric current flowing through a sample is not ohmic, namely, not linear to the voltage between both ends of the sample. This phenomenon is observed in many organic crystals and metal complexes [1–6]. In this chapter, we introduce the nonlinear conduction in halogen-bridged nickel(III) compounds and the current oscillation phenomena.

Most insulators obey to the ohmic law in the low current density region. As increasing the current or current density, they sometimes show nonohmic behaviors, which are the nonlinear conduction. One of the measures of the nonlinear conduction is the differential resistance, which is defined as the inverse of the slope in the current (I)–voltage (V) curves. These nonlinear conducting behaviors can be classified into two types. One is the case that the differential resistance increases with the increase of voltage. In the other case, the differential resistance decreases with the increase of the voltage. In both cases, the differential resistance can be negative as shown in Fig. 6.1a, b. Such phenomena are called negative differential resistance (NDR). In both types of nonlinear resistance, with the increase of the current (voltage) above the NDR region, the current density (electric field) increases again. A typical nonlinear resistance is a Gunn effect in semiconductors, which is applied in Gunn diodes. The Gunn effect is classified into the class shown by Fig. 6.1a. In the Gunn diode,

H. Kishida (✉)
Department of Applied Physics, Nagoya University, Nagoya 464-8603, Japan

JST CREST, Chiyoda-ku, Tokyo 102-0075, Japan
e-mail: kishida@nuap.nagoya-u.ac.jp

A. Nakamura
Department of Applied Physics, Nagoya University, Nagoya 464-8603, Japan

JST CREST, Chiyoda-ku, Tokyo 102-0075, Japan

Present Address: Toyota Physical and Chemical Research Institute, Nagakute, Aichi 480-1192, Japan

M. Yamashita and H. Okamoto (eds.), *Material Designs and New Physical Properties in MX- and MMX-Chain Compounds*, DOI 10.1007/978-3-7091-1317-2_6,

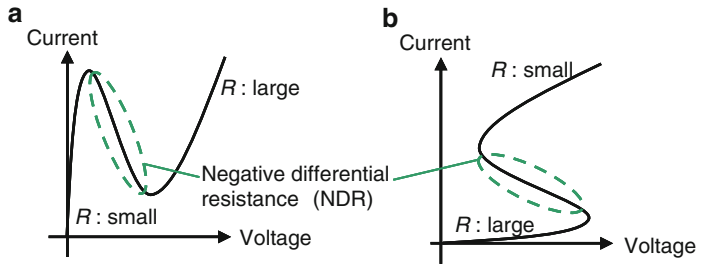

Fig. 6.1 Two types of nonlinear-conducting behaviors. In (**a**), the resistivity in nonlinear-conducting states is larger than that of the ohmic region under low voltage, while in (**b**) the resistivity decreases. The slope of the *I–V* curve can be negative in nonlinear-conducting behaviors. Such negative region is called negative differential resistance (NDR)

the high-resistance region induced near one electrode by high electric field appears and then moves from one edge to another edge of the crystal. After the high resistance region reaches the opposite electrode and disappears, a new high-resistance area appears and flows. This procedure is repeated. This leads to the current oscillation phenomena [7]. On the other hand, nonlinear conductance showing the decrease of the resistivity with the increase of the voltage (as shown in Fig. 6.1b) is widely observed in many molecular crystals [1–6]. The nonlinearity in this type is in some cases due to the breakdown of the Mott insulation. From theoretical viewpoints, several approaches have been attempted [8–10].

In this chapter, we discuss the nonlinear conducting behaviors of halogen-bridged nickel(III) compounds. Current oscillation phenomena based on the nonlinear conductivity are also introduced, in which the oscillation is assisted by the external circuits.

6.2 Negative Differential Resistance

The current density–electric field characteristics of $[Ni(chxn)_2Br]Br_2$ (Ni–Br) and $[Ni(chxn)_2Cl]Cl_2$ (Ni–Cl) is shown in Fig. 6.2a, b [6, 11], respectively. As for $[Ni(chxn)_2Br]Br_2$, the sample shows ohmic behavior under 0.35 mA/cm^2 at 90 K, while the voltage appearing on both ends of the sample decreases with the further increase of the current. Namely, the electric field inside the sample decreases with the larger current density. The clear NDR was observed under 150 K. The similar *I–V* curve is observed for Ni–Cl, which shows clear NDR under 160 K. Thus, the NDR behavior is a common feature for halogen-bridged nickel(III) compounds. At present, the reason for the large nonlinearity is not clear. The NDR has been so far reported in many types of organic compounds showing temperature-induced phase transitions. For example, the NDR in potassium–tetracyanoquinodimethane (K–TCNQ) is well established [12–14]. In the case of K–TCNQ, stacked TCNQ molecules form one-dimensional column and TCNQ molecules are dimerized in a column at the low

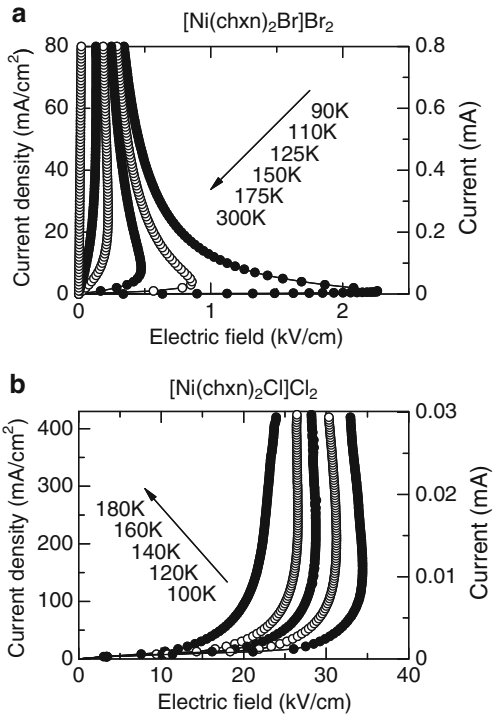

Fig. 6.2 Current densities are plotted versus electric field for (**a**) $[Ni(chxn)_2Br]Br_2$ and (**b**) $[Ni(chxn)_2Cl]Cl_2$. The original data shown in (**a**) and (**b**) are from [6] and [11], respectively

temperature phase. With increase of the temperature, the dimerization disappears. As the NDR can be observed only in the low temperature phase, the large change of the resistivity is assigned to the reduction of the degree of the dimerization [12]. On the other hand, in the halogen-bridged nickel(III) compounds, the NDR disappears between 150 and 300 K, though they show no temperature-induced phase transitions at such temperature region. Therefore, the NDR in halogen-bridged nickel(III) compounds cannot be assigned to the temperature-induced phase transitions. This is in contrast to the reported NDR phenomena. Another class of one-dimensional Mott insulator, Sr_2CuO_3, also shows NDR [15], but it also shows no temperature-induced phase transition. As for this compound, the breakdown of the Mott-insulating states is proposed. Similar mechanism might be a possible origin for the NDR in halogen-bridged nickel(III) compounds.

6.3 The Current Oscillation

The spontaneous current oscillation based on the nonlinear-conducting behaviors has been discussed for long years [2, 3, 16, 17]. One of the strategies and examples to achieve the spontaneous current oscillation using the NDR behaviors of organic compounds was proposed in [6]. According to the proposed method, the

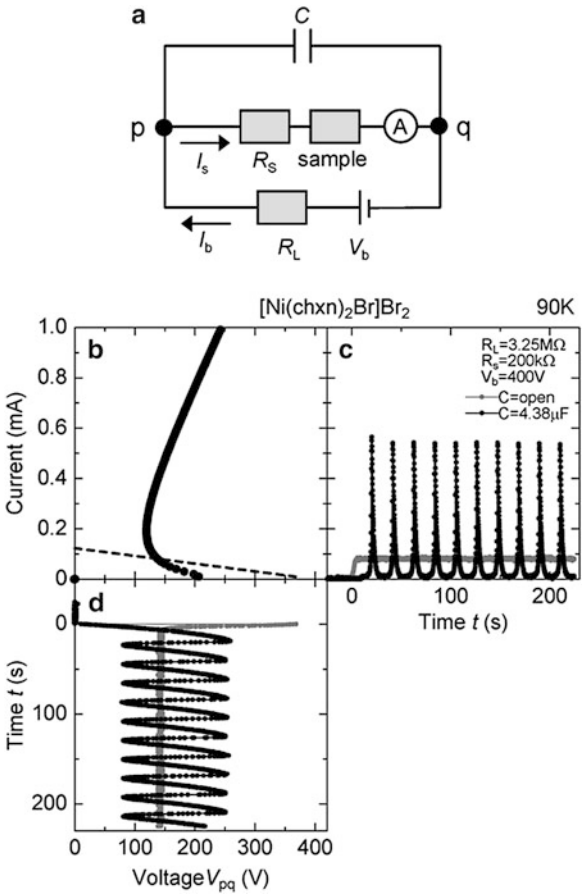

Fig. 6.3 (**a**) Circuit for current oscillation using an NDR sample. (**b**) Currents I_s (*dots*) and I_b (*broken line*) are plotted versus voltages V_{pq}. (**c**) Temporal profile of the current with and without the external capacitor. (**d**) Temporal profile of the voltage V_{pq} with and without the external capacitor. Reprinted with permission from [6]. Copyright (2009), American Institute of Physics

combination of NDR materials and external circuits leads to the current and voltage oscillation. The circuit is shown in Fig. 6.3a. By adding a serial resistor R_s to the NDR sample, we obtain the region in which the current increases with the increase of the voltage, which is located above the NDR region, as shown by filled dots in Fig. 6.3b. Resultantly, the current–voltage characteristic has an S-shape. Then, we add a voltage source V_b and a load resistor R_L. The *I*–*V* curve between points *p* and *q* through V_b and R_L is shown by a dotted line in Fig. 6.3b. The intersection of the dotted line and the S-shape curve (dots) gives a stationary solution of this circuit before attaching the capacitor. Moreover, by adding a parallel capacitor *C*, we obtain the nonstationary solution leading to the current oscillation. In Fig. 6.3c, d, we show the temporal profile of the current and voltage. In these figures, gray dots indicate the waveforms before attaching the capacitor and filled dots are those after attaching the capacitor. In the case of no capacitor (gray in Fig. 6.3c, d), the current increases along the lower branch of the S-shape curve and reach the stationary point. Meanwhile, the voltage passes a larger value than the stationary point. On the

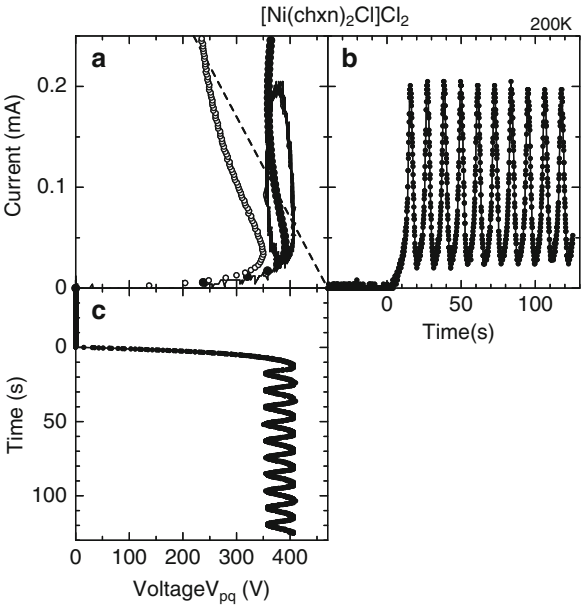

Fig. 6.4 Current and voltage behaviors for $[Ni(chxn)_2Cl]Cl_2$ at 200 K [11]. (**a**) Currents I_s (*filled dots*) and I_b (*broken line*) are plotted versus voltages V_{pq}. The *open circles* are the *I–V* characteristics of the sample without the serial resistor. The current–voltage trajectory in the current oscillation is also plotted. (**b**) Temporal profile of the current with and without the external capacitor. (**c**) Temporal profile of the voltage V_{pq} with and without the external capacitor

other hand, with the capacitor (black in Fig. 6.3c, d), the current and voltage do not reach the stationary point but oscillate. The period is roughly 20 s. The similar current oscillation can be obtained in Ni–Cl at 200 K shown in Fig. 6.4 [11]. In Fig. 6.4a, the *I–V* property of the sample is shown by open circles. The *I–V* properties of the combined resistance of the sample and the serial resistor R_s are shown by filled circles. We obtained the S-shape curve also for Ni–Cl. However, the obtained S-shape curve for Ni–Cl is elongated in the direction of current. Using the S-shape properties, we achieved the current oscillation. The temporal profiles of the current and voltage are shown in Fig. 6.4b, c, respectively. We obtained clear oscillations. The amplitude of the current is enough large, and the contrast of the oscillation (on–off ratio in current) is large. On the other hand, the amplitude is small for voltage. The obtained contrast is small. These contrasts in the amplitude of the oscillation are dependent on the original NDR properties of the sample. In Ni–Br, the slope is small in negative resistance region. Therefore, we achieved the clear S-shape properties in *I–V* plot (Fig. 6.2a) for Ni–Br, while the steep slope in negative resistance region for Ni–Cl leads to an unclear S-shape curve. Resultantly, the contrast in voltage is small.

The trajectory of the current and V_{pq} is shown in Fig. 6.4a by a solid line, which indicates that the current and V_{pq} oscillate counterclockwise in the current–voltage plot. In more detail, after turning on the current, the current increases along the

high-resistance branch of the *I–V* curve to around 400 V. At this voltage, the sample shows a sudden change in resistance to low resistance state, which is upper branch of the *I–V* plot. After reaching the low-resistance branch, the current begins to decrease along the low-resistance branch and jump down to the high-resistance branch. After this, the above procedures are repeated. In this behavior, the trajectory is not exactly coincident with the *I–V* curve. Particularly, in the low resistance state, the inconsistency is conspicuous. The resistivity in low-resistance state is dependent on the history of current flow. It may indicate that the Joule heating affects the resistivity in the low resistance state to some extent.

6.4 Control of the Current Oscillation

Because the current oscillation is assisted by the external circuit, the period of the oscillation can be controlled by the circuit constant of the external circuit. The period of the current oscillation is calculated using a simple model and the nonlinear circuit theory and described as shown below [6]. The total period is a sum of the transient times within the high-resistance state τ_{high} and low-resistance state τ_{low}

$$\tau_{\text{low}} = CR_1 \ln \frac{E_1 - V_{\text{low}}}{E_1 - V_{\text{high}}} \tag{6.1}$$

and

$$\tau_{\text{high}} = CR_2 \ln \frac{E_2 - V_{\text{high}}}{E_2 - V_{\text{low}}} \tag{6.2}$$

Here R_1, E_1, R_2, and E_2 are defined as follows:

$$R_1 = (R_{\text{L}} R_\alpha)/(R_{\text{L}} + R_\alpha) \tag{6.3}$$

$$E_1 = R_\alpha V_{\text{b}}/(R_{\text{L}} + R_\alpha) \tag{6.4}$$

$$R_2 = (R_{\text{L}} R_\gamma)/(R_{\text{L}} + R_\gamma) \tag{6.5}$$

$$E_2 = (R_\gamma V_{\text{b}} + V_{x0} R_{\text{L}})/(R_{\text{L}} + R_\gamma) \tag{6.6}$$

V_{low} (V_{high}) is the switching voltage from the low (high) to high (low) resistance state. R_α and R_γ are the differential resistance of high-resistance and low-resistance branch in *I–V* plot. V_{x0} is the *x*-intercept of the extrapolated line of the low-resistance branch. Equations (6.1) and (6.2) indicate that the period $\tau (= \tau_{\text{low}} + \tau_{\text{high}})$ can be controlled by the external parameters, C, V_{b}, and R_{L}.

In Fig. 6.5a, we show the C dependence of time evolution of the current for Ni–Br measured at 90 K. With no capacitance (open) and small capacitance

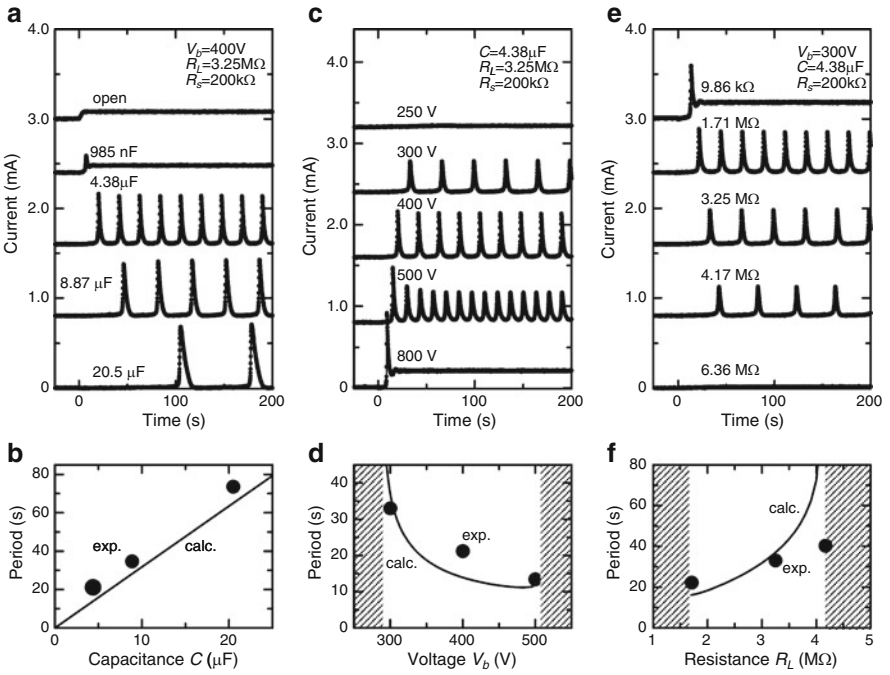

Fig. 6.5 Temporal profile of current oscillation and its period dependent on parallel capacitance, applied voltage, and resistance R_L for $[Ni(chxn)_2Br]Br_2$ measured at 90 K. (**a**) Temporal profiles for various capacitances (open, 985 nF, 1.38 μF, 8.87 μF and 20.5 μF) at $V_b = 400$ V, $R_L = 3.25$ MΩ, $R_s = 200$ kΩ, (**b**) The period values are plotted by *filled circles*. The *solid line* indicates the periods calculated by Eqs. (6.1) and (6.2) (**c**) Temporal profiles measured for various source voltages at $C = 4.38$ μF, $R_L = 3.25$ MΩ, $R_s = 200$ kΩ, (**d**) Periods dependent on the source voltage V_b. (**e**) Time profiles measured for various source voltages at $V_b = 300$ V, $C = 4.38$ μF, $R_s = 200$ kΩ; (**f**) The period dependent on source voltages V_b. The data of figures (**a**) and (**b**) are from [6] and others (**c**)-(**f**) from [19]

($C = 985$ nF), the oscillation does not occur. In these two cases, the circuit is stable at the crossing point of the load line (shown by dotted line in Fig. 6.5a) and the *I–V* curve. On the other hand, with the large capacitance ($C \geqslant 4.38$ μF), the oscillation appears, whose periods are roughly proportional to the capacitance of the parallel capacitor. In Fig. 6.5b, we show the capacitance dependence of the period by solid circles compared with the calculated values using Eqs. (6.1) and (6.2). The calculation reproduces the experimental results satisfactorily. However, the adapted model suggests that the oscillation should appear even at small capacitance. This discrepancy between the experimental results and the calculations might be ascribed to the time dependence of the nonlinear resistance behaviors. The sudden change in resistance is similar to a phase transition from insulating to metallic states. When the phase transition develops by domain growth, the formation of macroscopic domains is governed by the time of domain growth. As a result, the *I–V* curves and resistance would be time dependent. In the metal–insulator transition in a 3D Mott insulator (VO_2), the domain growth is observed in real space and its growth limits

the change in resistance [18]. In such studies, the reduction of the sample size leads to the realization of fast oscillation up to 0.2 MHz [20]. In view of this, we may realize faster oscillation in thin films of the present materials.

Moreover, the V_b dependence of the current is shown in Fig. 6.5c. Experimentally, the period decreases with increasing V_b between 300 and 500 V. No oscillation is observed outside this range. This behavior is reproduced by the calculation (Fig. 6.5d). In the case of the lower and higher V_b, the intersection of the load line and the *I–V* curves falls on not negative resistance state but high- or low-resistance state with a positive slope, respectively. In such cases, we do not obtain the oscillation.

The dependence on R_L is shown in Fig. 6.5e. The experimental data show the increase of the period with increasing R_L. This behavior can be roughly explained by the calculation (Fig. 6.5f). As in the case of the V_b dependence, the oscillation occurs only when the intersection falls on the negative differential region of the *I–V* curve.

The studies about the current path and the nonlinear conducting domains are also important. In another type of one-dimensional Mott insulator, K–TCNQ, it is revealed that the nonlinear current flows throughout the crystal [14]. However, it is often discussed that the nonlinear-conducting current flows in a filamentary current path. The study on the spatial information about the nonlinear current will be important to clarify the mechanism of nonlinear conductivity.

6.5 Conclusions

We introduced the nonlinear-conducting behaviors in halogen-bridged nickel(III) compounds, $[Ni(chxn)_2Br]Br_2$ and $[Ni(chxn)_2Cl]Cl_2$. These two compounds commonly show nonlinear-conducting behaviors. At low current density region, they show ohmic (linear) response, while they show clear negative differential resistance behaviors by increasing the current density. By attaching the external circuit components, we achieved and controlled the current oscillation. The mechanism is clearly explained by the nonlinear circuit theory. This indicates that halogen-bridged nickel(III) compounds can be a candidates of nonlinear circuit components.

Acknowledgments The authors thank Mr. Takafumi Ito, Mr. Atsuya Ito, Prof. Shinya Takaishi, and Prof. Masahiro Yamashita for collaboration.

References

1. Tokura Y, Okamoto H, Koda T, Mitani T, Saito G (1988) Phys Rev B 38:2215
2. Lopes EB, Matos MJ, Henriques RT, Almeida M, Dumas J (1995) Phys Rev B 52:R2237
3. Sawano F, Terasaki I, Mori H, Mori T, Watanabe M, Ikeda N et al (2005) Nature 437:522

4. Mori T, Terasaki I, Mori H (2007) J Mater Chem 17:4343, For a review
5. Mori T, Ozawa T, Bando Y, Kawamoto T, Niizeki S, Mori H et al (2009) Phys Rev B 79:115108
6. Kishida H, Ito T, Nakamura A, Takaishi S, Yamashita M (2009) J Appl Phys 106:016106
7. Pankove JI (1971) Optical process in semiconductors. Dover, New York
8. Oka T, Arita R, Aoki H (2003) Phys Rev Lett 91:066406
9. Sugimoto N, Onoda S, Nagaosa N (2008) Phys Rev B 78:155104
10. Tanaka Y, Yonemitsu K (2011) Phys Rev B 83:085113
11. Ito A, Kishida H, Nakamura A, Takaishi S, Yamashita M (unpublished)
12. Kumai R, Okimoto Y, Tokura Y (1999) Science 284:1645
13. Okimoto Y, Kumai R, Saitoh E, Izumi M, Horiuchi S, Tokura Y (2004) Phys Rev B 70:115104
14. Kishida H, Ito T, Ito A, Nakamura A (2011) Appl Phys Express 4:031601
15. Taguchi Y, Matsumoto T, Tokura Y (2000) Phys Rev B 62:7015
16. Taketa Y, Kato F, Nitta M, Haradome M (1975) Appl Phys Lett 27:212
17. Maeda A, Notomi N, Uchinokura K (1990) Phys Rev B 42:3290
18. Gu Q, Falk A, Wu J, Ouyang L, Park H (2007) Nano Lett 7:363
19. Ito T, Kishida H, Nakamura A, Takaishi S, Yamashita M (unpublished)
20. Lee YW, Kim BJ, Lim JW, Yun SJ, Choi S, Chae BG et al (2008) Appl Phys Lett 92:162903

Chapter 7
Third-Order Optical Nonlinearity of Halogen-Bridged Nickel(III) Compounds

Hideo Kishida and Hiroshi Okamoto

7.1 Introduction

In this chapter, we focus on the third-order optical nonlinearity of one-dimensional (1D) halogen (X)-bridged transition metal (M)-chain compounds (MX chain compounds). Third-order optical nonlinearity is an important physical property to achieve all-optical switching devices. The material having large third-order optical nonlinearity can show the large change of the optical constants by irradiation of light. Using such behaviors, we can control the intensity or traveling direction of a light beam in an ultrafast time scale. The enhancement of the performance of all-optical ultrafast switching is desired because they can be a key technology of the future ultrafast all-optical communications.

In order for the large optical nonlinearity to be obtained, extensive studies have been devoted to the development of third-order nonlinear optical materials. The simplest but sound way is the usage of low-dimensional electronic systems. Especially, in a 1D system, a clear van Hove singularity and/or a large excitonic effect is expected to enhance the oscillator strengths of the absorption near the band-edge or the absorption due to the lowest exciton transition. This necessarily enhances the third-order optical nonlinearity not only at around the optical gap energy but also the transparent region within the gap.

In 1990s, Pt–X chain compounds were studied from the viewpoints of nonlinear optical materials. Wada et al. clarified nature of electronic excited states of Pt–X chain compounds near the optical gap energies using the electroreflectance method [1].

H. Kishida (✉)
Department of Applied Physics, Nagoya University, Nagoya 464-8603, Japan
e-mail: kishida@nuap.nagoya-u.ac.jp

H. Okamoto (✉)
Department of Advanced Materials Science, Graduate School of Frontier Sciences, University of Tokyo, Kashiwa 277-8561, Japan
e-mail: okamotoh@k.u-tokyo.ac.jp

M. Yamashita and H. Okamoto (eds.), *Material Designs and New Physical Properties in MX- and MMX-Chain Compounds*, DOI 10.1007/978-3-7091-1317-2_7,

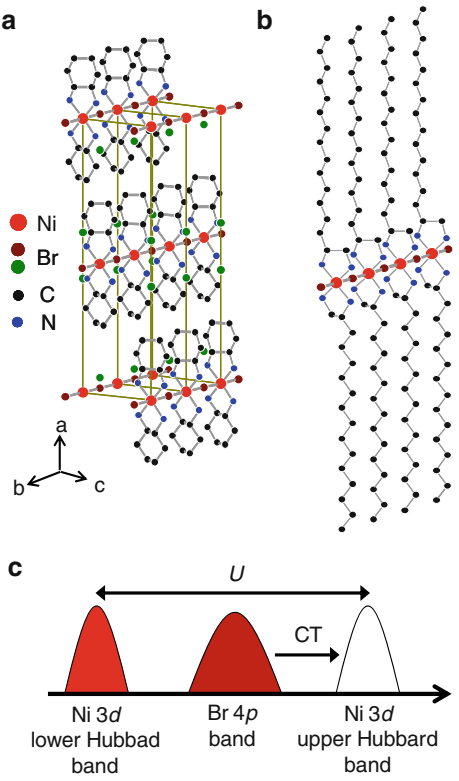

Fig. 7.1 Crystal structures of Ni–X chain compounds; (**a**) $[Ni(chxn)_2Br]Br_2$ and (**b**) $[Ni(L)_2Br]Br_2$ (from [5]). (**c**) The electronic structure of Ni–X chain compounds

They showed that the lowest optical transition was due to 1D excitons with large electron–hole-binding energy of about 0.5 eV. Subsequently, Iwasa et al. reported the third-order nonlinear susceptibility $\chi^{(3)}$ in the similar Pt–X chain compounds by using the third-harmonic generation (THG) method [2]. The evaluated $\chi^{(3)}$ values were, however, not so large being the order of 10^{-11} esu. In 2000, it was found that Ni–X chain compounds show very large $\chi^{(3)}$ [3] as compared to Pt–X chain compounds and other 1D semiconductors such as conjugated polymers. Since this discovery, a number of studies have been performed to clarify the origin of the enhancement of $\chi^{(3)}$ in Ni–X chain compounds. Those studies also activated time-resolved studies on the photo-responses in the Ni–X chain compounds and related materials [4–6].

Ni–X chain compounds (X = Cl and Br) are the 1D Mott insulators as discussed in Chap. 3. Figure 7.1a shows the crystal structure of $[Ni(chxn)_2Br]Br_2$ (chxn = cyclohexanediamine), which is a representative of Ni–X chain compounds. In this compound, Ni^{3+} ions and Br^- ions are arranged alternately along the *b* axis [7]. In the Ni^{3+} ions, an unpaired electron exists in the d_{z^2} orbital. The d_{z^2} orbital of Ni^{3+} and p_z orbital of Br^- form a purely 1D electronic state. Due to the large electron–electron Coulomb repulsion energy *U* on the Ni site, this compound is a Mott insulator [8, 9]. More strictly, the occupied Br 4p-band is located between the Ni 3d upper-Hubbard band and the lower Hubbard band as shown in Fig. 7.1c. Therefore, this compound is classified to the charge-transfer (CT) insulator,

in which the CT transition from Br 4p-valence band to the Ni-3d upper Hubbard band corresponds to the optical gap.

In the following subsections, we review spectroscopic studies on $\chi^{(3)}$ in Ni–X chain compounds and show that $\chi^{(3)}$ is significantly enhanced due to the specific feature of photoexcited states in Ni–X chains originating from the strong electron correlation [3, 10, 11]. We also review the demonstration of all-optical switching using thin film samples of a Ni–Br chain compound, in which the ultrafast control of the transmittance of the film with a 1 THz repetition was achieved [5].

7.2 Evaluation of Third-Order Optical Nonlinearity

Third-order nonlinear optical phenomenon is a result of the third-order nonlinear polarization $P^{(3)}$, which is governed by the third-order nonlinear susceptibility $\chi^{(3)}$. $\chi^{(3)}$ is defined as a function of three incident electric fields, $E(\omega_1), E(\omega_2)$, and $E(\omega_3)$ with the frequencies, ω_1, ω_2, and ω_3, as follows:

$$P^{(3)}(\omega_p) = K\varepsilon_0\chi^{(3)}(-\omega_p;\omega_1,\omega_2,\omega_3) \times E(\omega_1)E(\omega_2)E(\omega_3) \tag{7.1}$$

Here, $\omega_p = \omega_1 + \omega_2 + \omega_3$ is the frequency of the nonlinear polarization, and K is the constant depending on the measurement configuration [12]. By changing the frequencies of the incident electric fields, ω_1, ω_2, and ω_3, we can observe various kinds of third-order nonlinear optical phenomena. In this chapter, four kinds of the nonlinear optical measurement methods are presented. Each technique is briefly introduced below.

7.2.1 Electroreflectance Method

In the electroreflectance (ER) method, we measure the electric-field induced change of the reflectivity as shown in Fig. 7.2a. On the surface of the crystal, two electrodes are made with carbon paste or silver paste and with the gap of a few hundred micrometers. Using these two electrodes, the low frequency-alternating electric field with a typical frequency of 1 kHz is applied. The amplitude of the electric field is typically a few tens of kV/cm. The induced change ΔR of the reflectivity R is measured using the lock-in detection method. The obtained quantity is $\Delta R/R$ and its typical magnitude is 10^{-6}–10^{-3}. By applying Kramers–Kronig (KK) transformation to the $\Delta R/R$ spectrum, the change of the imaginary part of dielectric constants ($\Delta\varepsilon_2$) is obtained. $\Delta\varepsilon_2$ is directly connected to $\chi^{(3)}(-\omega;0,0,\omega)$ by the following relation:

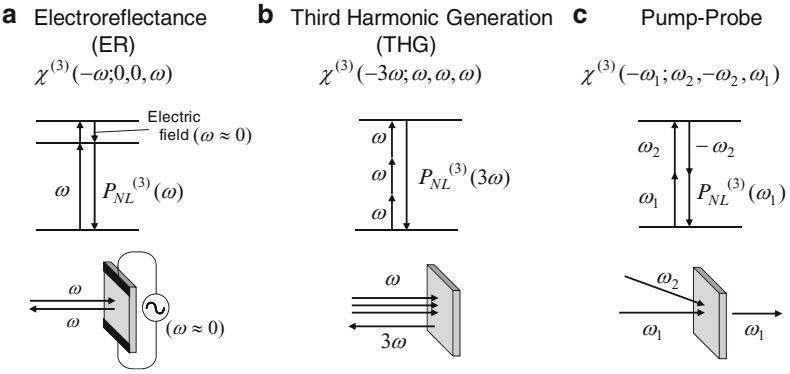

Fig. 7.2 Experimental methods and optical configurations for the evaluations of $\chi^{(3)}$

$$\Delta\varepsilon_2 = 3\,\mathrm{Im}\chi^{(3)}(-\omega;0,0,\omega)\{E(0)\}^2 \tag{7.2}$$

The experiments to measure the electric field-induced change of the transmittance are also used, especially in thin film samples. That is called the electroabsorption (EA) method. Both ER and EA give the same nonlinear susceptibility, $\chi^{(3)}(-\omega;0,0,\omega)$. The most important advantage of those techniques is that wide ranges of $\chi^{(3)}$ spectra are easily obtained, as compared to other nonlinear spectroscopies. Therefore, they are frequently used for the evaluations of spectral shapes of $\chi^{(3)}$ in nonlinear optical materials.

7.2.2 *Third-Harmonic Generation Method*

Third-harmonic generation (THG) method (Fig. 7.2b) is also a general method to evaluate $\chi^{(3)}$. In this method, a nonlinear optical material is irradiated by a laser pulse with the frequency of ω, and the light with triplicate frequency 3ω is emitted to forward and backward directions, which is detected in the transmission and reflection configuration, respectively. In most of THG experiments, the TH light in the forward direction is measured. However, in the case that the sample is bulky crystal and not transparent in the frequency region of THG, the TH light in the backward direction is useful to determine $\chi^{(3)}$. The THG experiments presented in this chapter were all performed in the backward configuration as shown in Fig. 7.2b. For the evaluation of $\chi^{(3)}$ in the THG method, THG intensities in the reference sample, $\chi^{(3)}$ of which is known, should be measured in the same experimental condition as the sample. As the reference sample in the following studies, $SrTiO_3$ substrates were used.

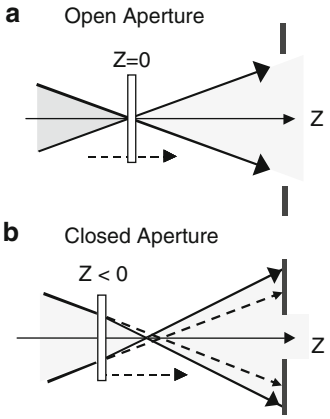

Fig. 7.3 Detailed experimental configurations of Z-scan method. Open (**a**) and closed (**b**) aperture experiments. Adapted from [5]

7.2.3 Pump–Probe and Z-Scan Methods

In the pump–probe method (Fig. 7.2c), picosecond or femtosecond laser pulses are used, and absorption changes for the probe light induced by the pump light are detected. This type of nonlinear optical processes is determined by Im $\chi^{(3)}(-\omega_1;\omega_2,-\omega_2,\omega_1)$, in which ω_1 and ω_2 are the frequencies of the probe and pump lights, respectively. By changing the delay time of the probe pulse relative to the pump pulse, the time characteristic of the nonlinear responses can also be measured. In this method, however, it is difficult to evaluate precise values of Im $\chi^{(3)}(-\omega_1;\omega_2,-\omega_2,\omega_1)$. It is because we can hardly use a reference sample, in contrast to the THG method.

In order to evaluate precise values of this type of $\chi^{(3)}$, the Z-scan method is generally used. In this method, both real and imaginary parts of $\chi^{(3)}(-\omega;\omega,-\omega,\omega)$ can be quantitatively measured from the efficiencies of the optical Kerr effect (nonlinear change of the refractive index n) and of the nonlinear absorption, respectively [13]. The experimental setups of the measurements are shown in Fig. 7.3.

In the Z-scan measurements, a sample is moved along the optical path (the z axis). In this procedure, the electric field strength on the sample is changed depending on the sample position z. Thus, one can evaluate the optical nonlinearity by detecting the transmitted light as a function of z. In the open aperture condition shown in Fig. 7.3a, nonlinear absorption changes can be measured from the transmittance changes of the sample, while in the partially closed aperture condition shown in Fig. 7.3b, the optical Kerr effect can be measured from the intensity changes of the light passing through the aperture, which are induced by the changes in the direction of the transmitted lights. By comparing those two kinds of transmittance changes of the sample as a function of z to those of a reference, we can obtain both the real and imaginary parts of $\chi^{(3)}(-\omega;\omega,-\omega,\omega)$ of the sample. The

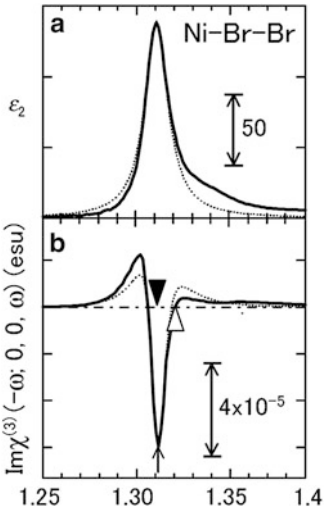

Fig. 7.4 Dielectric constants ε_2 (**a**) and its electric field-induced change $\Delta\varepsilon_2$ (**b**). *Solid line* is the experimental results and the *dotted line* is the fitting result using a discrete-level model. Adapted from [10]

most typical reference is a plate of SiO_2. The details of the measurements procedures of the *Z*-scan were reported in [13, 14].

7.3 Third-Order Optical Nonlinearity in Ni–X Chain Compounds

7.3.1 Electroreflectance Spectroscopy

Linear optical constants of Ni–X chain compounds were evaluated by the measurements of polarized reflectivity (*R*) spectra. Figure 7.4a shows the spectrum of the imaginary part of the dielectric constants, ε_2, in $[Ni(chxn)_2Br]Br_2$, which was obtained from the *R* spectrum by the KK transformation. A sharp peak is observed at around 1.3 eV, which is assigned to the CT transition from Br to Ni mentioned above [8, 9].

Electroreflectance (ER) spectra of three Ni–X chain compounds, $[Ni(chxn)_2Br]Br_2$ (abbreviated as Ni–Br–Br, hereafter), $[Ni(chxn)_2Cl]Cl_2$ (Ni–Cl–Cl), and $[Ni(chxn)_2Cl](NO_3)_2$ (Ni–Cl–NO_3), were reported first by Kishida et al. [3]. The electric field change $\Delta\varepsilon_2$ of ε_2 obtained from the ER spectrum was shown in Fig. 7.4b. Around the ε_2 peak, oscillation-type changes of ε_2 are observed. The positive and negative signals indicate the increase and the decrease of ε_2, respectively. $\Delta\varepsilon_2$ is converted to the imaginary part of $\chi^{(3)}$ as mentioned in Sect. 7.3.1, which is scaled by the right axis in Fig. 7.4b. The $\max|\mathrm{Im}\chi^{(3)}(-\omega;0,0,\omega)|$ (hereafter, abbreviated as $\max|\mathrm{Im}\chi^{(3)}|$) reaches 9×10^{-5} esu in Ni–Br–Br. The ER spectroscopy was performed in other Ni–X compounds. The $\max|\mathrm{Im}\chi^{(3)}|$ values of Ni–X compounds are plotted in Fig. 7.5 [3, 10], together with those of

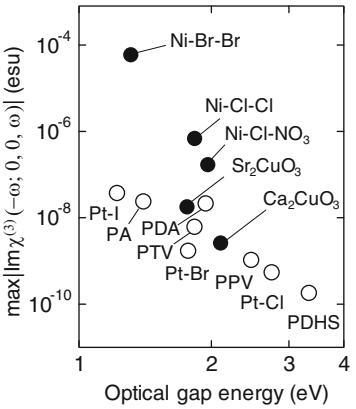

Fig. 7.5 $\max|\mathrm{Im}\chi^{(3)}(-\omega;0,0,\omega)|$ values for Ni–X and other 1D materials are plotted versus the optical gap energies. *PA* polyacetylene, *PDA* polydiacetylene, *PTV* poly (thienylene–vinylene), *PPV* poly(*p*-phenylene–vinylene), *PDHS* poly(di-hexylsilane). From [10]

other 1D semiconductors; 1D cuprates of Sr_2CuO_3 and Ca_2CuO_3, Pt–X chain compounds (X = Cl, Br, and I), π-conjugated polymers (PA, PDA, PTV, and PPV), and σ-conjugated polymers (PDHS). 1D cuprates have the same electronic structure (1D Mott insulator states) as Ni–X chain compounds and show similar linear and nonlinear optical properties. In Fig. 7.5, therefore, data points of both Ni–X chain compounds and 1D cuprates were shown by the same solid circles. Pt–X chain compounds (Pt–Cl, Pt–Br, and Pt–I in Fig. 7.5) and π-conjugated polymers (PA, PDA, PTV, and PPV in Fig. 7.5) belong to Peierls insulators, and a σ-conjugated polymer (PDHS in Fig. 7.5) to band insulators. $\max|\mathrm{Im}\chi^{(3)}|$ values of Pt–X chain compounds and conjugated polymers are roughly scaled by the optical gap energies E_g as $\max|\mathrm{Im}\chi^{(3)}| \propto {E_g}^{-6}$. On the other hand, $\max|\mathrm{Im}\chi^{(3)}|$ values of Ni–X chain compounds (Ni–Br–Br, Ni–Cl–Cl, and Ni–Cl–NO_3) show a significant enhancement as compared to those in 1D Peierls and band insulators.

In order to unravel the origin for the enhancement of $\chi^{(3)}$ in Ni–X chain compounds, the three-level model shown in Fig. 7.6a was adopted. In 1D electronic systems, it is known that the third-order optical nonlinearity is governed by three or four states, which are so-called essential states [15]. The three-level model consists of three states; ground state $|0>$, an odd-parity state $|1>$, and an even-parity state $|2>$. The odd-parity state $|1>$ is a one-photon-allowed state and observed by a linear optical measurement such as absorption and reflectance spectroscopy. The even-parity state $|2>$ is a one-photon-forbidden state. Within the three-level model, the dominant term of $\chi^{(3)}(-\omega;0,0,\omega)$ is expressed as follows:

$$\chi^{(3)}(-\omega;0,0,\omega) = \frac{Ne^4}{3\varepsilon_0\hbar^3}\frac{<2|x|1>^2<1|x|0>^2}{(\omega_1-\omega-i\gamma_1)^2(\omega_2-\omega-i\gamma_2)} \tag{7.3}$$

Here, N is the density of the relevant electrons, e is the charge of electron, ε_0 is the dielectric constant of vacuum, x is the displacement along the 1D axis, $\hbar\omega_1(\hbar\omega_2)$ is the energy position of the state $|1>$ ($|2>$) and $\gamma_1(\gamma_2)$ is the damping energy of the state $|1>$ ($|2>$). In the fitting calculation, all the 12 terms including the dominant term (7.3)

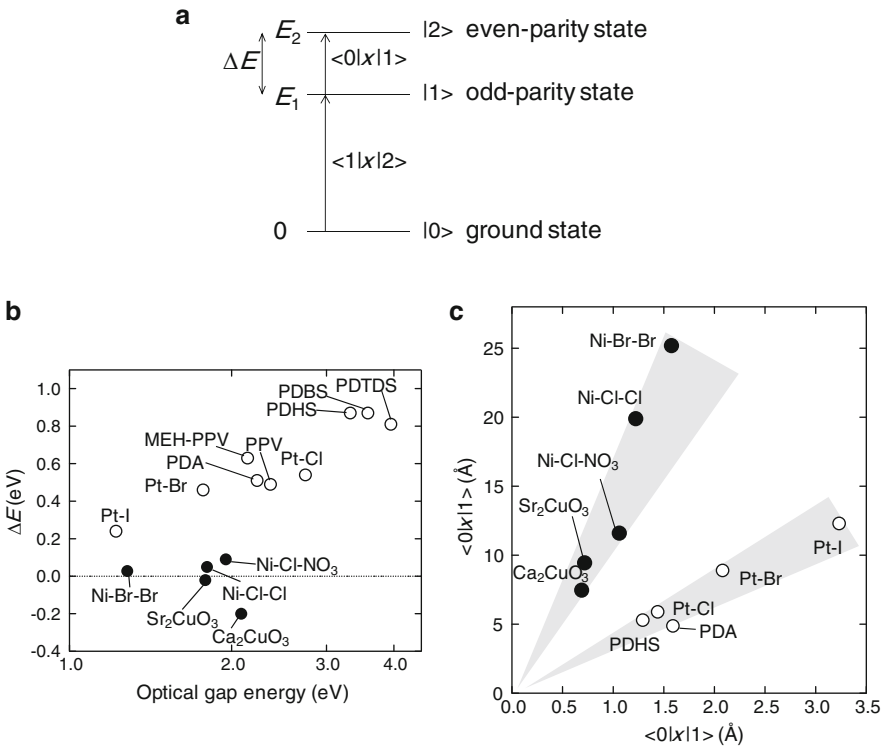

Fig. 7.6 (**a**) Three-level structure consisting of ground state, odd-parity state, and even-parity state. (**b**) The energy difference between the odd-parity state and even-parity state is plotted versus the optical gap energy. (**c**) The transition dipole moments between the two excited states |1> and |2> are plotted versus the transition dipole moment between the ground state and odd-parity state. From [10]

are taken into account. Moreover, considering the relation, $\varepsilon = \varepsilon_1 + i\varepsilon_2 = \varepsilon_0[1 + \chi^{(1)} + 3\chi^{(3)}E^2]$, $\Delta\varepsilon_2$ spectrum is obtained from the relation, $\Delta\varepsilon_2 = \mathrm{Im}[3\varepsilon_0\chi^{(3)}E^2]$. Here, E is the applied electric field.

The $\Delta\varepsilon_2$ curve for Ni–Br–Br calculated by the three-level model is shown in Fig. 7.4b by the broken line, which reproduces well the oscillating behavior of the experimental $\Delta\varepsilon_2$ spectrum. From this analysis, two important features are obtained; one is that the energy difference ($\Delta E = \hbar\omega_2 - \hbar\omega_1$) of the two excited states is very small, being 10 meV. The other is that the transition dipole moments between |1> and |2> ($<1|x|2>$) is very large, exceeding 20 Å. The analysis indicates the existence of two discrete levels of excited states. It is, therefore, reasonable to consider that both |1> and |2> are not due to the continuum but due to excitonic states.

Similar analyses of the ER spectra in the other Ni–X chain compounds revealed that those two features in the $\Delta\varepsilon_2$ or $\chi^{(3)}(-\omega; 0, 0, \omega)$ spectra are common in Ni–X chain compounds. In Fig. 7.6b, the energy difference ΔE of the two excited states is

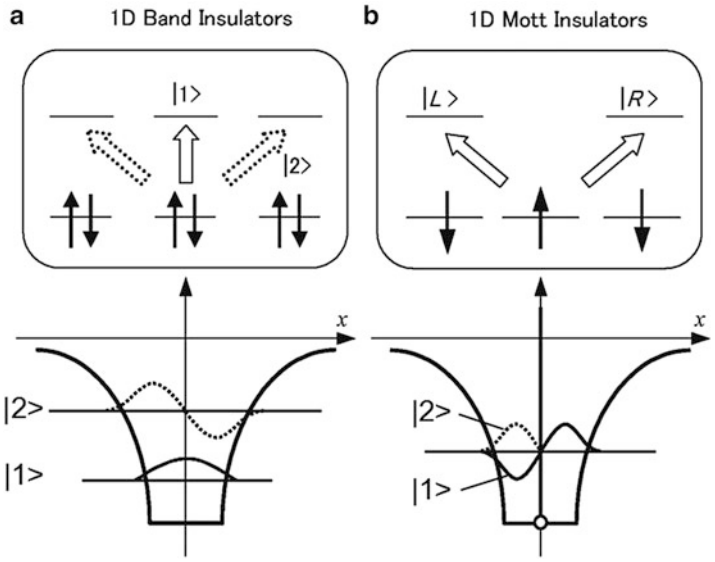

Fig. 7.7 Schematics of the excited states in 1D band insulators (**a**) and 1D Mott insulators (**b**). From [10]

plotted versus the optical gap energy. The absolute values of ΔE for Ni–X chain compounds and 1D cuprates are small, indicating that two excited states $|1>$ and $|2>$ are nearly degenerate. On the other hand, ΔE is relatively larger in Pt–X chain compounds and conjugated polymers ($\Delta E = 0.2$–1.0eV) than ΔE in Ni–X chain compounds. ΔE tends to increase with the increase of the optical gap energy not only in Pt–X chains and conjugated polymers but also in Ni–X chains. In Ca_2CuO_3, it was revealed that the excitonic effect is negligibly small and the spectrum of $\chi^{(3)}$ as well as of ε_2 is very broad. Therefore, the three-level model assuming the two discrete excited states would not be sufficient to explain the optical responses. This is the reason why ΔE is negative (~ -0.2 eV).

In Fig. 7.6c, $<1|x|2>$ values are plotted versus $<0|x|1>$ for various 1D semiconductors. Data points of $<1|x|2>$ in 1D Mott insulators (Ni–X chain compounds and 1D cuprates) are located on the same line, while data points of Peierls and band insulators (Pt–X chain compounds and conjugated polymers) are located on the different line. The slope, $<1|x|2>/<0|x|1>$, is larger for 1D Mott insulators. Thus, the difference between 1D Mott insulators and the other 1D semiconductors is clear.

These two features, that is, the small ΔE and the large $<1|x|2>$, in 1D Mott insulators are not observed in 1D Peierls and band insulators. They originate from strong electron correlation [16]. Here, let us briefly discuss the difference of electronic excited states between 1D band insulators and 1D Mott insulators. In Fig. 7.7a, we show the schematics of the electronic structure and excited states in a 1D band insulator by using a molecular orbital picture [10, 16]. In a 1D band

insulator, the intramolecular excitation indicated by the open arrow (the upper figure of Fig. 7.7a) corresponds to the lowest excited state |1> with odd-parity. The in-phase combination of the intermolecular CT excited states indicated by the broken arrows corresponds to the second lowest excited state |2> with even-parity. Excited electron and hole occupies the same site in |1>, but the different sites in |2>. State |1> forms an exciton with large binding energy due to the large electron–hole Coulomb attractive interaction and therefore ΔE is considerably enhanced. The envelopes of the exciton wave functions are shown in the lower part of Fig. 7.7a. A large difference in the spatial extensions of |1> and |2> is unfavorable for obtaining a large dipole moment $<1|x|2>$.

As for the electronic structure and excited states of 1D Mott insulators, we consider a single band Hubbard model shown in Fig. 7.7b. It is known that fundamental electronic properties of CT insulators can be discussed using such a simplified model. In this model, the electron vacancy (holon) and double electron occupancy (doublon) are prohibited to stay on the same site. As a result, the odd excited state |1> and the even excited state |2> correspond, respectively, to the out-of phase and in-phase combination of the two CT states |R> and |L> indicated by open arrows in the upper part of Fig. 7.7b. When U is much larger than the transfer energy t, splitting ΔE between |1> and |2> should be small and their wave functions should be similar to each other except for their phases as illustrated in the lower part of Fig. 7.7b. In this case, a spatial overlap of the wave functions between |1> and |2> becomes very large, leading to a large $<1|x|2>$ [16]. This is the enhancement mechanism of $\chi^{(3)}(-\omega; 0, 0, \omega)$ in 1D Mott insulators.

7.3.2 *Third-Harmonic Generation Spectroscopy*

The $|\chi^{(3)}(-3\omega; \omega, \omega, \omega)|$ spectrum obtained from the reflection-type THG measurements on a Ni–Br–Br single crystal is shown in Fig. 7.8b [11]. The spectrum exhibits a strong enhancement (labeled as A in the figure) when the photon energy of the incident light is 0.43 eV. This energy corresponds to the 1/3 of the CT transition energy of Ni–Br–Br. Therefore, the enhancement is attributed to the three-photon resonance to state |1>.

The $|\chi^{(3)}(-3\omega; \omega, \omega, \omega)|$ spectrum has other two resonant structures, B and C, which are located at around 0.65 eV and 0.5 eV, respectively. The twice energy of structure B (~1.3 eV) is close to the CT transition energy (1.27 eV), which is determined from the ε_2 spectrum. Since the ER spectroscopy revealed that even-parity CT state |2> is close in energy to odd-party CT state |1> as mentioned above, structure B could be assigned to the two-photon resonance to state |2>.

As for the assignment of structure C, the ε_2 spectrum at 4 K shown in the inset of Fig. 7.8c gives valuable information [11]. The ε_2 spectrum has a weak shoulder structure at around 1.5 eV, which is equal to the triplicate energy of structure C (0.5 eV) in Fig. 7.8b. This suggests that structure C would be related to the three-photon resonance to another odd-parity state |3> located at the higher energy

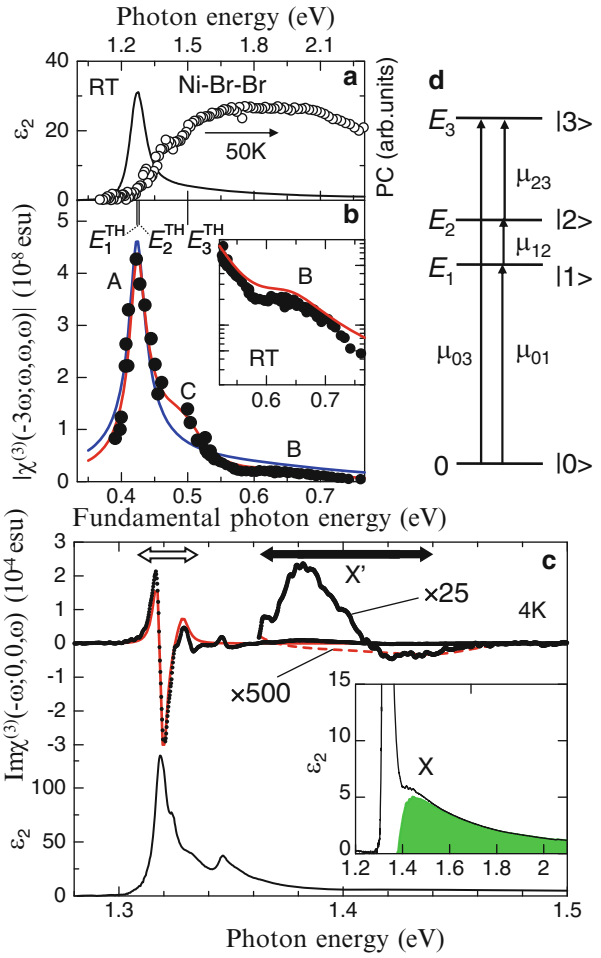

Fig. 7.8 (**a**) ε_2 spectrum and photoconductivity spectrum for Ni–Br–Br. (**b**) $|\chi^{(3)}(-3\omega;\omega,\omega,\omega)|$ spectrum for Ni–Br–Br (*dots*: experimental, *lines*: calculation) obtained from THG experiments. (**c**) $|\chi^{(3)}(-\omega;0,0,\omega)|$ spectrum for Ni–Br–Br obtained from ER experiments. (**d**) Four-level model. From [11]

(~ 1.5 eV) than even-parity state |2>. The schematic of the energy level structure consisting of the four states (four-level model) is shown in Fig. 7.8d.

The nonlinear optical process associated with state |3> plays an important role on the overall $|\chi^{(3)}(-3\omega;\omega,\omega,\omega)|$ spectrum. The $|\chi^{(3)}(-3\omega;\omega,\omega,\omega)|$ spectra calculated using the three-level model (blue line) and the four-level model (red line) are shown in Fig. 7.8b. In the three-level model, the transition process dominating the optical response is |0> → |1> → |2> → |1> → |0>. In the four-level model, the transition process related to |3>, e.g., |0> → |1> → |2> → |3> → |0>, is added in the optical response. The three-level model does not reproduce well structures C and B; the calculated $|\chi^{(3)}|$ values are smaller around structure C and larger around structure B than the experimental $|\chi^{(3)}|$. On the other hand, the four-level model reproduces the experimental result very well. This indicates that the process related to state |3> reduces the optical nonlinearity around structure B. In

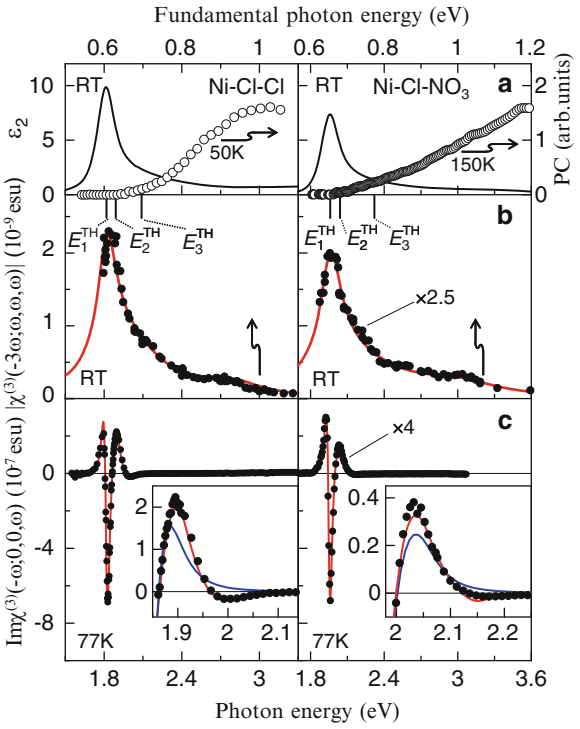

Fig. 7.9 (**a**) ε_2 and photoconductivity spectra for Ni–Cl–Cl and Ni–Cl–NO_3. (**b**) $|\chi^{(3)}(-3\omega;\omega,\omega,\omega)|$ spectrum for Ni–Cl–Cl and Ni–Cl–NO_3. (*dots*: experimental, *lines*: calculation) obtained from THG experiments. (**c**) $|\chi^{(3)}(-\omega;0,0,\omega)|$ spectrum for Ni–Cl–Cl and Ni–Cl–NO_3 obtained from ER experiments. From [11]

other words, in the process related to structure C, $\chi^{(3)}$ originating from the process $|0> \rightarrow |1> \rightarrow |2> \rightarrow |3> \rightarrow |0>$ partially cancels the process $|0> \rightarrow |1> \rightarrow |2> \rightarrow |1> \rightarrow |0>$. Thus, state |3> affects the spectral shape of $|\chi^{(3)}(-3\omega;\omega,\omega,\omega)|$ in the region not only of the three-photon resonance to |3> but also of the two-photon resonance to |2>.

The $\mathrm{Im}\chi^{(3)}(-\omega;0,0,\omega)$ spectrum at 4 K (Fig. 7.8c) obtained by the ER measurement gives more detailed information about state |3> in Ni–Br–Br [11]. At around 1.4 eV, a new structure labeled as X′ appeared, which had a plus–minus structure. Such a plus–minus structure can be explained not by the presence of a single discrete level but by the presence of continuum states. When continuum states exist, the zero-crossing energy in the $\mathrm{Im}\chi^{(3)}$ spectrum corresponds to the lower edge of the continuum (the band-edge), which is 1.41 eV in Ni–Br–Br.

This four-level picture was also confirmed from the results in Ni–Cl–Cl and Ni–Cl–NO_3, which are shown in Fig. 7.9. $|\chi^{(3)}(-3\omega;\omega,\omega,\omega)|$ and $\mathrm{Im}\chi^{(3)}(-\omega;0,0,\omega)$ spectra of Ni–Cl–Cl and Ni–Cl–NO_3 are shown in Fig. 7.9b, c, respectively. $|\chi^{(3)}(-3\omega;\omega,\omega,\omega)|$ spectra were reproduced well by the four-level model as shown by red solid line in Fig. 7.9b. $\mathrm{Im}\chi^{(3)}(-\omega;0,0,\omega)$ spectra were compared with the results of the three-level and the four-level calculations as shown by blue and red lines, respectively, in Fig 7.9c. The four-level model can reproduce the experimental results better. Particularly, the negative components at ~2.0 eV in

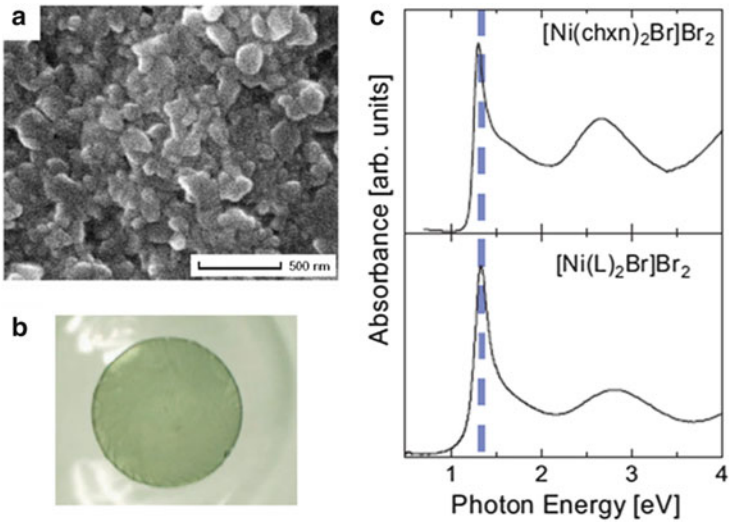

Fig. 7.10 (**a**) SEM image of nanocrystals of $[Ni(L)_2Br]Br_2$. (**b**) Photograph of a $[Ni(L)_2Br]Br_2$/PMMA film. (**c**) Absorption spectra of a single crystal of $[Ni(chxn)_2Br]Br_2$ (*upper panel*) and a $[Ni(L)_2Br]Br_2$/PMMA film (*lower panel*). Adapted from [5]

Ni–Cl–Cl and ~2.15 eV in Ni–Cl–NO_3 are the strong evidences for the higher-lying odd-parity state |3>.

Since the higher-lying odd-parity state |3> corresponds to the band-edge, the energy difference between |3> and the lowest exciton state |1> is a crude measure of the binding energy E_b of the lowest excitonic state. In Ni–Br–Br, E_b evaluated from the difference is about 90 meV. The magnitude of E_b increases as Ni–Br–Br < Ni–Cl–Cl < Ni–Cl–NO_3 in Ni–X chain compounds. The splitting ΔE between |1> and |2> also increases in this order. This tendency is also observed in the ER studies as mentioned above. In Ni–Br–Br, the small excitonic effect makes two CT excited states (|1> and |2>) almost degenerate, leading to the large transition dipole moment between |1> and |2> and therefore to the large $\chi^{(3)}$.

7.3.3 Z-Scan Measurements [5]

When we consider the application of the nonlinear optical materials to ultrafast optical switching devices using, for example, optical waveguides, fabrication of a thin film sample is necessary. Recently, the fabrication of high-quality thin films of the Ni–X compound was successfully made, in which nanocrystals of a Ni–X compound, $[Ni(L)_2Br]Br_2$ (*L*:1,2-diaminohexadecane), having long alkyl chains ($C_{14}H_{29}$) shown in Fig. 7.1b were dispersed in an optical polymer (PMMA = poly(methyl methacrylate)). Size of a nanocrystal is typically ~100 nm wide and a few tens of nanometers thick as seen in the scanning electron microscopy (SEM)

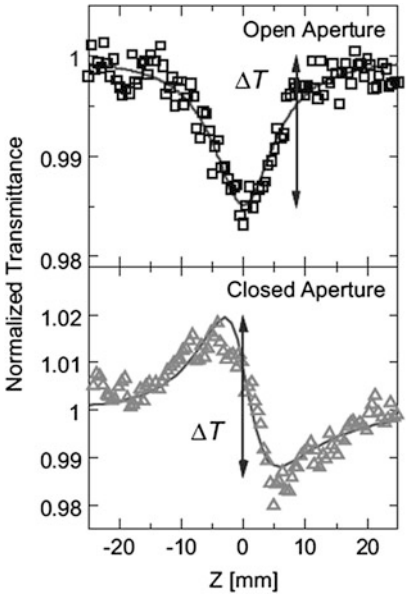

Fig. 7.11 Typical Z-scan profiles of the $[Ni(L)_2Br]Br_2$/PMMA film in the open and closed aperture condition. The *solid lines* show the theoretical fits. Adapted from [5]

image in Fig. 7.10a. The photograph of the film on a CaF_2 substrate is shown in Fig. 7.10b.

Figure 7.10c shows the absorption (α) spectrum of the $[Ni(L)_2Br]Br_2$ film, together with the spectrum of a single crystal of $[Ni(chxn)_2Br]Br_2$. The latter is obtained as the sum ($\alpha_{//}+2\alpha_{\perp}$) of the polarized absorption spectra $\alpha_{//}$ and $\alpha_{\perp}$, which were calculated from the polarized reflectivity spectra for the electric field of light parallel and perpendicular to b, respectively, through the KK transformation. The spectral shape of α in the $[Ni(L)_2Br]Br_2$ film is in good agreement with that in the $[Ni(chxn)_2Br]Br_2$ single crystal. No significant enhancement of the background due to light scattering is observed even in the higher energy region (~4 eV), suggesting the high quality of the film as an optical media.

Typical Z-scan profiles of the $[Ni(L)_2Br]Br_2$ film are presented in Fig. 7.11. The measurements were carried out with the light pulse of the optical communication wavelength $\lambda = 1.55$ μm (the photon energy $\hbar\omega = 0.80\,\mathrm{eV}$). The upper panel shows the nonlinear increase in the absorption (decrease of the transmittance) around the focal plane ($z = 0$) in the open aperture condition. The one-photon absorption is negligible at 0.8 eV so that the observed nonlinear signal can be attributed to two-photon absorption (TPA). The profile in the partially closed aperture condition includes the TPA component as well as the component for the optical Kerr effect described by $\mathrm{Re}\chi^{(3)}(-\omega;\omega,-\omega,\omega)$. By dividing the profile in the partially closed aperture condition by that in the open aperture condition, the profile for the optical Kerr effect alone was obtained, which exhibits a plus–minus structure characteristic of self-defocusing, as shown in the lower panel of Fig. 7.11.

The two profiles in Fig. 7.11 were well reproduced by the theoretical profiles predicted for the third-order nonlinear optical response, as shown by thin solid

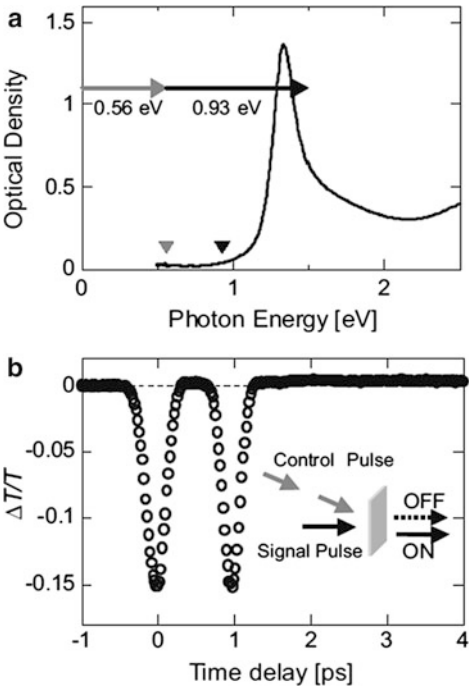

Fig. 7.12 Demonstration of the ultrafast optical switching. (**a**) The absorption spectrum and energies of pump (*gray*) and probe (*black*) pulses. (**b**) The transmittance modulation by the two pump pulses with an interval of 1 ps. From [5]

lines. From these profiles, $\mathrm{Re}\chi^{(3)}(-\omega;\omega,-\omega,\omega)$ and $\mathrm{Im}\chi^{(3)}(-\omega;\omega,-\omega,\omega)$ at 1.55 μm were evaluated to be -1.5×10^{-9} and 0.56×10^{-9} esu, respectively, both of which are also very large. Taking the discussions in the previous subsections into account, the two-photon state (1.6 eV) corresponds to the even-parity states within the continuum. The large TPA associated with the even-parity states could be also explained by the fact that the degeneracy of the odd- and even-parity states enhances the dipole moment $<1|x|2>$ between them.

7.3.4 Ultrafast Optical Switching [5]

High repeatability of the switching operation is the most important condition for all-optical switching devices. To investigate the performance of Ni–X chain compounds, the repeatability of the TPA phenomenon in the $[Ni(L)_2Br]Br_2$ film was investigated by double pump pulses. Energies of the pump and probe pulses were set at 0.56 and 0.93 eV, respectively, both of which are located in the transparent region as shown in Fig. 7.12a. Figure 7.12b shows the time characteristic of the transmittance change $\Delta T/T$. The first pulse gives rise to an instantaneous decrease in the transmittance, which is followed by its ultrafast recovery. This indicates that the decay time of the photoexcited states is much shorter than the time resolution of the measurement system, which is about 180 fs. The second pump

pulse applied 1 ps after the first pulse produces the same changes of the transmittance, $\Delta T/T$, as the first pulse. This result indicates that an optical modulation of more than 1 THz repetition is possible. Such high repeatability of optical switching by the TPA process as well as the large $\chi^{(3)}$, demonstrates that the $[Ni(L)_2Br]Br_2$ thin film has a really high potential as an optical switching medium.

7.4 Summary

The third-order optical nonlinearity in one-dimensional Mott–Hubbard insulators of Ni–X chain compounds is reviewed from the experimental viewpoint. The large $\chi^{(3)}$ values in Ni–X chain compounds were revealed by the electroreflectance method. The spectral analyses based on the discrete-level models clarified that the strong electron correlation results in the degeneracy of odd-parity and even-parity CT excited states. Such degeneracy of excited states leads to the large transition dipole moment between those excited states and is the origin for the large third-order nonlinear susceptibilities $\chi^{(3)}$ in Ni–X chain compounds. In other one-dimensional semiconductors belonging to Peierls or band insulators, on the other hand, the lowest two excitons are not degenerated and, therefore, $\chi^{(3)}$ is relatively small. In Ni–X chain compounds, detailed ER and THG measurements revealed the presence of another essential state with odd-parity, which corresponds to the edge of the continuum state. Such information also made clear the excitonic effects in Ni–X chain compounds. Z-scan experiments on the thin film samples evidenced that Ni–Br chain compounds show large optical nonlinearity at optical communication wavelength. Moreover, the pump–probe experiments demonstrated that all-optical switching operation is possible at 1 THz repetition rate. Thus, Ni–X chain compounds show hopeful ultrafast third-order optical nonlinearity based upon the novel mechanism resulting from strong electron correlation, which is different from that in other one-dimensional semiconductors.

References

1. Wada Y, Yamashita M (1990) Phys Rev B42:7398
2. Iwasa Y, Funatsu E, Hasegawa T, Koda T, Yamashita M (1991) Appl Phys Lett 59:2219
3. Kishida H, Matsuzaki H, Okamoto H, Manabe T, Yamashita M, Taguchi Y, Tokura Y (2000) Nature 405:929
4. Iwai S, Ono M, Maeda A, Matsuzaki H, Kishida H, Okamoto H, Tokura Y (2003) Phys Rev Lett 91:057401
5. Tao S, Miyagoe T, Maeda A, Matsuzaki H, Ohtsu H, Hasegawa M, Takaishi S, Yamashita M, Okamoto H (2007) Adv Mater 19:2707
6. Miyagoe T, Tao S, Maeda A, Matsuzaki H, Ohtsu H, Hasegawa M, Takaishi S, Yamashita M, Okamoto H (2008) J Phys Soc Jpn 77:023711

7. Toriumi K, Wada Y, Mitani T, Bandow S, Yamashita M, Fujii Y (1989) J Am Chem Soc 111:2341
8. Okamoto H, Toriumi K, Mitani T, Yamashita M (1990) Phys Rev B 42:10381
9. Okamoto H, Shimada Y, Oka Y, Chainani A, Takahashi T, Kitagawa H, Mitani T, Toriumi K, Inoue K, Manabe T, Yamashita M (1996) Phys Rev B 54:8438
10. Ono M, Miura K, Maeda A, Matsuzaki H, Kishida H, Taguchi Y, Tokura Y, Yamashita M, Okamoto H (2004) Phys Rev B 70:085101
11. Ono M, Kishida H, Okamoto H (2005) Phys Rev Lett 95:087401
12. Butcher PN, Cotter D (1990) The elements of nonlinear optics. Cambridge University Press, Cambridge
13. Sheik-Bahae M, Said AA, Wei T-H, Hagan DJ, Van Stryland EW (1990) IEEE J Quantum Electron 26:760
14. Maeda A, Ono M, Kishida H, Manako T, Sawa A, Kawasaki M, Tokura Y, Okamoto H (2004) Phys Rev B70:125117
15. Dixit SN, Guo D, Mazumdar S (1991) Phys Rev B 43:R6781
16. Mizuno Y, Tsutsui K, Tohyama T, Maekawa S (2000) Phys Rev B 62:R4769

Chapter 8
Theory of MX Chain Compounds

Kaoru Iwano

8.1 Theoretical Framework

8.1.1 Overview

MX chains are fascinating materials not only for experimentalists but also for theorists. They are almost ideal examples of one-dimensional systems and become very good stages for us to check and deepen our knowledge and experiences about the latter. Of course, we know famous polyacetylene and other conjugate polymers, which had already been known when we started the studies of MX chains. In fact, the models applied for polyacetylene are similar, in some sense, to those models for MX chains that we introduce from here on. However, we have more varieties in both the kinds of compounds and the types of electronic and lattice states. Here, we state the most important classification:

Pd and Pt complexes → Charge−density−wave (CDW) systems,
Ni complexes → Mott−insulator systems.

In Fig. 8.1, these two categories are very schematically illustrated. Readers may see apparent differences between them. Namely, in Pt and Pd complexes, the $5(4)d_{z^2}$ orbital of Pt (Pd) that extends along the chain direction is doubly occupied or empty, leading to a so-called mixed valence of +2 and +4. On the other hand, in Ni complexes, the corresponding $3d_{z^2}$ orbital contains one electron univocally, leading to the valency of +3. Here, it will be important to comment why we think about d_{z^2} electrons. Assuming a formal valency of +3, the d-electron configuration is d^7.

K. Iwano (✉)
Institute of Materials Structure Science, High Energy Accelerator Research Organization (KEK), 1-1 Oho, Tsukuba 305-0801, Japan
e-mail: kaoru.iwano@kek.jp

M. Yamashita and H. Okamoto (eds.), *Material Designs and New Physical Properties in MX- and MMX-Chain Compounds*, DOI 10.1007/978-3-7091-1317-2_8,

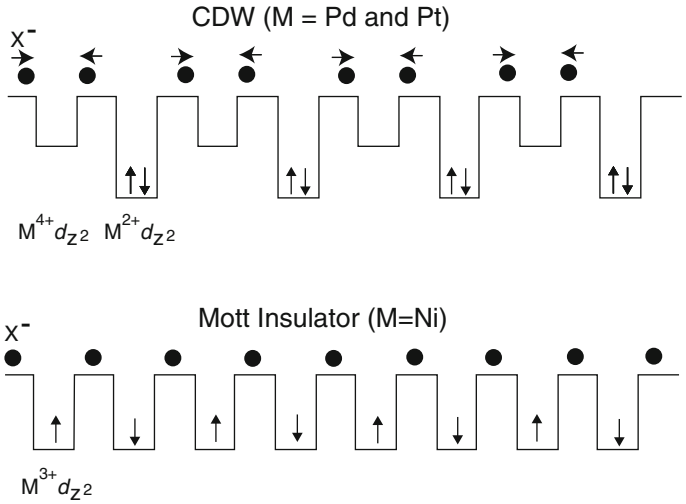

Fig. 8.1 Schematic picture of electron and halogen-lattice configurations

The metal ion is more closely surrounded by the ligands or more specifically by their N coordination atoms than the halogen ions. This structure relatively lowers the level of d_{z^2} compared with that of $d_{x^2-y^2}$, leading to the situation of a half-filled band of d_{z^2} as the average. Returning to the case of Ni, we also see an antiferromagnetic spin order at least within a short range. This monovalency and spin correlation are the central issues in the Ni complexes and we will discuss them extensively in later sections. We here only emphasize that the main driving force of this singly occupied electron configuration is the Coulombic repulsion working between the two electrons (spin $= \uparrow$ and $\downarrow$) occupying the same site.

Regarding the lattice configuration, the halogens dimerize in the Pt and Pd complexes. This dimerization inevitably makes two nonequivalent sites for Pt and Pd sites; the site to which the two neighboring halogens come closer and the site from which the same halogens apart. When we recall a general tendency that the halogens take (-1) valency, it will be easily understood that the electrostatic site energy goes higher (lower) for the former (latter). Meanwhile, the halogens in the Ni complexes make a striking contrast. It was experimentally observed that they reside at the midpoints. Thus, the monovalency in the Ni complexes is very consistent with its lattice configuration. The first purpose of theories is thus to describe these very different states in a unified manner, in other words, using a model that is almost common but a few key parameter values.

8.1.2 Model

First of all, we explain the simplest model, i.e., an extended Peierls–Hubbard model [1–4]:

$$H_{\mathrm{ePH}} = -t_0 \sum_{\sigma=\uparrow,\downarrow} \sum_{l=1}^{N} (C_{l+1\sigma}^{\dagger} C_{l\sigma} + \mathrm{h.c.}) + U \sum_{l=1}^{N} n_{l\uparrow} n_{l\downarrow} + V \sum_{l=1}^{N} n_l n_{l+1}$$
$$- \alpha \sum_{l=1}^{N} (Q_{l+1} - Q_l) n_l + \frac{K}{2} \sum_{l=1}^{N} Q_l^2. \tag{8.1}$$

The naming of this hamiltonian originally comes from one of the most typical hamiltonians in the solid-state physics, that is, the Hubbard model [5]. As is well known, the Hubbard hamiltonian describes an electronic system composed by one orbital at each site, being especially characterized by strong on-site (within-the-same-orbital) Coulombic repulsion of the energy scale U. This model is widely used as a minimum model of electron correlation typically for $3d$ electrons and is the basis for our model construction. Here, we also assume only one orbital for each site, i.e., the $5d_{z^2}$ orbital for the Pt site, the $4d_{z^2}$ orbital for the Pd site, and the $3d_{z^2}$ orbital for the Ni site, as we have already mentioned in the previous subsection. The first term and the second term are thus a Hubbard-like part, with $C_{l\sigma}$ and $C_{l\sigma}^{\dagger}$ being the corresponding destruction and creation operators of the electron at the lth site with σ spin.

However, in our MX-chain systems, only the first two terms are not sufficient. We must include at least two key ingredients. One is the long-range Coulombic repulsion working between different metal sites. In the above model, this effect is represented by its shortest part, i.e., the nearest-neighboring (n. n.) term of which the energy scale is V (see the third term). The word of "extended" in the model name just comes from this term. This term gives two essential effects. One is the stabilization of the CDW state. The other is the exciton effect that makes an electron–hole bound state and strongly modifies the optical spectra in both the CDW and Mott-insulator states. We will give detailed explanations about these effects in the forthcoming sections. Regarding the part beyond the nearest neighbors, we do not consider them explicitly, because any substantial effect originating from it such as frustration is not observed in these materials.

One more important effect originates from the lattice. As we have already discussed in Sect. 8.1.1, the most important and experimentally observed lattice effect is the halogen displacement [6]. We therefore include its effect as the second line, defining Q_l as its displacement along the chain direction as is illustrated in Fig. 8.2, and α as its electron–lattice (e–l) coupling strength. Since this type of e–l coupling usually induces a Peierls transition, we add "Peierls" to the name of our hamiltonian. It will also be necessary to add an explanation to the last term. In this model, the positions of the metal ions are assumed to be fixed because the metal ions are connected to the backbone of the crystal through the ligands surrounding them. For this reason, the halogen prefers the midpoint position between the two consecutive metal ions when they have the same valencies, and so we write the elastic term as that in Eq. (8.1).

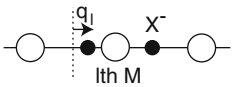

Fig. 8.2 Definition of the halogen displacements

As the last remark about this hamiltonian, we mention another type of e–l lattice coupling that modifies the electron transfer. Such type of coupling appears very typically in the model of polyacetylene [7], but it is missing here. The reason is that our transfer term originates from a super transfer via the halogen p_z orbital and that the halogen displacement Q_l only gives a second-order effect to it.

Next, we rewrite the hamiltonian slightly to make the following discussion more transparent [1]:

$$H_{\mathrm{ePH2}} = -t_0 \sum_{\sigma=\uparrow,\downarrow} \sum_{l=1}^{N} (C_{l+1\sigma}^{\dagger} C_{l\sigma} + \mathrm{h.c.}) + U \sum_{l=1}^{N} n_{l\uparrow} n_{l\downarrow} + V \sum_{l=1}^{N} n_l n_{l+1} - S \sum_{l=1}^{N} (q_{l+1} - q_l) n_l + \frac{S}{2} \sum_{l=1}^{N} q_l^2. \tag{8.2}$$

Here, the e–l coupling strength S is introduced by $S \equiv \alpha^2/K$, and the displacements are replaced by q_l by the definition of $Q_l = (\alpha/K) q_l$. Note that S has the dimension of energy and that q_l is dimensionless.

In the extended Peierls–Hubbard model, we neglect the contributions of the other electron orbitals. Thus, as candidates of other models, it is very natural to introduce such orbitals that may be located close to the corresponding d_{z^2} orbitals. Based on the results of first-principles calculation, which we briefly summarize in the next subsection, we know that the most important orbital to be added is the halogen outermost p_z orbital. In fact, as we have already mentioned, they play the role of an "island" in the super transfer that we have already mentioned. Moreover, this orbital is rather close to the Ni $3d_{z^2}$ orbital and comes into the Hubbard gap of the latter, as we will see in the forthcoming sections. For these reasons, we construct the following *dp* model [8, 9]:

$$H_{dp} = -\sum_{l\sigma} t(l)(C_{l+1\sigma}^{\dagger} C_{l\sigma} + \mathrm{h.c.}) + \sum_{l} e(l) n_l + \sum_{l=\mathrm{odd}} U_{\mathrm{p}} n_{l\uparrow} n_{l\downarrow} + \sum_{l=\mathrm{even}} U_{\mathrm{d}} n_{l\uparrow} n_{l\downarrow} + \sum_{l} V(l) n_l n_{l+1} + \sum_{l=\mathrm{odd}} V_{\mathrm{pp}} n_l n_{l+2} + \sum_{l=\mathrm{even}} V_{\mathrm{dd}} n_l n_{l+2} + \sum_{l} \frac{K_l}{2} Q_l^2, \tag{8.3}$$

where $C_{l\sigma}^{\dagger}$ and $C_{l\sigma}$ are assigned to the orbitals of the metal and halogen sites with l being even and odd, respectively. As for the other parameters, their meanings will be almost self-explanatory in Fig. 8.3 and we reserve the details including actual site-dependent expressions for later discussions.

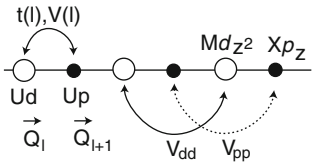

Fig. 8.3 Illustration of the *dp* model

Readers may notice that the relationship between these two models is analogous to that in cuprates. Namely, in the cuprates, both a single-band model consisting only of Cu $3d_{x^2-y^2}$ and a two-band model augmented by O $2p$ orbitals were discussed. In particular, the situation in the Ni complex is very similar to that in the cuprates, from the viewpoint of the charge-transfer (CT) insulator that will be commented later.

Another possible orbital to be added would be, for example, a molecular orbital in the ligand. Fortunately this is not the case of ethylenediamine (en), since the molecular orbitals in this ligand are all σ orbitals and are located relatively much higher or much lower. We must be careful that this simplification is not applied for ligands that have π orbitals.

8.1.3 Phase Diagram

In this section, we discuss a ground-state phase diagram expected for the extended Peierls–Hubbard model, because the ground state properties are essentially shared by the *dp* model. Before introducing a detailed result, we present a simple analysis in the localized limit, that is, the case of vanishing electron transfer. In the localized limit, the picture in Fig. 8.1 becomes exact and we easily calculate the energy for each state. In the CDW state, for example, the value of q_l is optimized using the last line in Eq. (8.2) (we rewrite the forth term as $-S\Sigma_l(n_{l-1}-n_l)q_l$ and setting n_l as ... , 0, 2, 0, 2, ... As a result, q_l becomes ± 2 alternately and gives the energy of $-4S+U$ per one unit cell, i.e., two pairs of "MX." In the case of the Mott-insulator, it has the energy of 2 V for the same segment of the chain. This easy arithmetic gives us a simple criterion for the relative stability between the two states; when $4S+2V>U$, the CDW is stabilized, while, when $4S+2V<U$, the Mott-insulator is stabilized. In other words, the e–l interaction S and the nearest-neighbor electron mutual repulsion V collaborate to drive the CDW state, while the on-site electron repulsion U drives the Mott-insulator state.

The validity of the above arithmetic is verified by further calculations including the effects of electron transfer. What is interesting is that the above criterion is exact within the framework of a Hartree–Fock (HF) calculation, as was shown by Nasu [1]. He further applied a random-phase approximation (RPA) to this model and considered a phase diagram even including the effects of magnon excitations. The result is shown in Fig. 8.4, and we see a slight intrusion of the Mott-insulator phase into the CDW phase, which was due to the stabilization of the former by the

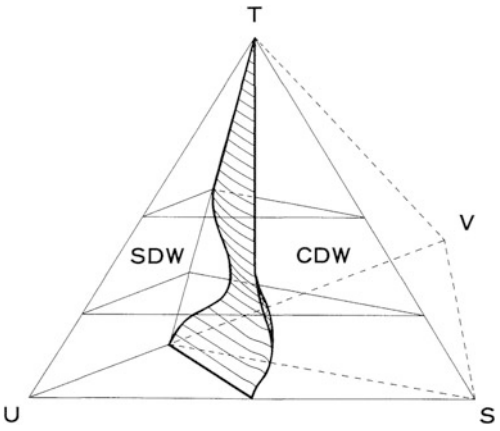

Fig. 8.4 Phase diagram expressed by a tetrahedron. The region named SDW corresponds to the Mott-insulator state in this article. Reprinted from Nasu [1]

magnon excitations, in the sense of a standard second-order perturbation. Such further stabilization of the Mott-insulator state beyond the HF level was also confirmed by a modern density-matrix renormalization group (DMRG) calculation [10].

8.1.4 First-Principles Calculation

First-principles calculations are generally very important in discussing materials especially when they are new and people do not have a rigid picture about them. An idealistic way of a theoretical approach will be, first, a first-principles calculation and, next, model calculations on the basis of it. In this sense, the history of theoretical development on these materials was reverse; first the ideas and investigations of model calculations, and then first-principles calculations appeared. I myself think that this is also allowed because such history seems to indicate a splendid intuition of the people who launched the theory represented by the models like Eqs. (8.1) and (8.3). In fact, the validity of those models was assured by the first principle calculations done afterward. Alouani et al. performed all-electron local-density-approximation (LDA) calculations extensively [11–13]. In their results, it was first confirmed that the most important orbitals around the Fermi energy were corresponding d_{z^2} orbitals, but they were strongly hybridized with the neighboring p_z orbitals. In this sense, a single-band model like Eq. (8.1) should be interpreted as an effective model in which the orbital at the metal site is a d_{z^2} orbital combined with neighboring p_z orbitals with appropriate signs, as is the case in the so-called Zahn–Rice singlet [14].

They also reported other important properties, for example, the realization of CDW for Pt systems and that of an undimerized antiferromagnetic insulating state for a Ni system. Exactly speaking, the latter state found in their calculation is not

truly realistic because we must have a Mott-insulator state, in which spins are strongly fluctuating, so as to reproduce the temperature dependence of magnetic susceptibility in this system, that is, that of a Bonner–Fischer type. In the LDA calculations, on the other hand, we find a long-range order of antiferromagnetic type, because of the mean-field nature of those calculations. Such deficiencies are solved in the model calculations.

Iwano et al. performed density-functional theory (DFT) calculations for [Pt $(en)_2$][$Pt(en)_2Cl_2$]$(ClO_4)_4$ (hereafter PtCl), using a quantum-chemical molecular-orbital method [15]. They also found a similar property, namely, the importance of $5d_{z^2}$ orbitals and its strong hybridization with the Cl $2p_z$ orbitals. What was a matter of interest was the atomic valencies of the Pt ions because people in this field (also in this book) often mention their nonequivalent two valencies, namely, +2 and +4. Unfortunately, the result of the usual Mulliken analysis was disappointing. They found +2.3 and +2.1, instead of +4 and +2, respectively. Nevertheless, they thought that the whole result was sound and consistent with the CDW picture, since the electronic excitations were correctly the CT excitations from $5d_{z^2}$ (allegedly Pt^{2+}) to $5d_{z^2}$ (allegedly Pt^{4+}). The above valency of +2.3 rather seems to indicate the strong hybridization with the halogen orbitals approaching to that, in a way like $(+4) + 2 \times (-1) \sim (+2)$. As one more comment, the hybridization of d_{z^2} orbitals with the molecular orbitals of en is rather small. It was once argued that that hybridization was a origin to reduce the on-site Coulombic repulsion effectively potentially yielding the electron density spread to the ligand, but their result demonstrated that such an effect was not a dominant one.

8.2 CDW (M=Pt and Pd) Systems

In this section, we discuss the CDW systems from various aspects. From the viewpoint of electron correlation, this system might be a little "boring" except for the case in the vicinity of the phase boundary to the Mott insulator. However, this has a great significance from the view point of e–l interaction and its manifestation both in the optical spectra and the photoexcitations of nonlinear excitations like solitons. The solitons are defined as a domain wall that separates the two equivalent phases of the CDW. The formation of a soliton pair thus means a domain formation in a uniform background. As far as we know, such a dynamical process has not been analyzed completely even until now, not only in this field but also in other fields, in spite of its importance as a many-body problem. The largest reason lies of course in its difficulty mainly due to the quantum nature of the lattice. In this sense, this section is also not a complete one and we are still on the way. We nevertheless believe that the results are correct at least as a rough sketch and that they will provide further motivation not only for the author himself but also for the readers.

8.2.1 Ground State

We start our analysis of the extended Peierls–Hubbard hamiltonian in Eq. (8.2), based on a Hartree-Fock HF approximation. Such a treatment is elementary, but it is a good exercise to prepare ourselves before advanced calculations. In this approximation, we simply replace the interaction terms in Eq. (8.2) using this recipe:

$$
\begin{aligned}
&n_{l\uparrow}n_{l\downarrow} \to n_{l\uparrow}\langle n_{l\downarrow}\rangle + \langle n_{l\uparrow}\rangle n_{l\downarrow} - \langle n_{l\uparrow}\rangle\langle n_{l\downarrow}\rangle \\
&n_l n_{l+1} \to n_l\langle n_{l+1}\rangle + \langle n_l\rangle n_{l+1} - \langle n_l\rangle\langle n_{l+1}\rangle \\
&\qquad - \sum_\sigma \left\{ C^\dagger_{l+1\sigma}C_{l\sigma}\langle C^\dagger_{l\sigma}C_{l+1\sigma}\rangle + \text{h.c.} - \langle C^\dagger_{l+1\sigma}C_{l\sigma}\rangle\langle C^\dagger_{l\sigma}C_{l+1\sigma}\rangle \right\}, \qquad (8.4)
\end{aligned}
$$

where the brackets $\langle \ldots \rangle$ are the mean fields to be determined self-consistently. In practical calculations, we start from $\langle n_{l\sigma}\rangle = \bar{n}_{l\sigma}$ and $\langle C^\dagger_{l\sigma}C_{l+1\sigma}\rangle = \bar{m}_{l\sigma}$ with $\bar{n}_{l\sigma}$ being and $\bar{m}_{l\sigma}$ appropriate c-number distributions. Such an assumption enables us to make a one-body mean-field hamiltonian as

$$
\begin{aligned}
H_{\text{ePH2,HF}} = &- \sum_{\sigma=\uparrow,\downarrow}\sum_{l=1}^{N}((t_0 + V\bar{m}_{l\sigma})C^\dagger_{l+1\sigma}C_{l\sigma} + \text{h.c.} - V|\bar{m}_{l\sigma}|^2) \\
&+ U\sum_{l=1}^{N}(\bar{n}_{l\uparrow}n_{l\downarrow} + n_{l\uparrow}\bar{n}_{l\downarrow} - \bar{n}_{l\uparrow}\bar{n}_{l\downarrow}) + V\sum_{l=1}^{N}(\bar{n}_l n_{l+1} + n_l\bar{n}_{l+1} - \bar{n}_l\bar{n}_{l+1}) \\
&- S\sum_{l=1}^{N}(q_{l+1} - q_l)n_l + \frac{S}{2}\sum_{l=1}^{N}q_l^2. \qquad (8.5)
\end{aligned}
$$

Assuming a classical distribution for q_l, we can now solve this hamiltonian very easily. Since we only treat the case of zero temperature throughout this article, the expectation values like $\langle n_{l\sigma}\rangle$ are obtained by selecting the lowest $N_e/2$ one-electron orbitals for each spin (N_e is the total electron number). We then try iterations until self-consistency conditions as $\langle n_{l\sigma}\rangle = \bar{n}_{l\sigma}$ and $\langle C^\dagger_{l\sigma}C_{l+1\sigma}\rangle = \bar{m}_{l\sigma}$ are satisfied. Thus, this is a type of mean-field treatment, while it is educational to emphasize that this is a variational method at the same time. The variables like $\bar{n}_{l\sigma}$ there work as variational variables that minimize the expectation value of the original hamiltonian through the Slater determinant determined by Eq. (8.5). This variational aspect, which is easily proved by taking functional derivatives of each one-electron orbital function, is very important, since modern methods like a density-matrix renormalization group DMRG treatment are also variational methods in a much more extended meaning.

Returning to the CDW problem, it is natural to set $q_l = q_0(-1)^l$, $\bar{n}_{l\sigma} = 1/2 + \delta n(-1)^l$, and $\bar{m}_{l\sigma} = \bar{m}$. Moreover, using the Hellmann–Feynman theorem,

we require that q_l be equal to $\langle n_{l-1}\rangle - \langle n_l\rangle$, which gives $q_0 = 4\delta n$. The electronic part to be solved is then

$$H_{\rm el} = -T\sum_{l\sigma}(C^{\dagger}_{l+1\sigma}C_{l\sigma} + \text{h.c.}) + \sum_{l\sigma}((U/2+2V) + (-1)^l D)n_{l\sigma}, \tag{8.6}$$

where T and D are defined as $t_0 + V\bar{m}$ and $(8S + 4V - U)\delta n$, respectively. To diagonalize this hamiltonian, we introduce one-electron states $C_{\mu\sigma}$ using one-electron wave functions $\phi_{\mu\sigma}$, as $C^{\dagger}_{\mu\sigma} \equiv \sum_l \phi_{\mu\sigma}(l)C^{\dagger}_{l\sigma}$. Then, the eigenvalue equation becomes

$$M^{\rm HF}_{ll'}\phi_{\mu\sigma}(l') = \varepsilon_{\mu\sigma}\phi_{\mu\sigma}(l), \tag{8.7}$$

where

$$M^{\rm HF}_{ll'} \equiv -T(\delta_{l,l'+1} + \delta_{l,l'-1}) + ((U/2+2V) + (-1)^l D)\delta_{ll'}. \tag{8.8}$$

This equation is easily solved writing the wave functions in the form of a Bloch state, namely, as $\phi_\mu(l) = \mathrm{e}^{ikl}u_k(l)$, with a periodic function $u_k(l)$ and a momentum k. We here drop the spin indices because the CDW state has no spin polarization. Since the spatial period of this case is two, we can express the periodic function as $u_k(l) = a(k) + (-1)^l b(k)$, and then the eigenvalue equation is reduced to the following 2×2 form:

$$\begin{pmatrix} -2T\cos(k) + (U/2+2V) & D \\ D & 2T\cos(k) + (U/2+2V) \end{pmatrix}\begin{pmatrix} a \\ b \end{pmatrix} = \varepsilon_\mu \begin{pmatrix} a \\ b \end{pmatrix}. \tag{8.9}$$

Solving this equation in an usual way, we find

$$\varepsilon_\mu = (U/2+2V) \pm \sqrt{D^2 + 4T^2\cos^2(k)} \equiv (U/2+2V) \pm \varepsilon_k \tag{8.10}$$

and the signs $\pm$ correspond to valence (v) and conduction (c) bands. It turns out here that the label μ corresponds to the sets of (v, k) and (c, k). As for the values of k, we impose a periodic boundary condition (PBC), i.e., $\phi_\mu(l+N) = \phi_\mu(l)$ and find $k = (2\pi/N)m$ with m being an integer. We also emphasize that the total number of the one-electron states is N, except for spins. We then restrict the range of k to $-\pi/2 \le k < \pi/2$ so as to count $N/2$ states for each band, which procedure is nothing but a band folding typical to a superlattice structure. Finally, we display a normal orthogonal basis set for the one-electron states thus obtained:

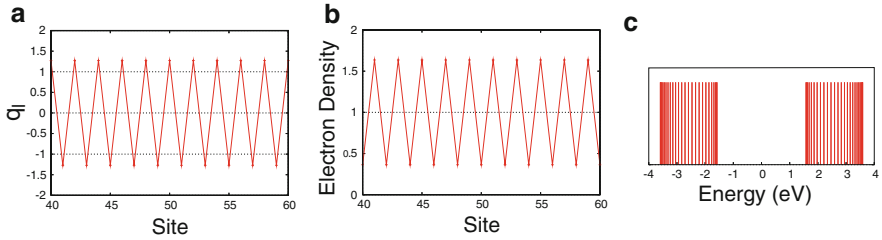

Fig. 8.5 HF solution for CDW. (**a**) Halogen lattice displacements, (**b**) electron density, and (**c**) a one-electron energy band diagram. In (**c**), the band center that is originally at $U/2 + 2V$ is set to the origin

$$\left\{ \frac{1}{\sqrt{N}} \mathrm{e}^{ikl} (a(k) + (-1)^l b(k)); k = -\pi/2, -\pi/2 + 2\pi/N, \ldots, \pi/2 - 2\pi/N \right\}, \tag{8.11}$$

where N is assumed to be a multiple of 4, and the coefficients are defined as

$$a(k) = \sqrt{\frac{E_k \mp 2T\cos(k)}{2E_k}}, \tag{8.12}$$

and

$$b(k) = \sqrt{\frac{E_k \pm 2T\cos(k)}{2E_k}}. \tag{8.13}$$

Now, we are prepared to determine the magnitudes of the mean fields, i.e., δn and $\bar{m}$, for each set of the model parameters. Below, we show one example of the results obtained for a realistic parameter set for the PtCl complex, that is, $(U, V, S, t_0) = (2.0, 1.2, 0.27, 1.3)$ in units of eV. Readers may remember a simple arithmetic, $4S + 2V > U$, for a stable CDW, which assures a truly stable CDW solution for this parameter set. In Fig. 8.5, we draw the lattice distribution and the electron density thus obtained also with the one-electron energy band diagram. As is seen in (b), the densities at the two nonequivalent sites are 1.64 and 0.36, which correspond to $M^{+2.36}$ and $M^{+3.64}$, respectively. Such fractional valencies are a feature of the itinerant system. When we pay attention to the energy bands, we notice the energy gap between the conduction and valence bands. The value of 3.15 eV is larger than the optical gap of the PtCl compound, i.e., about 2.7 eV [16, 17], and the readers may think that the present parameter set will not be appropriate for explaining this compound. In the next subsection, we explain how this discrepancy will be solved by a further analysis.

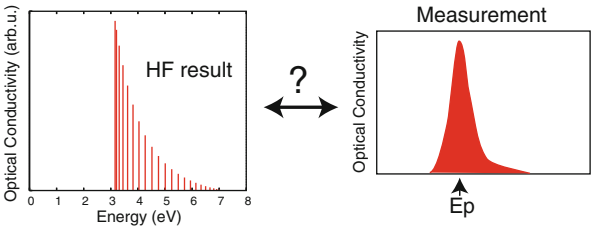

Fig. 8.6 Comparison of the optical conductivity spectrum calculated by the HF approximation and a schematic picture of the measured spectrum. In the case of PtCl, E_p is around 2.7 eV

8.2.2 *Optical Properties*

In this subsection, we discuss the optical properties of the CDW systems. As is introduced in the experimental section, a prominent feature in the absorption spectra is the strong absorption band whose intensity is more or less concentrated at the lower edge, as schematically illustrated in Fig. 8.6 (right panel). Moreover, the band takes the form of an asymmetric Lorentzian. These features are hard to explain solely by the HF calculation shown in the previous subsection. In fact, The HF calculation gives a broad absorption band extending from the HF gap to the excitation energy from the bottom of the valence band to the top of the conduction band (see the left panel of Fig. 8.6).

Iwano et al. thought that this discrepancy came from the effect beyond the HF approximation, namely, the exciton effect, and investigated it [18]. To start such a calculation, it will be convenient to separate the original hamiltonian in Eq. (8.2) into its HF part and the remaining part:

$$H_{\mathrm{ePH2}} = H_{\mathrm{ePH2,HF}} + \Delta H. \tag{8.14}$$

Our task is then to express ΔH in terms of the basis set that we constructed in the HF calculation. As the first step, we rewrite the fluctuating part ΔH as

$$\begin{aligned}\Delta H = U\sum_{l}(n_{l\uparrow} - \langle n_{l\uparrow}\rangle)(n_{l\downarrow} - \langle n_{l\downarrow}\rangle) + V\sum_{l}(n_l - \langle n_l\rangle)(n_{l+1} - \langle n_{l+1}\rangle) \\ + V\sum_{l\sigma}(\langle C^{\dagger}_{l+1\sigma}C_{l\sigma}\rangle C^{\dagger}_{l\sigma}C_{l+1\sigma} + \mathrm{h.c.}) - V\sum_{l\sigma}|\langle C^{\dagger}_{l+1\sigma}C_{l\sigma}\rangle|^2.\end{aligned} \tag{8.15}$$

Here, we assume that the mean field in the brackets are already adjusted self-consistently. We then insert $C_{l\sigma} = \sum_{\mu\sigma}\phi_{\mu\sigma}(l)C_{\mu\sigma}$, and rearrange the terms, keeping in mind $\langle n_l\rangle = \Sigma'_{\mu\sigma}|\phi_{\mu\sigma}(l)|^2$ and $\langle C^{\dagger}_{l+1\sigma}C_{l\sigma}\rangle = \Sigma'_{\mu\sigma}\phi^{*}_{\mu\sigma}(l+1)\phi_{\mu\sigma}(l)$ (Σ' means the summation over all the occupied states). From here on, we use the notation that μ and i are the unoccupied and occupied one-electron states, respectively. The results of the rearrangement are rather lengthy, so we only summarize their basic results. If we call the states like $C^{\dagger}_{\mu\sigma}C_{i\sigma}|\Phi_0\rangle$ particle-hole excitations ($|\Phi_0\rangle$ is the HF ground state), they constitute a subspace of bare one-electron-excited states (see Fig. 8.7a).

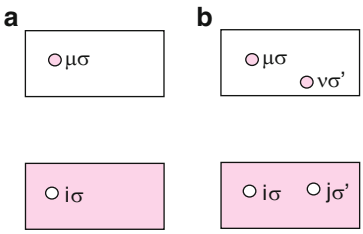

Fig. 8.7 (**a**) One-electron excited state and (**b**) two-electron excited state

Similarly, the states like $C^{\dagger}_{\mu\sigma}C_{i\sigma}C^{\dagger}_{\nu\sigma'}C_{j\sigma'}|\Phi_0\rangle$ also correspond to particle-hole excitations, but in this case two electrons are excited from the valence band to the conduction band, as shown in Fig. 8.7b. In the following calculations, we only treat the former states and diagonalize the hamiltonian within the subspace of one-electron excitations. This type of calculation is the simplest form of so-called configurational interaction (CI) calculations and is often called single CI. In this framework, the singlet excited state and the triplet excited state of $S_z = 0$ component are expressed as

$$|\Psi^S_\rho\rangle = (1/\sqrt{2})\sum_{\mu i} f^S_{\mu i}(C^{\dagger}_{\mu\uparrow}C_{i\uparrow} + C^{\dagger}_{\mu\downarrow}C_{i\downarrow})|\Phi_0\rangle \tag{8.16}$$

and

$$|\Psi^T_\rho\rangle = (1/\sqrt{2})\sum_{\mu i} f^T_{\mu i}(C^{\dagger}_{\mu\uparrow}C_{i\uparrow} - C^{\dagger}_{\mu\downarrow}C_{i\downarrow})|\Phi_0\rangle, \tag{8.17}$$

respectively. Here, the new functions, $f^S_{\mu i}$ and $f^T_{\mu i}$, are to be obtained by the following eigenvalue equation:

$$M^{(S,T)}_{\mu i,\nu j} f^{(S,T)}_\rho(\nu j) = E_\rho f^{(S,T)}_\rho(\mu i)\ , \tag{8.18}$$

where

$$\begin{aligned} M^S_{\mu i,\nu j} \equiv \delta_{\mu i,\nu j}(\varepsilon_\mu - \varepsilon_i) + \sum_l \Big(& -V\phi_\mu(l)\phi_\nu(l)\phi_i(l+1)\phi_j(l+1) - [l \leftrightarrow (l+1)] \\ & +2V\phi_\mu(l)\phi_\nu(l+1)\phi_i(l)\phi_j(l+1) + [l \leftrightarrow (l+1)] \\ & +U\phi_\mu(l)\phi_\nu(l)\phi_i(l)\phi_j(l) \Big), \end{aligned} \tag{8.19}$$

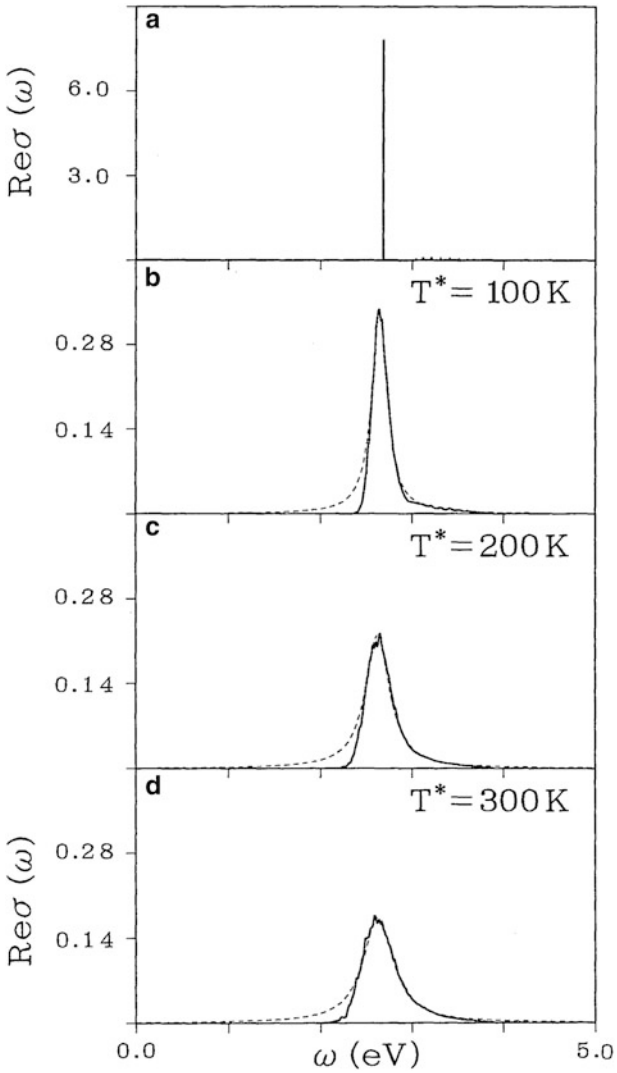

Fig. 8.8 Optical conductivity spectra without lattice fluctuation (**a**) and with lattice fluctuation (**b**–**d**). The *dotted curve* in (**b**–**d**) is a Lorentzian fitted to the high-energy side of each peak. Reprinted from Iwano and Nasu [18]

and

$$M^{T}_{\mu i,\nu j} \equiv \delta_{\mu i,\nu j}(\varepsilon_\mu - \varepsilon_i) + \sum_l \Big(-V\phi_\mu(l)\phi_\nu(l)\phi_i(l+1)\phi_j(l+1) - [l \leftrightarrow (l+1)]. \\ -U\phi_\mu(l)\phi_\nu(l)\phi_i(l)\phi_j(l) \Big). \tag{8.20}$$

Note that we assume real one-electron orbital functions to avoid any unnecessary use of complex values. Such a selection is really possible, because we only need to take the real and imaginary parts of Eq. (8.11).

Thus, we have reached a computer-friendly expression of the eigenvalue equation. The dimension of the matrix M is generally $(N/2)^2$ by definition. However, in a regular CDW case, it is reduced to $N/2$, because the states can be classified into $N/2$ groups having different momenta k. In Fig. 8.8a, we show an optical conductivity spectrum thus calculated. By the way, the parameter set is different from the previous one, but the essential features are maintained. Readers will see that the spectrum calculated by the HF approximation (the left panel of Fig. 8.6) is strongly renormalized to the new spectrum by the effect of ΔH. In particular, the intensities widely distributed in the former spectrum are now concentrated at the lowest position, accompanied by a downward shift of the absorption edge. This is nothing but an exciton effect, in which Coulombic attraction makes a pair of an electron and a hole bound to each other and forms an exciton. We usually call this downward shift of the absorption edge the binding energy of the exciton.

We are now closer to the understanding of the measurement shown in Fig. 8.6. As is seen in Fig. 8.8a, the main peak is a line spectrum, seemingly consistent with the measured one. This is deeply related to the nature of the exciton. First, the exciton has an energy band without losing a translational symmetry. We claim the mutual binding of an electron and a hole, not the binding of their center of gravity. Second, we must remember that visible or near-infra-red light has a long wave length of about several thousand Angstroms. Therefore, the exciton state that is accessible by such light is only $K \sim 0$ state (K is the momentum of its center of gravity). This restriction makes the main peak a line spectrum.

So, what happened to the free electron–hole pairs that existed before the renormalization? Obviously, a part of them have $K = 0$, and they in principle can contribute to the optical spectrum. This calculation, on the other hand, shows that their intensities, which are located at higher energies than that of the exciton peak, are almost negligible. This is a feature typical to one-dimensional systems, as reported by other authors [19, 20]. Instead of giving mathematics, we here explain it intuitively. In one-dimensional systems, an energy band has divergent density of states (DOS) at both its sides, as will be seen in Fig. 8.5c. This property enhances the renormalization, since the renormalization is accomplished gathering the states around the band edge.

Lastly, we give a final answer to this absorption-spectrum problem. While the treatment so far gives a line spectrum as the main peak of the optical conductivity, we must look for one more ingredient to make the spectrum as broad as the observation. To finish our quest, it is very important to recall that we are discussing the strong e–l system. This strong e–l interaction is one of the two factors that give the large CDW amplitude. Then, we think that this e–l interaction will also give a large fluctuation to the main peak. In Fig. 8.8b–d, we show spectra in which effects of lattice fluctuation are incorporated [18]. We here use a standard semi-classical formula as

$$k_{\mathrm{B}}T^{*} = \frac{\hbar\omega_0}{2}\coth\frac{\hbar\omega_0}{2k_{\mathrm{B}}T_{\mathrm{R}}}\ , \tag{8.21}$$

where T_{R}, T^*, and ω are a real temperature, an effective temperature, and the frequency of the relevant phonon mode, respectively. In these calculations, T^* is assumed to be several typical temperatures and we perform averaging over fluctuations by using a classical Monte-Carlo simulation. Note that T^* of 200 K almost corresponds to the real zero temperature case, because ω_0 of PtCl as that of the halogen symmetric stretching is about 38 meV. As a result of this treatment, we see that the observed main peak, which we described as an asymmetric Lorentzian, is reproduced satisfactorily including the spectral shape, and our first question about the nature of the CDW absorption spectrum is now answered as "Yes, it's an exciton!"

In the rest of this subsection, we mention some further works in this course. We already pointed out that only $K \sim 0$ states are accessible by visible or near-IR light. Even within this restriction, we can find out variety in the excited states. The point is that we sometimes have more than one exciton band. We usually call them the first exciton, the second exciton, the third exciton, and so on, in the increasing order of energies. The main peak we have discussed corresponds to the first exciton, and it has the odd parity with respect to the spatial inversion symmetry. As for the second and third excitons, if they exist, they have the even and odd parity, respectively. What is interesting is that we can detect the second exciton, which is usually optically forbidden, by applying a dc-electric field. This idea was also tried and confirmed both experimentally and theoretically [21, 22]. Furthermore, in a more general context, such an experiment belongs to nonlinear optics where more than one photon is involved in a optical process, because a dc-electric field can also be regarded as a photon with zero frequency. Extending the idea in this context, we also expect another nonlinear optical effect, for example, a third-harmonic generation, which was also confirmed by both a theory and an experiment [22, 23].

8.2.3 Soliton and Polaron

In this subsection, we discuss so-called nonlinear excitations such as a soliton and a polaron. Readers may be familiar with the polaron, a hole, or electron carrier moving with a phonon cloud around it, which is a rather popular concept in the solid-state physics. Even in the theory of MX-chains, polarons have the same meaning, while it is heavily renormalized with the strong e–l interaction that we have already mentioned. The solitons, on the other hand, have unique natures, which directly reflect the twofold degeneracy in the CDW ground states.

In Fig. 8.9, we illustrate possible nonlinear excitations inherent in this system, including one of the two CDW ground states (topmost panel) and its exciton state (below the CDW panel). All these nonlinear excitations or the paired states of them are thought to be possible to be created by photoexcitation. Let us start from the

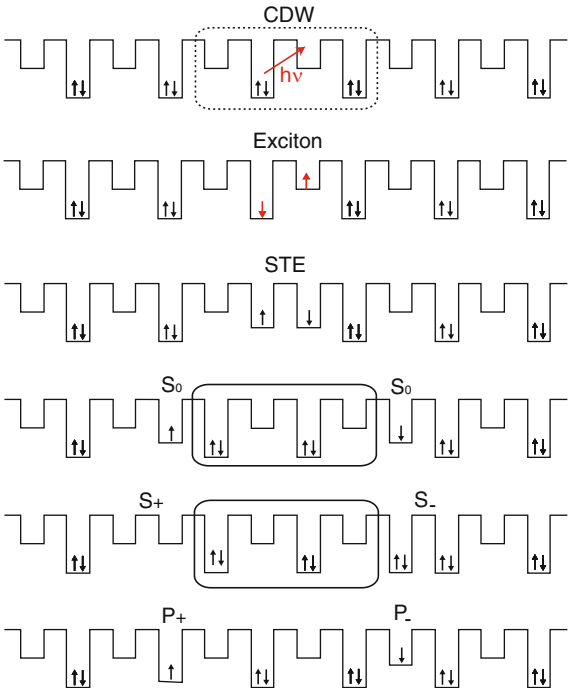

Fig. 8.9 Electron configurations of various states. The abbreviations of STE, S_0, $S_\pm$, and $P_\pm$ are a self-trapped exciton, a neutral soliton, a positively or negatively charged soliton, and a positively or negatively charged polaron, respectively

CDW state in the top panel. Shining light will excite one electron from the deep well (M^{2+} site) to the shallow well (M^{4+} site). As we have already discussed in detail, the exciton state is a bound electron–hole pair. In this case, the exciton resides at the two neighboring M sites as shown in the "Exciton" panel. We here emphasize that the localized position of the exciton, namely, the position at a particular pair of metals, i.e., $M^{4+}M^{2+}$, is just for convenience in drawing the figure. The exact form of the exciton must obey the translational symmetry and the spatial inversion symmetry (the inversion center is located at either the M^{2+} site or the M^{4+} site).

Following this excitation, we expect a self trapping of the exciton, that is, the localization of the center of gravity of the exciton. Of course, this cannot occur solely within the electronic degrees of freedom. We rather expect that a partial melting of the halogen-dimerized pattern will cause such localization. In a sense, this is very natural because the exciton, which is nothing but $M^{3+}M^{3+}$, prefers such a lattice deformation, as is so in the Mott-insulator state. This state is usually called a self-trapped exciton and abbreviated as "STE" (see the corresponding panel of Fig. 8.9). From the exciton to the STE, the elevation of the M^{2+} level and the dropping of the M^{4+} level occur, as shown in the top panel of Fig. 8.10.

If we proceed with this process by one more step, we will expect a complete inversion of the lattice pattern in this local area and a simultaneous electron transition following this lattice movements, as is shown in the third panel of Fig. 8.10. Furthermore, we continue the process as described in the third and fourth

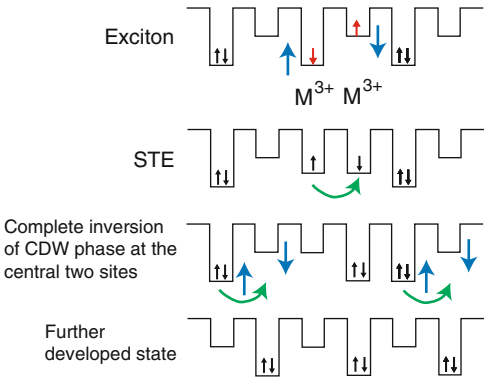

Fig. 8.10 Process to yield a soliton pair from the STE. The *blue vertical arrows* specify the directions of the potential (lattice) changes. The *green arrows* mean the supposed electron transitions

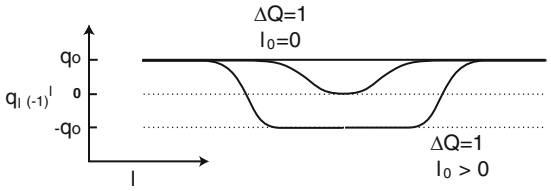

Fig. 8.11 Staggered lattice displacements leading to the inversion of the CDW phase

panels, and obtain an enlarged region of the inverted phase. Now, if the readers compare this fourth panel and that denoted by "S_+S_-" in Fig. 8.9, we notice that we have made the same state. This is nothing but a soliton state, and in this case we have made a pair of "charged solitons." On the other hand, we also think about a similar but slightly different state as denoted by "S_0S_0," which is called a pair of neutral solitons. Leaving the explanation why they are charged or neutral, we proceed with our gedanken experiment. In the case of polarons, we think that an electron and a hole in an exciton or in an STE will separate to each other. The isolated electron and hole thus formed deform the lattice around themselves, but no more invert the CDW state. As a more likely process, a free electron–hole pair will also yield the polarons independently. In any case, we expect a polaron pair, P^+P^-, as depicted in Fig. 8.9 (bottom panel).

From here on, we introduce a calculated result to demonstrate the validity of the above idea [24]. In this calculation, we trace the ground and excited states based on the following lattice configurations:

$$q_l = q_0(-1)^l \left[1 + \Delta Q \left(\tanh \left(\frac{|l - l_c| - \frac{l_0}{2}}{w} \right) - 1 \right) \right], \tag{8.22}$$

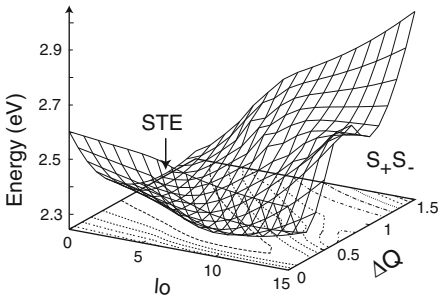

Fig. 8.12 Adiabatic potential surface of the first singlet excited state. Reprinted from Iwano [24]

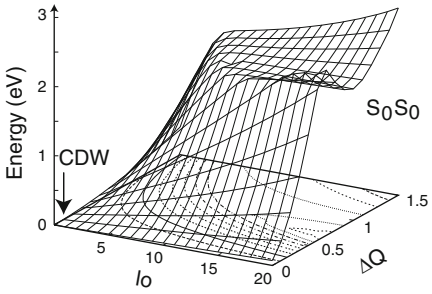

Fig. 8.13 Adiabatic potential surface of the ground state (singlet). Reprinted from Iwano [24]

two typical patterns of which are illustrated in Fig. 8.11. As is seen in the figure, these patterns continuously connect a local deformation like the STE and a kink-anti-kink structure with an inverted region in between as the structures of the solitons. Regarding the calculation method of the electronic states, we perform almost the same type of calculation that we introduced in the previous subsection, namely, the HF calculation for the ground state and the single-CI calculation for the excited states, although the lattice configuration is fixed and not optimized in this case. Using the same parameter set as that in the previous sections, namely, $(U, V, S, t_0) = (2.0, 1.2, 0.27, 1.3)$, in Figs. 8.12 and 8.13 we show adiabatic potential surfaces as functions of the degree of deformation, ΔQ, and the soliton–soliton distance, l_0. The amplitude of the regular dimerization, q_0, is of course determined beforehand. The width of each soliton, w, is optimized at each point of $(\Delta Q, l_0)$. Looking at Fig. 8.12, we now judge that the energy of the charged soliton pair is higher than that the STE in this parameter set. Moreover, inspecting both the two surfaces, we find that the STE is located higher than the neutral soliton pair. These features are understood within a general trend [24], although we do not enter into the details here. The cross section at $\Delta Q = 1.0$ in the next figure is placed to make these features more transparent.

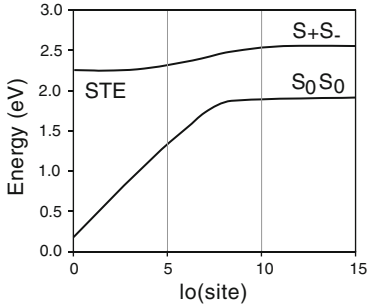

Fig. 8.14 Cross section of the two singlet potential surfaces at $\Delta Q = 1.0$. Reprinted from Iwano [24]

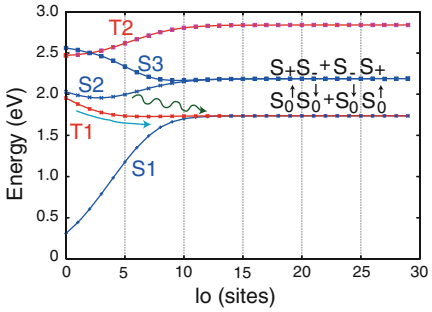

Fig. 8.15 Cross section of the adiabatic potential surfaces calculated by the DMRG calculation. $S1$, $S2$, and $S3$ are the first three excited states, while $T1$ and $T2$ are the first two triplet states

The readers might ask why we can distinguish the two types of solitons. Even within this calculation, it is possible by inspecting the electronic density distribution in each state. Meanwhile, it is much clearer if we try a more advanced calculation, that is, a DMRG calculation (K. Iwano, unpublished). In this method, we can maintain the spin and spatial inversion symmetry almost perfectly, while in the previous method the symmetries are not generally maintained except for some cases like the regular CDW. The DMRG method enables us to separate singlet and triplet states accurately, by which we are able to distinguish the soliton states. In fact, we observe the degeneracy between $S1$ and $T1$ for a large l_0, which clearly indicates that these are neutral solitons. As will be understood from Fig. 8.9, the neutral soliton has an unpaired spin, a pair of it having singlet and triplet states. It is natural that they degenerate for a large soliton–soliton distance, since the effective exchange coupling between them vanishes in the limit of a large distance. Meanwhile, we also notice a degeneracy between the $S2$ and $S3$ states. It is then naturally interpreted as a charged-soliton pair, since a pair of it has the two choices of S_+S_- and S_-S_+.

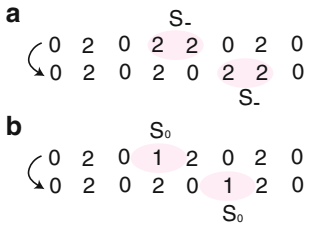

Fig. 8.16 Illustration to explain how to count soliton charges. (**a**) A charged soliton case and (**b**) a neutral soliton case. The numbers are the electron occupancies at each metal site

Finally, we discuss possible processes expected from these results of the adiabatic potential surfaces. Looking at Fig. 8.14 or Fig. 8.15, we judge that the charged soliton pair is unlikely to be formed using the same path as that the STE follows, since the former has a higher energy than the latter, as is already mentioned. Such a situation does not support the idea of a short life time of the STE due to the charged solitons. Of course we cannot completely exclude another possibility that the energy of the charged-soliton pair is lower than that of the STE. However, in our opinion, it is against a relatively large U value that is naturally deduced from a large V value. Here, it is emphasized that we need the latter to have the strong exciton effect. In turn, what about the possibility of forming the neutral solitons? We think that it has plenty of chances. We here mention two scenarios. One is the path within the singlet channel. In this case, it is a nonadiabatic transition from $S2$ to $S1$, as indicated by the wavy like in Fig. 8.15. Although a realistic calculation has not been performed yet, a prototype calculation predicts that appropriate inclusion of phonon modes will enhance the transition probability up to a realistic value, for example, several 10 ps as a life time of the STE [25]. The other scenario is based on a singlet–triplet conversion. Actually, Fig. 8.15 shows a downhill course on the $T1$ surface from the STE to the neutral-soliton pair. In this case, we need a sufficiently large singlet–triplet conversion rate and it is not unrealistic because Pt is a heavy atom.

In the rest of this subsection, we discuss the charge-spin property of a soliton. The soliton has its own charge and spin even though it is a composite particle made of several electrons. Regarding the spin, it will be easier to see. Just looking at Fig. 8.9 once more, we immediately notice an unpaired spin at each site of S_0. We therefore state in confidence that the neutral solitons have a spin 1/2. Similarly, we see that all the spins are paired in $S_{\pm}$, and so the charged solitons have no spin degree of freedom.

On the other hand, the charge will be difficult to imagine, because we have undulation of charge density in the background. We hence use the method to count the charge as described in Fig. 8.16. Namely, we calculate the change in the electric dipole moment before and after the movement of the soliton. For example, in the case of the charged soliton, we shift the soliton by one unit cell, i.e., $2a$, as in Fig. 8.16a (a is the distance between the neighboring metal ions). If we define the soliton charge as $Q_{S\_}$, the change in the dipole moment is $2aQ_{S\_}$. This should be

Table 8.1 Charge and spin of the three types of solitons

Type	Charge	Spin
$S_{\pm}$	$\mp e$	0
S_0	0	1/2

e is the charge of the electron

equal to the same value counted by the electrons, that is, $2ae$, where e is the charge of the electron. Just equating these two values, we evaluate $Q_{S-} = e$. Repeating the same procedure for the other solitons, we also find $Q_{S_+} = -e$ and $Q_{S_0} = 0$ (Fig. 8.16b). Although the above counting is done in the localized limit, we can perform the same type of counting in the itinerant case using real densities, and confirm the same conclusion (see the summary in Table 8.1).

8.3 Mott-Insulator (M = Ni) Systems

8.3.1 Ground State

The theory of the Ni system has a large overlap with that of the one-dimensional Hubbard or extended-Hubbard model. This means that we can borrow so much knowledge that was stored so far. The most important factor governing the ground state is the existence of large U. This excludes most of double or empty occupancy, leading to a single occupancy state like that in Fig. 8.1 (the Mott-insulator state). This state is really an insulator, which is confirmed by the existence of an optical gap, the absence of Drude weight in other words, which will be mentioned in the next subsection. Regarding the charge gap, it is also opened. This corresponds to the gap observed by photoemission, although we do not discuss it in this article.

Magnetic properties are more important in their ground state. As is well known, the antiferromagnetic correlation as shown in Fig. 8.1 is not of a long-range order but with a power decay, and there is no spin gap in this type of systems. Moreover, since they are one-dimensional, the magnetic excitations are described as a pair creation of spinons, instead of one magnon [26]. As a spin system, this can be described by a Heisenberg model with an appropriate value of the exchange coupling, J. We point out that we need no other term that destroys the isotropy of spin directions. The coupling J is approximated by the relationship with the parameters of the Hubbard or the extended Hubbard model, as $J = 4t_0^2/U$ and $J = 4t_0^2/(U - V)$, respectively, using the second-order perturbational theory, while it is much more complicated in the case of the dp model. The evaluation of the J value is most easily done by the comparison of the temperature dependence of susceptibility. In the theory, the same quantity is known to obey a Bonner–Fischer curve that has a broad maximum around a temperature corresponding to the J value [27]. However, it will be more accurate to estimate it from the dispersions of magnetic excitations based on a neutron scattering experiment. Such an experiment

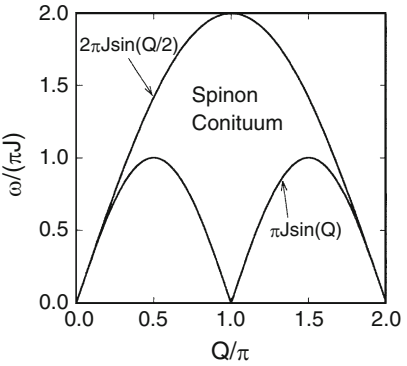

Fig. 8.17 Excitation spectrum of two spinon excitations

is now in progress at J-PARC. In Fig. 8.17, we sketch a simple expectation for the magnetic excitations.

8.3.2 Optical Properties

The optical conductivity spectrum of the Ni system was first observed by Okamoto et al. [28]. It consisted of a dominant sharp main peak, which suggested the role of the exciton effect. We already discussed the exciton effect in the CDW system. Although the simple treatment in the previous section cannot be applied, the physical meaning is not essentially different even in this strongly correlated system. By the way, we were not so surprised by this exciton-like feature from the analogy to the Pt system, of which the spectrum had been known to have the same feature. What rather attracted our attention was a long tail extending to higher energies. Because we lacked enough knowledge about the optical properties of strongly correlated systems at that time, there was no clear answer to that.

Before this finding, the spectra in other strongly correlated systems had been obtained. For instance, those of undoped cuprates, which were also Mott insulators, were known at that time. Their features were that they had no features, although this might sound paradoxical. In fact, their spectral shapes were broad band-like ones and simply interpreted to originate from its two-dimensional nature, namely, a relatively weak e–h binding.

In 2000, Jeckelmann calculated the optical conductivity spectrum of the one-dimensional Hubbard model for the first time [29]. While his model was not the extended Hubbard model, the long-tail feature was reproduced clearly. His method was based on a dynamical DMRG (DDMRG) and this became the first study that demonstrated the power of this method. According to this calculation, the above-mentioned long tail is mainly due to an unique type of dispersion of a doublon–holon pair. As is explained in detail below, a doublon and a holon correspond to the electron and the hole, respectively, in band insulators including the CDW insulator. In this sense, multielectron excitations that occur near the

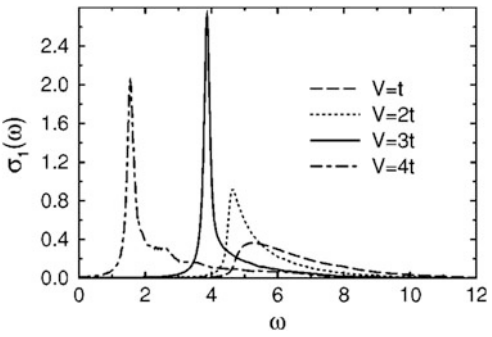

Fig. 8.18 Spectra calculated by DDMRG for the extended Hubbard model with $U = 8t$. t is the same as t_0. Reprinted figure with permission from Jeckelmann [30]. Copyright (2003) by the American Physical Society

CDW–Mott-insulator boundary, which we will mention at the end of this chapter, do not occur here.

Next, we proceed to the case in the presence of the nearest-neighbor repulsion, which is indispensable for the consideration of the Ni compounds. Detailed calculations over various combinations of U and V are performed for the extended Hubbard model [30] and the dp model [31]. These calculations, which are also based on the DDMRG method, reproduce the feature seen in the Ni compounds, namely, the sharpness of the main peak and its long tail on the higher-energy side, as shown in Fig. 8.18 (particularly the graph of $V = 3$).

Here, we instead introduce a very simple model, i.e., a so-called doublon–holon model [32, 33], as

$$H_{d-h} = -t_0 \sum_l (d_{l+1}^\dagger d_l + \text{h.c.}) - t_0 \sum_l (h_{l+1}^\dagger h_l + \text{h.c.}) + V \sum_l n_l^{(d)} n_{l+1}^{(h)}, \quad (8.23)$$

where d_l and h_l are the doublon and holon operators, respectively, and $n_l^{(d)}$ and $n_l^{(h)}$ are their number operators. Note that d_l is not the operator of the d electron. This model is regarded as an effective model of the extended Hubbard model with the infinite U, in the following meaning.

First of all, the ground states are the states of single occupancy in this limit, as we have already mentioned. Furthermore, the spin states heavily degenerate because of the vanishing J value. In other words, any spin configuration satisfying an assigned value of the total S_z can be a ground state. In Fig. 8.19a, we assume one spin configuration. Here, we no more assume the antiferromagnetic spin configuration. The doublon and the holon are then the states with one electron added or removed, as illustrated in Fig. 8.19b, c, and their pair state is also shown in Fig. 8.19d. Here, it will be better to give the present definition of each state. The ground state is expressed as $|g\rangle \equiv C_{1\uparrow}^\dagger C_{5\uparrow}^\dagger C_{6\uparrow}^\dagger C_{7\uparrow}^\dagger C_{2\downarrow}^\dagger C_{3\downarrow}^\dagger C_{4\downarrow}^\dagger C_{8\downarrow}^\dagger |0\rangle$, corresponding to Fig. 8.19a, in our "up–down" definition. Note that the spin-up operators come before the down ones. Let us think about the movement of the holon first. To move it by one unit to the right, we just transfer the up-spin electron at the right n. n. site to this site. Since there is no need for the sign change, it gives a matrix element $-t_0$ as appearing in

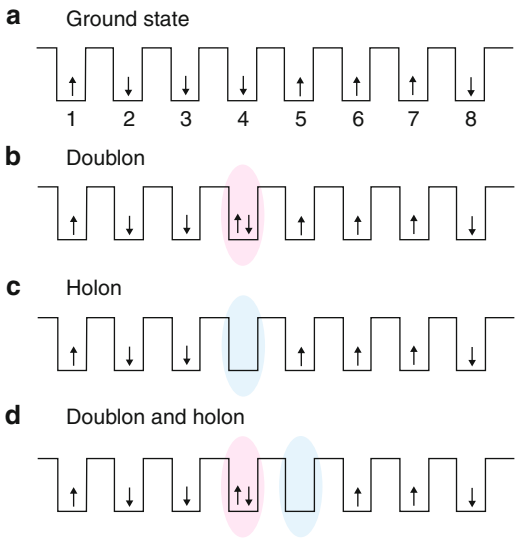

Fig. 8.19 Pictures for (**a**) a ground state, (**b**) a doublon state, (**c**) a holon state, and (**d**) a doublon–holon pair state

Eq. (8.22). In the case of the doublon, on the other hand, the movement by one unit to the right needs the transfer of the down electron at this site to the right n. n. site. Since our definition again needs no sign change, this also gives $-t_0$. As a special point of this model, the doublon and the hole never occupy the same site, because the same occupation returns back the state to the ground state. We hence exclude such N states to obtain the total $N(N-1)$ states.

At a glance, this model will give an impression that the picture is too simple, because the particle motion inevitably rearranges the spin configuration in the background. Furthermore, the frozen spin configurations would need some assumption for averaging if we treat them independently. Meanwhile, this hamiltonian exactly describes the charge part of the factorized eigenstate, which justifies our analyses from here on [32].

The analytical treatment of this model is easy when we use a PBC and consider a state with a total momentum, K, assuming the expression of

$$|\phi\rangle \equiv \left(1\Big/\sqrt{N}\right)\sum_l \mathrm{e}^{iKl}\sum_j h_l^\dagger d_{l+j}^\dagger \phi(j)|0\rangle \ . \tag{8.24}$$

By this analysis, it is found that (1) the exciton is formed when V is larger than $2t_0$. This threshold value of V presents a sharp contrast to ordinary one-dimensional cases, where infinitesimally small attraction forms a binding. The eigenstates of $K = 0$ and the associated optical conductivity spectrum are obtained as in Fig. 8.20a. What attracts our attention most will be (2) the degeneracy between the lowest exciton and the second lowest exciton. This feature is also unique to this system, because the ordinary 1D systems never show such feature except for a case

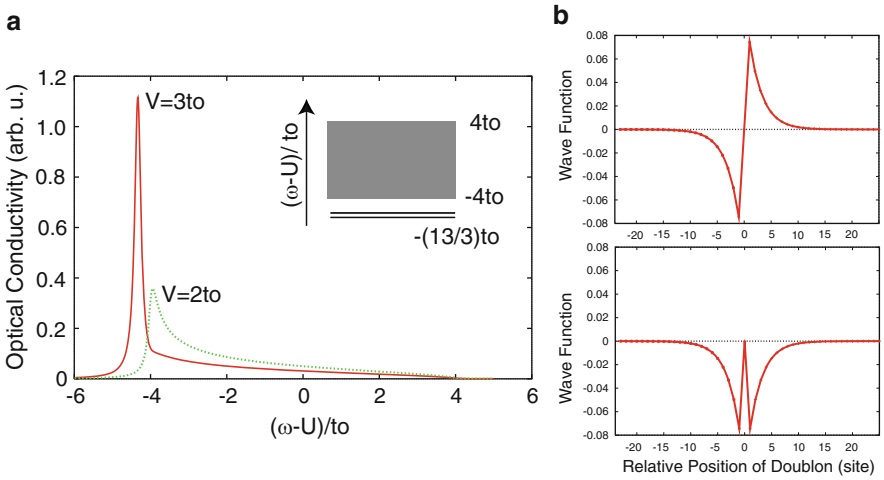

Fig. 8.20 (**a**) Spectra calculated by the doublon–holon model. Inset: Schematic energy diagram for $V = 3t_0$. The lowest two discrete levels are almost degenerate. In the figure, their splitting is exaggerated. (**b**) Two wave functions of the lowest two levels. The values as a function of the doublon position relative to that of the holon are plotted

of extremely large attraction. These marked features, (1) and (2), are well understood by the "semi-infiniteness" of this model. Namely, as we have already defined, the doublon and the holon do not occupy the same site. Moreover, we neglect the probability of the position exchange between them, because such transition occurs via the ground state and the probability is reduced by a factor comparable to $1/U$. Exactly speaking, a PBC, by which the system becomes a ring, makes the exchange possible. However, such effect is negligible when we consider a sufficiently large system size. In any way, the substantial inhibition of the doublon-hole exchange separate all the states into two spaces; the doublon is on the left-hand side of the holon, and vice versa. This situation enables us to consider the problem independently in each space. If we focus on the relative coordinate of the two particles, this situation corresponds to a semi-infinite system, in the sense of considering only a positive or negative region of the coordinate. It is well known that the semi-infinite system has a critical value of the attraction for the bound state formation, and this also applies for our problem. The energy degeneracy between the two lowest excitons is understood naturally in this context [33, 34], as illustrated in Fig. 8.20b. Regarding the spectral shape, the similarity between the spectra in Fig. 8.19 and those obtained using a full hamiltonian in Fig. 8.18 tells us the usefulness of this doublon-hole model in spite of its simpleness.

In the rest of this section, we discuss another aspect of the optical conductivity spectrum in the Ni compounds. The point is the sharpness of the main peak. As has been already discussed, this sharpness is nothing but an exciton effect, and, in this sense, it is not surprising. However, even in the Mott insulators, there must be e–l interaction to some degree, and, therefore, we must expect a certain amount of line

broadening. The actual peak width, on the other hand, is very small, for example, as small as 7 meV in $[Ni(chxn)_2Br]Br_2$ [35]. This value presents a sharp contrast to that in PtCl, which is approximately 300 meV. Although such a small width would suggest an almost zero e–l interaction, we do not agree with that idea, since the Ni compounds are also ionic crystals accompanied by relatively strong or intermediate Coulombic interaction.

To solve this paradox, let us think about another doublon–holon model [36], which is extended to include the e–l interaction:

$$H_{d-h-l} = -t_0 \sum_l (d_{l+1}^\dagger d_l + \text{h.c.}) - t_0 \sum_l (h_{l+1}^\dagger h_l + \text{h.c.}) + V \sum_l n_l^{(d)} n_{l+1}^{(h)} - S \sum_l (q_{l+1} - q_l)(n_l^{(d)} - n_l^{(h)}) + S2 \sum_l q_l^2, \tag{8.25}$$

where the newly added terms, the fourth and fifth terms, describe the doublon/holon–lattice interactions and the elastic energy, respectively. Of course, this form of interactions between the doublon/holon and the lattice are directly related to the original form of the e–l interaction. In the following, we discuss the case of one doublon for simplicity, because it is essentially the same even in the doublon–holon case. In the former case, the hamiltonian is reduced to a simpler form as

$$H_{d-l} = -t_0 \sum_l (d_{l+1}^\dagger d_l + \text{h.c.}) - S \sum_l (q_{l+1} - q_l) n_l^{(d)} + \frac{S}{2} \sum_l q_l^2. \tag{8.26}$$

In a sense, this is a very simple problem that includes only one particle and a classical lattice. At a glance, this looks similar to a popular model called the Holstein model [37, 38], which will be expressed as

$$H_{\text{Hols}} = -t_0 \sum_l (d_{l+1}^\dagger d_l + \text{h.c.}) - S \sum_l q_l n_l^{(d)} + \frac{S}{2} \sum_l q_l^2. \tag{8.27}$$

For the Holstein model, it well known that even infinitesimally weak interaction, S, makes a binding state, namely, the so-called polaron in one-dimensional systems. Meanwhile, in the model of H_{d-l}, a simple analysis of lattice optimization in the presence of one doublon reveals that there is a critical value to form a bound state. Although this fact seems to be against the "common sense" that there always exists a bound state in one-dimensional systems, the mechanism is easily understood by converting the model into its momentum representation:

$$H_{d-l} = -2t_0 \sum_k \cos(k) d_k^\dagger d_k + \sum_{k,p} g(p) d_{k+p}^\dagger d_k q_p + \frac{S}{2} \sum_p |q_p|^2, \tag{8.28}$$

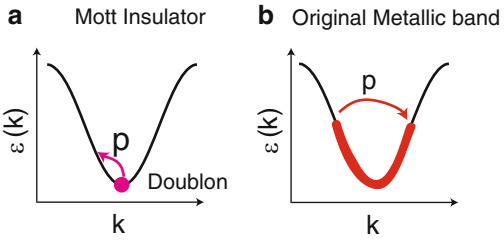

Fig. 8.21 (**a**) Electron–lattice interaction in the one-body problem of the doublon in the Mott insulator. (**b**) Same interaction in the original metallic band

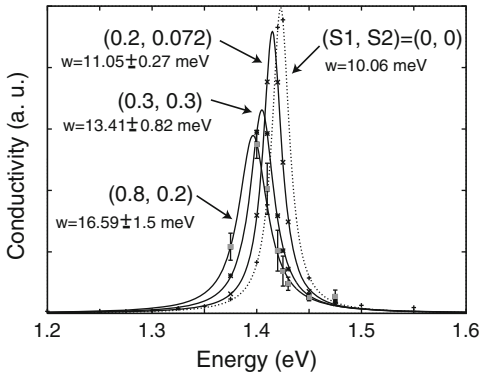

Fig. 8.22 Calculated spectra for the *dp* model. The curve of $(S_1, S_2) = (0.2, 0.072)$ corresponds to the NiBr case. Reprinted from Iwano [39]. Copyright (2006) by the American Physical Society

where d_k and q_p are the Fourier component of the doublon and the lattice, respectively. What is important is the functional form of the coupling function $g(p)$. In the Holstein model, it is constant leading to the efficient formation of the polaron. On the other hand, the function in $H_{d\text{–}l}$ has a functional form of $g(p) \propto 2S\sin(p/2)$. This means the suppression of the polaron formation that uses the components of $p \sim 0$, as illustrated in Fig. 8.21a. By the way, the polaron in the CDW insulator is formed mainly by the components around $p = \pi$. This is directly related to the fact that the wave vector of the CDW is π, which is the nesting vector of the original metallic band as shown in Fig. 8.21b. The polaron formation then occurs efficiently using this functional form. In contrast, the e–l interaction that a doublon or a holon feels is suppressed nontrivially, and this also holds for a doublon-hole pair. Calculations based on the full hamiltonian that incorporates the e–l interaction also support this idea. For example, a vanishing Raman Stokes shift [36] and a very small peak line broadening as small as 2 meV for realistic parameter values [39] are found in those calculations. The very sharp peak observed in the optical conductivity spectrum is thus concluded to be a manifestation of this effect. In Fig. 8.22, we show the spectra

calculated for the *dp* model. The appropriate parameter set $(S_1, S_2) = (0.2, 0.072)$ gives the effective width of 2 meV.

8.3.3 Photoinduced Metallic States

As was first demonstrated by Iwai et al., strong photoirradiation on these materials can convert them into a type of metallic states [40]. As has been discussed already, one-photon absorbed states are well described as a bound or unbound doublon–holon pair. Then, the next question is about the nature of the strongly excited states. In more detail, weak or intermediate excitation also causes some photoinduced effect, which is characterized as a photoinduced absorption within the gap region. However, this is not a so-called Drude peak, which is usually centered at $\omega = 0$, being a clear marker of the metallic state. We therefore know that there is some threshold for the formation of this metallic state in these compounds. This makes a contrast to the carrier-number dependency known for the one-dimensional Hubbard model, in which the singularity exists only at the half filling.

To understand this discrepancy, one key is the existence of the e–l interactions. There is a possibility that the e–l interactions exist to some extent and work as an inhibitor to the metallic state. However, as we have already discussed, the e–l interaction that works between the halogen stretching and the metal d_{z^2} orbital is suppressed effectively in the limit of low carrier density. Much more detailed analyses about the time scales of polaron formations, actual associated modes, and the excitation-density dependency will be necessary for better understanding.

Another key will be the result by Takahashi et al., which traced numerically the real-time evolution of photoexcited states within the Hubbard model [41]. Their results show some critical intensity of photoexcitation realizing the metallization and seems to be consistent with the observation. This result is therefore attractive, since it suggests a different situation in the photoexcited states from the doped cases, more specifically, a trend that the nature of the excited state is changed drastically beyond a certain amount of excitations. Unfortunately, the numerical calculation is limited to a small system size and does not allow a definite conclusion. A proof based on analytical treatments will be further required to finish this argument.

8.4 Bridging CDW and Mott Insulators

So far, we have argued the properties of the CDW insulator and the Mott insulator from each side, although we already discussed them from the universal point of view, i.e., the phase diagram. The phase diagram describes a phase transition between the two phases. In this sense, we implicitly expect a conversion between

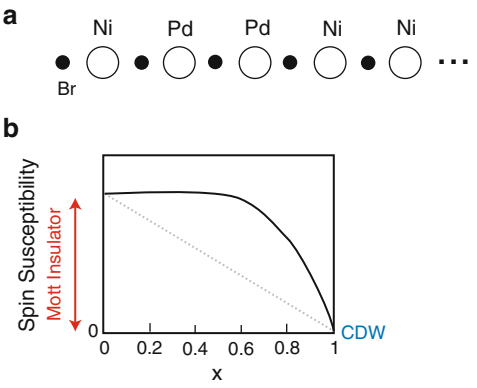

Fig. 8.23 (**a**) Example of a Pd–Ni mixed-metal chain segment. (**b**) Schematically drawn spin susceptibility as a function of x (*solid line*). The *dotted line* is the hypothetical linear behavior. *Vertical arrow* specifies the value in the pure Ni case, namely, that of the Mott insulator

the two phases by the adjustments of model parameters via the control of environmental conditions such as temperature and pressure. However, in the Pt and Ni compounds, they are deep inside each phase space, being very difficult to have any relationship with the other phase. Here comes the Pd complex. It is always a CDW insulator, except for the compound synthesized very recently, which shows a CDW–Mott-insulator at a certain temperature [42]. Although most of the Pd compounds are genuine CDW insulators, they have smaller CDW gaps, for example, 0.7 eV for $[Pd(chxn)_2Br]Br_2$ [43]. This small gap energy tells us that this material is close to the phase boundary and therefore has the potential to cause a phase transition, being a "bridge" between the two phases.

8.4.1 Pd and Ni Mixed-Metal Systems

We start from the beginning of this story, that is, the synthesis of Pd/Ni mixed-metal compounds. Regarding the details of this synthesis, we recommend the readers to read the experimental section of this book. We here only mention three important facts, that are, the behaviors of spin susceptibilities [44], and IR and Raman signals [45]. Before those, we make the meaning of the mixed metal clear. The metal sites are confirmed experimentally to be occupied by the Ni and Pd atoms replacing each other randomly (see Fig. 8.23a), that is, no interstitial site at all, which finding made a theoretical analysis simpler because we only need to use site-dependent parameter values. Returning back to the experimental facts, the magnitude of the spin susceptibility was found to be not linear as a function of the mixing degree x as expressed as $Ni_{1-x}Pd_x(chxn)_2Br_3$. As we have already seen, the CDW, in which all the sites are doubly occupied, is nonmagnetic, while the Mott insulator has many active spins and has a finite magnitude of susceptibility. If the selection of the states occurred independently at each site, the x-dependency would be linear, but it is not this case. Moreover, its functional form schematically drawn in Fig. 8.23b shows that even at 20% of Ni inclusion ($x = 0.2$) yields appreciable intensity of

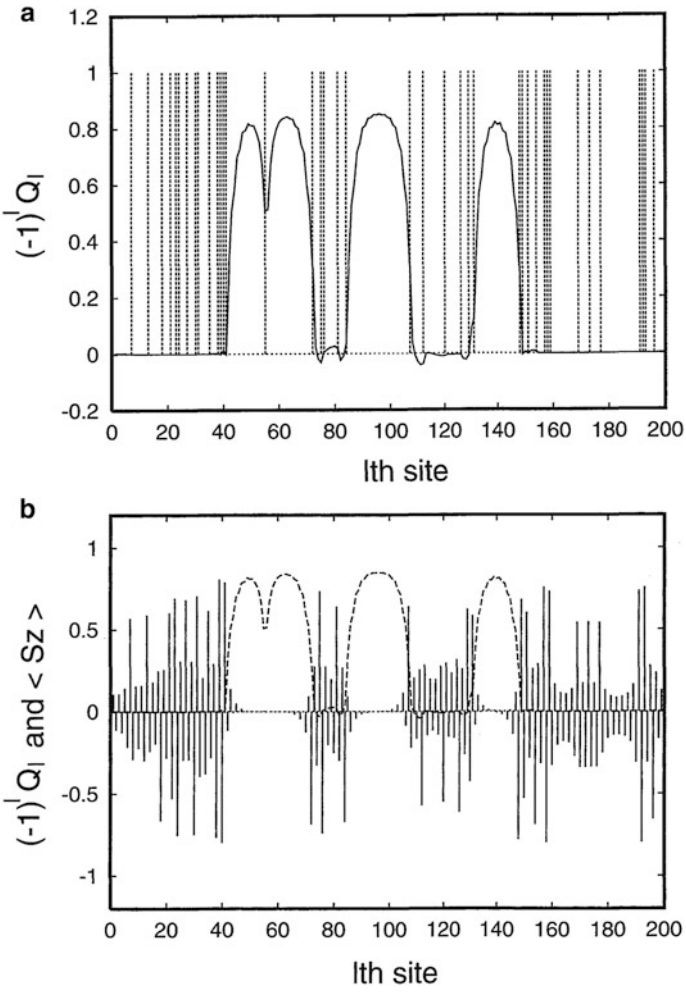

Fig. 8.24 Result of a simulation for the 20%-Ni concentration case. (**a**) Alternate component of the lattice (amplitude of dimerization) with the Ni-site positions depicted by the *vertical lines*. (**b**) Spin density distribution (*solid line*) also with the alternate lattice component (*dotted line*). Reprinted from Iwano [46]

susceptibility, suggesting that the substantial region of the system is converted into the Mott insulator even at this small mixing rate. Similarly, the other two observables also suggest the formation of the Mott-insulator state at lower Ni concentration than we expect from the linear behavior. More specifically, the IR signal detects the charge densities at the metal sites, while the Raman signal detects the dimerization of the halogen sublattice, both being indispensable in identifying the CDW.

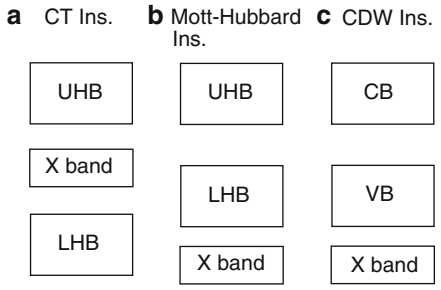

Fig. 8.25 Three type of insulators. In (**a**) and (**b**), UHB and LHB mean the lower and upper Hubbard bands, respectively. In (**c**), CB and VB are the conduction and valence bands of the CDW, respectively. All these bands consist of the metal d_{z^2} orbitals. The X band common to the three figures is the halogen p_z band

Upon these experimental findings, a theoretical calculation was performed within the HF framework [46]. In Fig. 8.24, we show one result of the simulation, in which 20%-Ni concentration is assumed in a 200-site system. In this calculation, the effects of metal mixing are incorporated by changing the site energy and the on-site repulsion energy from site to site. With this Ni distribution specified by the vertical dotted lines in Fig. 8.24a, we notice that some regions become a Mott-insulator state even involving a finite number of Pd sites. For example, the region from the 150th to 200th sites loses lattice dimerizations as shown in Fig. 8.24a, and simultaneously finite amplitude of spin density appears (Fig. 8.24b), in spite of relatively large number of Pd sites in it. At that time, it was interpreted as a kind of proximity effect, namely, that the Pd sites were involved in the Mott-insulator state forcibly by the Ni sites nearby. As another example, the cases with 50% Ni concentrations were also investigated to find that the most stable states were always Mott insulators with inhomogeneous spin densities in accordance with the Pd inclusion, which finding was consistent with the experimental tendency.

8.4.2 Pd Compound as a Mott–Hubbard Insulator

We now proceed our discussion about the metal mixing further to the next point. Although we have not made it clear so far, there are two types of Mott-insulator states. One is the CT insulator, while the other is the Mott–Hubbard insulator. The Ni compound belongs to the former category [47]. In Fig. 8.25, we show the three type of the insulators, adding the CDW insulator to the two Mott insulators. Regarding the ground state properties, the two Mott insulators are not so different. Meanwhile, the excited states have an important difference; the lowest-energy optical transition is the CT transfer from the halogen to the metal in the CT insulator, while it is the metal–metal transition from the lower Hubbard band (LHB) to the upper Hubbard band (UHB) in the Mott–Hubbard insulator. Since the pure Pd compound, $[Pd(chxn)_2Br]Br_2$ (hereafter PdBr), as one of the CDW insulators has the band scheme of Fig. 8.25c, it is natural to expect a band scheme as

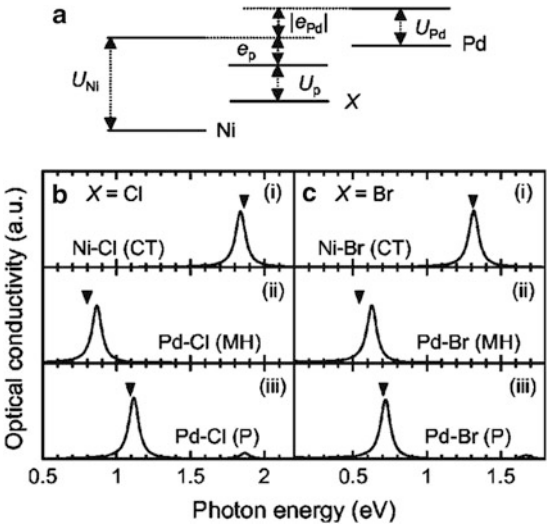

Fig. 8.26 (**a**) Level scheme and the parameters of the *dp* model. (**b**) Obtained optical conductivity spectra for X = Cl. (**c**) Same as (**b**), but for X = Br. Reprinted from Matsuzaki et al. [9]. Copyright (2004) by the American Physical Society

Fig. 8.25b for PdBr as a Mott insulator. According to this expectation, the measurements of optical conductivity spectra over the values of x from 0 to 1 were interpreted in the following way. Namely, the peak energy, which stays at approximately 1.2 eV for $x = 0 \sim 0.3$, makes a quick downward shift from $x = 0.3$ to 0.4, and stays at 0.7 eV for $x = 0.4 \sim 0.8$ [9]. Since, from the data of spin susceptibility, we already know that the compound is more or less in the Mott-insulator ground state, it was interpreted that these two Mott-insulator regions correspond to the CT insulator of Ni ($x = 0 \sim 0.3$) and the Mott–Hubbard insulator of Pd ($x = 0.4 \sim 0.8$). However, of course we have randomness from the metal mixing, and hence a support from the theoretical side was also required.

Here, we recall the hamiltonian H_{dp} in Eq. (8.3). Using this hamiltonian, which includes both the metal d_{z^2} and halogen p_z orbitals, we can treat the above three insulator states appearing in Fig. 8.25 from a unified point of view. Among the various terms in this hamiltonian, the readers may have a question about the e–l coupling here. This coupling is indeed included in the second and fifth terms via the site-dependent factors of $e(l) = e_p - 2\alpha(Q_{l+1} - Q_{l-1})$ for odd l (halogen site) and $e(l) = e_M + \alpha(Q_{l+1} - Q_{l-1})$ for even l (metal site), and $V(l) = V_{dp} - \alpha(Q_{l+1} - Q_l)$. Before introducing the calculated results, we explain the meaning of these terms. Let us think about the metal site. The contribution of the $(l + 1)$th halogen to this lth metal site is $+ \alpha Q_{l+1} n_l - \alpha Q_{l+1} n_l n_{l+1} = \alpha Q_{l+1}(1 - n_{l+1}) n_l$. We here emphasize that we use a "hole picture," namely, that the vacuum state is M^{2+} and X^- for the M (X) site, respectively. When the halogen loses no electron, the expectation value of n_{l+1} remains almost zero and then the term roughly gives $\alpha Q_{l+1} n_l$, which is a part of the fourth term of Eq. (8.1), with the reversed sign because of the hole picture. What is interesting is the effective reduction of this effect in the presence of a hole at the halogen site, namely, $\langle n_{l+1} \rangle \sim 1$. This is easily understood as the vanishing Coulombic interaction between M and X^0. We also have another type of e–l interaction in the first term of Eq. (8.3) through the factor form of $t(l) = t_{dp}$

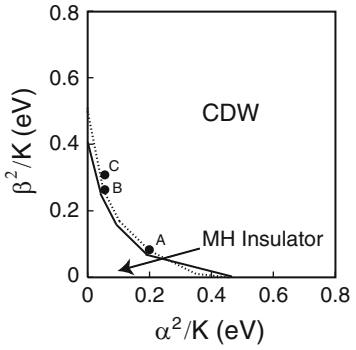

Fig. 8.27 A–C in the phase diagram are candidates for the realistic parameter combinations and the target points in the calculations. Reprinted from Iwano [49]. Copyright (2004) by the American Physical Society

$-\beta(Q_{l+1} - Q_l)$. This is nothing but the transfer modulation due to the bond-length change as intensively discussed in the Su–Schrieffer–Heeger model for polyacetylene [7].

The calculated results are summarized in Fig. 8.26b with a level scheme in the hole picture, Fig. 8.26a [9]. Regarding the parameter values, the readers are recommended to see [9]. Although all the values are not determined uniquely as will be shown in the next subsection, this successful reproduction of the observed peak energies supports the above-mentioned idea, namely, the PdBr compound as a metastable Mott–Hubbard insulator state.

8.4.3 Photoconverting CDW to a Mott Insulator

Following the previous subsection, we continue the discussion of the metastable Mott–Hubbard state of the Pd compound. Since we have already discussed from both the experimental and theoretical sides that it is very likely to exist, the next question is how we can detect such a state in the pure PdBr compound. To answer this question, Matsuzaki et al. performed the pump–probe experiment that shined the light to this compound in the CDW ground state and obtained a signal that really indicated the Mott–Hubbard state [48]. Here, we do not repeat this successful story and only describe the theoretical aspect.

In Fig. 8.27, we show a phase diagram that was obtained based on the calculation in the previous subsection [49]. As was mentioned previously, there is a factor undermined there. It was the combination of the two types of e–l couplings, namely, (α, β). In this diagram, we again make them have the dimension of energy, and use α^2/K and β^2/K as the coordinates. The solid line in this figure is the phase boundary between the two phases that we have been discussing, while the dotted line corresponds to the parameter combinations that give the observed CDW peak energy, 0.7 eV, in the Pd compound. The form of these curves understood by the expression of an effective total e–l interaction, $\bar{\alpha} \equiv \alpha + [2t_{dp}/(e_p - e_d)]\beta$. What is

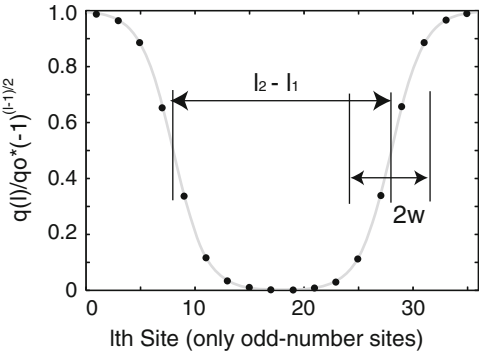

Fig. 8.28 Staggered lattice configurations used in the calculation

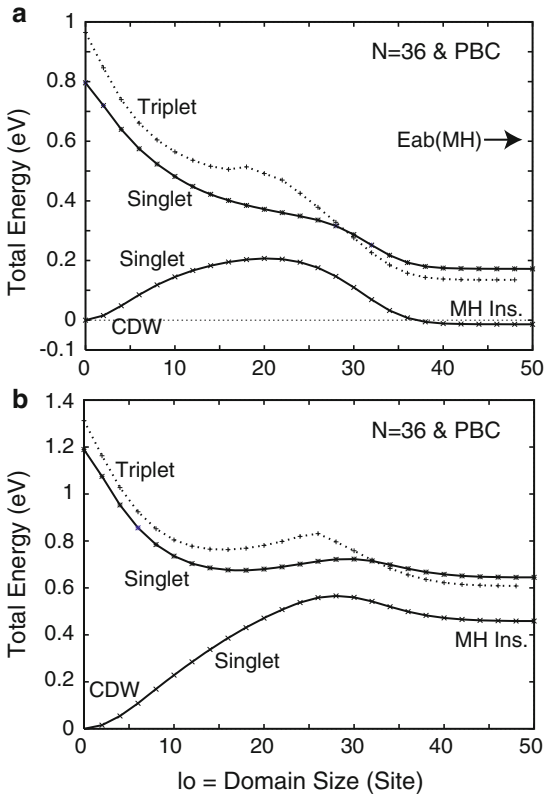

Fig. 8.29 Adiabatic potential *curves* of photoconversion on (**a**) A and (**b**) C points in Fig. 8.27. Reprinted from Iwano [49]. Copyright (2004) by the American Physical Society

more important is the proximity of these curves. As is easily seen in the figure, the two curves reside very close to each other and even a crossing occurs at one point.

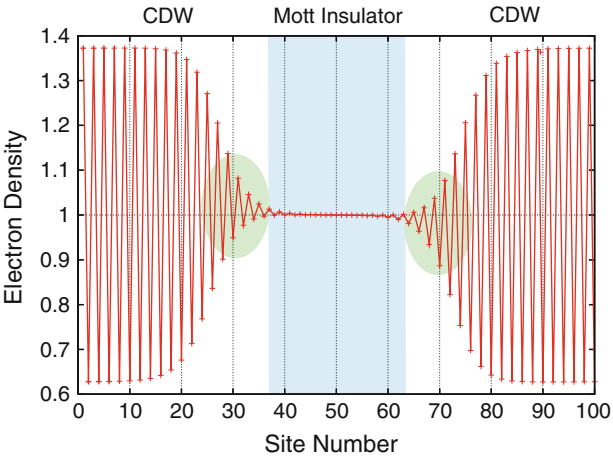

Fig. 8.30 Electron density in the presence of a Mott-insulator domain in the CDW background

This result tells us that the actual Pd compound is really located near the phase boundary whichever the parameter combination is.

We next introduce the result that demonstrates how the phase conversion occurs. The calculation was performed in almost the same manner as that was done in the soliton formation within the CDW phase, except for the assumed trajectory as in Fig. 8.28. Note that the formed domain in the central region loses the halogen lattice dimerization instead of the dimerization-phase inversion in the soliton case. In Fig. 8.29, we show the adiabatic potential curves calculated by the DMRG method, with Fig. 8.29a, b corresponding to the point A and C, respectively. The calculations indicate that the results are rather sensitive to the selection of the points. In fact, in Fig. 8.29a, the curve in the first singlet excited state has no energy barrier in its relaxational path from the photoexcitation down to the Mott–Hubbard-insulator domain, while that in Fig. 8.29b shows a slight energy barrier, meaning less efficient domain formation process. As for the point B, it gives a result similar to the point A. The actual PdBr compound shows a linear behavior in the photoinducing process of the Mott–Hubbard-insulator state [48]. This means that even one absorbed photon creates a substantial size of domain, and therefore the result in Fig. 8.29a is consistent with the observation.

In the rest of this subsection, we briefly mention the electric charges of the domain wall. If the system is exactly on the phase boundary, the domain feels no potential energy that increases with the domain size otherwise. In those cases, not the domain size but the positions of the domain walls are appropriate as the degrees of freedom of the system. In other words, the two domain walls are expected to move freely to each other, and allow the possibility to be detected separately. In particular, the charges are intriguing, because they are expected to become fractional. In Fig. 8.30, we show the distribution of the electron density, in which the central region corresponds to the Mott–Hubbard-insulator domain (K. Iwano, unpublished). Note that we here use the extended Hubbard model and the HF method to calculate the density in a large system, because we assume that the effect

of electron correlation is not relevant in the determination of the charges. If the readers carefully look at the domain wall area shaded in the figure, they will notice that the left (right) region has more (less) electrons. We then move each domain wall by one unit cell, and measure the increased or decreased dipole moments, resorting to the method described in the preceding subsection. The obtained charges are then found to be $\pm 0.46e$ approximately, with e being the charge of the electron. Thus, these values are fractional in the twofold meanings; first close to $\pm(1/2)e$ and then deviate from them with a substantial difference. We emphasize that the approximate values of $\pm(1/2)e$ are easily explained in the localized limit by using a figure like Fig. 8.16, while the deviation from them depends on the parameter value, being affected by the finite itinerancy.

8.4.4 Other Important Aspects of Photoconversions

At the end of this chapter, we briefly mention recent progresses on the photoconversion in the MX-chains. By the way, this photoconversion is nowadays called "photoinduced phase transition" in the field of optical properties of solids. The MX-chains have particular research advantage among other popular materials exhibiting photoinduced phase transitions because their optically excited states are already clarified to almost satisfactorily levels except for a few remaining points such as highly excited states in the Ni compounds, and therefore work well as model materials. The progress worth being mentioned first of all is the ultrafast nature of the domain formation. In the previous subsection, we described it based on the adiabatic potential curves. Such a description assumes that important dynamical changes, more specifically those in the electronic state, occur following the change in the lattice system. This type way of thinking will be true if the lattice system is the dominant driving force to determine the phases. Meanwhile, in our CDW case, the effect of V also plays the essential role as we have already discussed. For this reason, a concept of domain formation of purely electronic nature has been pursued from both the experimental and theoretical sides. In particular, the observation of the ultrafast time scale in the early process of the CDW to Mott–Hubbard conversion in the Pd compound is important, because it was much shorter than 80 fs, i.e., much less than the time scale of the relevant phonon frequency, about 0.1 ps. The contribution from the theoretical side was given with a quasi-one-dimensional molecular solid, tetrathiafulvalene-*p*-chloranil (TTF-CA), as the target material. Almost the same idea, namely, the ultrafast electronic domain formation, was also presented in this material, and a theoretical calculation was performed focusing on its optical conductivity spectra [50]. According to their results, the excited states are characterized by excited domain states, and such tendency is more conspicuous as the system goes closer to the phase boundary. By the way, TTF-CA has two phases as electronic states, that are, the neutral phase and the ionic phase, which are very similar to the CDW and Mott-insulator states, respectively, at least from the theoretical point of view. Therefore, the results are applicable also to the

MX-chains, more specifically, the Pd compound, and prompt further studies, for example, on entangled dynamics in which the two collective degrees of freedom in the electronic system and the lattice system evolve in time, affecting each other.

The second progress is the further photoconversion of the PdBr compound, that is, the second transition from the Mott–Hubbard state to a metallic state. As we already know that the Ni compound as another type of Mott insulator becomes metallic after the strong photoexcitation, this sounds very likely. In fact, Matsuzaki et al. have tried such detection and obtained a result supporting this (H. Matsuzaki, unpublished). Although a theoretical investigation has not been tried yet, the theorists face a novel field of dynamics in which a domain in its transient growth process is converted again into the third phase.

The last progress we want to mention is challenges toward more detailed and accurate understanding of this photoconversion process. So far, we have looked at the domain growth only focusing on its coherent aspect. In this case, we mean by the word of "coherent" a description based solely on the collective coordinate of the domain formation. Very recently, Uemura et al. have found the generations of various types of coherent phonons in TTF-CA during its photoconversion process [51]. This observation suggests substantial couplings between the collective coordinate and the other degrees of freedom, and tell us the necessity of a new theory that includes such effects. In a naive image, we expect that the collective motion of the domain growth will receive a kind of friction from the other degrees of freedom such as phonons, magnons, electron–hole excitations, and so on. Regarding this, the idea of quantum friction [52] is attractive, although we must keep the following two points in mind. First, at least at the initial stage of dynamics, the relevant modes are rather limited since the coherent phonons are observed. In this sense, this is a different problem from that considering all the other modes as a reservoir. Second, the domain has a translational invariance in ideal or sufficiently large systems. Not only its spatial extension but also the motion of its center of gravity will receive scattering effects from the other degrees of freedom. Such complexity will also be of central interest in the very recent paper [53] and is expected to make our understanding much deeper.

References

1. Nasu K (1984) J Phys Soc Jpn 53:302
2. Mishima A, Nasu K (1989) Phys Rev B 39:5758
3. Mishima A, Nasu K (1989) Phys Rev B 39:5763
4. Mishima A, Nasu K (1989) Phys Rev B 40:5593
5. Hubbard J (1963) Proc R So0063 A 276:238
6. Tanino H, Kobayashi K (1983) J Phys Soc Jpn 52:1446
7. Su WP, Schrieffer JR, Heeger AJ (1979) Phys Rev Lett 42:1698
8. Gammel JT, Saxena A, Batistic I, Bishop AR, Phillpot SR (1992) Phys Rev B 45:6408
9. Matsuzaki M, Iwano K, Aizawa T, Ono M, Kishida H, Yamashita M, Okamoto H (2004) Phys Rev B 70:035204

10. White SR (1993) Phys Rev B 48:10345
11. Alouani M, Albers RC, Wills JM, Springborg M (1992) Phys Rev Lett 69:3104
12. Alouani M, Wilkins JW, Albers RC, Wills JM (1993) Phys Rev Lett 71:1415
13. Anisimov VI, Albers RC, Wills JM, Alouani M, Wilkins JW (1995) Phys Rev B 52:6975 (R)
14. Zahn FC, Rice TM (1988) Phys Rev B 37:3759
15. Iwano K, Shimoi Y (2007) J Phys Soc Jpn 76:063708
16. Wada Y, Mitani T, Yamashita M, Koda T (1985) J Phys Soc Jpn 54:3143
17. Wada Y, Mitani T, Toriumi K, Yamashita M (1989) J Phys Soc Jpn 58:3013
18. Iwano K, Nasu K (1992) J Phys Soc Jpn 61:1380
19. Abe S (1989) J Phys Soc Jpn 58:62
20. Tagawa Y, Suzuki N (1990) J Phys Soc Jpn 59:4074
21. Wada Y, Yamashita M (1990) Phys Rev B 42:7398
22. Iwano K, Nasu K (1993) J Phys Soc Jpn 62:1778
23. Iwasa Y, Funatsu E, Hasegawa T, Koda T, Yamashita M (1991) Appl Phys Lett 59:2219
24. Iwano K (1997) J Phys Soc Jpn 66:1088
25. Iwano K (2001) Phys Rev B 64:184303
26. des Cloiseaux J, Pearson JJ (1962) Phys Rev 128:2131
27. Bonner JC, Fischer ME (1964) Phys Rev 135:A640
28. Okamoto H, Toriumi K, Mitani T, Yamashita M (1990) Phys Rev B 42:10381
29. Jeckelmann E, Gebhard F, Essler FH (2000) Phys Rev Lett 85:3910
30. Jeckelmann E (2003) Phys Rev B 67:075106
31. Matsueda H, Tohyama T, Maekawa S (2005) Phys Rev B 71:153106
32. Stephan W, Penc K (1996) Phys Rev B 54:17269R
33. Mizuno Y, Tsutsui K, Tohyama T, Maekawa S (2000) Phys Rev B 62:4769 (R)
34. Kishida H, Matsuzaki H, Okamoto H, Manabe T, Yamashita M, Taguchi Y, Tokura Y (2000) Nature (London) 405:929
35. Ono M, Miura K, Maeda A, Matsuzaki H, Kishida H, Taguchi Y, Tokura Y, Yamashita M, Okamoto H (2004) Phys Rev B 70:085101
36. Iwano K, Ono M, Okamoto H (2002) Phys Rev B 66:235103
37. Holstein H (1959) Ann Phys (NY) 8:325
38. Holstein H (1959) Ann Phys (NY) 8:343
39. Iwano K (2006) Phys Rev B 74:125104
40. Iwai S, Ono M, Maeda A, Matsuzaki H, Kishida H, Okamoto H, Tokura Y (2003) Phys Rev Lett 91:057401
41. Takahashi A, Itoh H, Aihara M (2008) Phys Rev B 77:205105
42. Takaishi S, Takamura M, Kajiwara T, Miyasaka H, Yamashita M, Iwata M, Matsuzaki H, Okamoto H, Tanaka H, Kuroda S, Nishikawa H, Oshio H, Kato K, Tanaka M (2008) J Am Chem Soc 130:12080
43. Okamoto H, Yamashita M (1998) Bull Chem Soc Jpn 71:2023
44. Marumoto M, Tanaka H, Kuroda G, Manabe T, Yamashita M (1999) Phys Rev B 60:7699
45. Yamashita M, Ishii T, Matsuzaka H, Manabe T, Kawashima T, Okamoto H, Kitagawa H, Mitani T, Marumoto K, Kuroda S (1999) Inorg Chem 38:5124
46. Iwano K (1999) J Phys Soc Jpn 68:935
47. Okamoto H, Shimada Y, Oka Y, Chainani A, Takahashi T, Kitagawa H, Mitani T, Toriumi K, Inoue K, Manabe T, Yamashita M (1996) Phys Rev B 54:8438
48. Matsuzaki H, Yamashita M, Okamoto H (2006) J Phys Soc Jpn 75:123701
49. Iwano K (2004) Phys Rev B 70:241102 (R)
50. Iwano K (2006) Phys Rev Lett 97:226404
51. Uemura H, Okamoto H (2010) Phys Rev Lett 105:258302
52. Caldeira AO, Leggett AJ (1983) Physica 121A:587
53. Iwano K (2011) Phys Rev B 84:235139

Part II
MMX-Chain Compounds

Chapter 9
Crystal Structures and Properties of MMX-Chain Compounds Based on Dithiocarboxylato-Bridged Dinuclear Complexes

Minoru Mitsumi

Abstract In this chapter, a comprehensive study of the syntheses, crystal structures, and properties of the series of one-dimensional (1D) halogen-bridged mixed-valence dimetal complexes, MMX-chain compounds, based on the dithiocarboxylato-bridged dinuclear complexes, $[Pt_2(RCS_2)_4I]_\infty$ (R = Me (**1**), Et (**2**), *n*-Pr (**3**), *n*-Bu (**4**), *n*-Pen (**5**), and *n*-Hex(**6**)) and $[Ni_2(RCS_2)_4I]_\infty$ (R = Me (**7**), Et (**8**), *n*-Pr (**9**), and *n*-Bu (**10**)) are described. The evolution from 1D halogen-bridged metal complex, MX-chain compounds, to MMX-chain compounds has produced a variety of electronic states and subtle balance of solid-state properties originating from the charge–spin–lattice coupling and the fluctuation of these degrees of freedom. With increasing the internal degrees of freedom originating from the mixed-valence diplatinum unit, the Pt MMX-chain compounds except for **3** show relatively high electrical conductivity of 0.84–43 S cm^{-1} at room temperature and exhibit metallic conducting behavior with T_{M-S} = 205–324 K. These compounds at room temperature are considered to take the valence-ordered state close to an averaged-valence (AV) state of $–Pt^{2.5+}–Pt^{2.5+}–I^-–$. The analyses of the diffuse scattering observed in the metallic state of **2** revealed that the metallic state has appeared by the valence fluctuation accompanying the dynamic valence-ordering state of the charge-density-wave (CDW) type of $–Pt^{2+}–Pt^{2+}–I^-–Pt^{3+}–Pt^{3+}–I^-–$. On the other hand, the metallic Pt MMX-chain compounds become insulators with lowering temperature due to the lattice dimerization originating from an effective half-filled metallic band. The synchrotron radiation crystal structure analysis of **2** at 48 K revealed that the valence-ordered state in the LT phase is the alternate charge-polarization (ACP) state of $–Pt^{2+}–Pt^{3+}–I^-–Pt^{3+}–Pt^{2+}–I^-–$. Furthermore, the elongation of the alkyl chains introduces increasing motional degrees of freedom in the

M. Mitsumi (✉)
Department of Material Science, Graduate School of Material Science, University of Hyogo, 3-2-1 Kouto, Kamigori-cho, Ako-gun, Hyogo 678-1297, Japan
e-mail: mitsumi@sci.u-hyogo.ac.jp

M. Yamashita and H. Okamoto (eds.), *Material Designs and New Physical Properties in MX- and MMX-Chain Compounds*, DOI 10.1007/978-3-7091-1317-2_9,

system. Interplay between electronic degrees of freedom and molecular dynamics is also expected to cause an intriguing structural phase transition accompanying an electronic and/or magnetic transition never observed for $[M_2(MeCS_2)_4I]_\infty$ (M = Pt (**1**), Ni (**7**)). With the elongation of alkyl chains in dithiocarboxylato ligands, the compounds **3**–**5** undergo two phase transitions at near 210 K and above room temperature, indicating the existence of the LT, RT, and HT phases. The periodicity of crystal lattice in the RT phase of **3**–**5** along 1D chain is threefold of a –Pt–Pt–I– unit, and the structural disorders have occurred for the dithiocarboxylato group and the alkyl chain belonging to only the central dinuclear units in the threefold periodicity. In the HT phase, the dithiocarboxylato groups of all the dinuclear units in **3**–**5** are disordered and the lattice periodicities in **3** and **4** change to onefold of a –Pt–Pt–I– period. Ikeuchi and Saito have revealed from the heat capacity measurements that the entropy (disorder) reserved in alkyl groups in the RT phase is transferred to the dithiocarboxylate groups with the RT–HT phase transition [50–52]. Whereas, the lattice periodicity of **4** in the LT phase changes to twofold periodicity being assigned to the ACP state similar to the LT phase of the compound **2** and the dithiocarboxylate groups of all the diplatinum units are ordered. Furthermore, accompanying to the RT–LT phase transition, the compound **4** exhibits the paramagnetic–nonmagnetic transition originating from the regular electronic Peierls transition. These facts suggest that the dynamics (motional degrees of freedom) of the dithiocarboxylato ligands and bridging iodine atoms affects the electronic and magnetic systems through the electron–lattice interaction.

On the other hand, unlike the metallic Pt MMX-chain compounds, all the Ni MMX-chain compounds are Mott–Hubbard semiconductor due to the strong on-site Columbic repulsion on the nickel atom. The room-temperature crystal structures of the compounds **7**–**10** indicate their valence states to be an averaged-valence (AV) state or a charge-polarization (CP) state of $-Ni^{(2.5-\delta)+}-Ni^{(2.5+\delta)+}-I^{-}-Ni^{(2.5-\delta)+}-Ni^{(2.5+\delta)+}-Ni^{(2.5-\delta)+}-I^{-}-$ ($\delta \ll 0.5$) close to an averaged-valence state. With the elongation of the alkyl chains in dithiocarboxylato ligands, the periodicity of crystal lattice in **9** and **10** along 1D chain in the RT phase is threefold of a –Ni–Ni–I– unit by the same origin as the diplatinum compounds **3**–**5**, and furthermore, the lattice periodicity of **9** changes to onefold in the LT phase with a first-order phase transition at 205.6 K. The high temperature magnetic susceptibilities of **8**–**10** can be described by an $S = 1/2$ 1D Heisenberg antiferromagnetic chain model with the very large exchange coupling constant $|J|/k_B$ ranging from 898(2) to 939(3) K. Furthermore, the compounds **8** and **9** undergo a spin-Peierls (SP) transition at relatively high $T_{sp} = 47$ and 36 K, respectively, which are accompanied by superlattice reflections corresponding to twofold of a –Ni–Ni–I– period below T_{sp}. The synchrotron radiation crystal structure analysis of **8** at 26 K revealed that the valence-ordered state changes from the CP state in the RT phase to the ACP state in the SP phase. These facts demonstrate that the electronic system of the Ni MMX-chain compounds in which the on-site Columbic repulsion U plays a dominant role in determining the electronic system is hardly affected by the molecular dynamics.

9.1 Introduction

Mixed valency has played a pivotal role in the appearance of many interesting properties such as electrical, magnetic, and optical or their combination [1]. Such a mixed valency was first realized in inorganic compound and, in particular, the mixed-valence platinum complexes. One-dimensional (1D) halogen-bridged metal complexes, MX-chain compounds, have received significant attention for several decades because they display a variety of electronic states originating from the competition between electron–lattice interaction and strong electron–electron correlation [2–6]. MX chain compounds with M = Pt and Pd are usually in a Class II mixed-valence state, $\text{-X}^{-}\text{–M}^{2+}\text{–X}^{-}\text{-M}^{4+}\text{-X}^{-}\text{–}$, and show a shift of the halogen atoms from the midpoint between two metal atoms due to Peierls instability. These Class II compounds exhibit characteristic physical properties such as strong intervalence charge-transfer (IVCT) absorption [7, 8], luminescence with a large Stokes shift [9], and resonance Raman scattering with high-overtone progression [10, 11] originating from the strong electron–lattice interactions. On the other hand, nickel compounds tend to be in a Class III-A averaged-valence state of $\text{–X}^{-}\text{–Ni}^{3+}\text{–X}^{-}\text{–Ni}^{3+}\text{–X}^{-}\text{–}$ and the bridging halogen atoms are located at the midpoint between two Ni atoms due to strong electron–electron correlation of the Ni atoms [12]. These Ni compounds are characterized as Mott–Hubbard semiconductors with a spin-density-wave (SDW) ground state [13], and exhibit very interesting solid-state properties such as gigantic third-order nonlinear optical susceptibility ($\chi^{(3)}$) [14] and an $S = 1/2$ 1D Heisenberg antiferromagnetic (AF) chain with a strong AF interaction ($J/k_B = 3{,}600$ K) between the Ni^{3+} ions [8]. Using magnetic susceptibility and nuclear quadrupole resonance (NQR) data, Takaishi et al. recently showed that $\{[NiBr(1R,2R\text{-chxn})_2]Br_2\}_\infty$ (1*R*,2*R*-chxn = 1*R*,2*R*-diaminocyclohexane) undergoes a spin-Peierls transition in the temperature range of 40–130 K [15]. The Ni compounds have also attracted attention as a 1D model candidate for high-T_c copper oxide superconductors because of the similarity in the electronic band structure to La_2CuO_4 which is the precursor compound to the series $La_{2-x}Sr_xCuO_4$ [16]. The details of the properties of these MX-chain compounds have been described in this book.

The evolution from MX-chain compounds to 1D halogen-bridged mixed-valence dinuclear chain compounds, MMX-chain compounds, has recently received increased attention, as they display a variety of electronic states and subtle balance of solid-state properties originating from the charge-spin-lattice coupling and the fluctuation of these degrees of freedom. MMX-chain compounds reported so far belong to two families, i.e., the pop-family of $A_4[Pt_2(pop)_4X]\cdot nH_2O$ (pop = $P_2O_5H_2^{2-}$; A = Li, K, Cs, various alkyl ammonium; X = Cl, Br, I) [17–27] and the dta-family (dta = dithioacetato, $MeCS_2^-$) $[M_2(RCS_2)_4I]_\infty$ (M = Pt, R = Me (**1**), Et (**2**), *n*-Pr (**3**), *n*-Bu (**4**), *n*-Pen (**5**), *n*-Hex (**6**); M = Ni, R = Me (**7**), Et (**8**), *n*-Pr (**9**), *n*-Bu (**10**)) [28–38]. These compounds exist in a mixed-valence state composed of M^{2+} (d^8, $S = 0$) and M^{3+} (d^7, $S = 1/2$) with a formal oxidation number of +2.5. Therefore, the MMX-chain compound is a 1D d–p electronic

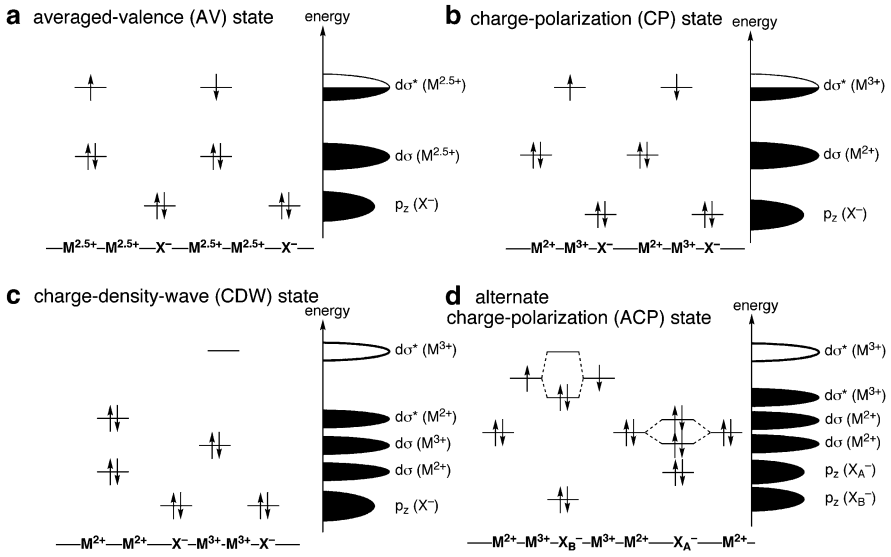

Fig. 9.1 Schematic electronic structures for the MMX-chain compound in the limit $U \rightarrow 0$; (**a**) averaged-valence (AV) state, (**b**) charge-polarization (CP) state, (**c**) charge-density-wave (CDW) state, and (**d**) alternate charge-polarization (ACP) state [31]

system based on a dinuclear unit containing a metal–metal bond with a formal bond order of one-half. Important features of MMX compounds are expected to arise from the increase of the internal degrees of freedom resulting from the mixed-valence state of the dinuclear unit. This property enables various electronic structures, which are represented by the four extreme valence-ordered states as shown in Fig. 9.1 [31].

The valence state, expressed as a $-M^{2+}-M^{3+}-$, represents an extreme case, which is more accurately represented as $-M^{(2+\delta)+}-M^{(3-\delta)+}-$ or $-M^{(2.5-\delta)+}-M^{(2.5+\delta)+}-$. The value of δ depends on the degree of orbital hybridization and lies between the limiting cases of 0 and 0.5. These valence-ordered states are classified based on the periodicity of the 1D chains as follows. The averaged valence (AV) and charge-polarization (CP) states in which the periodicity of the 1D chain is –M–M–X– correspond to a metallic state with an effective half-filled conduction band mainly composed of M–M dσ*–X p_z hybridized orbitals or to a Mott–Hubbard semiconducting state. In contrast, the periodicities of the 1D chains in the charge-density-wave (CDW) and alternate charge-polarization (ACP) states are doubled. Except for the averaged valence (AV) state, the valence-ordered states should undergo lattice distortions due to valence alternation. The magnitude of the on-site Coulomb repulsion U in MMX compounds is expected to be relatively small compared with MX compounds due to the sharing of one unpaired electron through a metal–metal bond. This facilitates valence delocalization and enhances valence fluctuation in the mixed-valence state. Furthermore, an MMX-chain compound should have a strong AF interaction arising from the superexchange interaction between the $S = 1/2$ spins of the M^{3+} ions through the large overlap of the metal d_{z^2} and halogen p_z

orbitals, analogous to the Ni MX compounds [8]. The details of the properties of the pop-family of $A_4[Pt_2(pop)_4X]\cdot nH_2O$ have been described in this book by Iguchi, Takaishi, and Yamashita.

$[M_2(MeCS_2)_4I]_\infty$ (M = Pt (**1**), Ni (**7**)) was first prepared and characterized by Bellitto et al. in 1983 and 1985, respectively [28, 37]. Yamashita et al. first reported in 1992 that the single crystal electrical conductivity of $[Pt_2(MeCS_2)_4I]_\infty$ (**1**) around room temperature is nearly temperature independent [29]. The transport and spectroscopic studies of **1** by Kitagawa et al. revealed that this compound shows a high-electrical conductivity of 13 S cm^{-1} at room temperature and exhibits metallic behavior above 300 K [31]. In contrast, $[Ni_2(MeCS_2)_4I]_\infty$ (**7**) has an AV state at RT, but exhibits a sharp peak near 0.6 eV in the reflectance spectrum for light polarized parallel to the 1D chain, which is attributed to a Mott–Hubbard gap due to a relatively large on-site Coulomb repulsion energy U of the nickel atoms [29]. Accordingly, this compound has been regarded as a Mott–Hubbard semiconductor.

To reveal the essence of these MMX compounds as a 1D electronic system, two series of Pt and Ni MMX-chain compounds, $[Pt_2(RCS_2)_4I]_\infty$ (R = Et (**2**), *n*-Pr (**3**), *n*-Bu (**4**), *n*-Pen (**5**), and *n*-Hex(**6**)) [32–36] and $[Ni_2(RCS_2)_4I]_\infty$ (R = Et (**8**), *n*-Pr (**9**), and *n*-Bu (**10**)) [38] have been prepared by our group, and the correlations between their crystal structures and properties have been studied in detail. In the platinum complexes, it was found that the valence fluctuation originating from the Pt^{2+} and Pt^{3+} mixed-valence state plays an essential role in the appearance of the metallic or dynamic electronic state. On the other hand, the nickel complexes do not exhibit such a valence fluctuation but behave as a Class III-A averaged-valence state of $-Ni^{2.5+}-Ni^{2.5+}-I^-$– due to strong electron–electron correlation of the Ni atoms. Theoretical studies of the MMX-chain compounds to reveal the electronic structure have also been described [39–43]. The elongation of the alkyl chains is expected to cause not only increasing one-dimensionality (reducing transversal effects) but also increasing motional degrees of freedom in the system. Furthermore, the interplay between electronic degrees of freedom and molecular dynamics has actually caused the diverse and intriguing structural phase transitions accompanying electronic and/or magnetic transition never observed for $[M_2(MeCS_2)_4I]_\infty$ (M = Pt (**1**) and Ni (**7**)).

9.2 Platinum Complexes

9.2.1 Syntheses

Dithiocarboxylic acids are prepared in moderate yields by the reaction between carbon disulfide and the corresponding alkylmagnesium halide in a mixed solvent of tetrahydrofuran and diethyl ether [44]. A precursor complex $[Pt_2^{II}(MeCS_2)_4]$ is prepared by the reaction of dithioacetic acid with $K_2[PtCl_4]$ in toluene under reflux, but the yield is at most 40 % because of the low reactivity of $K_2[PtCl_4]$ with dithioacetic acid in toluene [45]. However, the yield can be improved to about 90 % by using platinum(II) chloride instead of $K_2[PtCl_4]$. The precursor complexes

$[Pt_2(RCS_2)_4]$ (R = Me, Et, *n*-Pr, *n*-Bu, *n*-Pen) can be stored without decomposition for several months under an inert atmosphere in a freezer but gradually decompose upon exposure to air.

The precursor complex $[Pt_2^{II}(MeCS_2)_4]$ readily undergoes oxidative addition with halogens in hot toluene, giving $[Pt_2^{III}(MeCS_2)_4X_2]$ containing platinum atoms with formal oxidation state of +3 [28]. In the case of X = I, if the reaction is carried out with a ratio of $[Pt_2(MeCS_2)_4]$:I = 1:1, an MMX-chain compound $[Pt_2(MeCS_2)_4I]_\infty$ (**1**) with formal oxidation state of +2.5 is isolated. This compound can also be obtained from the reaction of $[Pt_2^{II}(MeCS_2)_4]$ and $[Pt_2^{III}(MeCS_2)_4I_2]$ in toluene under reflux [28]. As described in the next section, $[Pt_2(MeCS_2)_4I]_\infty$ (**1**) undergoes an order–disorder type phase transition associated with the conformation of two PtS_4 planes around 371–372 K [46]. One should be careful because the disordered diplatinum unit of **1** will be partially formed in the crystal when the crystals start to deposit above the transition temperature. $[Pt_2(RCS_2)_4I]_\infty$ (R = Et (**2**), *n*-Pr (**3**), *n*-Bu (**4**), and *n*-Pen (**5**)) can also be prepared by mixing equimolar amounts of $[Pt_2^{II}(RCS_2)_4]$ and $[Pt_2^{III}(RCS_2)_4I_2]$ [32–35]. $[Pt_2(n\text{-}BuCS_2)_4I]_\infty$ (**4**) and $[Pt_2(n\text{-}PenCS_2)_4I]_\infty$ (**5**) are prepared by cooling the corresponding toluene—*n*-hexane or *n*-hexane solution down to 2 ~ 0 °C, because the solubility of the MMX compounds increases with elongation of the alkyl chains. These MMX-chain compounds are relatively stable in air.

9.2.2 Crystal Structures

Before describing the crystal structures, the transition temperature and the entropy gain at the phase transition obtained by the heat capacity measurements of $[Pt_2(RCS_2)_4I]_\infty$ (Me (**1**), Et (**2**), *n*-Pr (**3**), *n*-Bu (**4**), and *n*-Pen (**5**)) are listed in Table 9.1 [47–52].

9.2.2.1 $[Pt_2(RCS_2)_4I]_\infty$ (R = Me (1), Et (2))

Miyazaki et al. have reported the heat capacity of $[Pt_2(MeCS_2)_4I]_\infty$ (**1**) in which a distinct heat capacity peak due to a phase transition was observed at T_{trs} = 373.4 K, indicating the presence of the room temperature (RT) and high-temperature (HT) phases [48]. On the other hand, DSC measurements of $[Pt_2(EtCS_2)_4I]_\infty$ (**2**) do not show any latent heat in the temperature range of 150–473 K [32]. $[Pt_2(RCS_2)_4I]_\infty$ (R = Me (**1**), Et (**2**)) crystallize in the same monoclinic space group *C*2/*c* and hence have similar structures [28, 32]. The crystal structure of **2** is shown in Fig. 9.2. The crystals of both compounds consist of neutral 1D chains with a repeating –Pt–Pt–I– unit lying on the crystallographic twofold axis parallel to the *b* axis. The crystal structure is exemplified with that of the compound **2** [32]. Two platinum atoms of **2** are bridged by four dithiopropanato ligands with a Pt–Pt distance of 2.684 (1) Å at 293 K, 0.189 Å shorter than the distance between the mean planes

Table 9.1 Transition temperature and the entropy gain at the phase transition in $[Pt_2(RCS_2)_4I]_\infty$ [47]

	LT phase → RT phase		RT phase → HT phase		
Compound	T_{trs} (K)	$\Delta_{trs}S$ ($J\,K^{-1}\,mol^{-1}$)	T_{trs} (K)	$\Delta_{trs}S$ ($J\,K^{-1}\,mol^{-1}$)	References
$[Pt_2(MeCS_2)_4I]_\infty$ (**1**) [a]			373.4	5.25 ± 0.07	[48]
$[Pt_2(EtCS_2)_4I]_\infty$ (**2**)[b]	≈180 and ≈230	0.21 and 0.13			[49]
$[Pt_2(n\text{-}PrCS_2)_4I]_\infty$ (**3**)	209	14.6	358.8	10.0	[50]
$[Pt_2(n\text{-}BuCS_2)_4I]_\infty$ (**4**)[c]	213.5	20.09	323.5	7.46	[51]
$[Pt_2(n\text{-}PenCS_2)_4I]_\infty$ (**5**)[d]	207.4	49.1	324	≈0	[52]
$[Pt_2(n\text{-}PenCS_2)_4I]_\infty$ (**5**)[e]	220.5	52.4			

[a]No thermal anomalies at $T_{M-S} = 300$ K and $T = 80$ K.
[b]Transport properties show a metal–semiconductor transition at $T_{M-S} = 205$ K.
[c]The additional small phase transition observed at 114 K.
[d]Data for as-grown sample.
[e]Data for the sample once heated above the RT–HT phase transition at 324 K and then supercooled. A very broad higher order phase transition was detected around 170 K

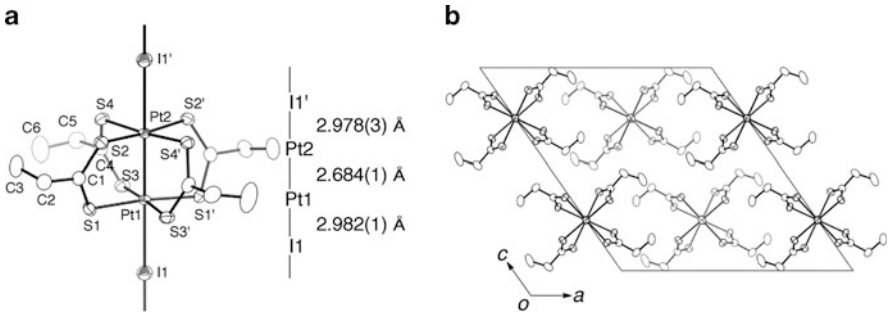

Fig. 9.2 (**a**) 1D chain structure of $[Pt_2(EtCS_2)_4I]_\infty$ (**2**) at 293 K with an atomic numbering scheme and relevant interatomic distances [32]. (**b**) Packing diagram projected down the *b* axis. Thermal ellipsoid set at the 50 % probability level.

defined by the four sulfur atoms. This Pt–Pt distance is intermediate between that of $[Pt_2^{II}(EtCS_2)_4]$ (d^8d^8) (2.764 (1) Å) [53] and $[Pt_2^{III}(EtCS_2)_4I_2]$ (d^7d^7) (2.582 (1) Å) [32] and is nearly equal to that of **1** (2.677 (2) Å) [28]. This is consistent with that the bond order of the Pt–Pt bond in **1** and **2** (d^8d^7) is formally one-half. Pt–I distances are 2.982 (1) and 2.978 (1) Å, which are longer than those observed in $[Pt_2^{III}(EtCS_2)_4I_2]$ (average 2.764 Å) [32] and are similar to those in **1** (average 2.978 Å) [28]. The dominant structural feature of $[Pt_2(RCS_2)_4I]_\infty$ is a twisting of two PtS_4 planes from an eclipsed arrangement characterized by the twist angle. The two PtS_4 planes of the dinuclear unit in **2** are twisted by ca. 23.0° at 293 K from the eclipsed D_{4h} structure. This results from the S ··· S distance (ca. 3.0 Å) of the SCS moiety being longer than the Pt–Pt distance (ca. 2.68 Å) [28, 32]. This twisting has enabled the stretching of the Pt–Pt bond by changing the twist angle.

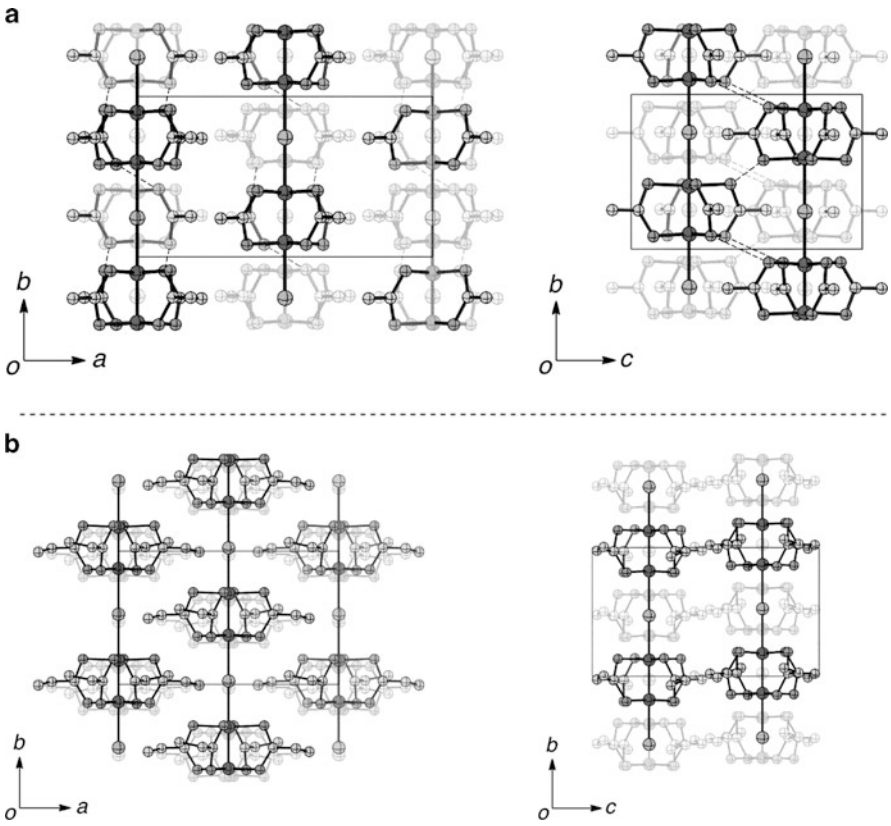

Fig. 9.3 Packing diagrams projected down the *c* and *a* axes for (**a**) $[Pt_2(MeCS_2)_4I]_\infty$ (**1**) and (**b**) $[Pt_2(EtCS_2)_4I]_\infty$ (**2**) [28, 32]. The dashed lines represent the interchain S···S contacts, which are relatively close to the van der Waals contact distance between sulfur atoms (3.60 Å)

As shown in Fig. 9.3, the neighboring 1D chains of **1** and **2** along the *a* axis are mutually shifted by 0.5*b* owing to the relation of the *C* lattice. Adjacent 1D chains along the *c* axis are related by the *c* glide plane, and hence the two PtS_4 planes of diplatinum units in the neighboring 1D chains twist in opposite directions. It is noteworthy that the arrangement of neighboring 1D chains along the *c* axis of **2** is different from that of **1**. Neighboring chains along *c* are shifted by about 0.5*b* in **1** but are shifted by only 0.444 Å (293 K) in **2**. The interchain S···S contact distances are 3.812 and 3.847 Å in **1**, which are relatively close to the van der Waals contact distance between sulfur atoms (3.60 Å), indicating the existence of two-dimensional (2D) interaction parallel to the *bc* plane [28]. On the other hand, the shorter interchain S···S distances in **2** are 4.140 (2) and 4.663 (2) Å, indicating no interchain S···S contacts [32]. Therefore, one-dimensionality of **2** is enhanced by the introduction of the ethyl group into dithiocarboxylato ligand instead of the methyl group. Interchain

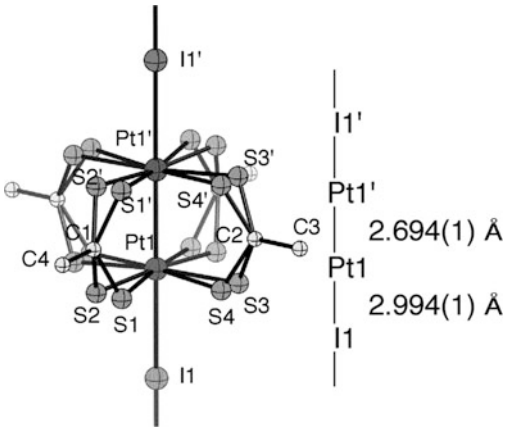

Fig. 9.4 1D chain structure of $[Pt_2(MeCS_2)_4I]_\infty$ (**1**) in the HT phase (403 K) with an atomic numbering scheme and relevant interatomic distances [46]

distances along the *a* and *c* directions in **2** are 8.719 and 9.285 Å, respectively, lengthened by 0.300 and 2.467 Å, in comparison with those of **1**.

Variable temperature X-ray crystal structure analyses by Ozawa, Toriumi et al. have revealed that **1** undergoes a structural phase transition near $T_{trs} = 373.4$ K and the space group changes from *C*2/*c* at room temperature to *A*2/*m* at high temperature [46] (Fig. 9.4). Crystallographic mirror planes perpendicular to the 1D chain exist on the I1 atoms and the midpoint of Pt1 and Pt1′ atoms (i.e., $y = 0, 0.5, 1$) and, therefore, the dinuclear units in the high-temperature (HT) phase at 403 K adopt two staggered arrangements with twist angles of 19.4° and −19.4°, respectively [46]. Whereas, the positional disorder of PtS_4 planes is not observed for **2** in the X-ray analysis up to 377 K, consistent with DSC data [32].

9.2.2.2 $[Pt_2(RCS_2)_4I]_\infty$ (R = *n*-Pr (3), *n*-Bu (4), and *n*-Pen (5))

RT Phases of $[Pt_2(RCS_2)_4I]_\infty$ (R = *n*-Pr (**3**), *n*-Bu (**4**), and *n*-Pen (**5**))

With increasing motional degrees of freedom in the system by the elongation of the alkyl chains in dithiocarboxylato ligands, $[Pt_2(RCS_2)_4I]_\infty$ (R = *n*-Pr (**3**) [50], *n*-Bu (**4**) [51], and *n*-Pen (**5**) [52]) undergo two phase transitions at near 210 K and above room temperature, indicating the presence of the low temperature (LT), room temperature (RT), and high-temperature (HT) phases. The transition temperature and the entropy gain at the phase transition of **3**–**5** are listed in Table 9.1. RT phases of $[Pt_2(RCS_2)_4I]_\infty$ (R = *n*-Pr (**3**), *n*-Bu (**4**), and *n*-Pen (**5**)) crystallize in the same tetragonal space group *I*4/*m* and have almost similar structures [33–35]. The 1D chain structures of **3**–**5** in the RT phases are shown in Fig. 9.5. Since these crystal structures are very similar, the RT phase of **4** is described here [33].

The structure consists of neutral 1D chains with a repeating –Pt–Pt–I– unit lying on the crystallographic fourfold axis parallel to the *c* axis. The unit cell dimension *c* along the 1D chain direction consists of three –Pt–Pt–I– units. Crystallographic

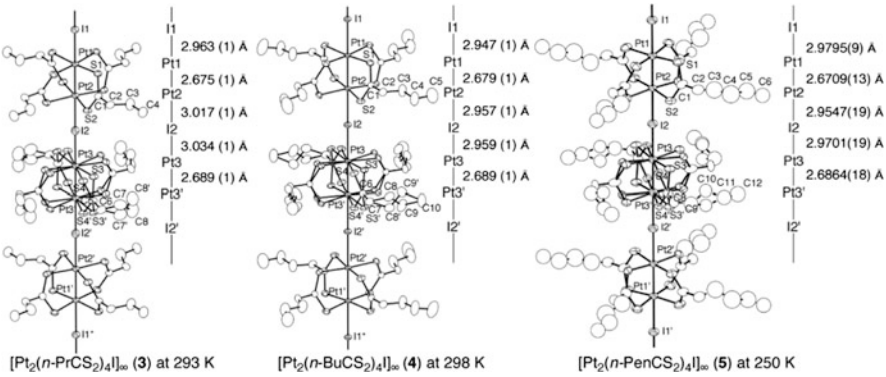

Fig. 9.5 1D chain structures of $[Pt_2(RCS_2)_4I]_\infty$ (R = *n*-Pr (**3**), *n*-Bu (**4**), *n*-Pen (**5**)) in the RT phase with an atomic numbering scheme and relevant interatomic distances (thermal ellipsoid set at the 50 % probability level) [33–35]. Crystallographic mirror planes perpendicular to the 1D chain exist on the I1 atoms and the midpoint of Pt3 and Pt3′ atoms (i.e., $z = 0, 0.5, 1$)

mirror planes perpendicular to the 1D chain exist on the I1 atoms and the midpoint of Pt3 and Pt3′ atoms (i.e., $z = 0, 0.5, 1$). Therefore, the ligand moieties including sulfur atoms bonded to Pt3–Pt3′ units are disordered on two positions and the twisting directions of two PtS_4 planes of adjacent dinuclear Pt1–Pt2 units in the 1D chain are opposite to each other. Two platinum atoms are bridged by four dithiohexanato ligands in a paddle-wheel fashion with Pt–Pt distances of Pt1–Pt2 = 2.679 (1) and Pt3–Pt3′ = 2.689 (1) Å. The twist angles between two PtS_4 planes are 21.45(7)° for a Pt1–Pt2 unit and ±20.3(2)° for a Pt3–Pt3′ unit, respectively. The three Pt–I distances are Pt1–I1 = 2.947 (1), Pt2–I2 = 2.957 (1), and Pt3–I2 = 2.959 (1) Å. Generally, a Pt^{2+}–I^- distance is greater than a Pt^{3+}–I^- distance because the d_{z^2} orbital of the Pt^{2+} site is occupied by a pair of electrons. Therefore, the difference between Pt–I bonds enables us to determine the valence state of Pt atoms. Taking into account the small but significant differences in the Pt–I and Pt–Pt distances, the valence-ordered state of the platinum atoms in the threefold periodic structure may be regarded as an extreme model of $-I^-$–Pt^{2+}–Pt^{3+}–I^-–$Pt^{2.5+}$–$Pt^{2.5+}$–I^-–Pt^{3+}–Pt^{2+}–I^-–. In such a valence state, a band gap formation occurs due to the structural distortion and the unpaired electrons on the adjacent Pt^{3+} sites are expected to take a singlet state due to the strong antiferromagnetic coupling through the bridging iodine atom. However, as described later, the RT and HT phases of **4** and **5** are a metallic or highly conductive paramagnetic state and diffuse streaks with the twofold periodicity of a –Pt–Pt–I– period were observed in the those RT and HT phases, indicating the presence of the valence fluctuation having the twofold periodicity of a –Pt–Pt–I– period [35, 54]. The RT phases of **4** and **5** should consequently be assigned to the valence-ordered state close to the AV state. On the other hand, the compound **3** at room temperature exhibits the Bragg reflections with the twofold periodicity of a –Pt–Pt–I– period instead of diffuse streaks, indicating that **3** takes the valence-localized state corresponding to ACP or

CDW state at room temperature [34]. Adjacent $Pt_2(CS_2)_4$ units of Pt1–Pt2 and Pt3–Pt3′ in **4** are twisted by ca. 14° from the eclipsed arrangement. In addition, the *n*-butyl groups of the dithiopentanato ligands bonded to the Pt3–Pt3′ unit are disordered over two sites. Therefore, the origin of threefold periodic structure cannot be attributed to the valence ordering of the platinum atoms but to both the twist of the adjacent diplatinum units and the difference in the conformation of the dithiopentanato ligands. The shortest interchain S · · · S distance is S(2) · · · S(2) $(1/2 - x,\ 1/2 - y,\ 1/2 - z) = 5.121(4)$ Å, indicating the absence of interchain S· · · S contact. With the elongation of the alkyl chains in dithiocarboxylato ligands, the interchain distances of **3**–**5** increase to 8.933, 9.563, and 10.082 Å, respectively.

HT Phases of $[Pt_2(RCS_2)_4I]_\infty$ (R = *n*-Pr (**3**), *n*-Bu (**4**), and *n*-Pen (**5**))

With the RT–HT phase transition, the periodicities of the crystal lattices in the 1D chain direction in the HT phases of **3** and **4** change to onefold of a –Pt–Pt–I– period while keeping the same tetragonal space group *I*4/*m* [34, 35]. The 1D chain structures of **3** and **4** in the HT phases are shown in Fig. 9.6.

The structural differences of the dithiocarboxylato ligands between adjacent diplatinum units observed in the RT phases of **3** and **4** are removed in the HT phases. The Pt1–Pt1′ distance of **4** is 2.6930 (5) Å, which is 0.22 Å shorter than the distance between the mean planes defined by the four sulfur atoms (2.916 (3) Å). Crystallographic mirror planes perpendicular to the 1D chain exist on the I1 atoms and the midpoint of Pt1 and Pt1′ atoms (i.e., $z = 0, 0.5, 1$). Therefore, the bridging iodine atom exists at the midpoint of the diplatinum units (Pt1–I1 = 2.9557 (5) Å), and two PtS_4 planes are disordered on two positions with the twist angle of ±18.41 (9)°. On the other hand, the structure of **5** in the HT phase adopts the same space group *I*4/*m* and keeps a similar threefold periodic structure as its RT phase [35]. Similar to the RT phase, the ligand moieties including sulfur atoms of Pt3–Pt3′ units in **5** are disordered on two positions with the twist angle of ±21.5(4)° due to the crystallographic mirror planes perpendicular to the 1D chain existing on the midpoint of Pt3 and Pt3′ atoms. Furthermore, there is a distinct structural difference between the RT and HT phases. It is found that two PtS_4 planes of the Pt1–Pt2 diplatinum unit are disordered over two positions with the ratio of 1:1 in the HT phase. These twist angles between two PtS_4 planes are 31.7 (4)° and 11.6 (5)°, respectively. In the case of **3** and **4**, the unit cell dimension *c* along the 1D chain direction is onefold of a –Pt–Pt–I– period in the HT phase, and the two PtS_4 planes of all the diplatinum units are disordered in two positions. Therefore, the RT–HT phase transition found in **5** is believed to originate from the fact that the two PtS_4 planes in all the diplatinum units are disordered in two positions in the HT phase. Ikeuchi and Saito have revealed from the detailed analysis of the heat capacity of **3**, **4**, and **5** that the entropy (disorder) once gained in alkyl chains in the RT phase is transferred to the dithiocarboxylato group upon the RT–HT phase transition [50–52]. To clarify the origin of the difference in the lattice periodicities, the *c* axis projection of **5** in the RT phase is shown in Fig. 9.7, together with those of **3** and **4**.

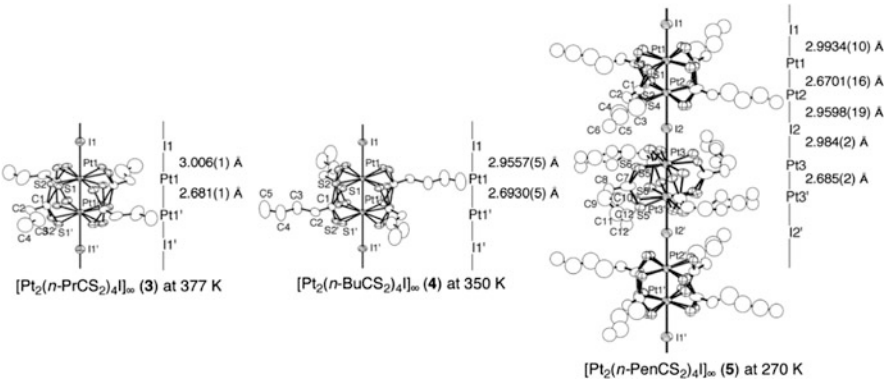

Fig. 9.6 1D chain structures of $[Pt_2(RCS_2)_4I]_\infty$ (R = *n*-Pr (**3**), *n*-Bu (**4**), *n*-Pen (**5**)) in the HT phase with an atomic numbering scheme and relevant interatomic distances (thermal ellipsoid set at the 50 % probability level) [34, 35]. Crystallographic mirror planes perpendicular to the 1D chain exist at $z = 0, 0.5, 1$

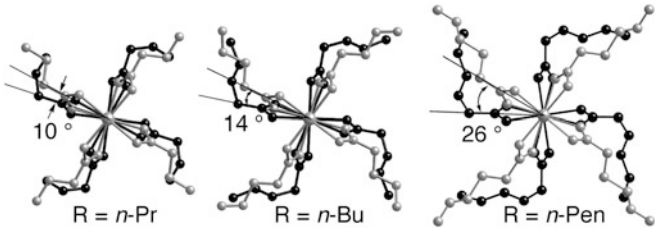

Fig. 9.7 Comparison of crystal structures of $[Pt_2(RCS_2)_4I]_\infty$ (R = *n*-Pr (**3**), *n*-Bu (**4**), *n*-Pen (**5**)) viewed along the *c* axis (1D chain direction) [35]

The molecule colored in black is disordered in two PtS_4 planes, whereas the two PtS_4 planes colored in gray are ordered. Twist angle between two kinds of adjacent $Pt_2(CS_2)_4$ units in each $[Pt_2(RCS_2)_4I]_\infty$ increases in order of R = *n*-Pr (**3**) (10°) [34], R = *n*-Bu (**4**) (14°) [33], and R = *n*-Pen (**5**) (26°) [35], and the differences in the ligand conformation between two kinds of the diplatinum units increase in the same order. Therefore, it is considered that **5** retains threefold periodic structure in the HT phase, since the twisting angle and the difference in the ligand conformation between two kinds of the diplatinum units are too large to take the onefold periodicity of a –Pt–Pt–I– period.

LT Phase of $[Pt_2(n\text{-}BuCS_2)_4I]_\infty$ (**4**)

The compound **4** undergoes a first-order phase transition at 213.5 K [51], where the space group changes from *I*4/*m* in the RT phase to *P*4/*n* in the LT phase [33]. The 1D chain structure of **4** in the LT phase at 167 K is shown in Fig. 9.8. The opposite

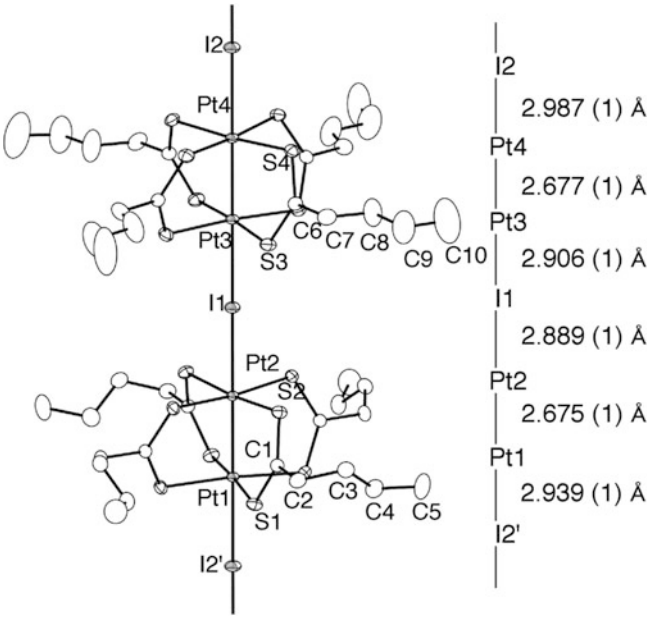

Fig. 9.8 1D chain structure of $[Pt_2(n\text{-}BuCS_2)_4I]_\infty$ (**4**) at 167 K in the LT phase with an atomic numbering scheme and relevant interatomic distances (thermal ellipsoid set at the 50 % probability level) [33]

twist of PtS_4 planes between the adjacent diplatinum units in the 1D chain and the difference in conformation of the ligands observed at RT phase disappeared in the LT phase, and the periodicity of the crystal lattice in the 1D chain direction changes from threefold of a –Pt–Pt–I– period in the RT phase to twofold in the LT phase. Two Pt–Pt distances are almost the same (Pt1–Pt2 = 2.675(1) and Pt3–Pt4 = 2.677(1) Å), whereas there are two different Pt–I bond distances. The short Pt–I distances (Pt2–I1 = 2.889(1) and Pt3–I1 = 2.906(1) Å) are about 0.07 Å less than those of the long Pt1–I2′ = 2.939(1) and Pt4–I2 = 2.987(1) Å). Based on the observed Pt–Pt and Pt–I distances, the valence-ordered state in the LT phase in **4** is assigned to be the ACP state of $–Pt^{2+}–Pt^{3+}–I^{-}–Pt^{3+}–Pt^{2+}–I^{-}–$.

9.2.3 X-Ray Photoelectron Spectra

As will be described in detail later in the Transport Properties section, $[Pt_2(RCS_2)_4I]_\infty$ (R = Me (**1**), Et (**2**)) undergo the metal–semiconductor transition near 300 and 205 K, respectively. To examine the valence state of the platinum atoms, the X-ray photoelectron spectra (XPS) measurements have been made on **1** and **2** [31, 32]. The Pt $4f_{7/2}$ and $4f_{5/2}$ core level spectrum for **2** at room temperature are shown in Fig. 9.9, together with that of $[Pt_2^{II,II}(EtCS_2)_4]$ and $[Pt_2^{III,III}(EtCS_2)_4I_2]$ [32].

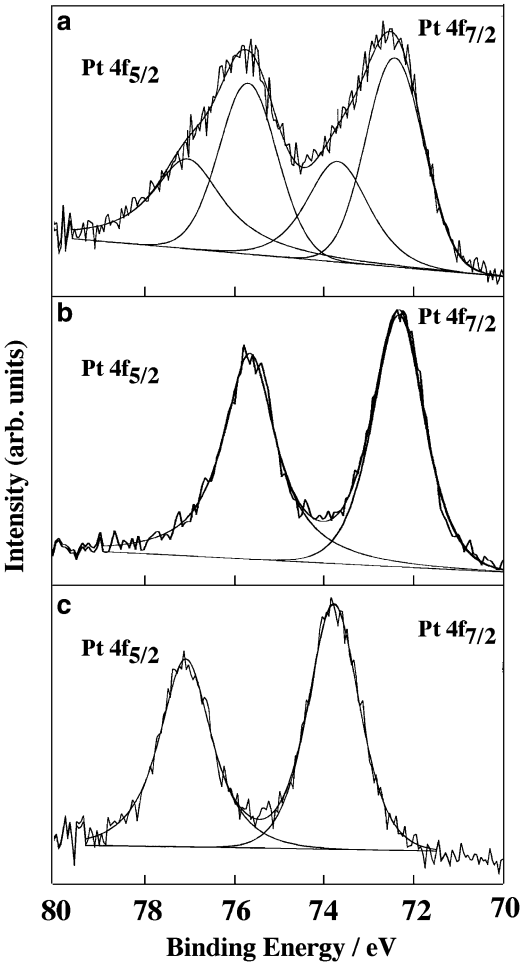

Fig. 9.9 Pt $4f_{7/2}$ and $4f_{5/2}$ core level spectra for (**a**) $[Pt_2(EtCS_2)_4I]_\infty$ (**2**), (**b**) $[Pt_2(EtCS_2)_4]$, and (**c**) $[Pt_2(EtCS_2)_4I_2]$ [32]

Binding energies of the Pt $4f_{7/2}$ and $4f_{5/2}$ core levels are summarized in Table 9.2. The Pt $4f_{7/2}$ and $4f_{5/2}$ peaks of **2** are broad compared to those of $[Pt_2(EtCS_2)_4]$ and $[Pt_2(EtCS_2)_4I_2]$ and can be resolved into Pt^{2+} $4f_{7/2,5/2}$ and Pt^{3+} $4f_{7/2,5/2}$ doublets using a curve deconvolution employing a Gaussian–Lorenztian line shape fit. The energies of each resolved doublet agree well with those observed for $[Pt_2(EtCS_2)_4]$ and $[Pt_2(EtCS_2)_4I_2]$. It is apparent that the compounds **1** and **2** in the metallic state exist not in the averaged-valence state of $Pt^{2.5+}$ but in the mixed-valence state composed of Pt^{2+} and Pt^{3+} on the timescale of XPS spectroscopy (ca. 10^{-17} s). The intensity of the Pt^{3+} $4f_{7/2,5/2}$ doublet is weak relative to that of Pt^{2+}. This may be due to the reduction of Pt^{3+} to Pt^{2+} by X-ray irradiation.

Table 9.2 XPS Data for $[Pt_2(RCS_2)_4I]_\infty$ (R = Me (**1**), Et (**2**)), together with those of $[Pt_2(EtCS_2)_4]$ and $[Pt_2(EtCS_2)_4I_2]$ [31, 32]

	Binding energies/eV[a,b]				
Compound	Pt^{2+} $4f_{7/2}$	Pt^{3+} $4f_{7/2}$	Pt^{2+} $4f_{5/2}$	Pt^{3+} $4f_{5/2}$	References
$[Pt_2(MeCS_2)_4I]_\infty$ (**1**)	72.9 (1.81)	74.4 (1.75)	76.2 (1.77)	77.7 (1.73)	[31]
$[Pt_2(EtCS_2)_4I]_\infty$ (**2**)	72.41 (1.52)	73.68 (1.66)	75.69 (1.57)	77.04 (1.89)	[32]
$[Pt_2(EtCS_2)_4]$	72.26 (1.39)		75.57 (1.39)		[32]
$[Pt_2(EtCS_2)_4I_2]$		73.74 (1.38)		77.05 (1.39)	[32]

[a]Full width at half-maximum values (fwhm) for peaks are given in parentheses.
[b]These values were corrected against C 1s peak using a value of 284.6 eV for C 1s peak.

9.2.4 Electronic Absorption Spectra

Electronic absorption spectra of **1**–**5** are very similar to one another. The electronic absorption spectrum of $[Pt_2(EtCS_2)_4I]_\infty$ (**2**) is, therefore, described as an example of those spectra [32]. The electronic absorption spectrum of $[Pt_2(EtCS_2)_4I]_\infty$ (**2**) is shown in Fig. 9.10 in addition to the spectra for $[Pt_2(EtCS_2)_4]$ and $[Pt_2(EtCS_2)_4I_2]$. Spectral data are summarized in Table 9.3. The dominant feature of the absorption spectrum of **2** is an intense broad band centered at 7,900 cm^{-1} (0.98 eV) that is absent from the spectra of $[Pt_2(EtCS_2)_4]$ and $[Pt_2(EtCS_2)_4I_2]$. Highly conducting 1D molecular-based conductors are known to show two intermolecular charge-transfer absorption bands, located at 7,000 ~ 11,000 and 2,000 ~ 4,000 cm^{-1} [56–60]. For TCNQ (A) salts ($\rho < 1$) (TCNQ = 7,7,8,8-tetracyanoquinodimethane), the former is usually attributed to a charge-transfer transition of the type, $A^0A^{2-} \leftarrow A^-A^-$ (CT_1), and the latter to the $A^0A^- \leftarrow A^-A^0$ (CT_2) transition. The energy of CT_1 is largely determined by the Coulomb repulsion between electrons on the same molecule, while electrical conductivity is related to the low energy CT_2 band. Since the compound **2** has formally one unpaired electron per an MMX unit, the lowest energy band can be attributed to the interdimer charge-transfer absorption CT_1, $d\sigma^{*0}d\sigma^{*2} \leftarrow d\sigma^{*1}d\sigma^{*1}$. This band extends to the infrared region, thus relatively high-electrical conductivity can be expected for **2**. The absorption maximum energies of **1** and **2** are 7,500 and 7,900 cm^{-1} [32], whereas those of **3**–**5** are shifted to higher energy of 9,300 cm^{-1} for **3** and 9,000 cm^{-1} for **4** and **5** [35, 55]. The absorption maximum energy of **3** that shows the semiconducting behavior at RT is shifted to the highest energy. The bands observed near 17,700 and 24,600 cm^{-1} for **2** are assigned to $d\sigma^* \leftarrow \sigma(I)$ and $d\sigma^* \leftarrow d\pi^*$ transitions, respectively, similarly to assignment for **1** [31].

9.2.5 Transport Properties

9.2.5.1 $[Pt_2(MeCS_2)_4I]_\infty$ (1)

The temperature dependence of the electrical conductivity and resistivity of $[Pt_2(MeCS_2)_4I]_\infty$ (**1**) parallel to the chain axis *b* are shown in Fig. 9.11 [31]. The

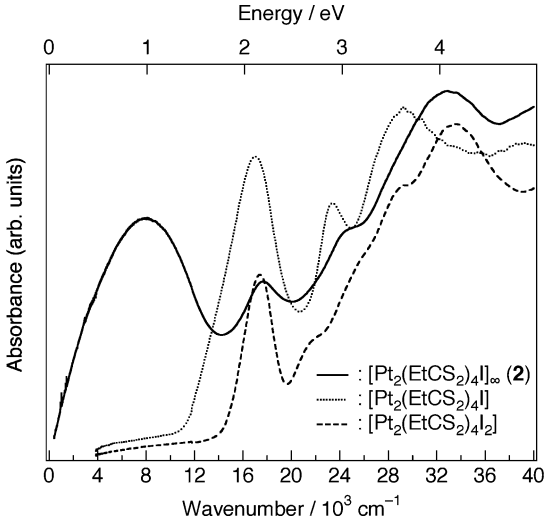

Fig. 9.10 Electronic absorption spectra of $[Pt_2(EtCS_2)_4I]_\infty$ (**2**), $[Pt_2(EtCS_2)_4]$, and $[Pt_2(EtCS_2)_4I_2]$ in the solid-state (KBr-pressed disks) [32]

Table 9.3 Electronic absorption spectral data of $[Pt_2(RCS_2)_4I]_\infty$ (R = Me (**1**), Et (**2**), *n*-Pr (**3**), *n*-Bu (**4**), *n*-Pen (**5**), and *n*-Hex (**6**)) in the solid-state, together with that of $[Pt_2(EtCS_2)_4]$ and $[Pt_2(EtCS_2)_4I_2]$

	Wave number/10^3 cm^{-1}	References
$[Pt_2(EtCS_2)_4I]_\infty$ (**2**)	7.9, 17.7, 24.6 (sh), 33.0	[32]
$[Pt_2(EtCS_2)_4]$	17.0, 23.4, 29.2	[32]
$[Pt_2(EtCS_2)_4I_2]$	17.4, 21.8 (sh), 26.1 (sh), 29.2, 33.1	[32]
$[Pt_2(MeCS_2)_4I]_\infty$ (**1**)	7.5, 17.9, 24.5 (sh), 31.8	[28]
$[Pt_2(n\text{-}PrCS_2)_4I]_\infty$ (**3**)	9.3, 17.9, 24.6 (sh)	[55]
$[Pt_2(n\text{-}BuCS_2)_4I]_\infty$ (**4**)	9.0, 18.1, 24.6 (sh), 32.8	[55]
$[Pt_2(n\text{-}PenCS_2)_4I]_\infty$ (**5**)	9.0, 17.8, 24.8 (sh), 32.9	[35]
$[Pt_2(n\text{-}HexCS_2)_4I]_\infty$ (**6**)	5.6[a]	[36]

Measured as KBr or KI pressed disks at 298 K. *sh* shoulder
[a]An absorption band in near IR reagion is only reported.

compound **1** shows relatively high-electrical conductivity (13 S cm^{-1}), which is about nine orders of magnitude higher than the typical value of a MX-chain complex. This value is also 10^4 times greater than that of $K_4[Pt_2(pop)_4Br]\cdot 3H_2O$ [20] but are ca. ten times lower than that found in $K_2[Pt(CN)_4]Br_{0.3}\cdot 3H_2O$ (KCP(Br)) [61]. The metallic conductivity in the one-dimensional (1D) halogen-bridged metal complexes has been observed for the first time for $[Pt_2(MeCS_2)_4I]_\infty$ (**1**) above $T_{M\text{–}S} = 300$ K [31]. This is the second example, following KCP(Br), of a transition metal complex exhibiting metallic transport under ambient pressure without π-electronic system of ligands. The resistance drop resulting from the order–disorder

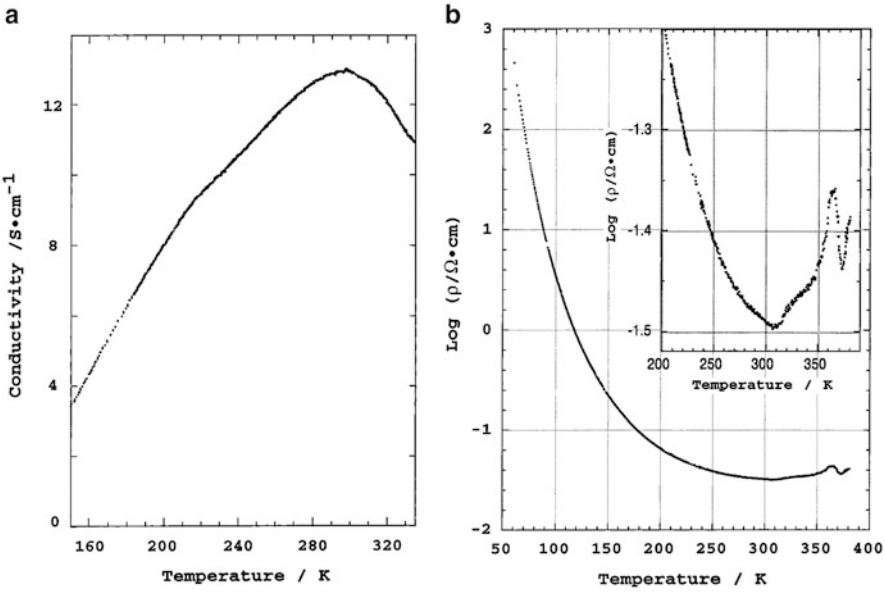

Fig. 9.11 (**a**) Temperature dependence of the electrical conductivity of a single-crystal $[Pt_2(MeCS_2)_4I]_\infty$ (**1**) parallel to the chain axis *b* [31]. (**b**) Temperature dependence of the electrical resistivity of a single-crystal of **1** parallel to the chain axis *b*

type phase transition concerning conformation change of the two PtS_4 planes has been observed at 365–375 K. The HT disordered phase is also metallic.

9.2.5.2 $[Pt_2(EtCS_2)_4I]_\infty$ (2)

The room temperature electrical conductivity of $[Pt_2(EtCS_2)_4I]_\infty$ (**2**) is 5–30 S cm^{-1}, which is of the same order as that reported for **1** [32]. The temperature dependence of electrical resistivity of crystal **2** along the 1D chain is represented in Fig. 9.12a. On decreasing temperature, the electrical resistivity increases and reaches a maximum around 235 K and then decreases down to a minimum at 205 K. Below 205 K, the electrical resistivity behaves as a semiconductor with an activated energy of 110 meV. To confirm whether the electrical conducting behavior is metallic or not, the thermoelectric power *S* has been measured (Fig. 9.12b). Above room temperature, the *S* takes the temperature-independent small negative value, -15 μV K^{-1}. Upon cooling, the *S* slightly increases and shows a slight swelling around 260–205 K and then changes its sign and increases rapidly. If the MMX units form a metallic band, it is an effective half-filled band mainly composed of a Pt–Pt dσ*–I pz combination since the present compound has formally an unpaired electron per an MMX unit. For the tight-binding approximation, the thermoelectric power of the half-filled band ($\rho = 1$) would give the temperature-independent value, zero [62–64]. The observed temperature-independent behavior of *S* above room temperature is consistent with the

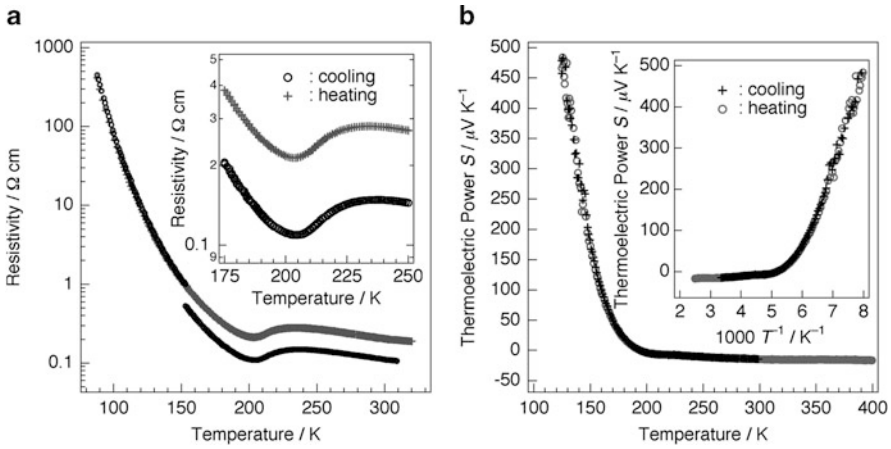

Fig. 9.12 (**a**) Temperature dependence of electrical resistivity measured along the chain axis *b* of $[Pt_2(EtCS_2)_4I]_\infty$ (**2**) [32]. (**b**) Temperature dependence of absolute thermoelectric power measured along the chain axis *b* of **2**

effective half-filled metallic band. The drastic change of *S* observed near 205 K indicates that an energy gap at the Fermi energy is opened below 205 K. Below the transition temperature, the thermoelectric power of **2** varies approximately as $1/T$, suggesting a semiconducting state [62–64]. These results demonstrate that the compound **2** undergoes a metal–semiconductor transition at $T_{M–S} = 205$ K.

Kitagawa et al. have reported the electrical resistivity of **2** under high pressure [65, 99]. The pressure dependences of the electrical resistivity of **2** along the *b*-axis (// 1D chain) are shown in Fig. 9.13. Upon increasing the pressure, the resistivity at 298 K decreases rapidly followed by a sharp transition at 3.0 GPa to a more resistive state and a gradual decrease up to 8.0 GPa. The metallic conduction at 2.2 GPa is maintained down to 70 K, that is, the metallic state is stabilized under pressure, surviving down to 70 K. The observed metal–semiconductor transition temperature ($T_{M–S} = 70$ K) is the lowest value in the 1D d-electronic conductors based on transition metal complexes. The $T_{M–S}$ of **2** is lowered by 140 K compared to KCP(Br) ($T_{M–I} = 210$ K under 3.2 GPa) [66], and its 1D metallic state is more stabilized. Above 3.0 GPa, on the contrary, the electrical transport behavior changed to be narrow gap semiconductor in the whole temperature region, where the activation energies are 17 meV at 4.0 GPa and 10 meV at 8.0 GPa. These results indicate that the resistivity jump at 3.0 GPa is attributable to a pressure-induced metal-semiconductor transition. To clarify the origin of the pressure-induced metal–insulator transition, X-ray oscillation photographs have been taken under high pressure at room temperature. Any diffuse scatterings or superlattice reflections at $k = n + 0.5$ (n being an integer) originating from the twofold periodic valence ordering such as CDW or ACP states have not been observed above 2.0 GPa, suggesting that the electronic state above 2.0 GPa is not CDW or ACP but AV or CP state [65].

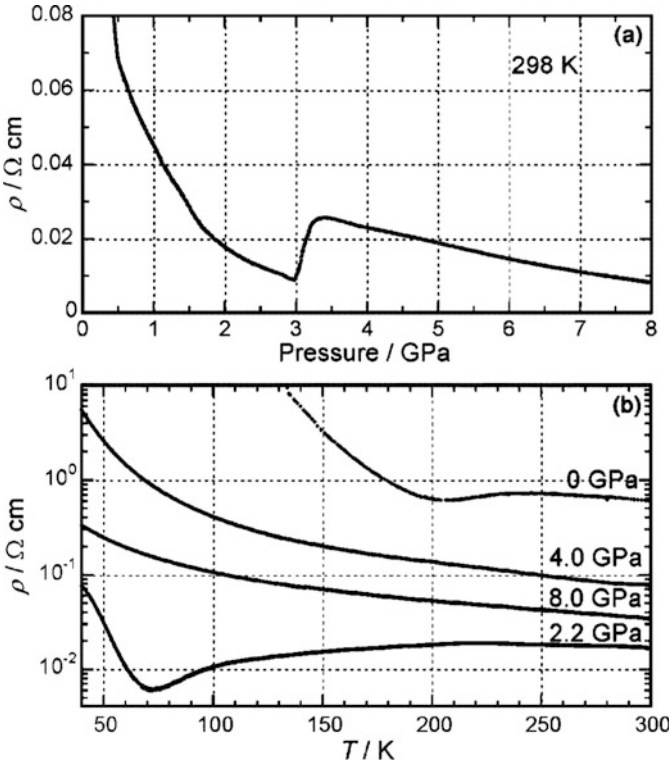

Fig. 9.13 (**a**) Pressure dependence of the electrical resistivity of $[Pt_2(EtCS_2)_4I]_\infty$ (**2**) [65]. (**b**) Temperature dependences of the electrical resistivity at 0, 2.2, 4.0, and 8.0 GPa

9.2.5.3 $[Pt_2(n\text{-}PrCS_2)_4I]_\infty$ (3)

The temperature dependence of electrical resistivity of $[Pt_2(n\text{-}PrCS_2)_4I]_\infty$ (**3**) along the 1D chain is represented in Fig. 9.14a [34]. The electrical conductivity along the *c* axis (1D chain direction) of **3** is 0.16–0.34 S cm^{-1} at 300 K, which are about two order of magnitude smaller than those of **1** and **2** [31, 32]. This is consistent with the appearance of the Bragg reflections with the twofold periodicity of a –Pt–Pt–I– period, indicating the valence-localized state corresponding to a static ACP or CDW state. The electrical resistivity shows a thermally activated behavior with activation energy of 363 meV in the temperature range of 245–320 K, but exhibits an apparent deviation from the thermally activated behavior in the temperature range of 320–359 K. Resistivity jump due to the first-order phase transition is also observed at 359 K. On the other hand, the thermoelectric power shows almost temperature independent behavior (-40 μV K^{-1}) in the range of 330–360 K (Fig. 9.14b). Above the phase transition temperature, the thermoelectric power tends to increase slightly with increasing temperature.

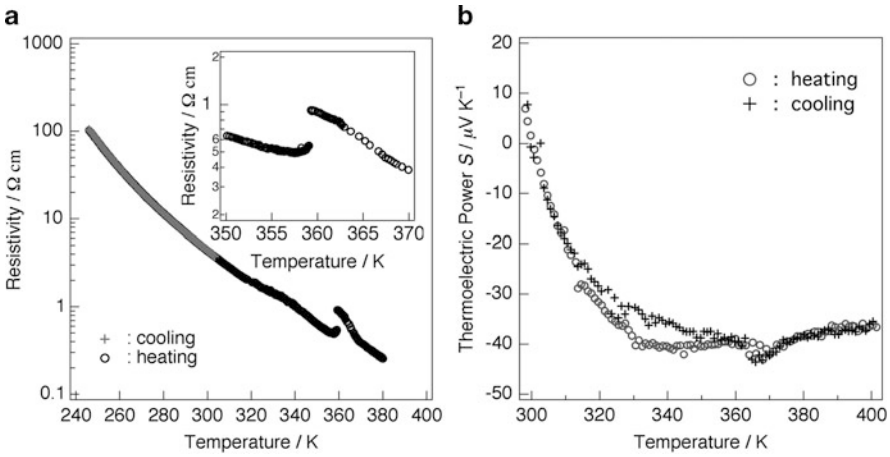

Fig. 9.14 (**a**) Temperature dependence of electrical resistivity measured along the chain axis *c* of $[Pt_2(n\text{-}PrCS_2)_4I]_\infty$ (**3**) [34]. (**b**) Temperature dependence of absolute thermoelectric power measured along the chain axis *c* of **3**

9.2.5.4 $[Pt_2(n\text{-}BuCS_2)_4I]_\infty$ (4)

The temperature dependence of electrical resistivity of $[Pt_2(n\text{-}BuCS_2)_4I]_\infty$ (**4**) along the 1D chain is represented in Fig. 9.15a [33]. The electrical conductivity along the *c* axis (1D chain direction) of **4** is 17–83 S cm^{-1} at room temperature, which is comparable to the conductivity of **1** and **2** [31, 32]. The temperature dependence of electrical resistivity exhibits metallic conduction above the RT–HT phase transition temperature, $T_{M-S} = 325$ K. LT and RT phases show semiconducting behavior with activation energies of 134 and 255 meV, respectively. The thermoelectric power, *S*, has also been measured in the temperature range of 200–400 K (Fig. 9.15b) [33]. The HT phase shows almost temperature-independent behavior of *S* (-10 μV K^{-1}), indicating a half-filled metallic band [62–64]. Below $T_{M-S} = 325$ K, *S* slightly decreases with lowering temperature, reaching a minimum value of -16 μV K^{-1} near 270 K and then, as is characteristic of semiconductors, increasing. Furthermore, ρ and *S* exhibit sharp increases at ca. 210 K, associated with the RT–LT phase transition.

9.2.5.5 $[Pt_2(n\text{-}PenCS_2)_4I]_\infty$ (5)

The electrical conductivity of $[Pt_2(n\text{-}PenCS_2)_4I]_\infty$ (**5**) at room temperature has a relatively high value of 0.84 S cm^{-1}, but it is lower than those of **1**, **2**, and **4** (Fig. 9.16a) [35]. The electrical resistivity in the cooling 1 process decreases with lowering temperature from RT and reaches a minimum around 235 K, indicating that **5** undergoes a metal–semiconductor transition at $T_{M-S} = 235$ K. This is the

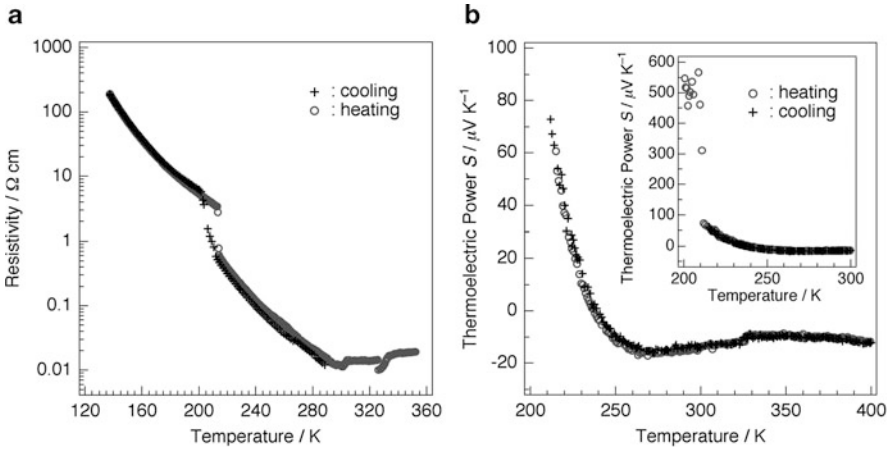

Fig. 9.15 (**a**) Temperature dependence of the resistivity of $[Pt_2(n\text{-}BuCS_2)_4I]_\infty$ (**4**) [33]. (**b**) Temperature dependence of the thermoelectric power of **4**

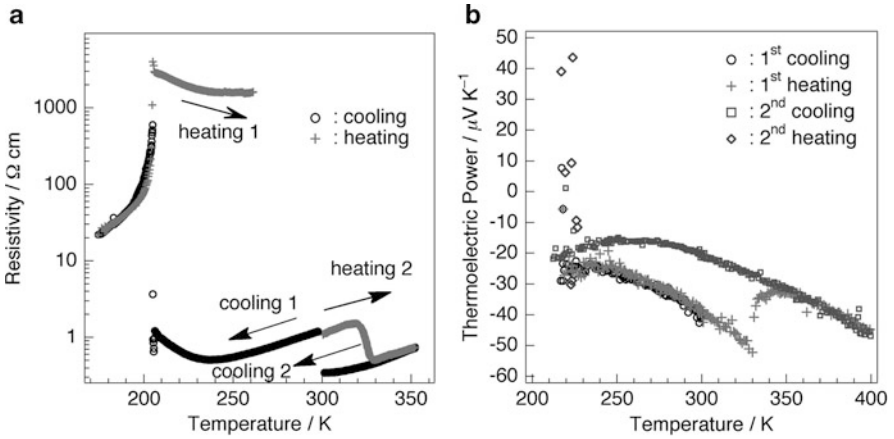

Fig. 9.16 (**a**) Temperature dependence of the electrical resistivity of $[Pt_2(n\text{-}PenCS_2)_4I]_\infty$ (**5**) measured along the chain axis *c* under different procedures [35]. (**b**) Temperature dependence of absolute thermoelectric power of **5** measured along the chain axis *c*

second stable metallic state next to $[Pt_2(EtCS_2)_4I]_\infty$ ($T_{M\text{–}S} = 205$ K) [32]. The electrical resistivity exhibits resistivity jump with the first-order RT–LT phase transition near 205 K and then decreases with lowering temperature. The resistivity in the heating 2 process measured using another as-grown crystals exhibits rapid decreases with the phase transition in the temperature range of 320–328 K, but the resistivity in the cooling 2 process from 350 K has never showed the HT–RT phase

transition. This behavior is consistent with the tendency observed in the heat capacity measurement and indicates that the phase transition is monotropic [52].

As shown in Fig. 9.16b, the thermoelectric power S in the first cooling process increases with lowering the temperature and exhibits a maximum at 235 K before rapidly increasing with the first-order RT–LT phase transition near 205 K. On first heating, S changes through the same pathway as the first cooling process, and then exhibits an increase at the RT–HT phase transition in the temperature range of 330–344 K. Upon second cooling from 400 K, S does not show the rapid decrease associated with the RT–HT phase transition and exhibits a round maximum near 260 K. The observed irreversibility is consistent with the tendency observed in the heat capacity and resistivity measurements. On the other hand, Guijarro et al. have reported the electrical transport property of the micrometer-length fibers of **5** with the typical height of ca. 1.5–2.5 nm formed by casting deposition on mica from sonicated diluted tetrahydrofuran (THF) solution [67].

9.2.6 X-Ray Diffuse Scattering

As already described in Sect. 9.2.2, the bridging iodine atom in $[Pt_2(EtCS_2)_4I]_\infty$ (**2**) is located near the midpoint between two diplatinum units. This indicates valence states of the platinum atoms of **2** are considered to be an averaged-valence state of +2.5. However, it is well known that X-ray crystal structure analysis gives only a time and spatially averaged structure. On the other hand, the XPS spectrum of **2** revealed that the diplatinum complex adopts the Pt^{2+}–Pt^{3+} mixed-valence state [32]. Furthermore, the compound **2** is expected to exhibit structural distortion even in the metallic state, since the 1D halogen-bridged mixed-valence platinum complex is a typical system having strong electron–lattice interactions. X-ray diffuse scattering techniques are used to examine subtle periodic lattice distortion [68–72]. To obtain the information for the crystal structure, including the periodical arrangement of platinum valences on the 1D chain system, X-ray diffuse scattering has been studied for **2**–**4** [32, 34, 35, 54].

9.2.6.1 $[Pt_2(EtCS_2)_4I]_\infty$ (2)

The X-ray diffraction photographs taken on the different reciprocal planes between 206 and 297 K are shown in Fig. 9.17 [32]. As shown in Fig. 9.17a, the X-ray diffraction pattern exhibits weak but sharp diffuse lines at the midpoint between layers of Bragg reflections, i.e., at the reciprocal lattice positions in $k = n + 0.5$ (n; integer). The intensity of diffuse scattering increases with increasing scattering angles. This strongly suggests that diffuse scattering arises from a displacive modulation of heavy atoms, i.e., static or dynamic distortion of the platinum and/or iodine positions. When the electron density ρ per unit cell with lattice constant b is 1, the Fermi wave number of the electron is $k_F = \rho b^*/4 = b^*/4$, where $b^* = 2\pi/$

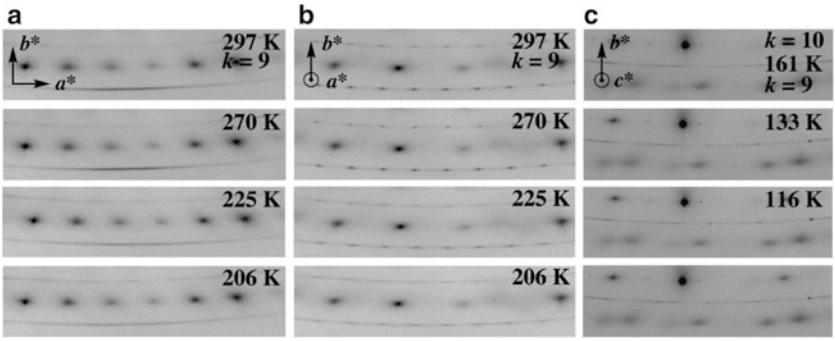

Fig. 9.17 Portions of X-ray diffraction photographs of $[Pt_2(EtCS_2)_4I]_\infty$ (**2**) taken at different temperatures and crystal orientations with a fixed-film and fixed-crystal method [32]. The b^* axis is vertical in these figures. The sample is oriented as (**a**) the a^* and b^* directions perpendicular to the incident X-ray beam, (**b**) the b^* direction perpendicular to the incident X-ray beam and the a^* direction parallel to it, (**c**) the b^* direction perpendicular to the incident X-ray beam and the c^* direction parallel to it

b is the reciprocal lattice vector, and the reciprocal-lattice vector $0.5b^*$ coincides with the $2k_F$ wave vector. Therefore, the observed diffuse scattering with twofold repetition length of a –Pt–Pt–I– period can be associated with $-Pt^{2+}-Pt^{2+}-I-\ Pt^{3+}-Pt^{3+}-I-$ ($2k_F$-CDW) or $-Pt^{2+}-Pt^{3+}-I-Pt^{3+}-Pt^{2+}-I-$ ($2k_F$).

We have proposed a possible valence-ordering model in the metallic state based on the twofold periodical ordering and the average temperature factor U_{22} of the platinum and iodine atoms along the 1D chain direction [32]. The crystal structure analyses of **2** have revealed that all the Pt–Pt distances are crystallographically identical, that the two Pt–I distances are almost equivalent within experimental errors, and that U_{22} of the iodine atom becomes exceptionally large above T_{M-S}. The exceptionally large temperature factor of the iodine atom along the 1D chain in the metallic state suggests the dynamic valence-ordering models, rather than the static ones, shown in Fig. 9.18, in which the valence fluctuation and phonon vibration are coupled with each other. If the bridging iodine atom of the MMX-chain compound is shifted from being bound to Pt^{3+} to a position close to the neighboring Pt^{2+}, electron transfer from Pt^{2+} to Pt^{3+} will be induced. This electron transfer is a result of the strong coupling between the coordination geometries of the Pt complexes and their valence states, the so-called electron–phonon coupling. The D1 model is the iodine vibration mode but does not correspond to twofold periodical ordering. The D3 model is the vibration mode of the diplatinum unit, whereas D2 is the mode in which the stretching of Pt–Pt bonds and the shifts of the bridging iodine atom positions are strongly coupled. Although the D3 model can reproduce the twofold periodical ordering, the large U_{22} of Pt rather than that of I must be expected. From the viewpoint of twofold periodical ordering and the large U_{22} of the iodine atom, the model D2 appears to be the most appropriate model in representing the valence-ordering state of **2** in the metallic state. On the other hand, the diffraction pattern in Fig. 9.17b exhibits distinct spots on diffuse lines. Considering both the diffraction patterns, it can be determined that the diffuse lines are extended

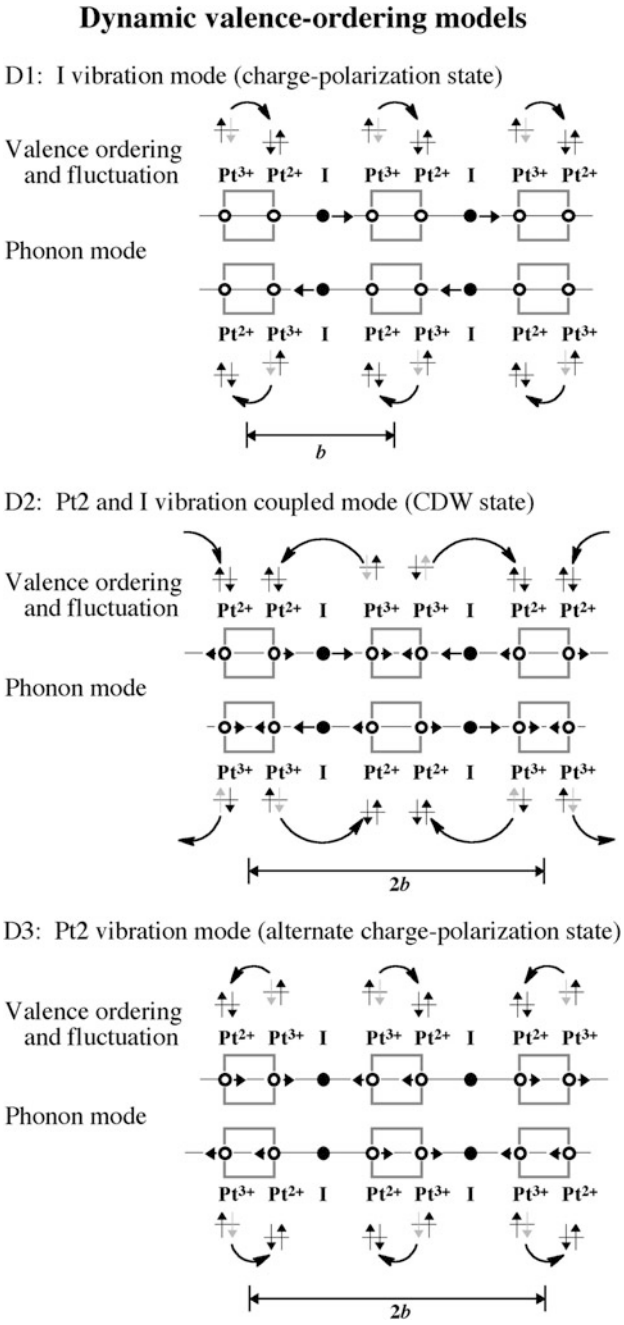

Fig. 9.18 Dynamic valence-ordering models proposed for **2** [32]

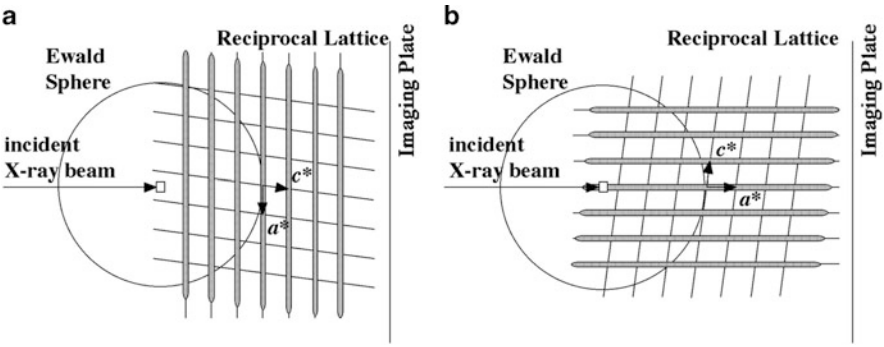

Fig. 9.19 Schematic representations of the diffuse lines $(-, n + 0.5, l)$ (n; integer) on a projection plane perpendicular to the b^* axis with the Ewald sphere [32]. The sample is oriented as (**a**) the a^* and b^* directions perpendicular to the incident X-ray beam (same orientation as Fig. 9.17a), and (**b**) the b^* direction perpendicular to the incident beam and the a^* parallel to it (same as Fig. 9.17b)

perpendicular to the b^* axis (= chain axis b) and parallel to the a^* axis and are indexed as $(-, n + 0.5, l)$ and shown in Fig. 9.19. This implies that the periodic ordering with twofold repetition length of the MMX unit existing in the 1D chain is strongly coupled with each other along the c direction, resulting in 2D order in the bc plane.

Wakabayashi et al. have reported that a quantitative analysis of the diffuse intensity distribution in the metallic state of **2** based on the method comprised of diffuse scattering and resonant X-ray scattering [73]. The observed diffuse scattering intensity distribution along the b^* axis at room temperature is shown in Fig. 9.20. This figure shows the $(0\ k\ 0)$ intensity within the region of $4.5 \leq k \leq 16.5$. Intense scattering was observed at $k = 3n \pm 0.5$. The intensity distribution is very similar to the calculation not for the ACP model but for the CDW model, indicating that **2** contains the CDW type atomic displacement. Incident energy dependence of the diffuse intensity has also been examined [73]. Figure 9.21a shows the ratio of the diffuse intensity at (0 6.5 0) to that at (0 7.5 0) around the Pt L_{III} absorption edge as well as the calculated spectrum for the A-type (CDW-type) structure. Furthermore, a similar experiment around the I K-absorption edge at (0 8.5 0) has also been carried out in Fig. 9.21b. These results indicate that the CDW-type structure is realized in the metallic state. These results strongly support the dynamic valence-ordering model D2 proposed for in the metallic phase of **2** [32].

As shown in Fig. 9.17, the intensity of the diffuse lines observed in **2** decreases progressively with decreasing temperature below 252 K accompanied by gradual changes in shape from lines to continuous sheets around T_{M-S} [32]. This indicates that the periodic ordering of the MMX units changes from 2D to 1D. This transformation in the dimensionality of valence ordering should be associated with a drastic change in the valence-ordering state. As shown in Fig. 9.17c, broad undulation in the intensity of the diffuse sheets gradually converts to weak but distinct Bragg spots corresponding to superlattice reflections around temperatures between 161 and 133 K. This fact suggests that new lateral correlation among 1D chains is remarkably developed and results in a three-dimensionally ordered array of 1D chains. In

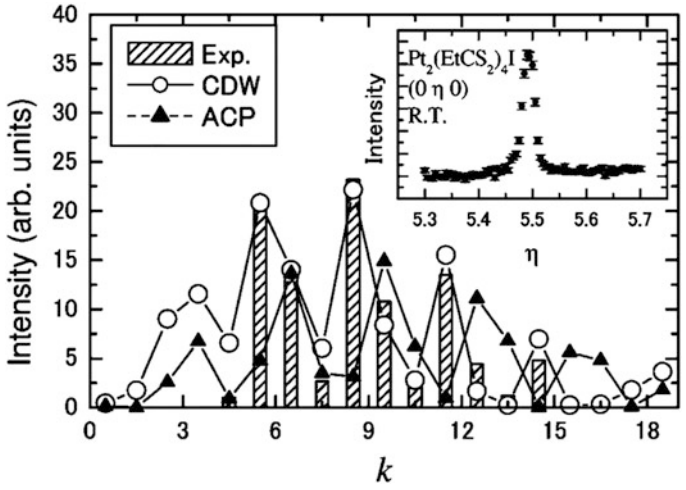

Fig. 9.20 Diffuse scattering intensity distribution of $[Pt_2(EtCS_2)_4I]_\infty$ (**2**) along the b^* axis at room temperature [73]. The calculated intensities of CDW- and ACP-type structures are also plotted. (*Inset*) Diffuse intensity distribution around (0, 5.5, 0)

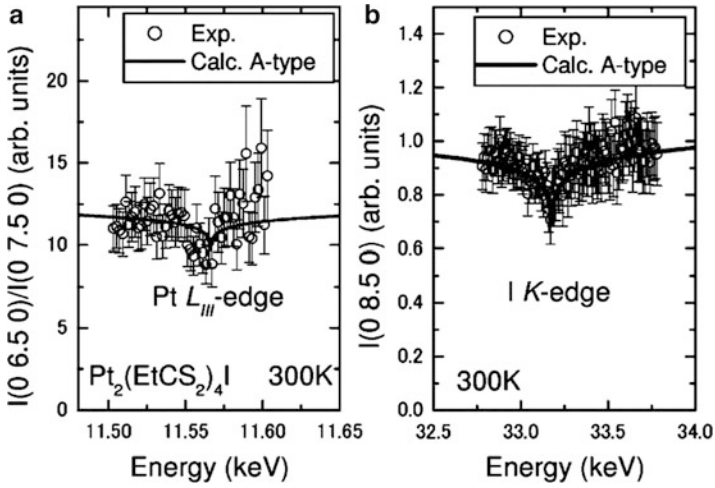

Fig. 9.21 Incident X-ray energy dependence of $[Pt_2(EtCS_2)_4I]_\infty$ (**2**) as well as the calculated spectra for the A-type (CDW-type) structure [73]. (**a**) Pt L_{III}-edge; (**b**) I *K*-edge

order to determine the LT superstructure of **2**, synchrotron radiation crystal structure analysis has been performed for data taken at 48 K. When the superlattice reflections are included, the supercell can be indexed by $a_{super} = 0.5a + 0.5b$, $b_{super} = -0.5a + 1.5b$, and $c_{super} = 0.5a - 0.5b + c$, and the space group changes from $C2/c$ to $P\bar{1}$. Figure 9.22 shows the superstructure of **2** at 48 K [33]. Two crystallographic independent $[Pt_2(EtCS_2)_4I]$ units exist in a unit cell in the LT phase and the periodicity of the crystal lattice is twofold of a –Pt–Pt–I– period. The two Pt–Pt

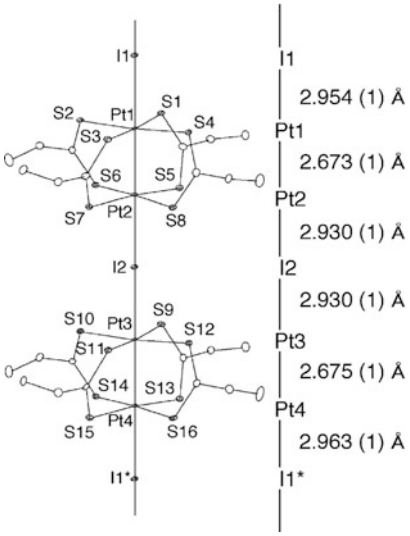

Fig. 9.22 1D chain structure of $[Pt_2(EtCS_2)_4I]_\infty$ (**2**) at 48 K with an atomic numbering scheme and relevant interatomic distances (thermal ellipsoid set at the 50 % probability level) [33]

distances are almost the same (Pt1–Pt2 = 2.673(1) and Pt3–Pt4 = 2.675(1) Å), but there are two different Pt–I bond distances. The short Pt–I distances (Pt2–I2 = 2.930 (1) and Pt3–I2 = 2.930(1) Å) are about 0.029 Å less than the long Pt–I distances (Pt1–I1 = 2.954(1) and Pt4–I1* = 2.963(1) Å). The twofold superstructure originates from the different Pt–I distances since the structures of the two crystallographic independent $[Pt_2(EtCS_2)_4]$ units are almost the same and twisting between the dinuclear units has not occurred. The observed Pt–Pt and Pt–I distances indicate that the valence-ordered state in the LT phase is the ACP state of $–Pt^{2+}–Pt^{3+}–I^{-}–Pt^{3+}–Pt^{2+}–I^{-}–$, similarly to the structure of **4** in the LT phase [33]. Kobayashi and Kitagawa have reported from ^{129}I Mössbauer spectroscopy of **2** that the chain structure and oxidation states of iodine in **2** at 11 K are considered to be as follows [26, 74]:

$$-\left[Pt^{2+}-Pt^{3+}\right]-I_A{}^{0.41-}-\left[Pt^{3+}-Pt^{2+}\right]-I_B{}^{0.31-}-$$

The valence state of Pt expressed as a $–[Pt^{3+}–Pt^{2+}]–$ represents a formal oxidation number. Almost the same results for the Mössbauer parameters have also been observed in **1**, indicating the existence of ACP type ground state in the both compounds [26, 31, 74].

9.2.6.2 $[Pt_2(n\text{-}PrCS_2)_4I]_\infty$ (3)

X-ray diffraction photographs of $[Pt_2(n\text{-}PrCS_2)_4I]_\infty$ (**3**) measured by rotating around the c axis using synchrotron radiation are shown in Fig. 9.23 [34]. At 300 K, weak but distinct Bragg spots were observed in the reciprocal positions indexed as $l \pm 1/3$ (c^*_{RT}) and $l + 1/2$ ($3/2c^*_{RT}$), where the l ($3c^*_{RT}$) is

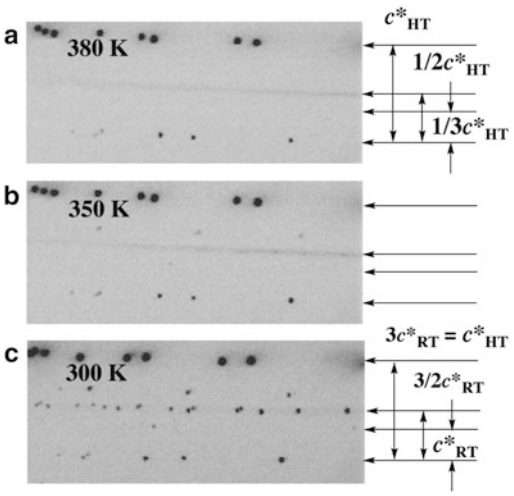

Fig. 9.23 Portions of X-ray diffraction photographs of $[Pt_2(n\text{-}PrCS_2)_4I]_\infty$ (**3**) [34]. The chain axis c is vertical. (**a**) At 380 K in HT phase. (**b**) At 350 K in RT phase. (**c**) At 300 K in RT phase

corresponding to a –Pt–Pt–I– period. The crystal structure of **3** in the RT phase, including the weak intensities of $l \pm 1/3$, has already shown in Fig. 9.5 [34]. The origin of threefold periodic structure results from both the twist of the adjacent diplatinum units and the difference in the conformation of the dithiobutanato ligands. On the other hand, the Bragg spots of $l + 1/2$ observed in the typical semiconducting region change to diffuse streaks around 350 K in the RT phase, in which the electric conductivity is deviated from the typical semiconducting behavior. The Bragg spots observed at $l + 1/2$ correspond to the three-dimensional valence ordering, that is, the valence-localized state corresponding to ACP or CDW state. As described above, the diffuse scattering with the twofold repetition length observed for **2** is ascribed to the dynamical valence-ordering with the twofold periodicity corresponding to CDW state existing in an extremely short time scale [32, 73]. Similarly, the diffuse scattering observed for **3** above 320 K can therefore be attributed to the valence-fluctuating state corresponding to a dynamic ACP or CDW state. The sixfold periodic structure including the twofold periodic valence ordering in the RT phase, in addition to the threefold periodic structure arising from the structural difference between the diplatinum units, has not been determined yet, since reflections indexed as $l \pm 1/6$ are entirely absent. As shown in Fig. 9.23, the intensities of reflections of $l \pm 1/3$ decrease above 300 K and disappear at 380 K, indicating that the lattice periodicity changes from the threefold of a –Pt–Pt–I– period in the RT phase to onefold in HT phase in agreement with the crystal structure in the HT phase.

9.2.6.3 $[Pt_2(n\text{-}BuCS_2)_4I]_\infty$ (4)

In the X-ray oscillation photographs taken in the RT phase of **4** (Fig. 9.24a, b), the weak Bragg spots have appeared at the reciprocal positions indexed as $l \pm 1/3$

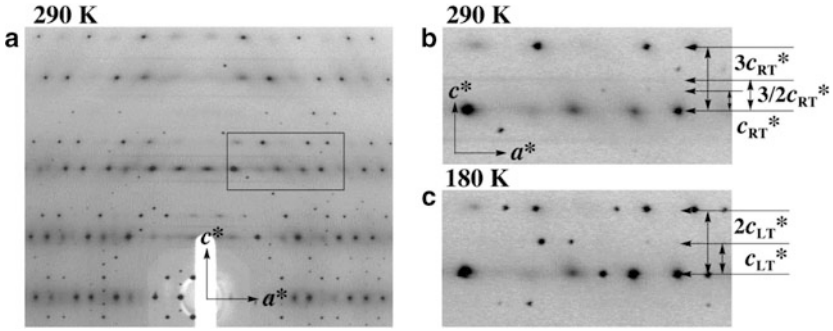

Fig. 9.24 (**a**) X-ray oscillation photographs of $[Pt_2(n\text{-}BuCS_2)_4I]_\infty$ (**4**) taken with an oscillation angle of 3° around *c* axis at 290 K [54]. Axis *c** (1D chain direction) is vertical. (**b**) At 290 K in RT phase. (**c**) At 180 K in LT phase

(c^*_{RT}), where the *l* ($3c^*_{RT}$) is corresponding to a –Pt–Pt–I– period. This is consistent with the periodicity of 1D chain being threefold of a –Pt–Pt–I– period [54]. In addition, diffuse scattering is observed at the reciprocal positions of $l \pm 1/2$ ($3/2c^*_{RT}$) corresponding to twofold of a –Pt–Pt–I– period. Analogously to the diffuse scattering observed for **2** and **3**, the diffuse scattering observed in **4** can therefore be attributed to the twofold periodicity corresponding to a dynamic ACP or CDW state. In Fig. 9.24c taken in the LT phase, the Bragg spots and diffuse scattering observed in the reciprocal positions indexed as $l \pm 1/3$ and $l + 1/2$, respectively, have disappeared and new Bragg spots have appeared at $l + 1/2$ (c^*_{LT}), which is consistent with the twofold periodicity observed in the crystal structure analysis [33]. This result indicates that the valence fluctuation observed as the diffuse streaks has frozen and then the 3D static valence-ordering develops in the LT phase. This is also consistent with the rapid increase in the resistivity at the RT–LT phase transition.

9.2.6.4 $[Pt_2(n\text{-}PenCS_2)_4I]_\infty$ (5)

X-ray diffraction photographs of **5** measured in the HT, RT, and LT phases are shown in Fig. 9.25 [35]. In Fig. 9.25b taken in the RT phase, the weak Bragg spots have appeared at the reciprocal positions indexed as $l \pm 1/3$ (c^*_{RT}), which is consistent with the periodicity of 1D chain being threefold of a –Pt–Pt–I– period [35]. In addition, diffuse streaks are observed at the reciprocal positions of $l \pm 1/2$ ($3/2$ c^*_{RT}) corresponding to twofold of a –Pt–Pt–I– period. The weak Bragg spots corresponding to c^*_{RT} are also observed in the HT and LT phases, and, therefore, the threefold periodic structure remains in the HT and LT phases. In Fig. 9.25a, b, diffuse streaks are observed at the reciprocal positions of $l \pm 1/2$ ($3/2$ c^*_{RT}) corresponding to a dynamic ACP or CDW state. In Fig. 9.25c, the diffuse scattering observed in the RT and HT phases changes to the distinct Bragg spots in the LT phase, indicating that the valence fluctuation has frozen and then the 3D static valence

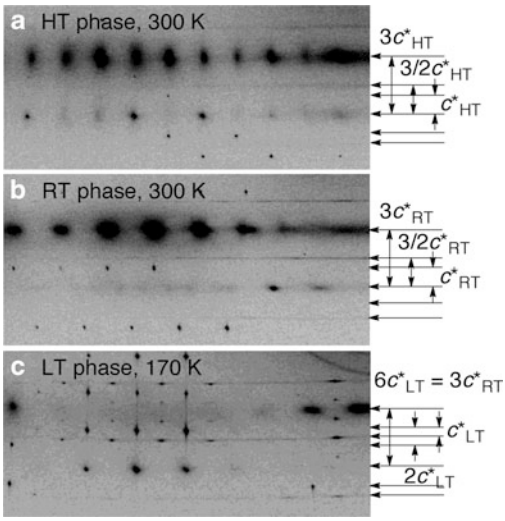

Fig. 9.25 Portions of X-ray oscillation photographs of $[Pt_2(n\text{-}PenCS_2)_4I]_\infty$ (**5**) in each phase taken with an oscillation angle of 3° around *c* axis [35]. Axis *c** (1D chain direction) is vertical. (a) The X-ray diffraction experiment of the supercooled HT phase was carried out at 300 K using a crystal once heated to 350 K

ordering with sixfold periodicity develops in the LT phase, similarly to the semiconducting region of **3** [34]. However, the crystal structure determination of the superstructure corresponding to sixfold of a –Pt–Pt–I– period were unsuccessful.

9.2.7 Magnetic Properties

9.2.7.1 $[Pt_2(MeCS_2)_4I]_\infty$ (1)

The temperature dependence of the magnetic susceptibility of $[Pt_2(MeCS_2)_4I]_\infty$ (**1**) is shown in Fig. 9.26 [31]. In the metallic region of $300 < T < 400$ K, the susceptibility decreases with lowering temperature on the order of 20 % as are often observed in 1D molecular conductors. In most of 1D molecule-based conductors, the temperature dependence of the susceptibility deviates considerably from the Pauli temperature-independent paramagnetism. Kitagawa et al. have stated that one of the most important effects on the deviations from the Pauli-like susceptibility in **1** is the Coulomb interactions which play an important role in the MMX-chain system considered as the Mott–Hubbard system with $U \approx 4t$ [75]. Below $T_{M\text{–}S} = 300$ K, on the other hand, the magnetic susceptibility increases slightly with a slight convex in the χ_M vs. T curve upon cooling to 90 K. If a transition relates to Peierls (CDW) instability, the magnetic susceptibility should become activated below the transition because of the freezing of both charge and spin degrees of freedom. However, the opposite behavior has been observed below 300 K in the susceptibility data. As described in the transport properties, the MMX-chain system is strongly suggested to be the electronic system having an effectively half-filled conduction band. The most important effect especially for the 1D half-filled system is on-site Coulomb repulsion (U)

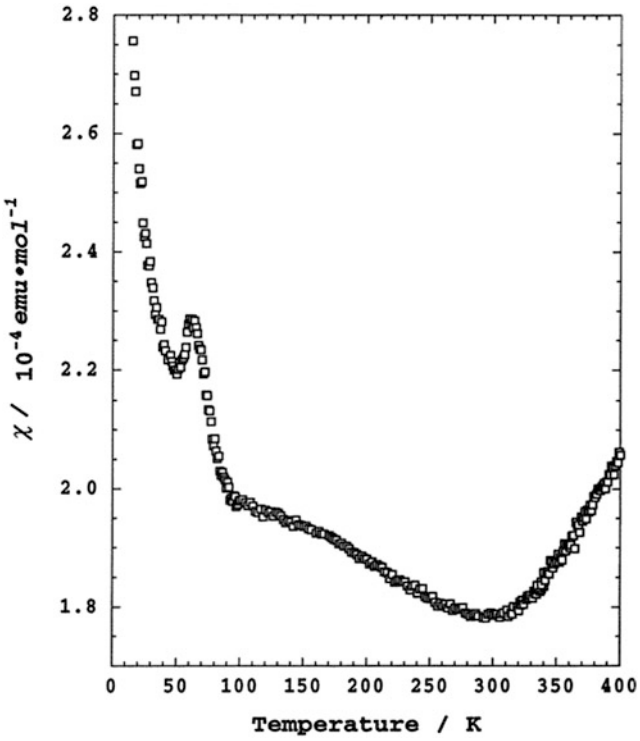

Fig. 9.26 Temperature dependence of the magnetic susceptibility of $[Pt_2(MeCS_2)_4I]_\infty$ (**1**) [31]

and nearest-neighbor interdimer Coulomb repulsion (V). Since only the charge degree of freedom is lost while the spin degree of freedom is maintained below T_{M-S}, Kitagawa et al. have concluded that the semiconducting state can be considered to be a $4k_F$ CDW, that is a Mott−Hubbard insulator in a half-filled band with magnetic disorder and often lead to a SDW or spin-Peierls ground state at low temperatures [31]. Such the Mott−Hubbard transition usually shows no obvious anomaly in χ_M since it is a crossover-type transition from the itinerant-electron (Pauli) paramagnetism to localized-electron paramagnetism.

9.2.7.2 $[Pt_2(EtCS_2)_4I]_\infty$ (2)

The temperature dependence of the magnetic susceptibility of $[Pt_2(EtCS_2)_4I]_\infty$ (**2**) is shown in Fig. 9.27 [32]. The magnetic susceptibility in the metallic state above $T_{M-S} = 205$ K is of the order of ca. 1×10^{-5} emu mol^{-1}. The low susceptibility is consistent with Pauli paramagnetism as one may expect for a conductor. Since this compound shows no obvious anomaly in χ_M with the metal–semiconductor transition, the Mott−Hubbard transition ($4k_F$-CDW) is considered to be a plausible origin of the metal–semiconductor transition, similar to compound **1**. However, the solid-state properties of **2** cannot be perfectly understood by a simple 1D band model.

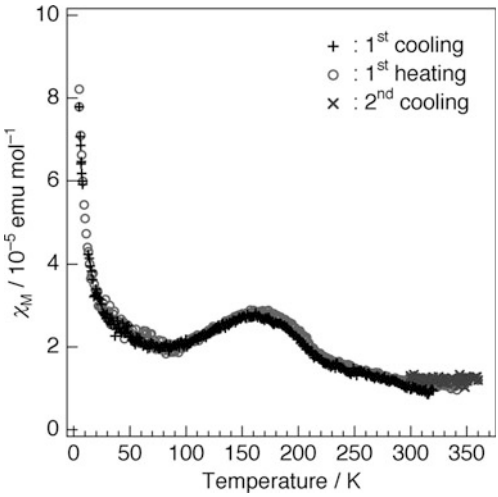

Fig. 9.27 Temperature dependence of the magnetic susceptibility of $[Pt_2(EtCS_2)_4I]_\infty$ (**2**) [32]

The magnetic susceptibility exhibits changes in slope near $T_{M–S}$ and a slight swelling near 160 K. As described in the X-ray Diffuse Scattering section, lateral correlation between 1D chains rapidly develops in this temperature region. The swelling observed in magnetic susceptibility seems to have appeared concerning the rapid development of the lateral correlation, though a clear explanation is not possible at this time. The spin degree of freedom survives at low temperature and loss of the spin degree of freedom accompanied by the transition to the ground state of the ACP state of $–Pt^{2+}–Pt^{3+}–I^-–Pt^{3+}–Pt^{2+}–I^-–$ has not been observed.

9.2.7.3 $[Pt_2(n\text{-}PrCS_2)_4I]_\infty$ (3)

The temperature dependence of the magnetic susceptibility, χ_M, of crystalline samples of **3** is shown in Fig. 9.28 [76]. The χ_M vs. T plot below ca. 300 K can account for paramagnetic impurities and/or lattice and end-of-chains defects. Therefore, the compound **3** takes the spin-singlet state below 300 K. This is consistent with the valence-localized state corresponding to ACP or CDW state observed by the X-ray diffraction study. Above 300 K, on the other hand, the compound **3** exhibits thermally activated magnetic susceptibility, in accordance with the valence-fluctuating state corresponding to a dynamic ACP or CDW state.

9.2.7.4 $[Pt_2(n\text{-}BuCS_2)_4I]_\infty$ (4)

The temperature dependence of the magnetic susceptibility, χ_M, of crystalline samples of **4** is shown in Fig. 9.29 [33]. χ_M of **4** in the RT phase is on the order of 2.9×10^{-5} emu mol^{-1}, which is in accordance with the results of EPR measurements (ca. 2×10^{-5} emu mol^{-1}) [77]. The tail, observed in the χ_M vs. T

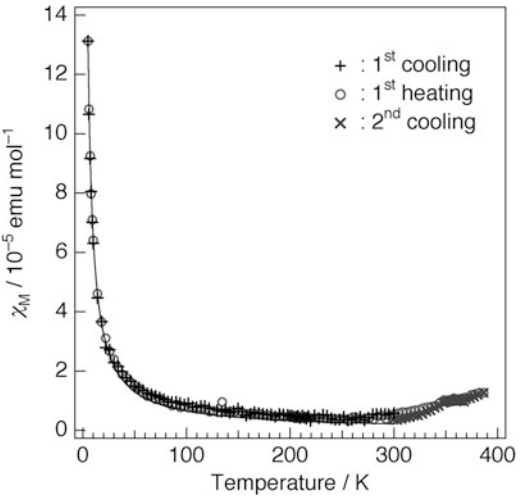

Fig. 9.28 Temperature dependence of the magnetic susceptibility of $[Pt_2(n\text{-}PrCS_2)_4I]_\infty$ (**3**) [76]. The *solid line* represents the fitting to estimate the impurity spin concentration. The estimated Curie spin concentration is only 0.17 %

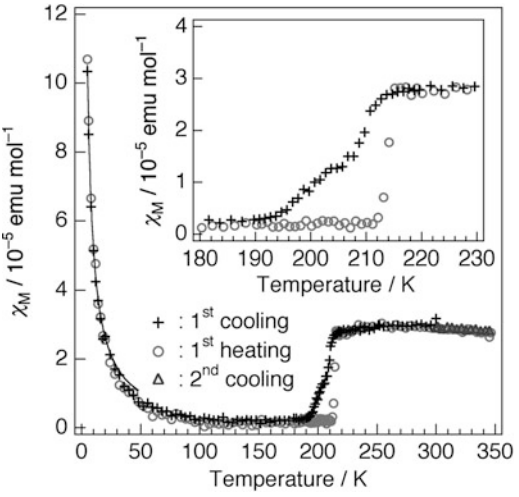

Fig. 9.29 Temperature dependence of the magnetic susceptibility of $[Pt_2(n\text{-}BuCS_2)_4I]_\infty$ (**4**) [33]. The *solid line* represents the fitting to estimate the impurity spin concentration. The estimated Curie spin concentration is only 0.14 %

plot below ca. 30 K, is assigned to paramagnetic centers originating from impurities and/or lattice defects. The most striking feature is an abrupt drop in the χ_M of **4** to the spin-singlet state, with hysteresis, around the first-order RT–LT phase transition from the AV state to the ACP state. The abrupt drop of χ_M in **4** is quite similar to spin-Peierls transitions. The observed magnetic behavior of **4**, however, seems to be well described not by the spin-Peierls transition but by the regular electronic Peierls transition. This is suggested as the transition is the first order in nature, the transition temperature is very high, and sharp increases in ρ and S are observed at the transition [33]. As described in the crystal structure section, the valence-ordering structures in the ground states of **2** and **4** can be regarded as an ACP state. However, an abrupt drop in χ_M has not been observed for **2**, indicating that the spin degree of

freedom persists down to 2 K, similar to **1** [32]. This quite remarkable difference in the magnetic behaviors of **2** and **4** is attributed to the degree of lattice distortion in the 1D MMX chains. As described in the Crystal Structures section, X-ray crystal structure analyses revealed that differences between Pt^{3+}–I^{-} and Pt^{2+}–I^{-} distances of **4** (ca. 0.07 Å) are remarkably larger than that for **2** (0.02–0.03 Å). As these distance differences correspond to the lattice distortion of a 1D MMX chain, it is reasonable to consider that the alternation of an exchange interaction in **4** increases with an increase in lattice distortion, resulting in the spin-singlet state of the low temperature ACP state.

9.2.7.5 $[Pt_2(n\text{-}PenCS_2)_4I]_\infty$ (5)

The temperature dependence of the magnetic susceptibility χ_M of $[Pt_2(n\text{-}PenCS_2)_4I]_\infty$ (**5**) is shown in Fig. 9.30 [35]. The magnetic susceptibility in the RT and HT phases is of the order of 1–2.5 $\times$ 10^{-5} emu mol^{-1}, which is of the same order of magnitude as those observed in **2** and **4**. The low susceptibility is consistent with Pauli paramagnetism as one may expect for a conductor. The most striking feature is an abrupt decrease in the χ_M to the spin-singlet state with the first-order RT–LT phase transition, analogous to compound **4**. In the case of **4**, the spin-singlet state appears with the first-order RT–LT phase transition from the AV state to the ACP state around 205 K [33]. As described in the X-ray diffraction, the compound **5** in the RT phase exhibits the diffuse scattering corresponding to twofold repetition length of a –Pt–Pt–I– period, in addition to the main Bragg spots, which changes to the Bragg spots in the LT phase. Therefore, the compound **5** is considered to take the spin-singlet state with the first-order phase transition from the valence-ordered state close to AV state in the RT phase to the ACP or CDW state in the LT phase. Taking into account the valence-ordered state of **2** and **4** in the LT phase [33], the most probable ground state of **3** and **5** would be the ACP state of –Pt^{2+}–Pt^{3+}–I^{-}–Pt^{3+}–Pt^{2+}–I^{-}–. The temperature dependence of χ_M in the first heating process below RT coincides with that in the first cooling process but exhibits a slight increase at the monotropic phase transition to the HT phase in the temperature range of 324–335 K. It is confirmed from the result of the second cooling process that the HT phase does not return to the RT phase in agreement with the results with the heat capacity measurement [52], EPR measurement [78], and transport properties [35].

9.3 Nickel Complexes

9.3.1 Syntheses

Unlike the diplatinum(III) complex $[Pt_2(RCS_2)_4I_2]$, it is difficult to isolate the dinickel (III) complex $[Ni_2(RCS_2)_4I_2]$ and, consequently, $[Ni_2(RCS_2)_4I]_\infty$ (R = Me (**7**), Et (**8**), *n*-Pr (**9**), and *n*-Bu (**10**)) are directly prepared by the reaction of $[Ni_2(RCS_2)_4]$ with

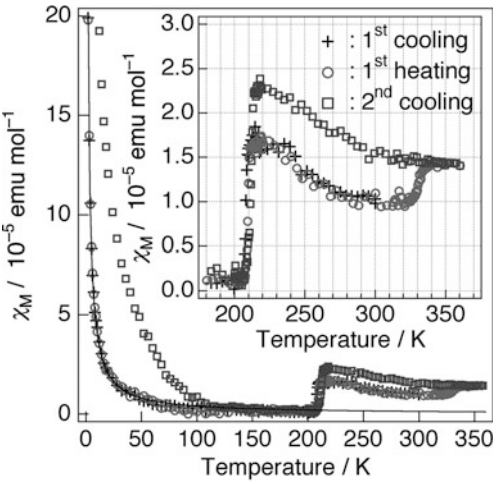

Fig. 9.30 Temperature dependence of the magnetic susceptibility χ_M of $[Pt_2(n\text{-}PenCS_2)_4I]_\infty$ (**5**) [35]. The *solid line* represents the fitting to estimate the impurity spin concentration. The estimated Curie spin concentration is only 0.11 %

iodine in an appropriate solvent [37, 38]. The reported synthetic conditions are listed in Table 9.4. With elongation of the ligand's alkyl chain, the isolation of target compound becomes difficult due to its high solubility. The Ni MMX-chain compounds can be stored without decomposition for several months under an inert atmosphere in a refrigerator but gradually decomposes upon exposure to air at room temperature.

9.3.2 Crystal Structures

9.3.2.1 $[Ni_2(RCS_2)_4I]_\infty$ (R = Me (7), Et (8))

$[Ni_2(RCS_2)_4I]_\infty$ (R = Me (**7**), Et (**8**)) crystallize in the monoclinic *P*2/*n* and *C*2/*c* space groups, respectively, and have analogous structures with the corresponding diplatinum compounds, $[Pt_2(RCS_2)_4I]_\infty$ (R = Me (**1**), Et (**2**)) [37, 38]. Each nickel compound is isostructural but not isomorphous with the corresponding platinum complex. The crystal structure is exemplified with that of the compound **8** [38]. The crystal structure of **8** is shown in Fig. 9.31.

The crystal of compound **8** consists of neutral 1D chains with a repeating –Ni–Ni–I– unit lying on the crystallographic twofold axis parallel to the *b* axis. Two nickel atoms are bridged by four dithiopropanato ligands and the Ni–Ni distance is 2.5479(7) Å, which is 0.22 Å shorter than the distance between the mean planes defined by the four sulfur atoms (2.77(3) Å). This Ni–Ni distance is marginally shorter than that of the dinuclear Ni^{2+}–Ni^{2+} complex, $[Ni_2(MeCS_2)_4]$ (2.564(1) Å), but longer than $[Ni_2(EtCS_2)_4]$ (2.5267(10) Å) [79]. The two NiS_4 square planes are twisted by 28.2(9)° from the eclipsed structure. In the case of diplatinum complexes, it is known that the Pt–Pt distance tends to shorten with increasing the formal oxidation number of the platinum atoms due to the Pt–Pt bond

Table 9.4 Synthetic conductions of $[Ni_2(RCS_2)_4I]_\infty$ (R = Me (**7**), Et (**8**), *n*-Pr (**9**), and *n*-Bu (**10**))

Compound	Precursor complex/mg (mmol)	Iodine/mg (mmol)	Solvent/mL	Yield/mg (%)	Temperature	References
$[Ni_2(MeCS_2)_4I]_\infty$(**7**)[a]	$[Ni_2(MeCS_2)_4]$/484 (1.00)	126 (0.5)	CS_2/100 + 30	–	r.t.	[37]
$[Ni_2(EtCS_2)_4I]_\infty$(**8**)[b]	$[Ni_2(EtCS_2)_4]$/608 (1.13)	110 (0.433)	*n*-hexane–CS_2 (1:1)/110	54 mg 7 %	5–6 °C	[38]
$[Ni_2(n\text{-}PrCS_2)_4I]_\infty$(**9**)[b]	$[Ni_2(n\text{-}PrCS_2)_4]$/1.002 (1.686)	192 (0.756)	*n*-hexane–benzene (1:1)/105	40 mg 3 %	r.t.	[38]
$[Ni_2(n\text{-}BuCS_2)_4I]_\infty$ (**10**)[b]	$[Ni_2(n\text{-}BuCS_2)_4]$/495 (0.761)	50 (0.20)	*n*-hexane–CS_2 (8:1)/30	23 mg 4 %	r.t.	[38]

[a]Suitable crystals for X-ray investigations were obtained by diffusion technique.
[b]This compound was prepared by the vapor diffusion of iodine into a solution containing precursor complex $[Ni_2(RCS_2)_4]$.

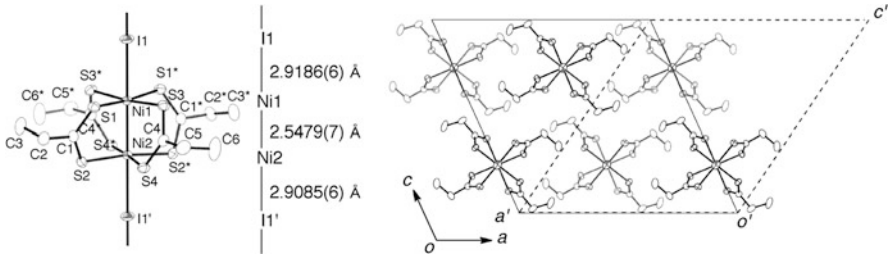

Fig. 9.31 (**a**) 1D chain structure of $[Ni_2(EtCS_2)_4I]_\infty$ (**8**) at 292 K with an atomic numbering scheme and relevant interatomic distances (thermal ellipsoid set at the 50 % probability level) [38]. (**b**) Packing diagrams projected down the *b* axis. A simple vectorial relationship between the unit cell dimensions of $[M_2(EtCS_2)_4I]_\infty$ (M = Ni (**8**), Pt (**2**)) are found to be $a = -a'$, $b' \approx -b$, $c' = a + c$, where the unit cell drawn with the dotted lines refers to the platinum compound **2**

formation by the removal of an electron from the filled dσ* orbital [32, 53]. In contrast, the Ni–Ni distance appears to be strongly influenced by the interaction with the surrounding atoms rather than by the formal oxidation number of the nickel atoms, i.e., Ni–I interaction in **8**, intermolecular Ni ··· S interaction in $[Ni_2(MeCS_2)_4]$ [37], and intermolecular Ni ··· Ni interaction in $[Ni_2(EtCS_2)_4]$ [79], in addition to the packing effect including the twist angle of the two NiS_4 planes. Therefore, the tendency for the M–M distance to shorten with increasing the formal oxidation state is not a criterion for the dinickel complex. The two Ni–I distances are Ni1–I1 = 2.9186(6) and Ni2–I1′ = 2.9085(6) Å, and the bridging iodine atom slightly deviates from the midpoint of the dinuclear units. Generally, the Ni^{2+}–I^- distance is longer than that of Ni^{3+}–I^- since a pair of electrons occupies the d_{z^2} orbital of Ni^{2+}, and therefore the difference between the Ni–I distances indicates a charge disproportionation of the nickel atoms. Taking into account the distinct difference of Ni–I distances, the valence-ordered state of **8** at RT should be assigned to a charge-polarization (CP) state of $-Ni^{(2.5-\delta)+}-Ni^{(2.5+\delta)+}-I^-Ni^{(2.5-\delta)+}-Ni^{(2.5+\delta)+}-I^-$– ($\delta \ll 0.5$) close to an averaged-valence (AV) state. In the case of $[Ni_2(MeCS_2)_4I]_\infty$ (**7**), the shorter interchain S ··· S distances are 3.619(8) and 3.810(5) Å, which are relatively close to the van der Waals contact distance between sulfur atoms (3.60 Å) and it can therefore be regarded as having a two-dimensional interaction [37]. Whereas, the shorter interchain S ··· S distances in **8** are 4.359(1) and 4.973(1) Å, indicating no interchain S ··· S contacts. Therefore, one-dimensionality of **8** is enhanced by the introduction of the ethyl group into dithiocarboxylato ligand instead of the methyl group.

9.3.2.2 $[Ni_2(RCS_2)_4I]_\infty$

RT Phases of $[Ni_2(RCS_2)_4I]_\infty$ (R = *n*-Pr (**9**), *n*-Bu (**10**))

Ikeuchi and Saito et al. have reported the heat capacities of **9** and **10** measured by adiabatic calorimetry [80, 81]. For the compound **9**, a first-order phase transition observed at 205.6 K, indicating the existence of a room-temperature (RT) phase and

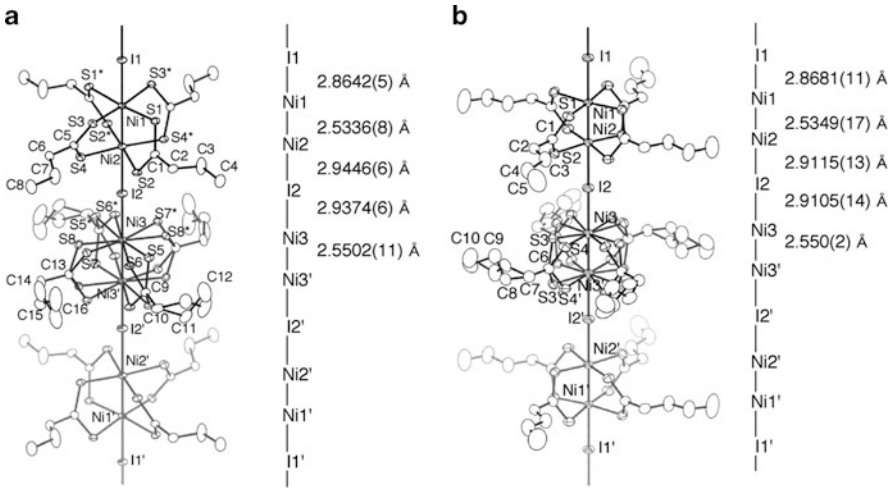

Fig. 9.32 1D chain structures of (**a**) $[Ni_2(n\text{-}PrCS_2)_4I]_\infty$ (**9**) in the RT phase at 240 K and (**b**) $[Ni_2(n\text{-}BuCS_2)_4I]_\infty$ (**10**) at 290 K with an atomic numbering scheme and relevant interatomic distances (thermal ellipsoid set at the 50 % probability level) [38]

a low-temperature (LT) phase [80]. In the compound **10**, on the other hand, three relatively sharp anomalies around 260 K were observed, while a broad anomaly was observed around 135 K [81] These facts indicate the existence of three phases of room temperature (RT), middle temperature (MT), and low temperature (LT). The 1D chain structures of **9** for the RT phase at 240 K and **10** at 290 K are shown in Fig. 9.32 [38].

The RT phase of **9** at 240 K and **10** at 290 K crystallize in the monoclinic space group *C*2/*m* and tetragonal space group *P*4/*mnc*, respectively. Since the crystal structures of **9** and **10** are very similar, the RT phase of **9** is described here. These structures are also analogous to those of the RT phases of the platinum compounds **3**–**5**. The unit cell dimension *b* along the 1D chain in **9** consists of three –Ni–Ni–I– units. Crystallographic mirror planes perpendicular to the 1D chain exist on the I1 atoms and the midpoint of Ni3 and Ni3′ atoms. Therefore, the ligand moieties including sulfur atoms of Ni3–Ni3′ units are disordered on two positions and the twisting directions of two NiS_4 planes of adjacent dinuclear Ni1–Ni2 units in the 1D chain are opposite to each other. Two nickel atoms are bridged by four dithiobutanato ligands and the Ni–Ni distances are Ni1–Ni2 = 2.5336 (8) and Ni3–Ni3′ = 2.5502 (11) Å, which are 0.23 Å shorter than the distances between the mean planes defined by the four sulfur atoms (2.763 (3) and 2.781 (3) Å), respectively. The twist angle between two NiS_4 planes are 28.9 (1)° for a Ni1–Ni2 unit and 27.4 (2)° for a Ni3–Ni3′ unit, respectively. Three Ni–I distances are Ni1–I1 = 2.8642(5), Ni2–I2 = 2.9446(6), and Ni3–I2 = 2.9374 (6) Å. Taking into account the differences in the Ni–I distances, the valence-ordered state of the nickel atoms in the threefold periodic structure may be regarded as $-I^-–Ni^{3+}–Ni^{2+}–I^-–Ni^{2.5+}–Ni^{2.5+}–I^-–Ni^{2+}–Ni^{3+}–I^-–$. In such a valence state, the

unpaired electrons on the adjacent Ni^{3+} sites are expected to take a singlet state due to the strong antiferromagnetic (AF) coupling through a bridging iodine atom. However, as will be described in the Magnetic Properties section, the magnetic data of **9** can be fitted as an $S = 1/2$ 1D AF Heisenberg model. Therefore, the compound **9** at RT phase can be assigned to the valence-ordered state close to the AV state. Adjacent $Ni_2(CS_2)_4$ units of Ni1–Ni2 and Ni3–Ni3′ are twisted by *ca.* 11° from the eclipsed arrangement. The *n*-propyl groups of the dithiobutanato ligands in the Ni1–Ni2 unit have the *anti* form, whereas those of the Ni3–Ni3′ unit take the *gauche* form. Therefore, the origin of threefold periodic structure cannot be attributed to the valence ordering of the nickel atoms, but to both the twist of the adjacent dinickel units and the difference in the conformation of the ligands.

LT Phase of $[Ni_2(n\text{-}PrCS_2)_4I]_\infty$ (**9**)

The space group of **9** changed from *C*2/*m* in the RT phase to *C*2 in the LT phase with the first-order phase transition [38]. Crystal structure of **9** in the LT phase at 140 K is shown in Fig. 9.33. The opposite twist of NiS_4 planes between the adjacent dinickel units in the 1D chain and the difference in conformation of the ligands observed at RT phase have disappeared in the LT phase, and the periodicity of the crystal lattice in the 1D chain direction changes from threefold of a –Ni–Ni–I– period in the RT phase to onefold in the LT phase. The structure consists of three crystallographically independent dinickel units; two of them lie on the crystallographic twofold axis parallel to the *b* axis. The Ni–Ni distances are Ni1–Ni2 = 2.5404 (11), Ni3–Ni4 = 2.5362(11), and Ni5–Ni6 = 2.5388(8) Å. The Ni–I distances in each dinickel unit are Ni1–I1 = 2.9235(8) and Ni2–I1′ = 2.8994(8) Å, Ni3–I2 = 2.9187 (9) and Ni4–I2′ = 2.9084(9) Å, Ni5–I3 = 2.9108(6) and Ni6–I3′ = 2.9152(7) Å, respectively. Taking into account the distinct difference of Ni–I distances, the valence-ordered state of **9** at LT phase should be assigned to a charge-polarization (CP) state of $–Ni^{(2.5-\delta)+}–Ni^{(2.5+\delta)+}–I^-–Ni^{(2.5-\delta)+}–Ni^{(2.5+\delta)+}–Ni^{(2.5-\delta)+}–I^-–$ ($\delta \ll 0.5$) close to the AV state, similarly to **8** in RT phase.

9.3.3 X-Ray Photoelectron Spectra

The Ni $2p_{3/2}$ and $2p_{1/2}$ core level spectra for the mixed-valence compounds **8**–**10** are shown in Fig. 9.34 [38]. Binding energies of the Ni $2p_{3/2}$ and $2p_{1/2}$ core level are summarized in Table 9.5, together with those of the Ni $2p_{3/2}$ core level for the compound **7** [82]. The Ni $2p_{3/2}$ and $2p_{1/2}$ peaks of **8**–**10** were broad compared to those of the corresponding Ni^{2+}–Ni^{2+} compounds, $[Ni_2(RCS_2)_4]$ (R = Et, *n*-Pr, *n*-Bu), and could be resolved into Ni^{2+} $2p_{3/2,1/2}$ and Ni^{3+} $2p_{3/2,1/2}$ doublets. The results have revealed that **8**–**10** exist in the mixed-valence state composed of Ni^{2+} and Ni^{3+} on the time scale of XPS spectroscopy (ca. 10^{-17} s). Although the peak area ratio of Ni^{2+} $2p_{3/2,1/2}$ and Ni^{3+} $2p_{3/2,1/2}$ doublets of **8**–**10** should be equal because of the

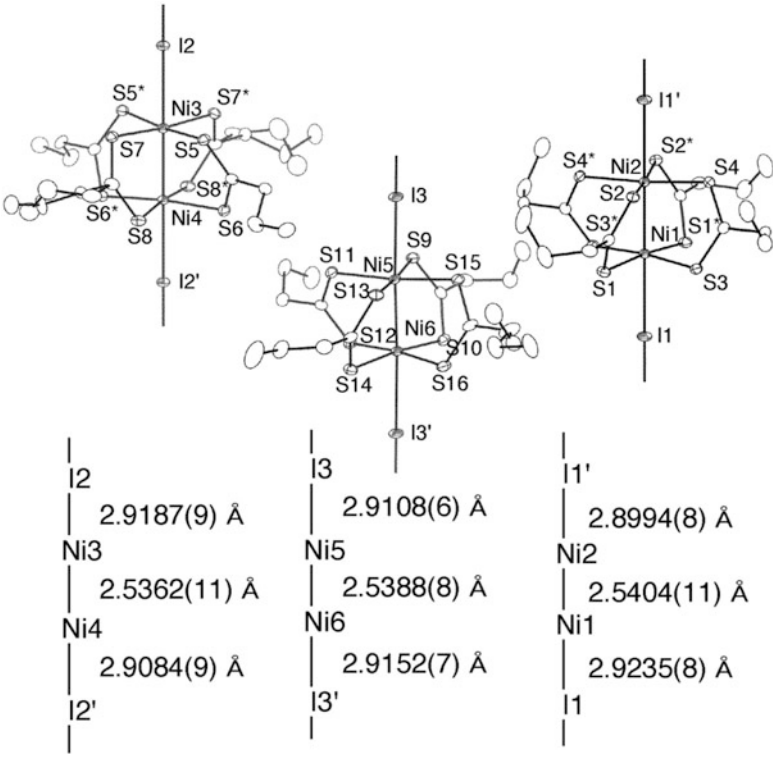

Fig. 9.33 1D chain structures of $[Ni_2(n\text{-}PrCS_2)_4I]_\infty$ (**9**) in the LT phase at 140 K with an atomic numbering scheme and relevant interatomic distances (thermal ellipsoid set at the 50 % probability level) [38]

Ni^{2+}–Ni^{3+} mixed-valence state, the intensity of the Ni^{3+} $2p_{3/2,1/2}$ doublet is very weak compared to that of Ni^{2+}. This would be due to the reduction of Ni^{3+} to Ni^{2+} by X-ray irradiation similar to the observation made for $[Pt_2(EtCS_2)_4I]_\infty$ (**2**) [32].

9.3.4 Electronic State

Electronic absorption spectra of $[Ni_2(RCS_2)_4I]_\infty$ (R = Et (**8**), *n*-Pr (**9**), *n*-Bu (**10**)) are shown in Fig. 9.35, together with that of $[Ni_2(EtCS_2)_4]$ [38]. Spectral data of **7**–**10** are summarized in Table 9.6 [38, 82]. The dominant feature of the absorption spectra of **7**–**10** is an intense sharp band centered at 5,200–5,600 cm^{-1}, which is absent from the spectra of $[Ni_2(RCS_2)_4]$ (R = Me, Et, *n*-Pr, *n*-Bu). To elucidate the electronic structure of the $[Ni_2(RCS_2)_4I]_\infty$, UB3LYP method has been applied to the model structure of $[Ni_2(MeCS_2)_4I]_\infty$ (**7**) [38]. HOMO and LUMO are composed of Ni d_{z^2} −Ni $d_{z^2}\sigma^*$ combination. Those HOMO and LUMO are assigned to a lower Hubbard (LH) dσ* and an upper Hubbard (UH) dσ* orbitals, that split by an on-site Coulomb

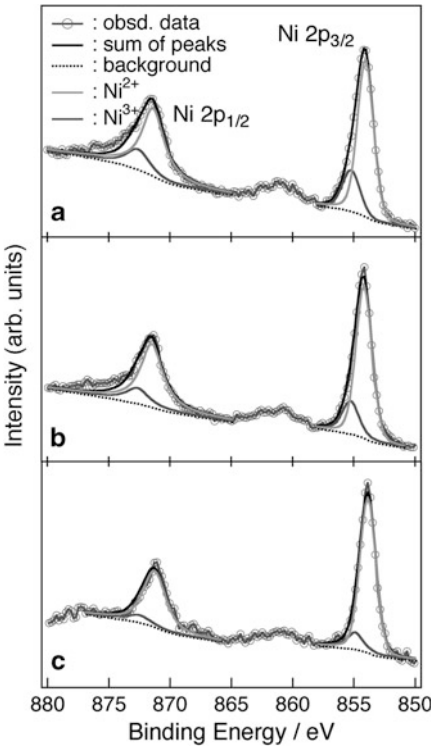

Fig. 9.34 The Ni $2p_{3/2}$ and $2p_{1/2}$ core level spectra for (**a**) $[Ni_2(EtCS_2)_4I]_\infty$ (**8**), (**b**) $[Ni_2(n\text{-}PrCS_2)_4I]_\infty$ (**9**), and (**c**) $[Ni_2(n\text{-}BuCS_2)_4I]_\infty$ (**10**). The *solid lines* are the deconvoluted and sum of the components [38]

Table 9.5 Binding energy (eV) and width of the peaks from the XPS Data for **7**–**10** and corresponding $[Ni_2(RCS_2)_4]$

Compound	Ni^{2+} $2p_{3/2}$	Ni^{3+} $2p_{3/2}$	Ni^{2+} $2p_{1/2}$	Ni^{3+} $2p_{1/2}$
$[Ni_2(MeCS_2)_4]$ [82]	853.8 (1.8)[a]			
$[Ni_2(EtCS_2)_4]$ [38]	854.09 (1.53)		871.29 (2.08)	
$[Ni_2(n\text{-}PrCS_2)_4]$ [38]	854.05 (1.53)		871.18 (2.03)	
$[Ni_2(n\text{-}BuCS_2)_4]$ [38]	854.22 (1.56)		871.38 (1.98)	
$[Ni_2(MeCS_2)_4I]_\infty$ (**7**) [82]	854.04 (1.8)[a]	855.0 (1.8)[a]		
$[Ni_2(EtCS_2)_4I]_\infty$ (**8**) [38]	854.04 (1.53)	855.21 (1.68)	871.37 (2.18)	872.61 (2.23)
$[Ni_2(n\text{-}PrCS_2)_4I]_\infty$ (**9**) [38]	854.16 (1.55)	855.26 (1.59)	871.47 (2.15)	872.65 (2.21)
$[Ni_2(n\text{-}BuCS_2)_4I]_\infty$ (**10**) [38]	853.86 (1.53)	854.90 (1.53)	871.26 (2.20)	872.50 (2.20)

Full width at half-maximum values (fwhm) for peaks are given in parentheses
These values were corrected against the C 1s peak using a value of 284.6 eV
[a]Only Ni $2p_{3/2}$ values were reported [82].

repulsion energy U on a MM unit originating from a strong electron–electron repulsion on the nickel atoms. Schematic energy-band structure of $[Ni_2(RCS_2)_4I]_\infty$ is also shown in Fig. 9.35. HOMO–LUMO gap corresponding to U is 1.97 eV. Next HOMO is

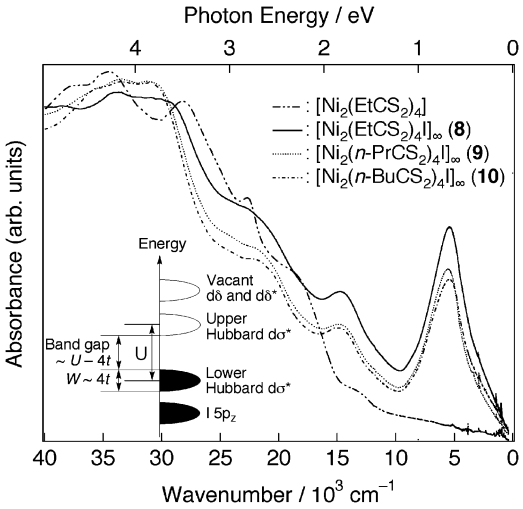

Fig. 9.35 Electronic absorption spectra of $[Ni_2(EtCS_2)_4I]_\infty$ (**8**), $[Ni_2(n\text{-}PrCS_2)_4I]_\infty$ (**9**), and $[Ni_2(n\text{-}BuCS_2)_4I]_\infty$ (**10**) in the solid state (KI pressed disks), together with that of $[Ni_2(EtCS_2)_4]$ [38]. The *inset* shows the schematic energy-band structure of $[Ni_2(MeCS_2)_4I]_\infty$ estimated by the unrestricted hybrid DFT calculation (UB3LYP) methods using the dimer and tetramer models

Table 9.6 Electronic absorption spectral data of **7**–**10** in the solid-state [38, 82]

Compound	Wavenumber/10^3 cm^{-1}[a]
$[Ni_2(EtCS_2)_4]$ [38]	13.5 (sh), 18.6 (sh), 22.7, 28.2
$[Ni_2(n\text{-}PrCS_2)_4]$ [38]	12.6 (sh), 17.4 (sh), 22.6 (sh), 27.2 (sh), 29.6
$[Ni_2(n\text{-}BuCS_2)_4]$ [38]	13.4 (sh), 18.5 (sh), 22.2, 27.5
$[Ni_2(MeCS_2)_4I]_\infty$ (**7**) [82]	5.2 (650 meV)[b]
$[Ni_2(EtCS_2)_4I]_\infty$ (**8**) [38]	5.4, 14.7, 22.0 (sh), 29.3
$[Ni_2(n\text{-}PrCS_2)_4I]_\infty$ (**9**) [38]	5.6, 14.8, 21.1 (sh), 30.7
$[Ni_2(n\text{-}BuCS_2)_4I]_\infty$ (**10**) [38]	5.5, 14.9, 21.0 (sh), 30.7

[a]Measured using KBr pressed disks for $[Ni_2(RCS_2)_4]$ (R = Et, *n*-Pr, *n*-Bu) and using both KBr and KI disks for **8**–**10** at 298 K.
[b]Only a strong absorption band observed in near-IR region was reported [82].

mainly composed of I $5p_z$ orbitals. In order to estimate transfer energy t and on-site Coulomb repulsion energy U in the bulk, the following equations concerning t, U, and an effective exchange integral J are used [42, 83, 84].

$$J = \frac{2(E^{LS} - E^{HS})}{\left\langle \hat{S}^2 \right\rangle^{HS} - \left\langle \hat{S}^2 \right\rangle^{LS}}$$

$$J = -\frac{4t^2}{U}$$

$$\frac{|t|}{U} = \frac{n-1}{2}$$

where E^X and $\left\langle \hat{S}^2 \right\rangle^X$ denote the total energy and the total spin angular momentum for the spin state X (X = broken symmetry low spin (LS) state ($S = 0$) and high spin (HS) state ($S = 1$), respectively). The equation for J values corrects a spin contamination error in LS state. And n is an occupation number of the highest occupied natural orbital, which is a magnetic orbital calculated by UB3LYP method [43]. From DFT results and above equations, the estimated parameters are $J = -975$ cm^{-1}, $n = 1.268$, $U = 1.68$ eV, and $t = 0.226$ eV, respectively. A result of the similar calculation using UBH and HLYP method with a tetra-MM units model also estimated $U = 1.03$ eV and $t = 0.116$ eV [42]. Assuming the bandwidth $W = 4t$ is valid since the 1D Ni MMX system is 1D strong electron correlated system, $4t$ is 0.904 eV (0.464 eV for the tetramer model). Accordingly, band energy gap, $E_g \sim U - 4t$ is 0.776 eV (0.566 eV for the tetramer model). On the assumption that the energy difference between the di-MM and tetra-MM models approximates error limits, the E_g is 570–780 meV, which is consistent with the E_{opt} observed for **7**–**10**. Therefore, the intense absorption band observed near 650–670 meV has been attributed to the transition from the LH dσ* band to UH dσ* band.

9.3.5 Electrical Conductivity

Yamashita et al. have reported that the single crystals of $[Ni_2(MeCS_2)_4I]_\infty$ (**7**) show semiconducting behavior with a small activation energy E_a of 100–250 meV and a relatively high conductivity at RT of $\sigma_{RT} = 2.5 \times 10^{-2}$ S cm^{-1} [29]. Temperature dependences of the electrical conductivity σ of $[Ni_2(RCS_2)_4I]_\infty$ (R = Et (**8**), *n*-Pr (**9**), *n*-Bu (**10**)) are shown in Fig. 9.36 [38]. The electrical conductivity of **8**–**10** are 1.6×10^{-3} S cm^{-1} at 290 K, 7.6×10^{-4} S cm^{-1} at 290 K, and 6.0×10^{-4} S cm^{-1} at 287 K, respectively, which are one or two order of magnitude smaller than that of **7**. The compounds **8**–**10** show typical semiconducting behavior in the temperature range measured and the activation energy E_a of **8**–**10** estimated from the Arrhenius equation, a plot of ln σ vs. T^{-1}, are 198(1), 143(3), and 339(2) meV, respectively. These values are relatively close to that of **7** [29]. **10** satisfies the relationship of $2E_a = E_{opt}$, where E_a is an activation energy estimated by the electrical conductivity and E_{opt} is the optical band gap, whereas the relationship of $2E_a = E_{opt}$ does not hold for **8** and **9**. This is presumably attributable to a decrease in the E_a by impurity existing in the sample.

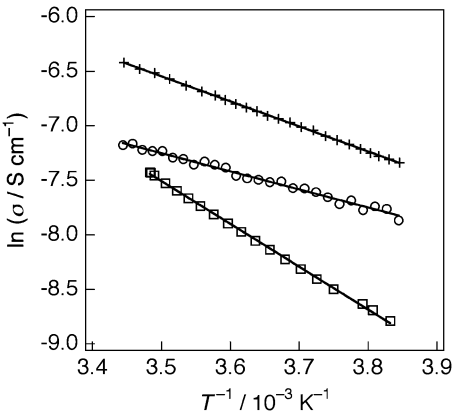

Fig. 9.36 Temperature dependence of the electrical conductivity of **4** (*plus*), **5** (*circle*), and **6** (*square*) [38]

9.3.6 *Magnetic Properties*

Yamashita et al. have reported that the magnetic susceptibility of $[Ni_2(MeCS_2)_4I]_\infty$ (**7**) is essentially temperature independent down to about 50 K (ca. 10^{-6} emu g^{-1}) and then rapidly increases at lower temperature [29]. The observed temperature independent behavior has been ascribed to the very strong antiferromagnetic coupling between the unpaired electrons on the Ni^{3+} sites. The temperature dependences of the magnetic susceptibilities χ_M of $[Ni_2(RCS_2)_4I]_\infty$ (R = Et (**8**), *n*-Pr (**9**), *n*-Bu (**10**)) are shown in Fig. 9.37 [38]. The common feature of the three compounds is that the susceptibility at room temperature is considerably lower than that expected for one $S = 1/2$ spin per dimer. Furthermore, there are distinct differences between those of **8** and **9** and that of **10** regarding the appearance of a gradual drop around 50 K for the former two. In addition, **9** exhibits an anomaly in the temperature range 200–212 K, which is associated with the first-order phase transition from the RT phase to the LT phase, as discussed already. Assuming an $S = 1/2$ 1D Heisenberg AF chain model, the Bonner–Fisher equation ($H = J \Sigma S_i \cdot S_{i+1}$) [85, 100] has been applied to fit the susceptibility data above 100 K for **8** and 68 K for **9**. The fitting gives exchange coupling constant of $|J|/k_B = 936(2)$ K for **8** and $|J|/k_B = 898(2)$ K for **9**. These J values are in fair agreement with the theoretical J value of −1,160 K calculated for $[Ni_2(MeCS_2)_4I]_\infty$ (**7**) using the UB3LYP method [42]. The very large J value indicates a very strong AF interaction between the spin of the Ni^{3+} ions through the bridging iodide ion, justifying considerable electronic overlap between the d_{z^2} (Ni) and p_z (I) orbitals. The key feature of the magnetic susceptibility is that it decreases more rapidly below 47 K for **8** and 36 K for **9**. The χ_M values of **8** and **9** take a minimum at about 30 and 16 K, respectively, and then show an increase due to the presence of paramagnetism originating from impurities or lattice and end-of-chain defects. Assuming that the impurities have have an S = 1/2 spin, their concentrations are estimated to be 0.35 % for **8** and 0.07 % for **9**. By subtracting these contributions from the experimental data, the corrected χ_M values of **8** and **9** are found to decrease to a small constant value. This rapid decrease in χ_M strongly

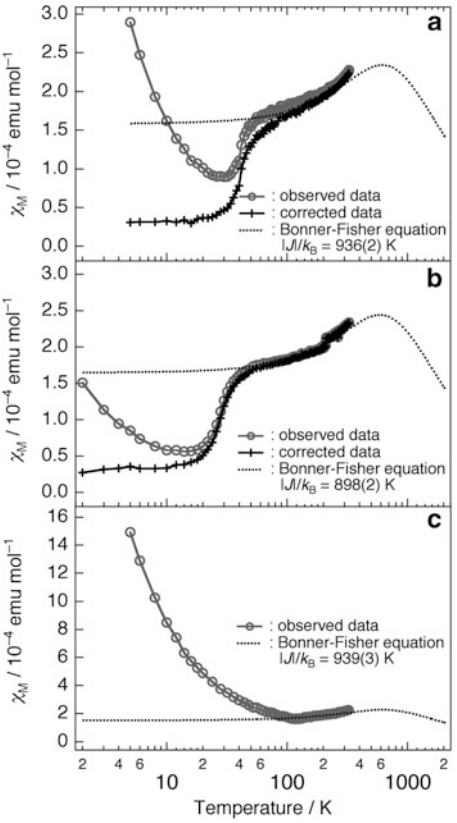

Fig. 9.37 Temperature dependence of the observed (*circle*) and corrected (*plus*) magnetic susceptibilities of **8** (**a**), **9** (**b**), and **10** (**c**) and the Bonner–Fisher fits (*dotted lines*) [38]. The estimated impurity Curie spin contributions are subtracted in the corrected data

suggests the possibility of a spin-Peierls (SP) transition [86–94]. Ikeuchi and Saito et al. have reported that, for each compound, a small broad thermal anomaly due to a spin-Peierls transition was observed around 40 K in the relaxation calorimetry. [80]. A spin-Peierls system undergoes a phase transition at T_{sp}, where for $T < T_{sp}$ a temperature-dependent structural dimerization takes place, creating an opening of a spin gap between the singlet and triplet spin states. To date, numerous spin-Peierls materials have been reported, as represented by the organic system TTF-CuBDT [87] and the inorganic system $CuGeO_3$ [88, 89]. The exchange constants and transition temperatures are $|J|/k_B = 77$K and $T_{sp} = 12$ K for TTF-CuBDT and $|J|/k_B = 120$ K and $T_{sp} = 14$ K for $CuGeO_3$. On the other hand, α'-NaV_2O_5 was also considered a possible inorganic spin-Peierls system with a large exchange coupling constant of $|J|/k_B = 560$ K and a high-transition temperature $T_c = 35.3$ K [90–92], but more recent studies have revealed that this phase transition may be a novel cooperative phase transition associated with valence ordering, lattice dimerization, and spin gap formation [93, 94]. The spin Hamiltonian of the spin-Peierls phase below T_{sp} may be described by the alternating AF chain:

$$H = J' \Sigma [S_{2i} \cdot S_{2i-1} + \gamma S_{2i} \cdot S_{2i+1}].$$

γ is the alternation parameter, where $\gamma = 1$ corresponds to a uniform chain limit, while $\gamma = 0$ corresponds to the dimer limit. According to the analysis by Ohama et al. [92], which is based on the theory of Bulaevskii [95], the LT magnetic susceptibility is approximated by

$$x = \frac{Ng^2{\mu_B}^2\alpha}{k_B T} \exp(-J'\zeta/T)$$

where α and ζ are parameters that depend on the alternating parameter γ and approach unity as $\gamma \to 0$ (the dimer model) and approach zero as $\gamma \to 1$ (the uniform chain model). By fitting the equation to a ln $\chi_M T$ vs. T^{-1} plot, the estimated value of $J'\zeta$, which corresponds to an excitation energy gap Δ, is 95(7) K for **8** and 77(2) K for **9**. When the lattice dimerizes, the two unequal and alternating J_1 and J_2 values are expressed as follows [87]

$$J_{1,2}(T) = J\{1 \pm \delta(T)\}.$$

According to the mean field theory of Pytte, the relationship between $\delta(T)$ and the excitation energy gap $\Delta(T)$ at temperature T is expressed as [96]

$$\delta(T) = \Delta(T)/pJ$$

where the value of p is 1.637. Using this method, $\delta(T) = 0.062$ and $J_2/J_1 = 0.88$ for **8** and $\delta(T) = 0.052$ and $J_2/J_1 = 0.90$ for **9** have been obtained. The values of $2\Delta(0)/k_B T_{sp}$ of **8** and **9** are 4.04 and 4.28, respectively, which are larger than the value of the typical spin-Peierls materials (TTF-CuBDT, MEM-$(TCNQ)_2$ [97], and $CuGeO_3$) that satisfy the BCS formula $2\Delta(0)/k_B T_{sp} = 3.53$ but are smaller than that of α'-NaV_2O_5 (6.44) [91]. This discrepancy of $2\Delta(0)/k_B T_{sp}$ is attributed to the larger fluctuation effects compared to ordinary spin-Peierls materials. According to the theory of Cross and Fisher [98], T_{sp} is given by

$$T_{sp} = 0.8J\eta'$$

where η' is the spin–lattice coupling constant and $\eta' = 0.063$ for **8** and 0.050 for **9**, which is smaller than the value of typical spin-Peierls materials (0.195, 0.209, and 0.146 for TTF-CuBDT, MEM-$(TCNQ)_2$, and $CuGeO_3$) but is relatively close to the value of α'-NaV_2O_5 (0.079). The phase-transition temperatures of **8** and **9** are suppressed since the coupling between the spin and lattice system is weak due to the large 1D fluctuations. Parameters defining spin-Peierls systems are listed in Table 9.7.

On the other hand, the magnetic susceptibility of **10** gradually decreases with a lowering of the temperature, as shown in Fig. 9.37c and shows a broad minimum at around 135 K. When the experimental data above 140 K are fitted by the Bonner–Fisher equation, $|J|/k_B$ is estimated to be 939(3) K. Below 135 K, χ_M

Table 9.7 Parameters defining some spin-Peierls systems

Compound	$\lvert J\rvert/k_B$	$\Delta(0)$/K	T_{sp}/K	η'	$2\Delta(0)/k_BT_{sp}$	References
TTF-CuBDT	77	21	12	0.195	3.50	[87]
MEM-$(TCNQ)_2$	106	28	17.7	0.209	3.16	[86, 97]
$CuGeO_3$	120	24.5	14	0.146	3.50	[88, 89]
α'-NaV_2O_5	560	113.7	35.3	0.079	6.44	[90–94]
8	936(2)	95(7)	47	0.063	4.04	[38]
9	898(2)	77(2)	36	0.050	4.28	[38]

rapidly increases with a lowering of the temperature. Assuming that the increase of χ_M below 50 K is originated from the impurity spin, the impurity spin concentration is estimated to be 1.8 %. However, the origin is considered not to be impurity spin but another factor, since this value is much larger than those of **8** and **9**. Saito et al. observed a broad thermal anomaly in the heat capacity measurement of **10**, which is attributed to a higher order phase transition around 135 K [81]. Therefore, it is reasonable to assume that the structural modulation occurs with the higher order phase transition, and the magnetic defects giving free spins would be formed in the 1D chain below 135 K. As a consequence, a spin-Peierls transition appears to be suppressed in **10**.

9.3.7 Synchrotron Radiation X-ray Crystallography

A spin-Peierls system undergoes a lattice instability at T_{sp}, and when $T < T_{sp}$, the system dimerizes and the spin gap opens. Figure 9.38 shows the synchrotron X-ray diffraction photographs of **8** [38]. In contrast to the diplatinum compounds **2**–**5** [32, 34, 35, 54, 73], the dinickel compounds **8** and **9** do not show any X-ray diffuse scattering, demonstrating that the dinickel compounds do not exhibit valence fluctuation. Whereas, new reflections clearly appear in the photographs of **8** taken below 35 K, indicating a twofold superstructure. The number and intensities of the superlattice reflections increase as the temperature is lowered. This fact indicates that the unit cell along the *b* axis has doubled, which strongly implies that the lattice dimerizes along the –Ni–Ni–I– chain. When the superlattice reflections are included, the supercell can be indexed by $a_{super} = -0.5a - 0.5b$, $b_{super} = 0.5a - 1.5b$, and $c_{super} = 0.5a + 0.5b + c$, and the space group changes from $C2/c$ to $P\bar{1}$. Figure 9.39 shows the crystal structure of the superstructure of **8** at 26 K [38].

Two crystallographically independent $[Ni_2(EtCS_2)_4I]$ units exist in a unit cell of **8** in the LT phase, and the periodicity of the crystal lattice is twofold of a –Ni–Ni–I– period. The two Ni–Ni distances are almost the same (Ni1–Ni2 = 2.5387(9) and Ni3–Ni4 = 2.5402(9) Å), but there are two different Ni–I distances. The short Ni–I distances (Ni2–I2 = 2.8773(7) and Ni3–I2 = 2.8839(7) Å) are about 0.013 Å less than the long Ni–I distances (Ni1–I1 = 2.8975(7) and Ni4–I1* = 2.8888(7) Å). The twofold superstructure originates from the different Ni−I distances since the structures of the two crystallographically independent $[Ni_2(EtCS_2)_4]$ units are almost the same and twisting between dinuclear units does not occur. The doubling

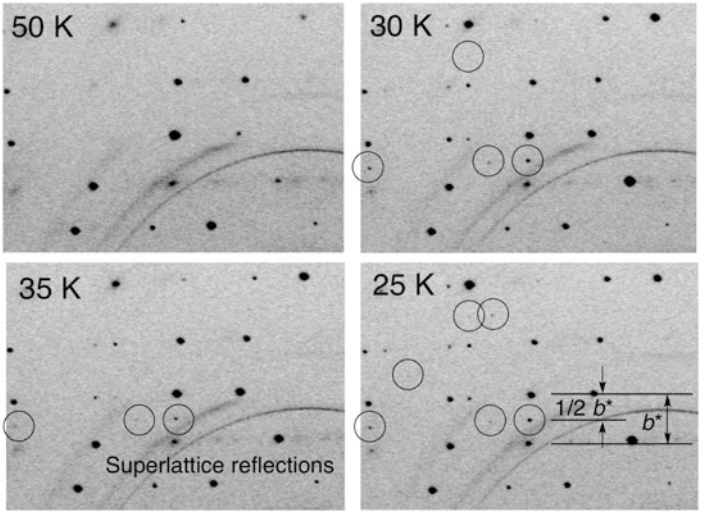

Fig. 9.38 X-ray diffraction photographs of $[Ni_2(EtCS_2)_4I]_\infty$ (**8**) taken at different temperatures. b^* (1D chain direction) is vertical in these photographs [38]. The diffuse circular lines originate from the carbon fiber mounting a single crystal

of the lattice periodicity and the increase of the superlattice reflections on lowering the temperature strongly support the spin-Peierls transition at 47 K. The Ni–Ni and Ni–I distances indicate that the valence-ordered state in the LT phase is the ACP state of $-Ni^{(2.5-\delta)+}-Ni^{(2.5+\delta)+}-I^-Ni^{(2.5+\delta)+}-Ni^{(2.5-\delta)+}-I^-$ ($\delta \ll 0.5$). This phase transition is a spin-Peierls transition that accompanies the rearrangement of the valence ordering. In diplatinum compounds $[Pt_2(RCS_2)_4I]_\infty$ (R = Et (**2**), *n*-Bu (**4**)), the difference between the long and short Pt–I distances, that characterizes the degree of the lattice distortion, is 0.029 and 0.066 Å, respectively [33]. The lattice distortion of **8** is therefore smaller than those of the diplatinum compounds. The diplatinum compounds can be largely polarized due to the larger span of the $5d_{z^2}$ orbitals, whereas the degree of charge polarization of the nickel compound is small since this material tends to retain a valence state close to the AV state due to the strong electron–electron correlation effect on the $3d_{z^2}$ orbitals of the nickel atoms. Compound **9** also exhibits superlattice reflections at the positions of $1/2b^*$ corresponding to the twofold –Ni–Ni–I– period at temperatures below $T_{sp} = 36$ K. Attempts to index the superlattice reflections have been, however, unsuccessful because of their very weak intensities [38].

On the basis of the crystal structure analyses of the superstructure, the valence-ordered states of $[M_2(EtCS_2)_4I]_\infty$ (M = Ni (**8**), Pt (**2**)) are assigned to the ACP state. In contrast, the spin-Peierls transition has not been observed in $[Ni_2(MeCS_2)_4I]_\infty$ (**7**), and the superlattice reflections due to the development of the superstructure associated with the twofold periodic valence ordering have not been reported in $[M_2(MeCS_2)_4I]_\infty$ (M = Ni (**7**), Pt (**1**)). The reasons for these results are discussed

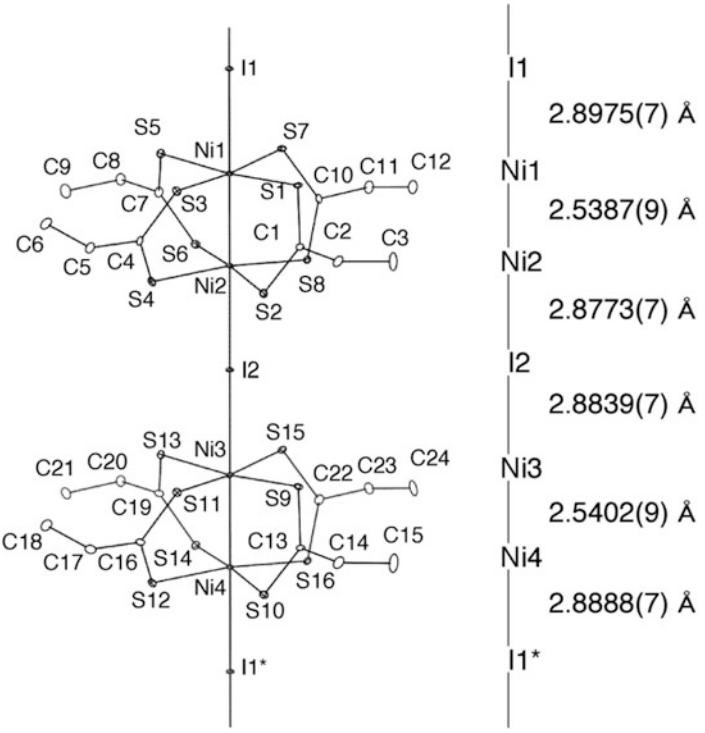

Fig. 9.39 1D chain structure of $[Ni_2(EtCS_2)_4I]_\infty$ (**8**) at 26 K with an atomic numbering scheme and relevant interatomic distances (thermal ellipsoid set at the 50 % probability level) [38]

here based on the relative arrangement of 1D chains in the crystal, which minimizes the Coulomb repulsion between them. As shown in Fig. 9.40, there are two types for the arrangements of 1D chains [38].

Adjacent 1D chains in arrangement type (a) shift about a half period from each other, whereas the 1D chains in arrangement type (b) are aligned with the same phase. Here I discuss the twofold periodic valence ordering which minimizes the Coulomb repulsion between the 1D chains. The type (b) arrangement is capable of taking both valence-ordered ACP and CDW states. $[M_2(MeCS_2)_4I]_\infty$ (M = Ni (**7**), Pt (**1**)) have relatively short interchain S $\cdots$ S contacts in the type (a) arrangement, and these compounds are considered to have two-dimensional interactions [28, 37]. When a 1D chain takes the ACP state in type (a), adjacent 1D chains should take the CDW state to minimize the Coulomb repulsion. As a result, it is presumed that these compounds would have difficulty adopting the superstructure associated with the twofold periodic valence ordering, and consequently, $[Ni_2(MeCS_2)_4I]_\infty$ (**7**) would be difficult to show the spin-Peierls transition associated with the ACP state. On the other hand, it is possible for $[Ni_2(RCS_2)_4I]_\infty$ (R = Et (**8**), *n*-Pr (**9**)) to adopt twofold periodic valence ordering, since the one-dimensionality of these compounds

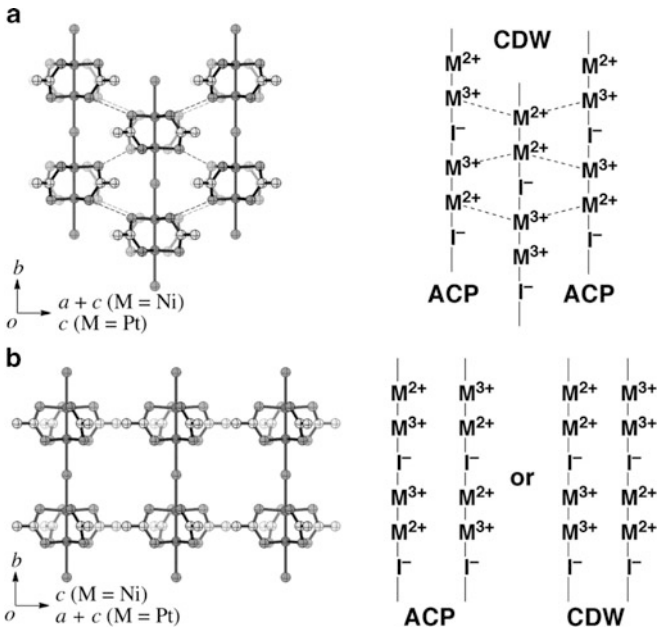

Fig. 9.40 Relationship between relative arrangement of 1D chains in the crystal of $[M_2(MeCS_2)_4I]_\infty$ (M = Ni (**7**), Pt(**1**)) and possible twofold periodic valence ordering to minimize the Coulomb repulsion [38]. The dashed lines represent the interchain S···S contacts, which are relatively close to the van der Waals contact distance between sulfur atoms (3.60 Å)

becomes more pronounced with the elongation of the alkyl chain of the dithiocarboxylato ligands.

9.4 Conclusions

Unlike the MX-chain compounds, an unpaired electron of the MMX-chain compounds is possible to behave as an itinerant electron, since the influence of U becomes smaller by sharing of an unpaired electron through a metal–metal bond. Actually, the first observation of metallic conductivity was made for $[Pt_2(MeCS_2)_4I]_\infty$ (**1**) above 300 K. The analyses of the diffuse scattering observed in the metallic state of $[Pt_2(EtCS_2)_4I]_\infty$ (**2**) has revealed that the metallic state has appeared by the valence fluctuation accompanying the dynamic valence-ordering state of the CDW type. The fact indicates that the electron–lattice interaction has also governed the electronic states of the Pt MMX compounds, in analogy with the Pt MX-chain compounds. The observed dynamic electronic state is considered to appear through the electron–lattice interaction by the thermal energy being comparable to the stretching vibration energy of Pt–I bonds, because the electronic states of the Pt MMX compounds $[Pt_2(RCS_2)_4I]_\infty$ (R = Et (**2**), *n*-Bu (**4**), and

n-Pen (**5**)) change from a static state to dynamic one at near 200 K (≈140 cm^{-1}). The Pt compounds become insulator with lowering temperature due to the lattice dimerization originating from an effectively half-filled metallic band. The Pt compounds shows not only small magnetic susceptibility corresponding to the itinerancy of the unpaired electrons in the metallic state but also the paramagnetic–nonmagnetic transition originating from the regular electronic Peierls transition. The valence-ordering state of the Pt MMX compounds of the dta family at the low temperature is assigned to be the ACP state of $–Pt^{2+}–Pt^{3+}–I^{-}–Pt^{3+}–Pt^{2+}–I^{-}–$. On the other hand, all the Ni MMX-chain compounds are Mott-Hubbard semiconductor due to the strong on-site Columbic repulsion on the nickel atom and exhibit very strong antiferromagnetic interaction. Furthermore, the spin-Peierls transition has been observed in $[Ni_2(RCS_2)_4I]_\infty$ (R = Et (**8**), *n*-Pr (**9**)) at low temperature.

The partial oxidation of the metal atoms is essential to realize the metallic state being stable down to the low temperature. In the case of the copper oxide superconductors, the superconductivity has been realized by the partial oxidation of the CuO_2 plane in the strongly correlated electronic systems ($U/t \gg 1$) [16]. Therefore, the partial oxidation of the Ni MMX compounds having strong electron correlation is very interesting from the viewpoint of appearance of the superconductivity that is never realized in the 1D electronic system.

The elongation of alkyl chain of the dithiocarboxylato ligand not only eliminated the interchain S···S contacts and enhanced the one-dimensionality of the chains, but also introduced motional degrees of freedom in the system. As a consequence, several interesting properties that were never observed in $[M_2(MeCS_2)_4I]_\infty$ (M = Pt (**1**), Ni (**7**)) have appeared. By the elongation of the alkyl chains in dithiocarboxylato ligands, $[Pt_2(RCS_2)_4I]_\infty$ (R = *n*-Pr (**3**), *n*-Bu (**4**), and *n*-Pen (**5**)) underwent two phase transitions at near 210 K and above room temperature, indicating the existence of the LT, RT, and HT phases. The periodicity of crystal lattice along 1D chain is threefold of a –Pt–Pt–I– unit, and the structural disorders were detected for the dithiocarboxylato group and the alkyl chain belonging to only the central dinuclear units in the threefold periodicity. In the HT phase, the dithiocarboxylato groups of all the dinuclear units were disordered. Ikeuchi and Saito have revealed from the heat capacity measurements that the entropy (disorder) reserved in alkyl groups in the RT phase is transferred to the dithiocarboxylate groups with the RT–HT phase transition. Whereas, the dithiocarboxylate groups of all the dimetal units in the LT phase of $[Pt_2(n\text{-}BuCS_2)_4I]_\infty$ (**4**) were ordered. The Pt MMX-chain compounds exhibited a rapid increase in resistivity and a drastic change in the magnetism to the diamagnetic state with the structural phase transition from the RT phase to LT one at near 200 K. This fact suggests that the dynamics (motional degrees of freedom) of the dithiocarboxylato ligands and bridging iodine atoms affects the electronic and magnetic systems through the electron–lattice interaction. On the other hand, the Ni MMX-chain compound, $[Ni_2(n\text{-}PrCS_2)_4I]_\infty$ (**9**), behaved the 1D antiferromagnetic chain in the both RT and LT phases, and only the coupling constant *J* slightly changed with the structural phase transition. This fact demonstrates that, unlike the platinum compounds, the electronic system of the Ni MMX-chain compounds in which the

on-site Columbic repulsion U plays a dominant role in determining the electronic system is hardly affected by the molecular dynamics.

References

1. Robin MB, Day P (1967) Adv Inorg Chem Radiochem 10:247–422
2. Day P (1975) In: Keller HJ (ed) Low-dimensional Cooperative Phenomena, vol. 7, NATO ASI series, series B, Plenum Press, New York, NY, pp 191–214
3. Day P (1977) In: Keller HJ (ed) Chemistry and physics of one-dimensional metals, vol 25, NATO ASI series, series B. Plenum, New York, NY, pp 197–223
4. Soos ZG, Keller HJ (1977) In: Keller HJ (ed) Chemistry and physics of one-dimensional metals, vol 25, NATO ASI series, series B. Plenum, New York, NY, pp 391–412
5. Keller HJ (1983) In: Miller JS (ed) Extended linear chain compounds, vol 1. Plenum, New York, NY, Chapter 8
6. Clark RJH (1990) Chem Soc Rev 19:107–131
7. Yamada S, Tsuchida R (1956) Bull Chem Soc Jpn 29:894–898
8. Okamoto H, Toriumi K, Mitani T, Yamashita M (1990) Phys Rev B 42:10381–10387
9. Tanaka M, Kurita S, Okada Y, Kojima T, Yamada Y (1985) Chem Phys 96:343–348
10. Clark RJH, Kurmoo M (1980) Inorg Chem 19:3522–3527
11. Tanino H, Kobayashi K (1983) J Phys Soc Jpn 52:1446–1456
12. Toriumi K, Wada Y, Mitani T, Bandow S, Yamashita M, Fujii Y (1989) J Am Chem Soc 111:2341–2342
13. Nasu K (1983) J Phys Soc Jpn 52:3865–3873
14. Kishida H, Matsuzaki H, Okamoto H, Manabe T, Yamashita M, Taguchi Y, Tokura Y (2000) Nature 405:929–932
15. Takaishi S, Tobu Y, Kitagawa H, Goto A, Shimizu T, Okubo T, Mitani T, Ikeda R (2004) J Am Chem Soc 126:1614–1615
16. Guo Y, Langlois J-M, Goddard WA (1988) Science 239:896–899
17. Che C-M, Herbstein FH, Schaefer WP, Marsh RE, Gray HB (1983) J Am Chem Soc 105:4604–4607
18. Kurmoo M, Clark RJH (1985) Inorg Chem 24:4420–4425
19. Clark RJH, Kurmoo M, Dawes HM, Hursthouse MB (1986) Inorg Chem 25:409–412
20. Butler LG, Zietlow MH, Che C-M, Schaefer WP, Sridhar S, Grunthaner PJ, Swanson BI, Clark RJH, Gray HB (1988) J Am Chem Soc 110:1155–1162
21. Stroud MA, Drickamer HG, Zietlow MH, Gray HB, Swanson BI (1989) J Am Chem Soc 111:66–72
22. Mitani T, Wada Y, Yamashita M, Toriumi K, Kobayashi A, Kobayashi H (1994) Synth Met 64:291–294
23. Yamashita M, Miya S, Kawashima T, Manabe T, Sonoyama T, Kitagawa H, Mitani T, Okamoto H, Ikeda R (1999) J Am Chem Soc 121:2321–2322
24. Matsuzaki H, Matsuoka T, Kishida H, Takizawa K, Miyasaka H, Sugiura K, Yamashita M, Okamoto H (2003) Phys Rev Lett 90:046401 (4 pages)
25. Mastuzaki H, Kishida H, Okamoto H, Takizawa K, Matsunaga S, Takaishi S, Miyasaka H, Sugiura K, Yamashita M (2005) Angew Chem Int Ed 44:3240–3243
26. Yamashita M, Takaishi S, Kobayashi A, Kitagawa H, Matsuzaki H, Okamoto H (2006) Coord Chem Rev 250:2335–2346
27. Iguchi H, Takaishi S, Kajiwara T, Miyasaka H, Yamashita M, Matsuzaki H, Okamoto H (2008) J Am Chem Soc 130:17668–17669
28. Bellitto C, Flamini A, Gastaldi L, Scaramuzza L (1983) Inorg Chem 22:444–449
29. Yamashita M, Wada Y, Toriumi K, Mitani T (1992) Mol Cryst Liq Cryst 216:207–212

30. Shirotani I, Kawamura A, Yamashita M, Toriumi K, Kawamura H, Yagi T (1994) Synth Met 64:265–270
31. Kitagawa H, Onodera N, Sonoyama T, Yamamoto M, Fukawa T, Mitani T, Seto M, Maeda Y (1999) J Am Chem Soc 121:10068–10080
32. Mitsumi M, Murase T, Kishida H, Yoshinari T, Ozawa Y, Toriumi K, Sonoyama T, Kitagawa H, Mitani T (2001) J Am Chem Soc 123:11179–11192
33. Mitsumi M, Kitamura K, Morinaga A, Ozawa Y, Kobayashi M, Toriumi K, Iso Y, Kitagawa H, Mitani T (2002) Angew Chem Int Ed 41:2767–2771
34. Mitsumi M, Umebayashi S, Ozawa Y, Toriumi K, Kitagawa H, Mitani T (2002) Chem Lett 31:258–259
35. Mitsumi M, Yamashita T, Aiga Y, Toriumi K, Kitagawa H, Mitani T, Kurmoo M (2011) Inorg Chem 50:4368–4377
36. Ikeuchi S, Yamamura Y, Mitsumi M, Toriumi K, Saitoh H, Atake T, Saito K (2009) Chem Lett 38:1190–1191
37. Bellitto C, Dessy G, Fares V (1985) Inorg Chem 24:2815–2820
38. Mitsumi M, Yoshida Y, Kohyama A, Kitagawa Y, Ozawa Y, Kobayashi M, Toriumi K, Tadokoro M, Ikeda N, Okumura M, Kurmoo M (2009) Inorg Chem 48:6680–6691
39. Calzolari A, Alexandre SS, Zamora F, Felice RD (2008) J Am Chem Soc 130:5552–5562
40. Robert V, Petit S, Borshch SA (1999) Inorg Chem 38:1573–1578
41. Borshch SA, Prassides K, Robert V, Solonenko AO (1998) J Chem Phys 109:4562–4568
42. Nakano S, Kitagawa Y, Kawakami T, Yamaguchi K (2003) Polyhedron 22:2027–2038
43. Kitagawa Y, Shoji M, Koizumi K, Kawakami T, Okumura M, Yamaguchi K (2007) Polyhedron 26:2154–2160
44. Hartke K, Rettberg N, Dutta D, Gerber H.-D (1993) Liebigs Ann Chem 1993:1081–1089
45. Bellitto C, Flamini A, Piovesana O, Zanazzi PF (1980) Inorg Chem 19:3632–3636
46. Ozawa, Y.; Kim, M.; Takata, K.; Toriumi, K. unpublished results.
47. Sorai M, Nakano M, Miyazaki Y (2006) Chem Rev 106:976–1031
48. Miyazaki Y, Wang Q, Sato A, Saito K, Yamamoto M, Kitagawa H, Mitani T, Sorai MJ (2002) Phys Chem B 106:197–202
49. Ikeuchi, S.; Sato, A.; Saito, K.; Nakazawa, Y.; Mitsumi, M.; Toriumi,K.; Sorai, M. unpublished results.
50. Ikeuchi S, Saito K, Nakazawa Y, Mitsumi M, Toriumi K, Sorai MJ (2004) Phys Chem B 108:387–392
51. Ikeuchi S, Saito K, Nakazawa Y, Sato A, Mitsumi M, Toriumi K, Sorai M (2002) Phys Rev B 66:115110 (7 pages)
52. Saito K, Ikeuchi S, Nakazawa Y, Sato A, Mitsumi M, Yamashita T, Toriumi K, Sorai MJ (2005) Phys Chem B 109:2956–2961
53. Mitsumi M, Yoshinari T, Ozawa Y, Toriumi K (2000) Mol Cryst Liq Cryst 342:127–132
54. Diffuse scattering of $[Pt_2(n\text{-}BuCS_2)_4I]_\infty$ (**4**). Mitsumi, M.; Toriumi, K. unpublished results.
55. Electronic absorption spectra of $[Pt_2(RCS_2)_4I]_\infty$ (R = *n*-Pr (**3**), *n*-Bu (**4**)). Mitsumi, M.; Toriumi, K. unpublished results.
56. Torrance JB, Scott BA, Kaufman FB (1975) Solid State Commun 17:1369–1375
57. Torrance JB, Scott BA, Welber B, Kaufman FB, Seiden PE (1979) Phys Rev B 19:730–741
58. Tanaka J, Tanaka M, Kawai T, Takabe T, Maki O (1976) Bull Chem Soc Jpn 49:2358–2373
59. Torrance JB (1987) In: Jérome D, Caron LG (eds) Low-dimensional conductors and superconductors, vol 155, NATO ASI series, series B. Plenum, New York, NY, pp 113–133
60. Graja A (1994) In: Farges J-P (ed) Organic conductors. Dekker, New York, NY, pp 229–267
61. Zeller HR, Beck A (1974) J Phys Chem Solids 35:77–80
62. Kwak JF, Beni G, Chaikin PM (1976) Phys Rev B 13:641–646
63. Chaikin PM, Greene RL, Etemad S, Engler E (1976) Phys Rev B 13:1627–1632
64. Chaikin PM (1980) In: Alcácer L (ed) The physics and chemistry of low dimensional solids, vol 56, NATO ASI series. D. Reidel Publishing, Dordrecht, pp 53–75

65. Otsubo K, Kobayashi A, Kitagawa H, Hedo M, Uwatoko Y, Sagayama H, Wakabayashi Y, Sawa H (2006) J Am Chem Soc 128:8140–8141
66. Thielemans M, Deltour R, Jerome D, Cooper RJ (1976) Solid State Commun 19:21–27
67. Guijarro A, Castillo O, Welte L, Calzolari A, Sanz Miguel PJ, Gómez-García CJ, Olea D, di Felice R, Gómez-Herrero J, Zamora F (2010) Adv Funct Mater 20:1451–1457
68. Comès R (1977) In: Keller HJ (ed) Chemistry and physics of one-dimensional metals, vol 25, NATO ASI series, series B. Plenum, New York, NY, pp 315–339
69. Pouget JP, Comès R, Bechgaard K (1980) In: Alcácer L (ed) The physics and chemistry of low dimensional solids, NATO ASI series, series C. D. Reidel Publishing, Dordrecht, pp 113–121
70. Pouget JP (1987) In: Jérome D, Caron LG (eds) Low-dimensional conductors and superconductors, vol 155, NATO ASI series, series B. Plenum, New York, pp 17–45
71. Filhol A (1994) In: Farges J-P (ed) Organic conductors. Dekker, New York, NY, pp 147–228
72. Henriques RT, Alcácer L, Pouget JP, Jérome D (1984) J Phys C Solid State Phys 17:5197–5208
73. Wakabayashi Y, Kobayashi A, Sawa H, Ohsumi H, Ikeda N, Kitagawa H (2006) J Am Chem Soc 128:6676–6682
74. Kobayashi A, Kitao S, Seto M, Ikeda R, Kitagawa H (2009) Inorg Chem 48:8044–8049
75. Scott JC (1988) Highly conducting quasi-one-dimensional organic crystals. In: Conwell E (ed) Magnetic properties, vol 27, Semiconductors and semimetals. Academic, San Diego, CA, p 386, and references therein
76. Temperature dependence of magnetic susceptibility of $[Pt_2(n\text{-}PrCS_2)_4I]_\infty$ (**3**). Mitsumi, M.; Toriumi, K. unpublished results.
77. Tanaka H, Kuroda S, Yamashita T, Mitsumi M, Toriumi K (2003) J Phys Soc Jpn 72:2169–2172
78. Tanaka H, Kuroda S, Yamashita T, Mitsumi M, Toriumi K (2006) Phys Rev B 73:245102 (12 pages)
79. Kobayashi A, Kojima T, Ikeda R, Kitagawa H (2006) Inorg Chem 45:322–327
80. Ikeuchi S, Yamamura Y, Yoshida Y, Mitsumi M, Toriumi K, Saito K (2009) J Phys Soc Jpn 78:094704 (6pages)
81. Ikeuchi S, Yamamura Y, Yoshida Y, Mitsumi M, Toriumi K, Saito K (2010) Bull Chem Soc Jpn 83:261–266
82. Makiura R, Kitagawa H, Ikeda R (2002) Mol Cryst Liq Cryst 379:309–314
83. Yamaguchi K, Kitagawa Y, Onishi T, Isobe H, Kawakami T, Nagao H, Takamizawa S (2002) Coord Chem Rev 226:235–249
84. Yamaguchi K, Kawakami T, Takano Y, Kitagawa Y, Yamashita Y, Fujita H (2002) Int J Quant Chem 90:370–385
85. Estes WE, Gavel DP, Hatfield WE, Hodgson DJ (1978) Inorg Chem 17:1415–1421
86. Bray JW, Interrante LV, Jacobs IS, Bonner JC (1983) In: Miller JS (ed) Extended linear chain compounds, vol 3. Plenum, New York, NY, Chapter 7
87. Bray JW, Hart HR Jr, Interrante LV, Jacobs IS, Kasper JS, Watkins GD, Wee SH, Bonner JC (1975) Phys Rev Lett 35:744–747
88. Hase M, Terasaki I, Uchinokura K (1993) Phys Rev Lett 70:3651–3654
89. Nishi M, Fujita O, Akimitsu J (1994) Phys Rev B 50:6508–6510
90. Isobe M, Ueda Y (1996) J Phys Soc Jpn 65:1178–1181
91. Fujii Y, Nakao H, Yosihama T, Nishi M, Nakajima K, Kakurai K, Isobe M, Ueda Y, Sawa H (1997) J Phys Soc Jpn 66:326–329
92. Ohama T, Isobe M, Yasuoka H, Ueda Y (1997) J Phys Soc Jpn 66:545–547
93. Fagot-Revurat Y, Mehring M, Kremer RK (2000) Phys Rev Lett 84:4176–4179
94. Ohwada K, Fujii Y, Katsuki Y, Muraoka J, Nakao H, Murakami Y, Sawa H, Ninomiya E, Isobe M, Ueda Y (2005) Phys Rev Lett 94:106401 (4 pages)
95. Bulaevskii LN (1969) Sov Phys Solid State 11:921–924
96. Pytte E (1974) Phys Rev B 10:4637–4642

97. Huizinga S, Kommandeur J, Sawatzky GA, Thole BT, Kopinga K, de Jonge WJM, Roos J (1979) Phys Rev B 19:4723–4732
98. Cross MC, Fisher DS (1979) Phys Rev B 19:402–419
99. Otsubo K, Kobayashi A, Hedo M, Uwatoko Y, Kitagawa H (2009) Chem Asian J 4:1673–1676
100. Bonner JC, Fisher ME (1964) Phys Rev 135:A640–A658

Chapter 10
POP-Type MMX-Chain Compounds with Binary Countercations and Vapochromism

Hiroaki Iguchi, Shinya Takaishi, and Masahiro Yamashita

10.1 Introduction

10.1.1 Chemistry of pop-Type Discrete Diplatinum Complexes

Pyrophosphito-bridged diplatinum complex is one of the most studied dinuclear complexes in a paddle-wheel structure. The chemistry of pyrophosphito-bridged diplatinum complex began at the discovery of the Pt(II)–Pt(II) complex, $K_4[Pt_2(pop)_4]\cdot 2H_2O$ (pop = $P_2H_2O_5^{2-}$) by Roundhill et al. in 1977 [1]. Since $[Pt_2(pop)_4]^{4-}$ shows intense long-lived phosphorescence, photochemistry and excited-state chemistry of $[Pt_2(pop)_4]^{4-}$ has been attracted much attention (see following early reviews and references therein [2, 3]). Although no chemical bond exist between two Pt(II) atoms in the ground state, $5d\sigma^* \rightarrow 6p\sigma$ transition should induce the bonding character between them. This excited-state structure has been confirmed by several optical methods [4–9]. The excited state of $[Pt_2(pop)_4]^{4-}$ is powerful one-electron reductant, therefore, it can be used as a photochemical catalyst for converting ethanol to acetaldehyde and hydrogen [10] and for the transfer hydrogenation of alkenes and alkynes [11, 12]. The Pt(III)–Pt(III) complex, $[Pt_2(pop)_4H_2]^{4-}$, is the active species of the catalytic reaction [13].

Although $[Pt_2(pop)_4H_2]^{4-}$ is unstable species, many stable Pt(III)–Pt(III) complexes, $[Pt_2(pop)_4X_2]^{4-}$ (X = Cl, Br, I, NO_2, SCN, etc.) and $[Pt_2(pop)_4L_2]^{2-}$ (L = H_2O, py, CH_3CN, etc.), have been synthesized by the oxidative additions, occasionally in the presence of the chemical oxidants (see following early reviews and references therein [2, 3]). Some Pt(III)–Pt(III) complexes exhibit unique strong red luminescence [14].

H. Iguchi (✉) • S. Takaishi • M. Yamashita
Department of Chemistry, Graduate School of Science, Tohoku University, 6-3 Aza-Aoba, Aramaki, Aoba-ku, Sendai 980-8578, Japan
e-mail: h-iguchi@agnus.chem.tohoku.ac.jp

M. Yamashita and H. Okamoto (eds.), *Material Designs and New Physical Properties in MX- and MMX-Chain Compounds*, DOI 10.1007/978-3-7091-1317-2_10,

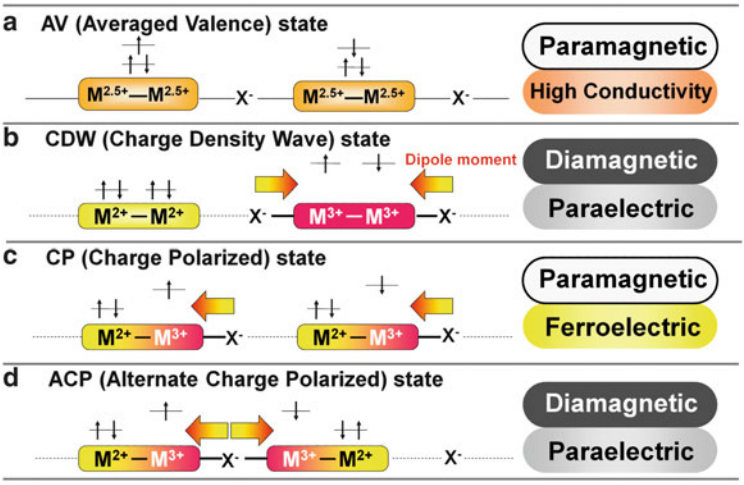

Fig. 10.1 Electronic state and expected physical properties of MMX chains

In contrast to the stability of Pt(II)–Pt(II) and Pt(III)–Pt(III) complexes, mixed valence Pt(II)–Pt(III) complex is quite unstable in the solution because of the disproportionation to Pt(II)–Pt(II) and Pt(III)–Pt(III) complexes. Very recently, one Pt(II)–Pt(III) complex was reported in CH_2Cl_2, the weakly coordinating solvent, and its structure was determined as the discrete Pt(II)–Pt(III) complex, $(PPN)_3[Pt_2(pop)_4(NO)]\cdot 2Et_2O\cdot CH_2Cl_2$ ($PPN^+ = [Ph_3P{=}N{=}PPh_3]^+$), by the single-crystal X-ray structural analysis [15]. However, the overwhelming number of the Pt(II)–Pt(III) complexes have been reported as the infinite linear-chain complexes, which are in attractive one-dimensional (1D) electron system. This intriguing study of mixed valence chain complexes was triggered by the discovery of $K_4[Pt_2(pop)_4Br]\cdot 3H_2O$ in 1983 [16].

10.1.2 Introduction to pop-Type MMX Chains

The linear-chain complexes based on pyrophosphito-bridged diplatinum complex are called as pop-type "quasi-1D halogen-bridged dinuclear metal complexes (MMX chains)." Although 1D electron system of quasi-1D halogen-bridged mononuclear metal complexes (MX chains) originates two electronic states bringing about unique physical properties as shown in Part I, MMX chains have attracted intense interest, because their higher degrees of freedom of the electrons provide the competition and/or cooperation among more diverse energetic factors, which causes a larger variety of electronic states and smaller energy gaps among them. Based on the theoretical calculations (see Chap. 12) and experimental data, the electronic states of the MMX chains can be classified into four states as shown in Fig. 10.1.

These electronic states are strongly correlated to the position of the bridging halide ion. Except for AV state, the bridging halide ion is close to M^{3+} ion. A formal

oxidation number is used in this chapter unless otherwise noted. Strictly, 3+ and 2+ should be represented as (3–δ)+ and (2+δ)+, respectively. AV state is classified into class III by Robin–Day classification, while CDW, CP and ACP are classified into class II [17, 18]. Because each electronic state exhibits various physical properties, MMX chains have the potential to be multifunctional switching materials.

MMX chains synthesized to date have been categorized into two ligand systems: dithioacetate (dta) $[M_2(RCS_2)_4I]$ (M = Ni, and Pt; R = alkyl chain group), which are discussed in Chap. 9, and pyrophosphite (pop) $Y_4[Pt_2(pop)_4X]\cdot nH_2O$ or $Y'_2[Pt_2(pop)_4X]\cdot nH_2O$ (Y = alkali metal, alkyl ammonium, etc.; Y′ = alkyldiammonium; X = Cl, Br, and I; $pop^{2-} = P_2H_2O_5^{2-}$).

In the dta system, as mentioned in Chap. 9, a high conductivity and a metal–semiconductor transition have been reported so far. Recently, Zamora et al. reported the formation of nanowires on the substrate, which is promising for the future molecule-based devices [19–22]. However, establishing the method to obtain the desired electronic states and accompanying physical properties of MMX chains is remaining issue that needs to be solved. The negative chain in the pop system requires the countercations, which have advantages to synthesize the various derivatives and to control the electronic states of MMX chains. Furthermore, the removal of lattice water can also change the electronic states of MMX chains. Although many pop-type MMX chains have been synthesized so far [23–30], in this chapter, we focus on the chemistry of pop-type MMX chains containing two kinds of countercation (binary countercations), which was discovered recently. We also focus on the response of pop-type MMX chains to chemical external stimuli that is water-vapor-induced changes of the physical properties of pop-type MMX chains as represented by vapochromism. The other important response to physical external stimuli, that is photoinduced phase transition, is explained in Chap. 11.

10.2 Structure and Electronic States of MMX Chains with Binary Countercations

Since all MMX chains thus far synthesized are in one of the four electronic states shown in Fig. 10.1 without exception, searching the new electronic states in MMX chains are very important for bringing about new physical and chemical properties of low-dimensional materials. It should be noted that all of the known pop-type MMX chains contain only one kind of countercation (unitary countercation). In order to extend the system, introducing two kinds of countercation (binary countercations) was performed.

10.2.1 Forming Condition of MMX Chains with Binary Countercations

The general formula of MMX chains with binary countercations are $A_2B[Pt_2(pop)_4I]\cdot nH_2O$ (A = K and Rb; B = alkyldiammonium (Scheme 10.1);

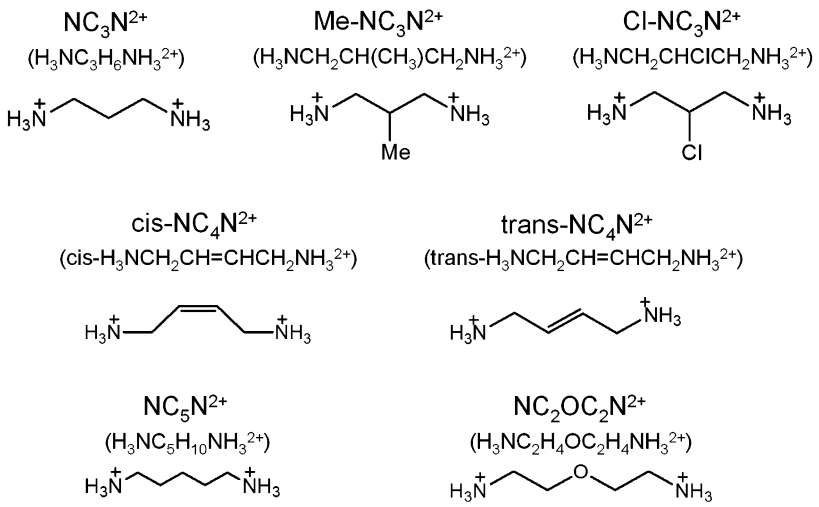

Scheme 10.1 Structure and abbreviation of alkyldiammonium ions

$n = 2$ and 4). A^+, which is coordinated by eight oxygen atoms, links both intra- and inter-chain $[Pt_2(pop)_4]$ units by $A^+ \cdots O$ coordination bond. B^{2+} links inter-chain $[Pt_2(pop)_4]$ units by $N^+ - H \cdots O$ hydrogen bond.

Other alkali metal ions, Li^+, Na^+, and Cs^+, were not able to be introduced because of the size mismatch [31]. In the case of alkyldiammonium ions, only the B^{2+} which has three to five atoms in main backbone between terminated $–NH_3^+$ substituents was able to be introduced. The selectivity of the B^{2+} can be explained as follows.

The B^{2+} exist in the space surrounded by the four $[Pt_2(pop)_4]$ units connected by $A^+ \cdots O$ coordination bonds (e.g., $K_2(NC_3N)[Pt_2(pop)_4I]\cdot 4H_2O$ in Fig. 10.2). Because the length of coordination bonds is limited, the size of the space is less variable. This is the reason why longer alkyldiammonium ions such as $H_3NC_6H_{12}NH_3^{2+}$ cannot be introduced as one of the binary countercations. Similarly, the shorter alkyldiammonium ions such as $H_3NC_2H_4NH_3^{2+}$ cannot form the hydrogen bonding network among the pop ligands, inducing the destabilization of the MMX chains with binary countercations.

10.2.2 Determination of Electronic State by the Crystal Structure and Polarized Raman Spectra

As mentioned above, it has been known that the oxidation state are concerned with the distance between bridging iodide ion and platinum ion (Pt–I distance). As the oxidation number becomes higher, Pt–I distance becomes shorter. Therefore, the electronic state can be determined from the chain structure.

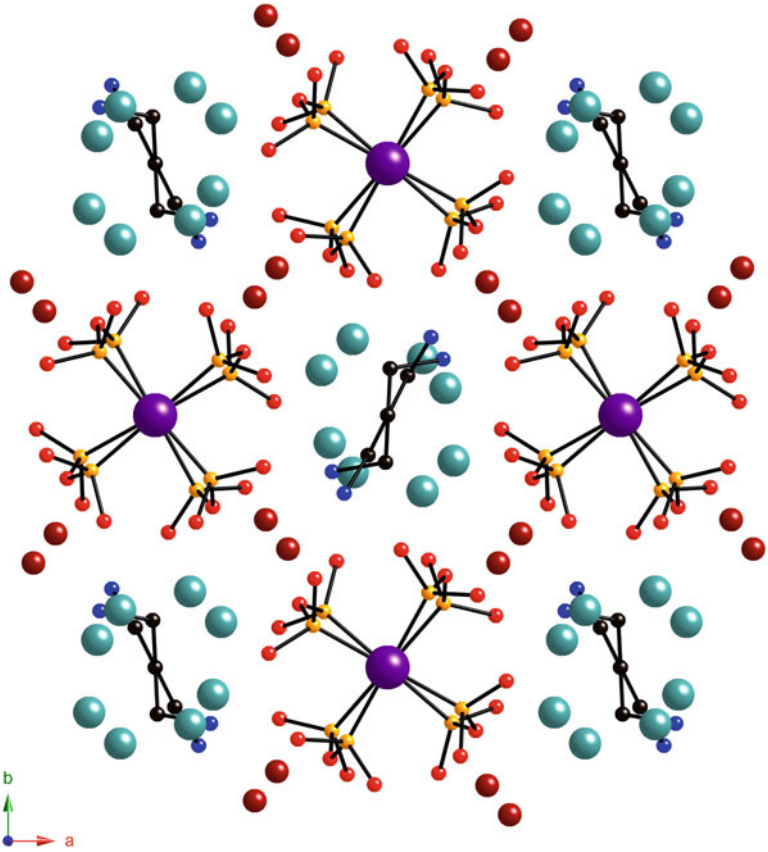

Fig. 10.2 Perspective view of the region around $H_3NC_3H_6NH_3^{2+}$ along *c*-axis of $K_2(NC_3N)[Pt_2(pop)_4I]\cdot 4H_2O$ (*black*, C; *blue*, N; *red*, O(ligand); *light blue*, $O(H_2O)$; *orange*, P; *brown*, K; *purple*, I; *yellow*, Pt). Hydrogen atoms are omitted for clarity

However, in some MMX chains with binary countercations, the bridging halide was disordered because of the random arrangement of the chains. Therefore, polarized Raman spectroscopy was performed to distinguish CDW state, which induces two peaks derived from symmetric-stretching mode of Pt–Pt bonds [Pt(III)–Pt(III) and Pt(II)–Pt(II)], from CP and ACP state, which induce only one peak [Pt(II)–Pt(III)] [23, 24, 32, 33]. Consequently, two peaks observed around 100 cm^{-1} indicate the existence of CDW-like distortion in MMX chains with binary countercations [31].

According to the crystal structure analyses, the complexes containing *cis*-NC_4N^{2+}, *trans*-NC_4N^{2+}, NC_5N^{2+}, or $NC_2OC_2N^{2+}$ have unique Pt–I–Pt distance (*d*(Pt–I–Pt)). Therefore, these complexes are in typical CDW state.

However, in the complexes containing NC_3N^{2+}, Me–NC_3N^{2+}, or Cl–NC_3N^{2+}, there are two kinds of *d*(Pt–I–Pt), which are the characteristics of ACP state.

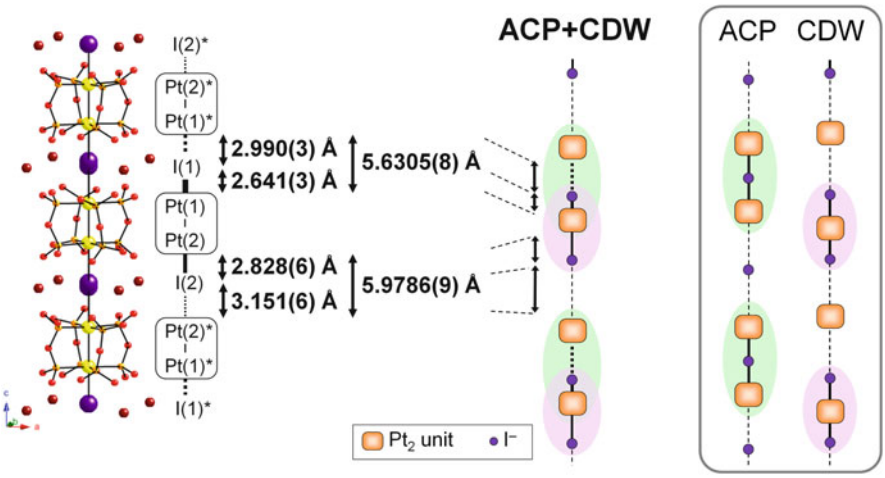

Fig. 10.3 Crystal structure of $K_2(NC_3N)[Pt_2(pop)_4I]{\cdot}4H_2O$ (*red*, O; *orange*, P; *purple*, I; *yellow*, Pt) and schematic chain structure in ACP, CDW and ACP + CDW state. The countercations, lattice water, and hydrogen atoms are omitted for clarity

The ACP-like distortion is corresponding to spin-Peierls distortion, which has the stable structure of 1D metal at low temperature. Very few compounds have been reported to have spin-Peierls distortion even at room temperature [34, 35]. Although ACP state has been reported in dta-type MMX chains [36–45], the complexes containing NC_3N^{2+}, $Me–NC_3N^{2+}$ or $Cl–NC_3N^{2+}$ are the first comopounds with ACP-like distortion in pop-type MMX chains. However, the structure is not the simple ACP state because Pt–I distances are shorter in one $[Pt_2(pop)_4]$ unit (d(Pt–I)), but are longer in the other $[Pt_2(pop)_4]$ unit $(d(\mathrm{Pt}\cdots\mathrm{I}))$, which is the characteristic of CDW state and is consistent with the polarized Raman spectra.

Figure 10.3 shows the chain structure of $K_2(NC_3N)[Pt_2(pop)_4I]{\cdot}4H_2O$ at 100 K, for example [46]. Two different d(Pt–I–Pt) (5.6305(8) Å, 5.9786(9) Å) indicate a ACP-like twofold periodicity along the chain. One $[Pt_2(pop)_4]$ unit is coordinated by neighboring I^- ions with short Pt–I distances (d(Pt–I) = 2.641(3) Å, 2.828 (6) Å), whereas the other is coordinated by I^- ions with a long $\mathrm{Pt}\cdots\mathrm{I}$ bond distances $(d(\mathrm{Pt}\cdots\mathrm{I}) = 2.990(3)$Å, 3.151(6)Å), which is the characteristic of the CDW state.

This new electronic state of the MMX chains containing NC_3N^{2+}, $Me–NC_3N^{2+}$ or $Cl–NC_3N^{2+}$ is named ACP + CDW state [46, 47]. Schematic representations of the structure in ACP, CDW and ACP + CDW state are shown in Fig. 10.3. Except for $K_2(NC_3N)[Pt_2(pop)_4I]{\cdot}4H_2O$, the positions of the bridging iodide ions are three-dimensionally ordered, which is very rare and has been reported only recently [48]. The d(Pt–I–Pt), d(Pt–I) and $d(\mathrm{Pt}\cdots\mathrm{I})$ of MMX chains with binary countercations are summarized in Table 10.1.

Table 10.1 Selected interatomic distances and electronic state of MMX chains with binary countercations

Complex	d(Pt–I–Pt)/Å	d(Pt–I)/Å	d(Pt···I)/Å	Electronic state	References
$K_2(NC_3N)[Pt_2(pop)_4I]\cdot 4H_2O$	5.6305(8)	2.641(3)	2.990(3)	ACP + CDW	[31, 46]
	5.9786(9)	2.828(6)	3.151(6)		
$K_2(Me–NC_3N)[Pt_2(pop)_4I]\cdot 4H_2O$	5.7179(11)	2.7496(8)	2.9683(8)	ACP + CDW	[31, 47]
	5.9254(11)	2.7993(7)	3.1261(8)		
$K_2(Cl–NC_3N)[Pt_2(pop)_4I]\cdot 4H_2O$	5.7262(11)	2.755(2)	2.951(2)	ACP + CDW	[31, 46]
	5.9403(12)	2.8082(18)	3.1320(18)		
$K_2(cis\text{-}NC_4N)[Pt_2(pop)_4I]\cdot 4H_2O$	5.7625(18)	2.7430(9)	3.0195(10)	CDW	[31]
$K_2(trans\text{-}NC_4N)[Pt_2(pop)_4I]\cdot 4H_2O$	5.7921(11)	2.732(3)	3.060(3)	CDW	[31]
$K_2(NC_5N)[Pt_2(pop)_4I]\cdot 4H_2O$	5.7225(7)	2.729(9)	2.993(6)	CDW	[31]
$K_2(NC_2OC_2N)[Pt_2(pop)_4I]\cdot 4H_2O$	5.7244(11)	2.8757(6)		CDW	[31]
$Rb_2(NC_3N)[Pt_2(pop)_4I]\cdot 4H_2O$	5.7521(5)	2.7430(3)	3.0091(4)	ACP + CDW	[31]
	6.1928(5)	2.8217(3)	3.3710(3)		
$Rb_2(Me–NC_3N)[Pt_2(pop)_4I]\cdot 4H_2O$	5.7782(7)	2.7478(5)	3.0304(4)	ACP + CDW	[31]
	6.1226(7)	2.8073(4)	3.3152(5)		
$Rb_2(Cl–NC_3N)[Pt_2(pop)_4I]\cdot 4H_2O$	5.7726(13)	2.7532(16)	3.0194(15)	ACP + CDW	[31]
	6.1518(13)	2.8155(16)	3.3363(16)		
$Rb_2(cis\text{-}NC_4N)[Pt_2(pop)_4I]\cdot 4H_2O$	5.8554(15)	2.735(5)	3.120(4)	CDW	[31]
$Rb_2(trans\text{-}NC_4N)[Pt_2(pop)_4I]\cdot 2H_2O$	5.7930(9)	2.8965(4)		CDW	[31]
$Rb_2(NC_5N)[Pt_2(pop)_4I]\cdot 4H_2O$	5.8219(15)	2.742(3)	3.080(3)	CDW	[31]
$Rb_2(NC_2OC_2N)[Pt_2(pop)_4I]\cdot 4H_2O$	5.823(2)	2.740(4)	3.097(4)	CDW	[31]

10.2.3 Origin of ACP-Like Distortion in ACP + CDW State

As mentioned above, only the MMX chains containing $H_3NCH_2CHXCH_2NH_3^{2+}$ (X = H, Me, Cl) are in ACP + CDW state. Other MMX chains with binary countercations containing longer B^{2+} are in CDW state. To design the new electronic state of MMX chains in the future, revealing the mechanism of the ACP-like distortion is very important.

In the most MMX chains with binary countercations, B^{2+} mainly arranged along *b*-axis, resulting longer unit cell parameter *b* compared with *a*. Table 10.2 shows the ratio *b*/*a* of all MMX chains with binary countercations. The electronic state is ACP + CDW state when $b/a \leq 1.10$, and is CDW state when $b/a \geq 1.19$. Small *b*/*a* induces the steric hindrance around A^+ explained as follows:

Figure 10.4 shows the schematic representation of the 1D chain and its oxygen atoms, lattice H_2O molecules, A^+ and B^{2+}. Ten oxygen atoms, eight from pop ligands O(pop) and two from lattice H_2O molecules (O(H_2O)) exist around alkali metal ion. When $b/a \leq 1.10$, because at most only eight oxygen atoms can coordinate to A^+, pop ligands twist to remove two O(pop) away from A^+. On the other hand, when $b/a \geq 1.19$, two O(pop) are initially far from A^+ without the twisting of ligands. The distance between A^+ and coordinating O(pop) (d(A–O(pop))), and the distance between A^+ and farther O(pop) (d(A···O(pop))), are shown in Table 10.2. Since d(A···O(pop)) is longer than the sum of ionic radii of A^+ (1.65 Å for K^+ and 1.75 Å for Rb^+) [49] and van der Waals radii of O atom (1.52 Å), [50] no coordination bond exist between these atoms.

Table 10.2 Ratio of unit cell parameter (*b*/*a*), distances between A^+ and O(pop) for MMX chains with binary countercations

Complex	*b*/*a*	*d*(A–O)/Å	*d*(A ⋯ O)/Å
$K_2(NC_3N)[Pt_2(pop)_4I]\cdot 4H_2O$	1.087	2.777(8)–2.985(8)	3.981, 4.355
$K_2(Me–NC_3N)[Pt_2(pop)_4I]\cdot 4H_2O$	1	2.791(3)–3.007(3)	4.112, 4.340
$K_2(Cl–NC_3N)[Pt_2(pop)_4I]\cdot 4H_2O$	1	2.827(7)–3.003(8)	4.169, 4.317
$K_2(cis\text{-}NC_4N)[Pt_2(pop)_4I]\cdot 4H_2O$	1.197	2.7780(10)–3.0349(11)	3.706
$K_2(trans\text{-}NC_4N)[Pt_2(pop)_4I]\cdot 4H_2O$	1.248	2.835(3)–3.054(3)	3.847
$K_2(NC_5N)[Pt_2(pop)_4I]\cdot 4H_2O$	1.191	2.791(2)–3.049(2)	3.949
$K_2(NC_2OC_2N)[Pt_2(pop)_4I]\cdot 4H_2O$	1.261	2.808(5)–3.22(2)	4.070
$Rb_2(NC_3N)[Pt_2(pop)_4I]\cdot 4H_2O$	1.104	2.8900(17)–3.0551(17)	4.001–4.542
$Rb_2(Me–NC_3N)[Pt_2(pop)_4I]\cdot 4H_2O$	1	2.9105(15)–3.0740(16)	4.146, 4.432
$Rb_2(Cl–NC_3N)[Pt_2(pop)_4I]\cdot 4H_2O$	1	2.944(7)–3.080(7)	4.222, 4.417
$Rb_2(cis\text{-}NC_4N)[Pt_2(pop)_4I]\cdot 4H_2O$	1.205	2.858(8)–3.112(9)	3.745
$Rb_2(trans\text{-}NC_4N)[Pt_2(pop)_4I]\cdot 2H_2O$	1.263	2.913(5)–3.094(5)	3.659
$Rb_2(NC_5N)[Pt_2(pop)_4I]\cdot 4H_2O$	1.196	2.908(3)–3.089(3)	3.940
$Rb_2(NC_2OC_2N)[Pt_2(pop)_4I]\cdot 4H_2O$	1.266	2.829(5)–3.214(6)	3.899

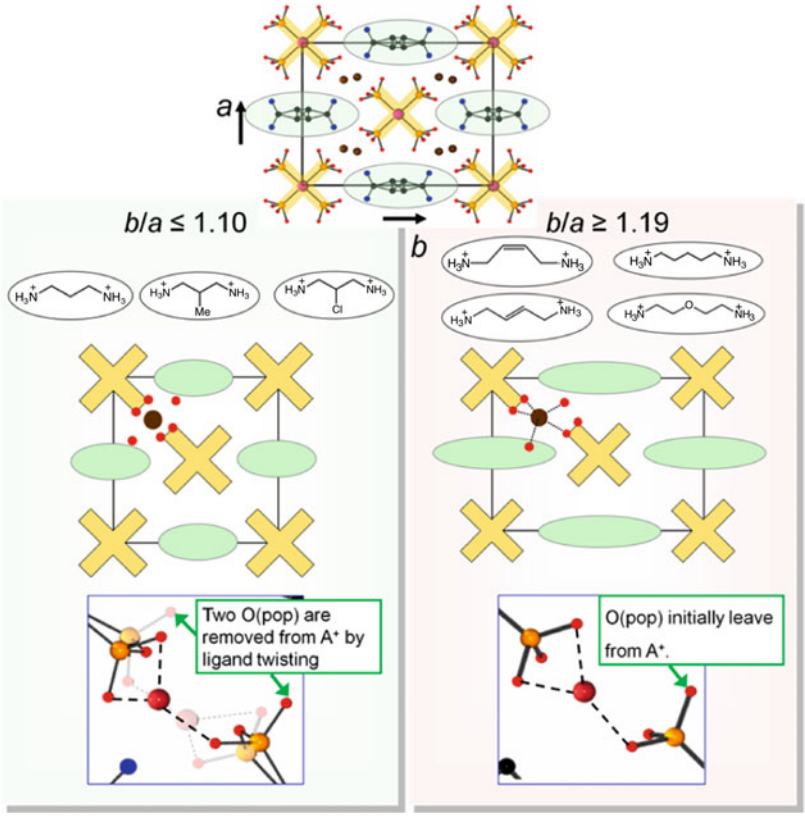

Fig. 10.4 Schematic representation of the environment around alkali metal ion when $b/a \leq 1.10$ (*left*) and when $b/a \geq 1.19$ (*right*). The lowermost figures are the magnification of the crystal strucucture of $K_2(NC_3N)[Pt_2(pop)_4I]\cdot 4H_2O$ (*left*) and $K_2(NC_5N)[Pt_2(pop)_4I]\cdot 4H_2O$ (*right*)

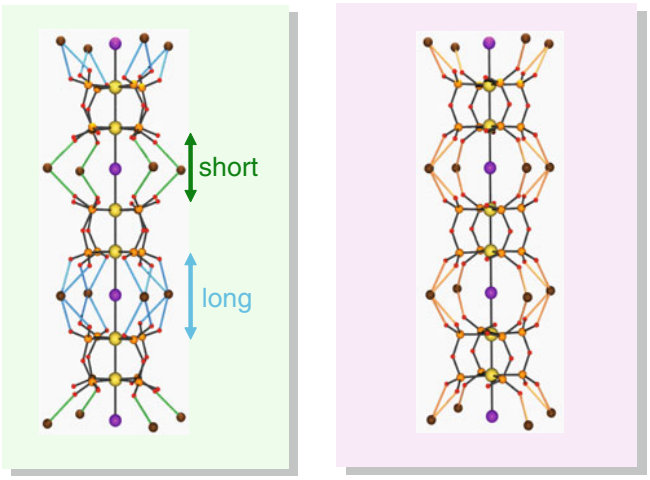

Fig. 10.5 Chain structure of $K_2(NC_3N)[Pt_2(pop)_4I]\cdot 4H_2O$ (*left*) and $K_2(NC_5N)[Pt_2(pop)_4I]\cdot 4H_2O$ (*right*) with the representation of colored K–O(pop) coordination bonds

The twisting of pop ligands induces two different coordination features between two $[Pt_2(pop)_4]$ units and A^+, that is, monodentate and bidentate coordination to A^+, as shown in Fig. 10.5. *d*(Pt–I–Pt) is different between each coordination feature. On the other hand, $K_2(NC_5N)[Pt_2(pop)_4I]\cdot 4H_2O$, which is in CDW state, has equal coordination features (two monodentate and two bidentate coordination to A^+) between two $[Pt_2(pop)_4]$ units (Fig. 10.5), resulting in the unique *d*(Pt–I–Pt). Consequently, the different coordination bonds induced by the twisting of pop ligands are the origin of the ACP-like distortion.

10.2.4 Electronic Structure of ACP + CDW State

The optical conductivity spectra were measured to reveal the detailed electronic structure of MMX chains with binary countercations [31]. Photon energy of the peaks in the spectra are summarized in Table 10.3.

Optical conductivity spectra of all measured MMX chains with binary countercations consisted of the strong lowest charge transfer (CT) band around 1 eV (indicated by boldface) and weak bands around 2.2 eV, 3.2 eV, and 3.9 eV. It has been known that the photon energy of CT (E_{CT}) increases with an increase of Pt–I–Pt distance (*d*(Pt–I–Pt)) in CDW and CP states of pop-type MMX chains, and that the dependency of E_{CT} on *d*(Pt–I–Pt) in CDW state is larger than that in CP state because the inter-dimer CT in CDW state is more sensitive to *d*(Pt–I–Pt) than is the intra-dimer CT in CP state [51]. This dependence of E_{CT} on *d*(Pt–I–Pt) was applied to the phase diagram of CDW and CP states. Figure 10.6 shows the phase diagram of already-known MMX chains together with the plots of complexes in Table 10.3. It should be noted that the average value of two kinds of

Table 10.3 Photon energy of the peak in optical conductivity spectra of the present MMX chains. Photon energy attributed to strong lowest charge transfer (CT) band are indicated by boldface

Complex	Photon energy/eV
$K_2(NC_3N)[Pt_2(pop)_4I]\cdot 4H_2O$	**0.85**, 2.15, 3.25, 3.95
$K_2(Me–NC_3N)[Pt_2(pop)_4I]\cdot 4H_2O$	**0.85**, 2.23, 3.30, 3.83
$K_2(Cl–NC_3N)[Pt_2(pop)_4I]\cdot 4H_2O$	**0.89**, 2.28, 3.26, 3.9
$K_2(cis\text{-}NC_4N)[Pt_2(pop)_4I]\cdot 4H_2O$	**0.79**, 2.22, 3.18, 3.91
$K_2(trans\text{-}NC_4N)[Pt_2(pop)_4I]\cdot 4H_2O$	**0.81**, 2.22, 3.19, 3.92
$K_2(NC_5N)[Pt_2(pop)_4I]\cdot 4H_2O$	**0.64**, 2.19, 3.18, 3.94
$Rb_2(NC_3N)[Pt_2(pop)_4I]\cdot 4H_2O$	**1.14**, 2.13, 3.29, 3.86
$Rb_2(Me–NC_3N)[Pt_2(pop)_4I]\cdot 4H_2O$	**1.14**, 2.2, 3.29, 3.80
$Rb_2(Cl–NC_3N)[Pt_2(pop)_4I]\cdot 4H_2O$	**1.12**, 2.2, 3.27, 3.78
$Rb_2(trans\text{-}NC_4N)[Pt_2(pop)_4I]\cdot 2H_2O$	**0.94**, 2.16, 3.18, 3.80
$Rb_2(NC_2OC_2N)[Pt_2(pop)_4I]\cdot 4H_2O$	**0.92**, 2.15, 3.19, 3.82

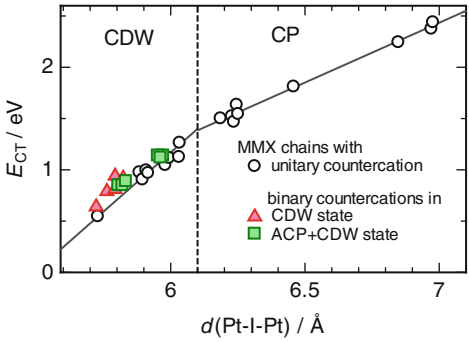

Fig. 10.6 Phase diagram in already-known pop-type MMX chains (*black*) with the plot of MMX chains with binary countercations (*red triangle* for CDW state; *green square* for ACP + CDW state). *Solid line* is the fitting of the data of already-known pop-type MMX chains with unitary countercation in each phase

d(Pt–I–Pt) is applied in the case of ACP + CDW state, on the assumption that the effect of *d*(Pt–I–Pt) on the perturbation to energy level of Pt ions is averaged. All MMX chains with binary countercations obey the fitting line in CDW state, indicating that the charge transfer occurs from electron-rich Pt dimer to electron-poor Pt dimer in ACP + CDW state as well as in CDW state. The peak energy of the weak bands were almost independent of the compounds and nearly identical to that of MMX chains in typical CDW state [51, 52], which also support that the electronic structure in ACP + CDW state is similar to that in CDW state. These results are consistent with the nonmagnetic property of $K_2(NC_3N)[Pt_2(pop)_4I]\cdot 4H_2O$ [46, 53].

Consequently, the introduction of the ACP-like distortion into MMX chains can be controlled by changing the length of B^{2+}, with retention of the electronic structure of CDW state.

10.2.5 Structural Features of MMX Chains with Binary Countercations

Compared with MMX chains with unitary countercation, those with binary countercations have two important structural features. One is the "synchronized" packing.

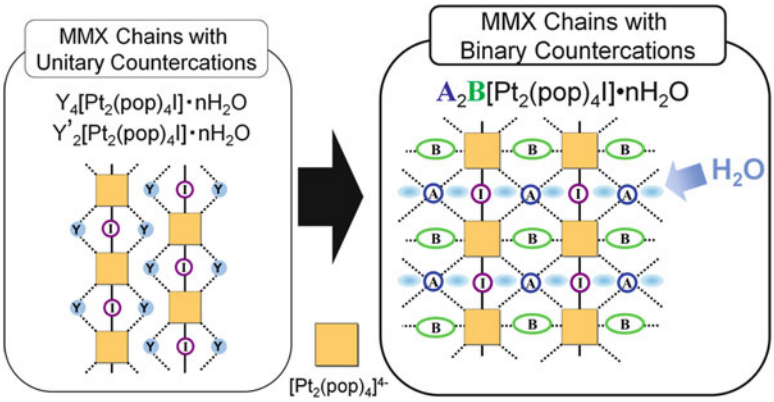

Fig. 10.7 Schematic representation of the chain structure of MMX chains with unitary (*left*) and binary (*right*) countercations

The typical MMX chains with unitary countercation, whose countercation links only intra-chain $[Pt_2(pop)_4]$ units, are in "alternate" packing (Fig. 10.7 left) [54]. On the other hand, in all MMX chains with binary countercations, A^+ links not only intra-chain but also inter-chain $[Pt_2(pop)_4]$ units by $A^+ \cdots O$ coordination bonds, and B^{2+} links inter-chain $[Pt_2(pop)_4]$ units by $N^+ - H \cdots O$ hydrogen bonds. These hydrogen bonds and coordination bond networks constrain each $[Pt_2(pop)_4]$ unit in same *ab* plane, that is in "synchronized" packing (Fig. 10.7 right). The example of hydrogen bond and coordination bond networks in $K_2(NC_5N)[Pt_2(pop)_4I]\cdot 4H_2O$ is shown in Fig. 10.8. Because of the "synchronized" packing, the layer-like structure appeared perpendicular to *c*-axis (chain axis). The larger anion and cation, $[Pt_2(pop)_4]^{3-}$ unit and B^{2+}, exist in the same *ab* plane. Formal charge in this *ab* plane is -1 per formula, therefore, the layer is densely packed anionic layer. On the other hand, loosely packed cationic layer consists of smaller anion and cation, I^- and two A^+, per formula. The vacancy in loosely packed cationic layer is filled with H_2O molecules, which coordinate to A^+ ions. These H_2O molecules and lattice fixed by hydrogen bond and coordination bond networks play an important role in dehydration–rehydration of the MMX chains discussed later.

The other important structural feature is the short *d*(Pt–I–Pt). The reason of the short *d*(Pt–I–Pt) can be explained as follows:

The hydrogen bonds between pop ligands and $-NH_3^+$ of countercations link intra-chain $[Pt_2(pop)_4]$ units in typical MMX chains with unitary countercation. On the other hand, coordination bonds between pop ligands and A^+ ions link intra-chain (and also inter-chain) $[Pt_2(pop)_4]$ units in MMX chains with binary countercations. Although the distances between nitrogen atom of $-NH_3^+$ and O(pop) are almost comparable to those between A^+ and O(pop) ($d(N–O) \approx d(A–O)$) [31], the minimum values of coordination bond angle ($\angle$(O–A–O)) are smaller than those of hydrogen bond angles ($\angle$(O–N–O)), resulting in the shorter *d*(Pt–I–Pt) in MMX chains with binary countercations. This difference originates from the isotropic

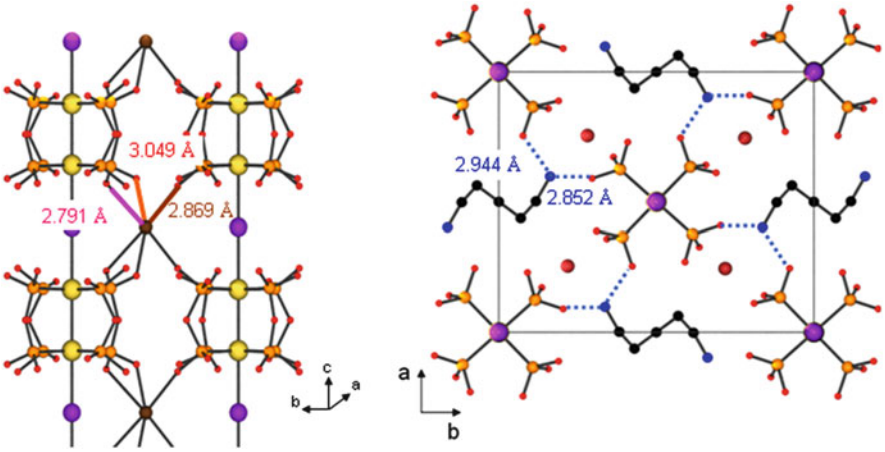

Fig. 10.8 $K^+ \cdots O$ coordination bonds (*left*) and $N^+ - H \cdots O$ hydrogen bonds (*right*) in $K_2(NC_5N)[Pt_2(pop)_4I]\cdot 4H_2O$

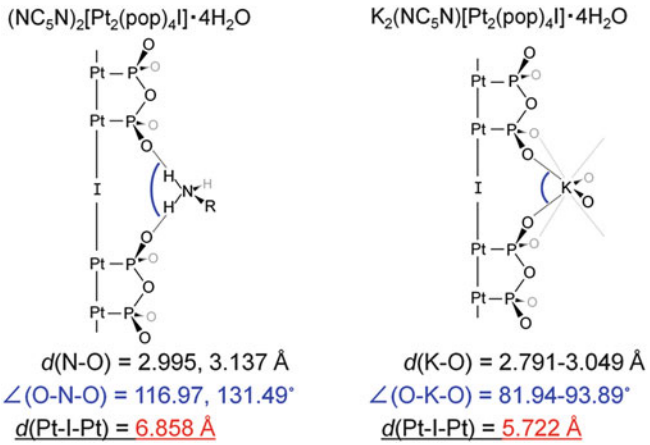

Fig. 10.9 The difference between ∠(O–N–O) and ∠(O–A–O) and difference in *d*(Pt–I–Pt) of $(NC_5N)_2[Pt_2(pop)_4I]\cdot 4H_2O$ and $K_2(NC_5N)[Pt_2(pop)_4]\cdot 4H_2O$

electron distribution of A^+. In other words, oxygen atoms can coordinate to A^+ from any direction unless steric hindrance among oxygen atoms occurs. In contrast, ∠(H–N–H) is limited around 109° due to the characteristic of sp^3 orbital, hence typical (O–N–O) is not smaller than 109°. Schematic representation of the comparison between $(NC_5N)_2[Pt_2(pop)_4I]\cdot 4H_2O$ and $K_2(NC_5N)_2[Pt_2(pop)_4I]\cdot 4H_2O$ are shown in Fig. 10.9.

Although the most pop-type MMX chains synthesized so far were less conductive (the typical electrical conductivity at room temperature (σ_{RT}) $< 10^{-7}$ S cm^{-1}), MMX chains with binary countercations show the higher conductivity, at most 10^{-2} S cm^{-1}, due to the short *d*(Pt–I–Pt) [31, 46].

10.3 Water-Vapor-Induced Switching in MMX Chains

From the viewpoints of both fundamental and applied sciences, the development of the materials responsive to external stimuli in the solid state has been becoming more and more important. Especially, the response to chemical stimuli, such as exposure to molecular vapor, has recently attracted much attention. Porous coordination polymers (PCPs) or metal–organic frameworks (MOFs) are the latest candidates. Their adsorption and desorption behaviors can be applied in both chemical applications, such as storage [55], separation [56], and catalysis [57] and switching of the physical properties, such as magnetism [58, 59], photoluminescence [60, 61], and electrical conductivity [62–64]. From this point of view, 1D electron system is promising candidate because its electronic states strongly correlate with the lattice freedom and interesting physical properties.

The study of the guest dehydration–rehydration in MX and MMX chains has scarcely been explored to date. Only $[\{[Pt(en)_2][PtCl_2(en)_2]\}_3][\{(MnCl_5)Cl_3\}_2]\cdot 12H_2O$ was reported as MX chain which shows reversible dehydration–rehydration of lattice water [65]. However, detail structure and electronic state of the dehydrated complex, $[\{[Pt(en)_2][PtCl_2(en)_2]\}_3][\{(MnCl_5)Cl_3\}_2]$, have not been characterized. Further studies of the guest dehydration–rehydration in MX chains are eagerly anticipated.

10.3.1 Vapochromism in MMX Chains

Because the energy of each electronic states are more comparable in MMX chains than in MX chains, MMX chains are more promising for developing the multifunctional switching materials responsive to guest molecules.

$(NC_4N)_2[Pt_2(pop)_4I]\cdot 4H_2O$ ($NC_4N^{2+} = H_3NC_4H_8NH_3^{2+}$) is the first MMX chain that show the reversible changes in color upon exposure to water vapor [52]. This phenomenon is called "vapochromism."

Figure 10.10 shows the polarized Raman spectra of hydrated $(NC_4N)_2[Pt_2(pop)_4I]\cdot 4H_2O$ (296 K, green) and dehydrated $(NC_4N)_2[Pt_2(pop)_4I]$ (340 K, red). Apparently, single peak attributed to CP state of hydrated complex changed to double peaks attributed to CDW state of dehydrated complex. The color of the crystal dramatically changed by dehydration, which is confirmed by the change of optical conductivity spectra (Fig. 10.11). The dehydrated state could return to hydrated state by putting the crystal under water-saturated atmosphere. The more versatile vapochromic behavior was found in similar complex, $(NC_5N)_2[Pt_2(pop)_4I]\cdot 4H_2O$ [54]. In this complex, the rehydration occurred easily just by varying temperature in the atmosphere because of the larger inter-chain spaces.

Although the crystal structure of the dehydrated complex was not analyzed from the heated crystal because of the reduction in quality of the crystal, direct synthesis

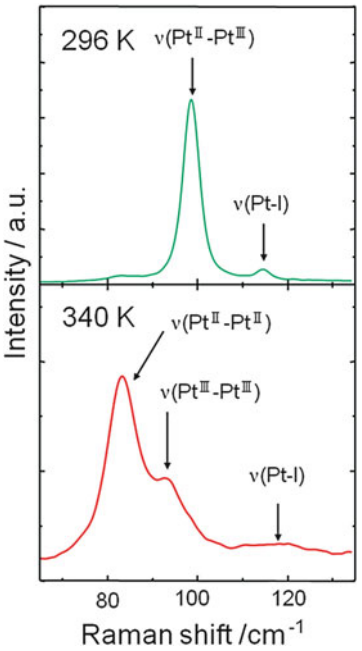

Fig. 10.10 'Polarized Raman spectra of $(NC_4N)_2[Pt_2(pop)_4I]\cdot 4H_2O$ (296 K, *green*) and $(NC_4N)_2[Pt_2(pop)_4I]$ (340 K, *red*) with polarization of light parallel to the chain axis

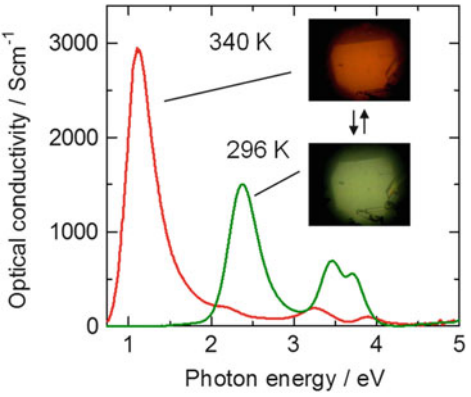

Fig. 10.11 Optical conductivity spectra of $(NC_4N)_2[Pt_2(pop)_4I]\cdot 4H_2O$ (296 K, *green*) and $(NC_4N)_2[Pt_2(pop)_4I]$ (340 K, *red*) with polarization of light parallel to the chain axis. The insets show the corresponding microscope images for the single crystal taken in reflection mode

and structural analysis of $(NC_4N)_2[Pt_2(pop)_4I]$ were achieved by the slow diffusion of starting materials in methanol solution [66]. *d*(Pt–I–Pt) of $(NC_4N)_2[Pt_2(pop)_4I]$ is 5.859 Å, which is in the region of CDW state in the phase diagram (Fig. 10.6) [51]. This structure is consistent with the double peaks attributed to CDW state observed in polarized Raman spectra shown above. In $(NC_4N)_2[Pt_2(pop)_4I]$, the pop ligands and NC_4N^{2+} ions arrange so as to fill in the vacancy of water molecules. Since the general volume of water molecule is approximately 30 Å^3, the total volume of eight water molecules in unit cell of compound $(NC_4N)_2[Pt_2(pop)_4I]\cdot 4H_2O$ is approximately 240 Å^3. However, the difference between the lattice volume of

$(NC_4N)_2[Pt_2(pop)_4I]\cdot 4H_2O$ and $(NC_4N)_2[Pt_2(pop)_4I]$ is only approximately 150 $Å^3$. Therefore, the vacancy of the water molecules is not filled perfectly in $(NC_4N)_2[Pt_2(pop)_4I]$. This is probably the reason why the compound $(NC_4N)_2[Pt_2(pop)_4I]$ is able to absorb the water molecules in humid atmosphere.

10.3.2 Single-Crystal-to-Single-Crystal Transformation of $K_2(NC_3N)[Pt_2(pop)_4I]\cdot 4H_2O$ to $K_2(NC_3N)[Pt_2(pop)_4I]$

While the single crystal of dehydrated complex, $(NC_4N)_2[Pt_2(pop)_4I]$ was synthesized directly, more robust crystal which retains single crystallinity under dehydration condition has been required. MMX chains with binary countercations mentioned in Sect. 10.2 are promising candidates, because the multiple coordination bond and hydrogen bond networks among 1D chains can support the frameworks.

Recently, desired single-crystal-to-single-crystal transformation of hydrated complex, $K_2(NC_3N)[Pt_2(pop)_4I]\cdot 4H_2O$, to dehydrated complex, $K_2(NC_3N)[Pt_2(pop)_4I]$, was achieved [46]. The crystal structure and chain structure are shown in Fig. 10.12. ACP-like distortion disappears, and there is only one *d*(Pt–I–Pt) and *d*(Pt–I) in dehydrated state. In other words, $K_2(NC_3N)[Pt_2(pop)_4I]$ is no longer in an ACP + CDW state. The *d*(Pt–I–Pt) of $K_2(NC_3N)[Pt_2(pop)_4I]$ (5.689(2) Å) is the shortest of all MMX chains thus far reported, and iodide ion is at the midpoint between neighboring $[Pt_2(pop)_4]$ units without disorder. These structural features of $K_2(NC_3N)[Pt_2(pop)_4I]$ are characteristic of the AV state. However, there is still a possibility that the disorder of the bridging iodide ion is beyond the resolution of the X-ray single-crystal analysis. The E_{CT} determined from the peak in the optical conductivity spectrum decreases from 0.85 to 0.45 eV by the dehydration, indicating a decrease in band gap. Although the peaks are in infrared region not in visible region, this spectral change is also a kind of vapochromism.

Figure 10.13 shows ^{31}P MAS NMR spectra of $K_2(NC_3N)[Pt_2(pop)_4I]\cdot 4H_2O$ and $K_2(NC_3N)[Pt_2(pop)_4I]$. As reported by Kimura et al [67], the ^{31}P chemical shift (δ) is larger for P atoms coordinated to Pt ions in a lower oxidation state. Four intense peaks with the satellite peaks due to the coupling between ^{31}P and ^{195}Pt are observed in the ^{31}P MAS NMR spectrum of $K_2(NC_3N)[Pt_2(pop)_4I]\cdot 4H_2O$, attributed to the four inequivalent P atoms in the crystal. On the other hand, only two intense peaks were observed in the spectrum of $K_2(NC_3N)[Pt_2(pop)_4I]$, indicating the existence of two sets of inequivalent P atoms. This large difference of δ between the peaks (26 ppm) derives from Pt ions in different oxidation states. In addition, two peaks in the polarized Raman spectrum of $K_2(NC_3N)[Pt_2(pop)_4I]$ indicates the existence of two different $[Pt_2(pop)_4]$ units [46]. Therefore, the electronic state of $K_2(NC_3N)[Pt_2(pop)_4I]$ can be concluded as a CDW state. Curiously, the broadened peaks in the ^{31}P MAS NMR spectrum suggest the generation of paramagnetic spins, which should not exist in nonmagnetic CDW state.

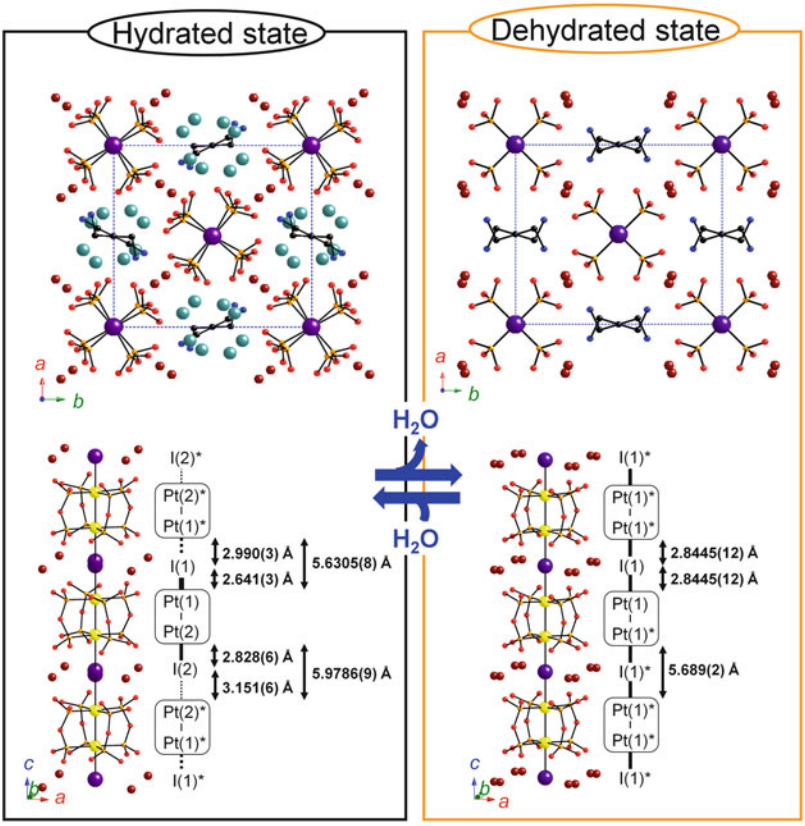

Fig. 10.12 Crystal structure and chain structure of $K_2(NC_3N)[Pt_2(pop)_4I]\cdot 4H_2O$ (*left*) and $K_2(NC_3N)[Pt_2(pop)_4I]$ (*right*). Pt–I and Pt–I–Pt distance are described with the schematic figure. Hydrogen atoms are omitted for clarity. I(1) and I(2) in $K_2(NC_3N)[Pt_2(pop)_4I]\cdot 4H_2O$ and K^+ ions in $K_2(NC_3N)[Pt_2(pop)_4I]$ are disordered. Pt *yellow*, I *purple*, K *brown*, P *orange*, O (ligand) *red*, O (H_2O) *light blue*, N *blue*, C *black*

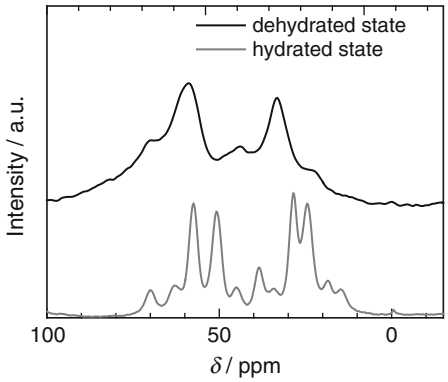

Fig. 10.13 ^{31}P MAS NMR spectra of $K_2(NC_3N)[Pt_2(pop)_4I]\cdot 4H_2O$ (*gray*) and $K_2(NC_3N)[Pt_2(pop)_4I]$ (*black*) measured at room temperature in the solid state

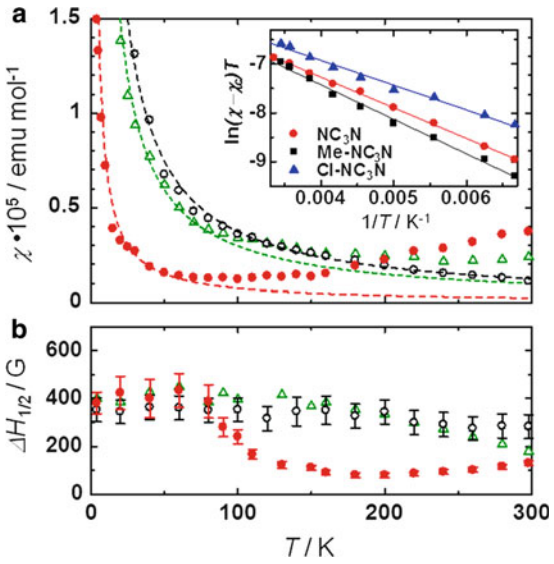

Fig. 10.14 Temperature dependence of (**a**) spin susceptibility (χ) and (**b**) ESR linewidth ($\Delta H_{1/2}$) obtained for the initial (*open circles*), dehydrated (*solid circles*), and rehydrated (*open triangles*) samples of $K_2(NC_3N)[Pt_2(pop)_4I]\cdot 4H_2O$. The *dashed curves* in (**a**) represent the fitting by the Curie law. The inset in (**a**) shows the plot of $\Delta\chi\cdot T$ vs.T^{-1} obtained for the three dehydrated salts of $K_2(NC_3N)[Pt_2(pop)_4I]$ (*circles*), $K_2(Me–NC_3N)[Pt_2(pop)_4I]$ (*rectangles*), and $K_2(Cl–NC_3N)[Pt_2(pop)_4I]$ (*triangles*). The *solid lines* show the fitting by the activation formula

The temperature dependence of the molar spin susceptibility (χ) of $K_2(NC_3N)[Pt_2(pop)_4I]\cdot 4H_2O$ and $K_2(NC_3N)[Pt_2(pop)_4I]$ obtained by using ESR spectroscopy (Fig. 10.14) indicates the interesting electronic state in the dehydrated state [46, 53]. Although the χ of $K_2(NC_3N)[Pt_2(pop)_4I]\cdot 4H_2O$ followed the Curie law (dashed line), which is consistent with the nonmagnetic ACP + CDW state, the χ of $K_2(NC_3N)[Pt_2(pop)_4I]$ gradually increased above about 80 K, and followed the Curie law (dashed line) below about 80 K. The principal g values were determined from the single-crystal rotation measurements at room temperature to reveal the origin of the spin [53]. As a result, the anisotropic g value of uniaxial type with the principal values of $g_{//} = 1.966$ and $g_{\perp} = 2.147$ for the parallel and perpendicular directions to the chain, respectively, were observed in the dehydrated state. Observed anisotropy of $g_{\perp} > 2 > g_{//}$ is consistent with that expected for the low-spin Pt^{3+} ($S = 1/2$), where the unpaired electron resides on the $Pt(5d_{z^2})$ orbital.

The resultant susceptibility ($\Delta\chi = \chi–\chi_c$), where χ_c is Curie component, obeyed an activation type equation above about 80 K: $\Delta\chi\cdot T = C\exp(–E_g/k_BT)$, where C is the Curie constant of activated spins, E_g is the activation energy, and k_B is the Boltzmann constant. Concomitantly, the ESR linewidth ($\Delta H_{1/2}$) exhibited distinct motional narrowing above the same temperature range as the spin excitation took place, suggesting that the activated Pt^{3+} spins are mobile solitons generated in the doubly degenerated CDW state with small d(Pt–I–Pt). The origin of solitons are

isolated Pt^{3+} state (or [Pt^{2+}–Pt^{3+}] unit) locating at the mismatch of the doubly degenerate valence ordering phases of $[\cdots Pt^{2+} - Pt^{2+} \cdots I^- - Pt^{3+} - Pt^{3+} - I^- \cdots]$ and $[-Pt^{3+} - Pt^{3+} - I^- \cdots Pt^{2+} - Pt^{2+} \cdots I^- -]$. The formation of solitons has been predicted theoretically in the case of CDW and ACP states in the MMX chains by using Peierls–Hubbard model [68–70]. However, it has been actually demonstrated only in the case of the ACP state of a dta system $Pt_2(n\text{-pentylCS}_2)_4I$ by the ESR technique [38, 44, 45]. Therefore, the solitons in CDW state and those in pop system are demonstrated for the first time in $K_2(NC_3N)[Pt_2(pop)_4I]$. Similar phenomena are also found in $K_2(Me–NC_3N)[Pt_2(pop)_4I]\cdot 4H_2O$ and $K_2(Cl–NC_3N)[Pt_2(pop)_4I]\cdot 4H_2O$ (Fig. 10.14a inset) whereas the crystal becomes polycrystal after the dehydration in these compounds.

Taken together, reversible single-crystal-to-single-crystal transformation accompanied by changes in the optical gap and electronic state was realized in $K_2(NC_3N)[Pt_2(pop)_4I]\cdot 4H_2O$ by the dehydration and rehydration.

10.3.3 Dependence of Water-Vapor-Induced Switching in MMX Chains on the Length of Alkyldiammonium Ions

To reveal the dependence of the dehydration–rehydration of the complexes on alkyldiammonium ion, XRD patterns of $K_2(B)[Pt_2(pop)_4I]\cdot 4H_2O$ were measured at three stages (1) Initial hydrated complex. (2) Dehydrated complex. (3) After the exposure of dehydrated complex to H_2O vapor for a day. As a result, for $B^{2+} = NC_3N^{2+}$, $Me–NC_3N^{2+}$, $Cl–NC_3N^{2+}$, *cis*-NC_4N^{2+}, and *trans*-NC_4N^{2+}, structural changes by dehydration–rehydration were reversible (Fig. 10.15a, $K_2(NC_3N)[Pt_2(pop)_4I]\cdot 4H_2O$ as a example). The XRD patterns of dehydrated complexes can be fitted as orthorhombic *C*-lattice. Because the unit cell parameter *c* (chain axis) of dehydrated complexes are almost equal to that of $K_2(NC_3N)[Pt_2(pop)_4I]$, the *d*(Pt–I–Pt) of the dehydrated complexes ($B^{2+} = Me–NC_3N^{2+}$, $Cl–NC_3N^{2+}$, *cis*-NC_4N^{2+}, *trans*-NC_4N^{2+}) are estimated to be close to that of $K_2(NC_3N)[Pt_2(pop)_4I]$. In contrast, for $B^{2+} = NC_5N^{2+}$ and $NC_2OC_2N^{2+}$, the changes were only partly reversible and perfectly irreversible, respectively (Fig. 10.15b, c). Moreover, the XRD patterns of dehydrated $K_2(NC_5N)[Pt_2(pop)_4I]$ and $K_2(NC_2OC_2N)[Pt_2(pop)_4I]$ were quite different from their hydrated state. The detail structural analysis is remaining issue that need to be solved.

The temperature dependence of the electrical conductivity parallel to chain axis (*c*) of $K_2(B)[Pt_2(pop)_4I]\cdot 4H_2O$ in each stage are shown in Fig. 10.16 [31, 46]. The σ_{RT} and activation energy (E_a) in each stage are summarized in Table 10.4. The conductivity of $K_2(NC_2OC_2N)[Pt_2(pop)_4I]\cdot 4H_2O$ at stage 2 and 3 were unavailable due to the quite low conductivity.

Except $K_2(NC_2OC_2N)[Pt_2(pop)_4I]\cdot 4H_2O$, E_a decreased by the dehydration due to the shrinking of *d*(Pt–I–Pt), that is, increase of orbital overlap between the Pt($5d_{z^2}$) and I ($5p_z$) atoms.

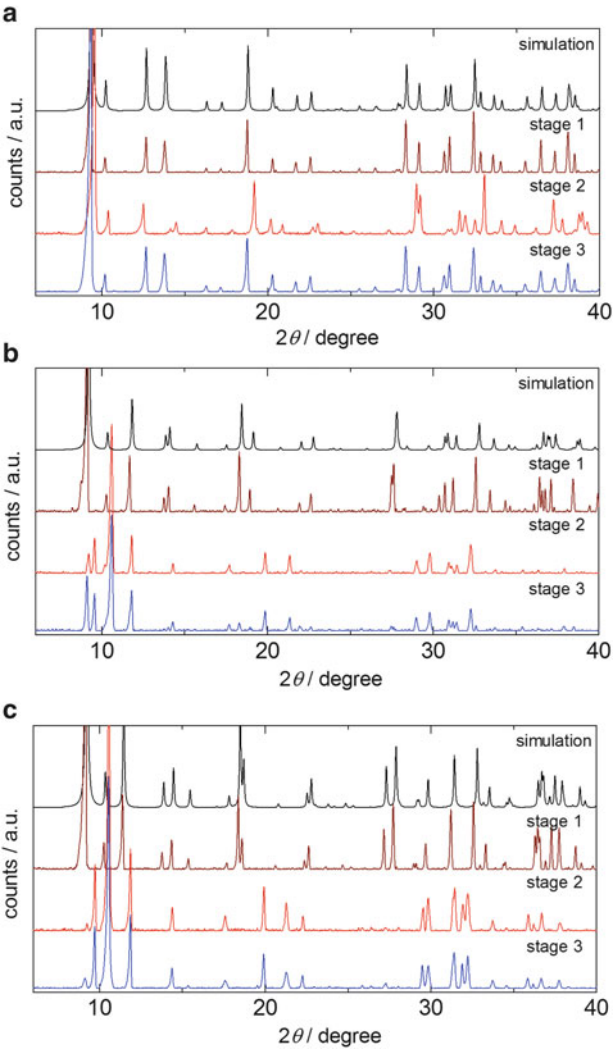

Fig. 10.15 XRD patterns of (**a**) $K_2(NC_3N)[Pt_2(pop)_4I]\cdot 4H_2O$, (**b**) $K_2(NC_5N)[Pt_2(pop)_4I]\cdot 4H_2O$, (**c**) $K_2(NC_2OC_2N)[Pt_2(pop)_4I]\cdot 4H_2O$ simulated by the crystal structure (*black*), measured at stage 1 (*brown*), stage 2 (*red*) and stage 3 (*blue*)

The change of σ_{RT} by dehydration and rehydration depends on the complex. In the case of the complexes ($B^{2+} = NC_3N^{2+}$, Me–NC_3N^{2+}, Cl–NC_3N^{2+}, *trans*-NC_4N^{2+}), σ_{RT} at stage 2 (dehydrated state) were 10–100 times larger than that at stage 1 (initial states). Contrastingly, in the case of the complexes ($B^{2+} =$ *cis*-NC_4N^{2+}, NC_5N^{2+}), σ_{RT} at stage 2 were 0.25 and 0.04 times larger than those at stage 1, respectively. These decrease of σ_{RT} may be due to the partial degradation of

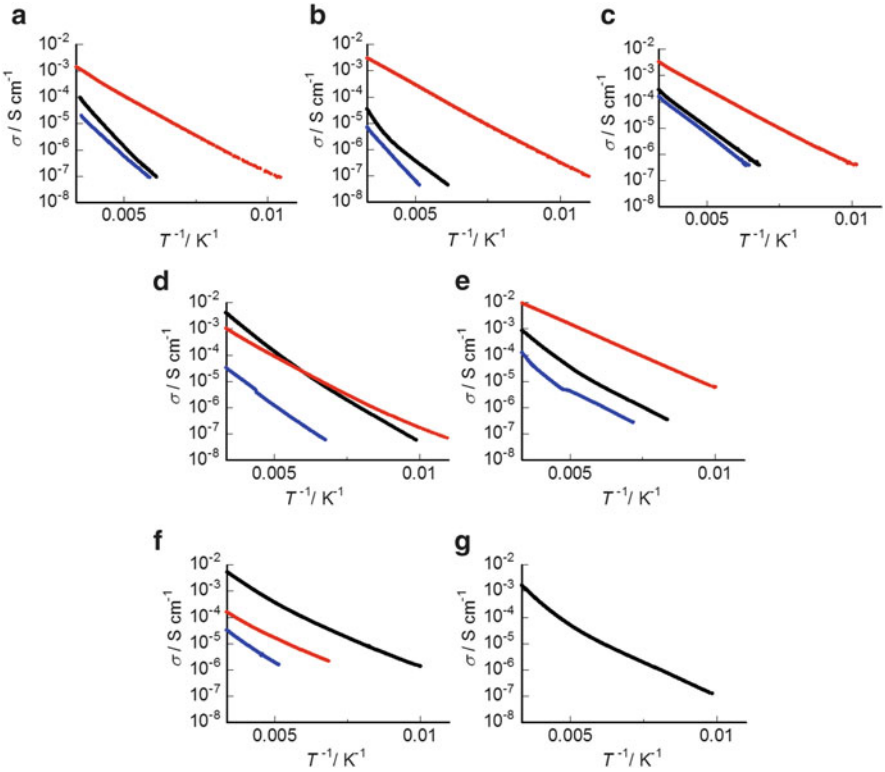

Fig. 10.16 Temperature dependence of the electrical conductivity at stage 1 (*black*), 2 (*red*), and 3 (*blue*) of $K_2(B)[Pt_2(pop)_4I]\cdot 4H_2O$, where B^{2+} = (**a**) NC_3N^{2+}, (**b**) Me–NC_3N^{2+}, (**c**) Cl–NC_3N^{2+}, (**d**) *cis*-NC_4N^{2+}, (**e**) *trans*-NC_4N^{2+}, (**f**) NC_5N^{2+}, and (**g**) $NC_2OC_2N^{2+}$

Table 10.4 σ_{RT} (RT = 298 K) and E_a at high temperature of $K_2(B)[Pt_2(pop)_4I]\cdot 4H_2O$ measured in each stage

	σ_{RT}/S cm^{-1} (RT = 298 K)			E_a/meV		
	Stage 1	Stage 2	Stage 3	Stage 1	Stage 2	Stage 3
$K_2(NC_3N)[Pt_2(pop)_4I]\cdot 4H_2O$	1.5×10^{-4}	1.4×10^{-3}	8.0×10^{-5}	226	122	196
$K_2(Me–NC_3N)[Pt_2(pop)_4I]\cdot 4H_2O$	3.3×10^{-5}	3.3×10^{-3}	6.9×10^{-6}	319	119	240
$K_2(Cl–NC_3N)[Pt_2(pop)_4I]\cdot 4H_2O$	2.8×10^{-4}	3.3×10^{-3}	1.5×10^{-4}	161	120	167
$K_2(cis\text{-}NC_4N)[Pt_2(pop)_4I]\cdot 4H_2O$	4.0×10^{-3}	1.0×10^{-3}	3.3×10^{-5}	174	122	151
$K_2(trans\text{-}NC_4N)[Pt_2(pop)_4I]\cdot 4H_2O$	8.4×10^{-4}	9.4×10^{-3}	1.2×10^{-4}	169	96	195
$K_2(NC_5N)[Pt_2(pop)_4I]\cdot 4H_2O$	4.4×10^{-3}	1.6×10^{-4}	3.2×10^{-5}	145	126	148
$K_2(NC_2OC_2N)[Pt_2(pop)_4I]\cdot 4H_2O$	1.6×10^{-3}			200		

the sample such as small cracks generated in the crystal. These cracks limit the current pass in the crystal to reduce the effective cross-sectional area of the crystal.

Compared with the σ_{RT} at stage 1 and 3, σ_{RT} at each stages were comparable in the case of the complexes (B^{2+} = NC_3N^{2+}, Me–NC_3N^{2+}, Cl–NC_3N^{2+}), whereas they decreased to 0.008, 0.14 and 0.007 times larger than those of stage 1 in the case of the complexes (B^{2+} = *cis*-NC_4N^{2+}, *trans*-NC_4N^{2+}, NC_5N^{2+}, respectively). Since the crystal structure recovered perfectly in K_2(*cis*-NC_4N)[$Pt_2(pop)_4I$]·$4H_2O$ and K_2(*trans*-NC_4N)[$Pt_2(pop)_4I$]·$4H_2O$, this decrease may also be due to the partial degradation of the sample. The slight rehydration of $K_2(NC_5N)[Pt_2(pop)_4I]$ also reduced the quality of the crystal.

Hence, we can summarize that the robustness of the MMX chains with binary countercations decreases in the following order of B^{2+}: NC_3N^{2+}, Me–NC_3N^{2+}, Cl–NC_3N^{2+} > *trans*-NC_4N^{2+} > *cis*-NC_4N^{2+} > NC_5N^{2+} > $NC_2OC_2N^{2+}$. This order indicates that the complex with longer B^{2+} has weaker framework. In the case of the complexes (B^{2+} = NC_3N^{2+}, Me–NC_3N^{2+}, Cl–NC_3N^{2+}), B^{2+} are in well-ordered zigzag conformation, while in the case of the complexes (B^{2+} = *cis*-NC_4N^{2+}, *trans*-NC_4N^{2+}, NC_5N^{2+}, $NC_2OC_2N^{2+}$), longer B^{2+} are disordered and/or in less stable bending conformation due to the limitation of the region, as mentioned above (Fig. 10.2.). These differences in stability of B^{2+} are assumed to induce the different robustness of the complexes.

10.4 Conclusion

In this study, the development of new electronic state of MMX chains by introducing binary countercations, the control of the electronic states, and the conductance of MMX chains by dehydration–rehydration were carried out.

Single-crystal X-ray structure analysis indicates that MMX chains in binary system, $A_2B[Pt_2(pop)_4I]\cdot nH_2O$ (A = K^+, Rb^+; B = alkyldiammonium; n = 2 or 4) have rare "synchronized" packing induced by the hydrogen bond and coordination bond networks among the chains and short Pt–I–Pt distance. These features play an important role in water-vapor-induced changes and high conductivity of the complexes. Various analyses indicated that the electronic state is novel ACP + CDW state when MMX chains contain shorter alkyldiammonium ion (B^{2+} = NC_3N^{2+}, Me–NC_3N^{2+} Cl–NC_3N^{2+}) but is general CDW state in other cases. The twisting of pop ligands caused by steric hindrance around A^+ is the origin of the ACP-like distortion in ACP + CDW state.

Water-vapor-induced switching of MMX chains is the other focus of this chapter. $(NC_4N)_2[Pt_2(pop)_4I]\cdot 4H_2O$ and $(NC_5N)_2[Pt_2(pop)_4I]\cdot 4H_2O$ showed vapochromism with the switching of the electronic states from CP to CDW state by the dehydration. MMX chains with binary countercations also showed water-vapor-induced switching. The single-crystal X-ray structure analysis of $K_2(NC_3N)[Pt_2(pop)_4I]$ provided us the important information about the electronic state in the dehydrated state. $K_2(NC_3N)[Pt_2(pop)_4I]\cdot 4H_2O$ is the first MMX

chain that shows reversible dehydration–rehydration with retention of single crystallinity. Other MMX chains with binary countercations also shows reversible dehydration–rehydration except the MMX chains containing longer alkyldiammonium ion ($B^{2+} = NC_5N^{2+}$, $NC_2OC_2N^{2+}$). Various spectroscopic analyses indicated that the electronic state of $K_2(NC_3N)[Pt_2(pop)_4I]$ is CDW state but is close to the border of CDW and AV state because the band gap is very small and the solitons are excited at room temperature. MMX chains with binary countercations are also the first examples that show vapor-induced reversible switching of electrical conductivity in MMX chains. The robustness of the complexes becomes weaker as the length of B^{2+} of the complexes becomes longer.

References

1. Sperline RP, Dickson MK, Roundhill DM (1977) J Chem Soc Commun 62
2. Zipp AP (1988) Coord Chem Rev 84:47
3. Roundhill DM, Gray HB, Che C-M (1989) Acc Chem Res 22:55
4. Thiel DJ, Livins P, Stern EA, Lewis A (1993) Nature 362:40
5. Thiel DJ, Livins P, Stern EA, Lewis A (1993) Nature 363:565
6. Kim CD, Pillet S, Wu G, Fullagar WK, Coppens P (2002) Acta Crystallogr Sect A Found Crystallogr A58:133
7. Ozawa Y, Terashima M, Mitsumi M, Toriumi K, Yasuda N, Uekusa H, Ohashi Y (2003) Chem Lett 32:62
8. Yasuda N, Uekusa H, Ohashi Y (2004) Bull Chem Soc Jpn 77:933
9. Christensen M, Haldrup K, Bechgaard K, Feidenhans'l R, Kong Q, Cammarata M, Russo ML, Wulff M, Harrit N, Nielsen MM (2009) J Am Chem Soc 131:502
10. Harvey PD, Gray HB (1987) New J Chem 11:595
11. Che C-M, Lee W-M (1986) J Chem Soc Chem Commun 512
12. Lin J, Pittman CU Jr (1996) J Organomet Chem 512:69
13. Harvey EL, Stiegman AE, Vlćek A Jr, Gray HB (1987) J Am Chem Soc 109:5233
14. Stiegman AE, Miskowski VM, Gray HB (1986) J Am Chem Soc 108:2781
15. Bennett MA, Bhargava SK, Bond AM, Bansal V, Forsyth CM, Guo S-X, Privér SH (2009) Inorg Chem 48:2593
16. Che C-M, Herbstein FH, Schaefer WP, Marsh RE, Gray HB (1983) J Am Chem Soc 105:4604
17. Robin MB, Day P (1967) Adv Inorg Chem Radiochem 9:247
18. Day P (1974) Low-dimensional cooperative phenomena In: Keller HJ (ed) Plenum Press, New York, pp 191–214
19. Welte L, Garcia-Couceiro U, Castillo O, Olea D, Polop C, Guijarro A, Luque A, Gomez-Rodriguez JM, Gomez-Herrero J, Zamora F (2009) Adv Mater 21:2025
20. Welte L, Calzolari A, Felice RD, Zamora F, Gomez-Herrero J (2010) Nat Nanotechnol 5:110
21. Guijarro A, Castillo O, Welte L, Calzolari A, Miguel PJS, Gomez-Garcia CJ, Olea D, Felice RD, Gomez-Herrero J, Zamora F (2010) Adv Funct Mater 20:1451
22. Mas-Balleste R, Gomez-Herrero J, Zamora F (2010) Chem Soc Rev 39:4220
23. Kurmoo M, Clark RJH (1985) Inorg Chem 24:4420
24. Clark RJH, Kurmoo M, Dawes H, Hursthouse MB (1986) Inorg Chem 25:409
25. Butler LG, Zietlow MH, Che C-M, Schaefer WP, Sridhar S, Grunthaner PJ, Swanson BI, Clark RJH, Gray HB (1988) J Am Chem Soc 110:1155

26. Stroud MA, Drickamer HG, Zietlow MH, Gray HB, Swanson BI (1989) J Am Chem Soc 111:66
27. Yamashita M, Miya S, Kawashima T, Manabe T, Sonoyama T, Kitagawa H, Mitani T, Okamoto H, Ikeda R (1999) J Am Chem Soc 121:2321
28. Takizawa K, Ishii T, Miyasaka H, Matsuzaka H, Yamashita M, Kawashima T, Matsuzaki H, Kishida H, Okamoto H (2002) Mol Cryst Liq Cryst 376:159
29. Yamashita M, Takaishi S, Kobayashi A, Kitagawa H, Matsuzaki H, Okamoto H (2006) Coord Chem Rev 250:2335
30. Iguchi H, Jiang D, Xie J, Takaishi S, Yamashita M (2011) Polymers 3:1652
31. Iguchi H, Takaishi S, Breedlove BK, Yamashita M, Matsuzaki H, Okamoto H (2012) Inorg Chem 51:9967
32. Clark RJH (1984) Chem Soc Rev 13:219
33. Clark RJH (1990) Chem Soc Rev 19:107
34. Terauchi H (1978) Phys Rev B 17:2446
35. Fujita W, Awaga K (1999) Science 286:261
36. Kitagawa H, Onodera N, Sonoyama T, Yamamoto M, Fukawa T, Mitani T, Seto M, Maeda Y (1999) J Am Chem Soc 121:10068
37. Ikeuchi S, Saito K, Nakazawa Y, Sato A, Mitsumi M, Toriumi K, Sorai M (2002) Phys Rev B 66:115110
38. Tanaka H, Kuroda S, Yamashita T, Mitsumi M, Toriumi K (2003) J Phys Soc Jpn 72:2169
39. Mitsumi M, Murase T, Kishida H, Yoshinari T, Ozawa Y, Toriumi K, Sonoyama T, Kitagawa H, Mitani T (2001) J Am Chem Soc 123:11179
40. Mitsumi M, Kitamura K, Morinaga A, Ozawa Y, Kobayashi M, Toriumi K, Iso Y, Kitagawa H, Mitani T (2002) Angew Chem Int Ed 41:2767
41. Mitsumi M, Yoshida Y, Kohyama A, Kitagawa Y, Ozawa Y, Kobayashi M, Toriumi K, Tadokoro M, Ikeda N, Okumura M, Kurmoo M (2009) Inorg Chem 48:6680
42. Kobayashi A, Kitao S, Seto M, Ikeda R, Kitagawa H (2009) Inorg Chem 48:8044
43. Ikeuchi S, Saito K, Nakazawa Y, Mitsumi M, Toriumi K, Sorai M (2004) J Phys Chem B 108:387
44. Tanaka H, Hasegawa Y, Ito H, Kuroda S, Yamashita T, Mitsumi M, Toriumi K (2005) Synth Met 152:141
45. Tanaka H, Kuroda S, Yamashita T, Mitsumi M, Toriumi K (2006) Phys Rev B 73:245102
46. Iguchi H, Takaishi S, Miyasaka H, Yamashita M, Matsuzaki H, Okamoto H, Tanaka H, Kuroda S (2010) Angew Chem Int Ed 49:552
47. Iguchi H, Takaishi S, Kajiwara T, Miyasaka H, Yamashita M, Matsuzaki H, Okamoto H (2008) J Am Chem Soc 130:17668
48. Matsunaga S, Takizawa K, Kawakami D, Iguchi H, Takaishi S, Kajiwara T, Miyasaka H, Yamashita M, Matsuzaki H, Okamoto H (2008) Eur J Inorg Chem 3269
49. Shannon RD (1976) Acta Cryst A32:751
50. Bondi A (1964) J Phys Chem 68:441
51. Matsuzaki H, Matsuoka T, Kishida H, Takizawa K, Miyasaka H, Sugiura K, Yamashita M, Okamoto H (2003) Phys Rev Lett 90:046401
52. Matsuzaki H, Kishida H, Okamoto H, Takizawa K, Matsunaga S, Takaishi S, Miyasaka H, Sugiura K, Yamashita M (2005) Angew Chem Int Ed 44:3240
53. Tanaka H, Kuroda S, Iguchi H, Takaishi S, Yamashita M (2012) Phys Rev B 85:073104
54. Yamashita M, Takizawa K, Matsunaga S, Kawakami D, Iguchi H, Takaishi S, Kajiwara T, Iwahori F, Ishii T, Miyasaka H, Sugiura KI, Matsuzaki H, Kishida H, Okamoto H (2006) Bull Chem Soc Jpn 79:1404
55. Murray LJ, Dinca M, Long JR (2009) Chem Soc Rev 38:1294
56. Li JR, Kuppler RJ, Zhou HC (2009) Chem Soc Rev 38:1477
57. Lee J, Farha OK, Roberts J, Scheidt KA, Nguyen ST, Hupp JT (2009) Chem Soc Rev 38:1450
58. Kurmoo M (2009) Chem Soc Rev 38:1353

59. Ohba M, Yoneda K, Agusti G, Munoz MC, Gaspar AB, Real JA, Yamasaki M, Ando H, Nakao Y, Sakaki S, Kitagawa S (2009) Angew Chem Int Ed 48:4767
60. Kato M (2007) Bull Chem Soc Jpn 80:287
61. Allendorf MD, Bauer CA, Bhakta RK, Houk RJ (2009) Chem Soc Rev 38:1330
62. Fuma Y, Ebihara M, Kutsumizu S, Kawamura T (2004) J Am Chem Soc 126:12238
63. Takaishi S, Hosoda M, Kajiwara T, Miyasaka H, Yamashita M, Nakanishi Y, Kitagawa Y, Yamaguchi K, Kobayashi A, Kitagawa H (2009) Inorg Chem 48:9048
64. Kobayashi Y, Jacobs B, Allendorf MD, Long JR (2010) Chem Mater 22:4120
65. Yamashita M, Kawakami D, Matsunaga S, Nakayama Y, Sasaki M, Takaishi S, Iwahori F, Miyasaka H, Sugiura K, Wada Y, Miyamae H, Matsuzaki H, Okamoto H, Tanaka H, Marumoto K, Kuroda S (2004) Angew Chem Int Ed 43:4763
66. Iguchi H, Takaishi S, Kajiwara T, Miyasaka H, Yamashita M, Matsuzaki H, Okamoto H (2009) J Inorg Organomet Polym Mater 19:85
67. Kimura N, Ohki H, Ikeda R, Yamashita M (1994) Chem Phys Lett 220:40
68. Yamamoto S, Ichioka M (2002) J Phys Soc Jpn 71:189
69. Ohara J, Yamamoto S (2006) Phys Rev B 73:045122
70. Kuwabara M, Yonemitsu K, Ohta H (2002) In: Kawamori A, Yamaguchi J, Ohta H (ed) EPR in the 21st century, Elsevier Science, p 59

Chapter 11
Photoinduced Phase Transitions in MMX-Chain Compounds

Hiroyuki Matsuzaki and Hiroshi Okamoto

11.1 Introduction

As mentioned in Chap. 5, 1D electronic systems are good targets for the exploration of characteristic photoinduced phase transitions (PIPTs), since photocarrier generations and/or charge-transfer excitations by photoirradiation can stimulate instabilities inherent to the 1D nature of electronic states through strong electron–electron interactions and electron (spin)–lattice interactions. Actually, MX-chain compounds, the prototypical 1D electronic systems, exhibit characteristic PIPTs such as the photoinduced transition from Mott insulator to metal, the photoinduced transition from charge-density-wave state to Mott–Hubbard state, and photoinduced transition from charge-density-wave state to metallic state (see Chap. 5). The halogen-bridged binuclear metal compounds (the MMX-chain compounds) focused here are other typical 1D electronic systems with strong electron–electron interactions and electron (spin)–lattice interactions and are promising targets for realizing characteristic PIPTs. In this chapter, we review the PIPTs observed in the MMX-chain compounds.

The materials discussed here are iodine-bridged binuclear platinum compounds (PtPtI-chain compounds), in which PtPtI chains dominate their electronic properties [1–5]. Before discussing the phase control and PIPT in the PtPtI-chain compound, we briefly review its crystal and electronic structure. This compounds have purely

H. Matsuzaki (✉)
Department of Advanced Materials Science, Faculty of Frontier Sciences, University of Tokyo, 5-1-5 Kashiwanoha, Kashiwa, Chiba 277-8561, Japan

Research Institute of Instrumentation Frontier, National Institute of Advanced Industrial Science and Technology (AIST), Tsukuba Central 5, 1-1-1 Higashi, Tsukaba, Ibaraki 305-8565, Japan
e-mail: hiroyuki-matsuzaki@aist.go.jp

H. Okamoto (✉)
Department of Advanced Materials Science, Faculty of Frontier Sciences, University of Tokyo, 5-1-5 Kashiwanoha, Kashiwa, Chiba 277-8561, Japan
e-mail: okamotoh@k.u-tokyo.ac.jp

M. Yamashita and H. Okamoto (eds.), *Material Designs and New Physical Properties in MX- and MMX-Chain Compounds*, DOI 10.1007/978-3-7091-1317-2_11,

1D chains composed of repeating metal–metal–halogen (M–M–X) units with M = Pt and X = I (the MMX chain). In the MMX chain, a 1D electronic state is formed by d_{z^2} orbitals of M and p_z orbitals of X as schematically illustrated in Fig. 11.2b. The average valence of M is 2.5, and one unpaired electron exists per two d_{z^2} orbitals. Four charge-ordering states shown below are theoretically expected to exist in this system [2, 6–9].

$$\text{Average valence state (AV)}: -M^{2.5+}-M^{2.5+}-X^{-}-M^{2.5+}-M^{2.5+}-X^{-}-$$

$$\text{Charge density wave state (CDW)}: -M^{2+}-M^{2+}-X^{-}-M^{3+}-M^{3+}-X^{-}-$$

$$\text{Charge polarization state (CP)}: -M^{2+}-M^{3+}-X^{-}-M^{2+}-M^{3+}-X^{-}-$$

$$\text{Alternating charge polarization state (ACP)}: -M^{2+}-M^{3+}-X^{-}-M^{3+}-M^{2+}-X^{-}-$$

The CDW and CP states are stabilized by the displacements of X, while the ACP state is stabilized by the displacements of M dimers. Two classes of MMX chains with different ligand molecules, $R_4[Pt_2(pop)_4X]nH_2O$ [(pop) = $P_2O_5H_2^{2-}$, R = K, NH_4, and X = Cl, Br] [3, 10] and $Pt_2(dta)_4I$ (dta = $CH_3CS_2^{-}$) [11, 12] have been studied so far. The ground state of $R_4[Pt_2(pop)_4X]nH_2O$ (R = K, NH_4 and X = Cl, Br) has been revealed to be CDW [13, 14]. For $Pt_2(dta)_4I$, it has been suggested that ACP is stabilized at low temperature [12]. As a general trend, the hybridization between the p orbital of halogens and the d orbital of metals in the I-bridged compounds is larger than that in the Cl- or Br-bridged compounds. The larger pd hybridization will stabilize the various oxidation states (or charge-ordering states) of the metals.

In this chapter, first we show that the ground states on the PtPtI chains ($R_4[Pt_2(pop)_4I]nH_2O$ and $R'_2[Pt_2(pop)_4I]nH_2O$) can be controlled between a diamagnetic CDW state and a paramagnetic charge polarization (CP) state by modification of the counter ions (R, R′) located between chains. After that, we show that in $[(C_2H_5)_2NH_2]_4[Pt_2(pop)_4I]$, the pressure-induced transition from CP to CDW accompanied by a large hysteresis loop occurs. In the last part of this chapter, we report that in the hysteresis region of the pressure-induced CP to CDW transition of $[(C_2H_5)_2NH_2]_4[Pt_2(pop)_4I]$, the photoinduced phase transition from the CDW state to the CP state could be driven.

11.2 Experimental Methods

11.2.1 Steady-State Optical Spectroscopy Under High Pressure

Applying external pressure to materials is one of the powerful tools for altering their electronic states. To achieve the electronic phase control of MMX-chain compound, we adopted the steady-state optical spectroscopies (polarized Raman scattering and reflection spectroscopy) under high pressure using a diamond anvil cell (DAC). DAC is a typical device used in high-pressure measurements. It allows

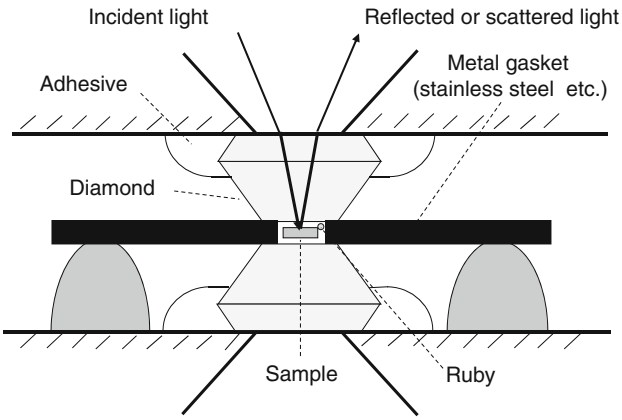

Fig. 11.1 Schematic of a diamond anvil cell (DAC) used for steady-state optical measurements under the pressure

compressing a small (submillimeter sized) piece of material to high pressures [15]. The schematic illustration of DAC is shown in Fig. 11.1. A DAC consists of two opposing diamonds and a metal gasket with a hole of ~500 μm diameter. A sample is in the small hole of a metal gasket sandwiched by two diamonds and is compressed between the culets of diamond as shown in the figure. In the spectroscopic measurements using DAC, liquid paraffin was used as a pressure-transmitting medium. In a DAC, a tiny piece of ruby is also located together with a sample to monitor the pressure. The pressure within the cell was calibrated by the wavelength shift of the R_1 fluorescence line of the ruby excited by a He–Ne laser. Polarized Raman-scattering spectra were measured using a Raman spectrometer equipped with a He–Ne laser (1.96 eV) and an optical microscope. Polarized reflection measurements were performed using a Fourier-transformed infrared (IR) spectrometer in the IR region and specially designed spectrometer with a grating monochromator in the visible to ultraviolet region.

11.3 Phase Control and Photoinduced Phase Transition in 1D Halogen-Bridged Binuclear Platinum Compound

11.3.1 Control of Electronic Phases in PtPtI-Chain Compounds

To control the electronic structures of the MMX-chain compounds, Yamashita and their collaborators have synthesized about 20 compounds of $R_4[Pt_2(pop)_4I]nH_2O$ and $R'_2[Pt_2(pop)_4I]nH_2O$, with counter ions (R^+ or R'^{2+}) of the alkyl-ammonium ($R = C_nH_{2n+1}NH_3$, $(C_nH_{2n+1})_2NH_2$ and $R' = H_3N(C_nH_{2n})NH_3$) and the alkali-metal (R = Na, K, NH_4, Rb, and Cs) [1, 3–5]. The substitution of the counter

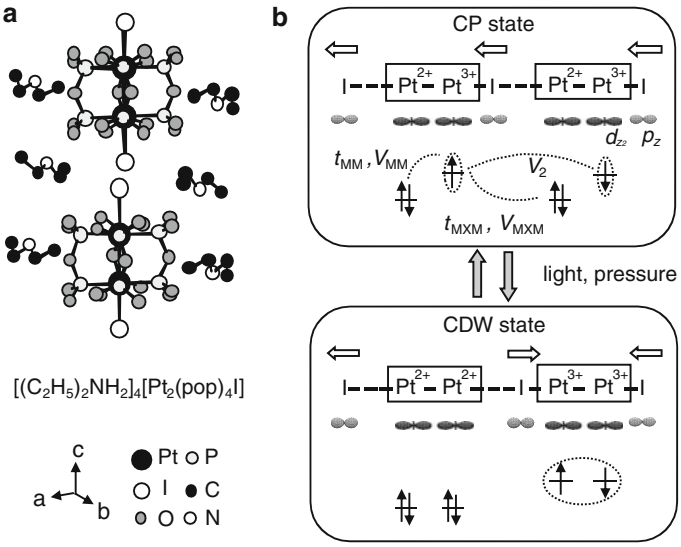

Fig. 11.2 (**a**) Crystal structure of $[(C_2H_5)_2NH_2]_4[Pt_2(pop)_4I]$. H atoms have been omitted for clarity. (**b**) Schematic electronic structures of CDW and CP. t_{MM} and t_{MXM} denote the electron transfer energies. V_{MM}, V_{MXM}, and V_2 denote the Coulomb interactions

ions greatly alters the distance d(Pt–I–Pt) between two Pt ions bridged by the I ion. Such control of d(Pt–I–Pt) makes it possible to control the various electronic parameters such as intersite e–e interaction and e–l interaction and to realize the paramagnetic CP state as well as the diamagnetic CDW state.

Figure 11.2a represents the structure of a typical PtPtI chain, $[(C_2H_5)_2NH_2]_4[Pt_2(pop)_4I]$. Two Pt ions are linked by four pop molecules, forming a binuclear $Pt_2(pop)_4$ unit. The two neighboring $Pt_2(pop)_4$ units are bridged by I and the PtPtI-chain structure is formed along the c axis. The iodine ion deviates from the midpoints between the two neighboring Pt ions, indicating that this compound is in CDW state or CP state, as illustrated in Fig. 11.2b. Figure 11.2a shows the two possible positions of I as the displacements of I are not three-dimensionally ordered. X-ray structural analysis was unable to resolve whether the ground state is CDW state or CP state. CP state is composed of Pt^{2+}–Pt^{3+} units, and the Pt^{3+} ions have spin ($S = 1/2$), forming a 1D antiferromagnetic spin chain. CDW state on the other hand is composed of Pt^{2+}–Pt^{2+} and Pt^{3+}–Pt^{3+} units and is diamagnetic since the two neighboring Pt^{3+} ions form singlet states. The ground states of the PtPtI chains can then be discussed keeping these characteristics of the two charge ordering states in mind.

Figure 11.3a shows the optical conductivity spectra of $[H_3N(C_6H_{12})NH_3]_2[Pt_2(pop)_4I]$ and $[(C_2H_5)_2NH_2]_4[Pt_2(pop)_4I]$ as typical examples. The optical gap energies E_{gap} (1.0 and 2.4 eV) of the two compounds differ considerably. The Raman-scattering spectra are shown in the inset to provide information concerning the valence of M [3–5]. Strong bands at 80–100 cm^{-1} are attributed to the Pt–Pt

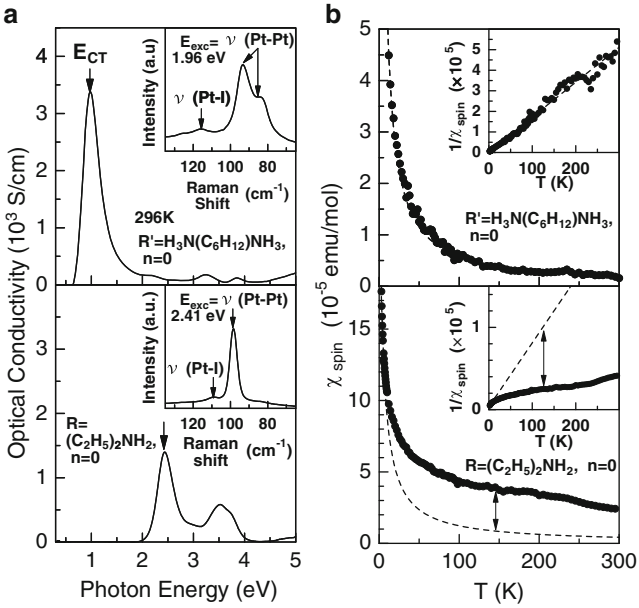

Fig. 11.3 (**a**) Optical conductivity spectra with light polarization parallel to the chain axis in the $[(C_2H_5)_2NH_2]_4[Pt_2(pop)_4I]$ and $[H_3N(C_6H_{12})NH_3]_2[Pt_2(pop)_4I]$, and Raman spectra (inset) for the polarization of $z(xx)z$ (x//chain axis). (**b**) Temperature dependence of χ_{spin} and $1/\chi_{spin}$ (insets). *Broken lines* represent Curie components

stretching mode of the Pt–Pt unit. The splitting of this mode indicates the formation of two kinds of Pt–Pt units, in this case Pt^{2+}–Pt^{2+} and Pt^{3+}–Pt^{3+}. The ground state of $[H_3N(C_6H_{12})NH_3]_2[Pt_2(pop)_4I]$ can therefore be considered to be CDW state. In $[(C_2H_5)_2NH_2]_4[Pt_2(pop)_4I]$, this Pt–Pt stretching Raman mode is a single band, suggesting that the ground state is CP state. The weak bands at around 110 cm^{-1} can be attributed to the Pt–I stretching mode, which is activated by the displacements of I in both compounds.

The magnetic properties of the materials were then investigated to confirm these assignments. The temperature dependence of χ_{spin} ($1/\chi_{spin}$) is shown in Fig. 11.3b. In $[H_3N(C_6H_{12})NH_3]_2[Pt_2(pop)_4I]$, χ_{spin} follows the Curie law as shown by the broken line in Fig.11.3b (the upper figure). Curie impurities make up 0.16 % per Pt site. No paramagnetic components originate from the 1D spin chains. In $[(C_2H_5)_2NH_2]_4[Pt_2(pop)_4I]$, on the other hand, the temperature dependence of χ_{spin} cannot be explained by the Curie component alone. χ_{spin} has a finite component independent of temperature, which is attributable to a contribution from the 1D spin chain. The result in Fig.11.3b (the lower figure) can be largely reproduced by the sum of the Bonner–Fisher curve [16] with $J \sim 3{,}000$ K (J: antiferromagnetic interaction) and Curie component with the concentration of 0.34 % per Pt site. From these comparative studies, it can be concluded that the ground states of $[(C_2H_5)_2NH_2]_4[Pt_2(pop)_4I]$ and $[H_3N(C_6H_{12})NH_3]_2[Pt_2(pop)_4I]$ are CP state and CDW state, respectively.

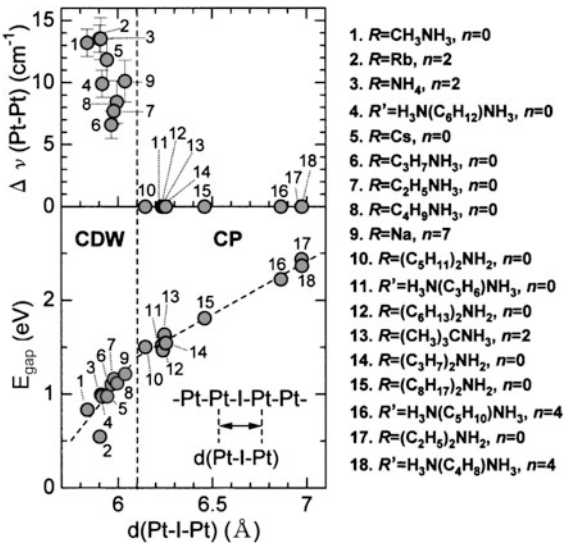

Fig. 11.4 The magnitude of the splitting in the Pt–Pt stretching Raman band Δν(Pt–Pt) (the *upper panel*) and the optical gap energy E_{gap} as functions of d(Pt–I–Pt) in various PtPtI chain compounds (the *lower panel*)

Systematic optical, magnetic, and X-ray studies have been performed on various PtPtI-chain compounds with different counter ions. From the results, the phase diagram shown in Fig. 11.4 was obtained. The upper figure shows the magnitude of the splitting in the Pt–Pt stretching Raman band Δν(Pt–Pt), which is the evidence of CDW state. The lower figure shows the optical gap energy E_{gap}. The ground state changes from CP to CDW state with decreasing d(Pt–I–Pt), and there is a clear boundary at around 6.1 Å.

Here let us discuss the stability of CP and CDW as a function of d(Pt–I–Pt), taking account of the theoretical studies based on the one-band-extended Peierls–Hubbard model presented by Kuwabara and Yonemitsu [6, 17]. When d(Pt–I–Pt) is large, the intradimer Coulomb interaction V_{MM} and the intradimer transfer energy t_{MM} are important parameters dominating the ground state in addition to the on-site Coulomb repulsion U on M and the site-diagonal-type e–l interaction β. The interdimer interactions such as the transfer energy t_{MXM}, the Coulomb interaction V_{MXM}, and the second nearest neighbor Coulomb interaction V_2 (see Fig. 11.2b) can be neglected. A simple picture is given by considering the localized limit $t_{MM} = 0$. In this case, the relative energy of CP and CDW is determined by V_{MM}. The sum of the Coulomb energy for two neighboring M dimers in CDW ($5V_{MM}$) is larger than that in CP ($4V_{MM}$). Therefore, V_{MM} stabilizes CP. Under the presence of t_{MM}, the bonding orbital in the M dimer is formed in CP but not formed in CDW because of large U_M. As a result, t_{MM} also stabilizes CP. As d(Pt–I–Pt) decreases, V_{MXM}, V_2, t_{MXM}, and β will increase. The increase of V_2 makes CP rather unstable, while V_{MXM} does not affect the relative energy of CP and CDW. The effects of t_{MXM} and β are not so straightforward. The theoretical calculations have revealed that the increase of β and t_{MXM} also stabilize CDW relatively to CP [17]. Thus, the theoretical studies can explain well the experimental result that the ground state changes from CP to CDW with a decrease of d(Pt–I–Pt).

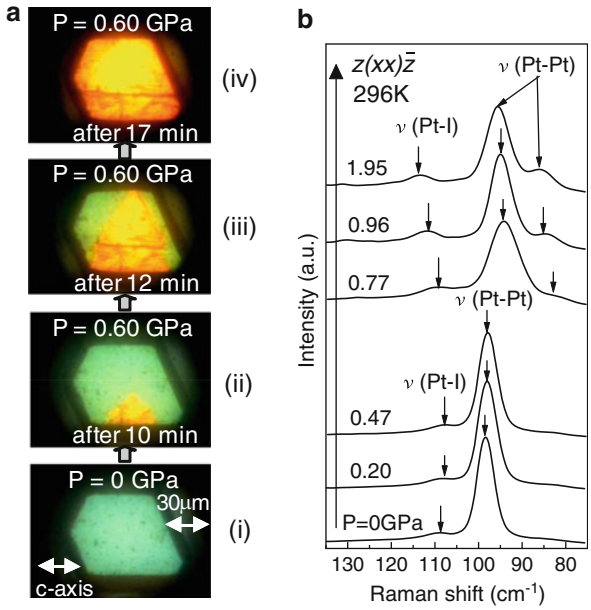

Fig. 11.5 (**a**) Photographic images of $[(C_2H_5)_2NH_2]_4[Pt_2(pop)_4I]$ in the pressure-applying run. (**b**) Pressure dependence of Raman-scattering spectra

11.3.2 Pressure-Induced Phase Transition in PtPtI-Chain Compounds

From the phase diagram shown in Fig. 11.4, it is expected that a phase transition can be driven by applying pressure to the materials in CP state. Such a pressure-induced phase transition from CP to CDW state has been indeed observed for $[(C_2H_5)_2NH_2]_4[Pt_2(pop)_4I]$ (material 17 in Fig. 11.4), $[(C_5H_{11})_2NH_2]_4[Pt_2(pop)_4I]$ (material 10 in Fig. 11.4), and $[(C_3H_7)_2NH_2]_4[Pt_2(pop)_4I]$ (material 14 in Fig. 11.4) in the optical measurements using a diamond anvil pressure cell. Photographs of the pressure-induced transition in $[(C_2H_5)_2NH_2]_4[Pt_2(pop)_4I]$ are presented in Fig. 11.5a. At ambient pressure, this material is green [Fig. 11.5a(i)]. When the pressure is increased to 0.6 GPa, a brown region appears [Fig. 11.5a(ii)] and grows gradually [Fig. 11.5a(iii), (iv)]. Figure 11.5b shows the change in the Raman-scattering spectra accompanying this pressure-induced transition. The Pt–Pt-stretching band clearly splits at above 0.6 GPa, indicating that the high-pressure brown phase is CDW state. Figure 11.6a shows the pressure dependence of the polarized reflectivity spectra for the light polarization (E_i) parallel to the chain axis c ($E_i//c$). The corresponding optical conductivity σ spectra are presented in Fig. 11.6b. In Fig. 11.7a, we show the pressure dependence of E_{gap} obtained from the σ spectra. As can be seen, the phase transition is a first-order reversible one with a large hysteresis loop (ca. 0.4 GPa).

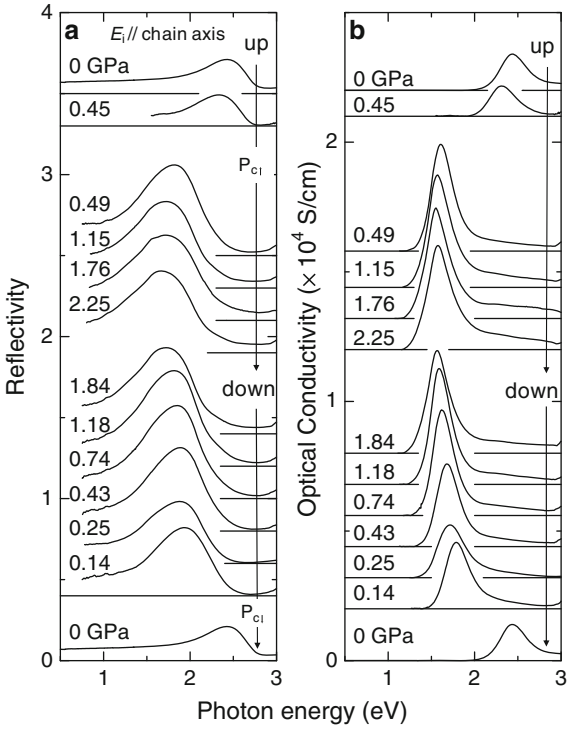

Fig. 11.6 Pressure dependences of (**a**) polarized reflectivity spectra and (**b**) optical conductivity of $[(C_2H_5)_2NH_2]_4[Pt_2(pop)_4I]$ in the pressure-applying and pressure-decreasing runs

From the photographs of the crystal, the reduction of the sample size along the chain axis *c* was observed. Figure 11.8 shows the magnitude of reduction of sample size along the chain axis as a function of the pressure. As shown in the figure, the sample size along the chain axis is reduced by about 8 % at 0.85 GPa compared to ambient pressure. If the Pt–Pt distance *d*(Pt–Pt) of the Pt–Pt unit is assumed to remain constant under pressure, *d*(Pt–I–Pt) at 0.85 GPa is estimated to be 6.2 Å. This assumption is reasonable because *d*(Pt–Pt) is almost constant in various MMX-chain compounds. The obtained values, *d*(Pt–I–Pt) = 6.2 Å and E_{gap} = 1.6 eV at 0.85 GPa, are very close to those in CDW state (see Fig. 11.4). These observations support the fact that the pressure-induced transition from CP to CDW state is driven by a decrease in *d*(Pt–I–Pt) in $[(C_2H_5)_2NH_2]_4[Pt_2(pop)_4I]$.

11.3.3 Photoinduced Phase Transition in PtPtI-Chain Compounds

At the points *A* and *B* within the hysteresis loop shown in Fig. 11.7a, the material is in a meta-stable state as illustrated in the energy potential curves (insets). The PIPT

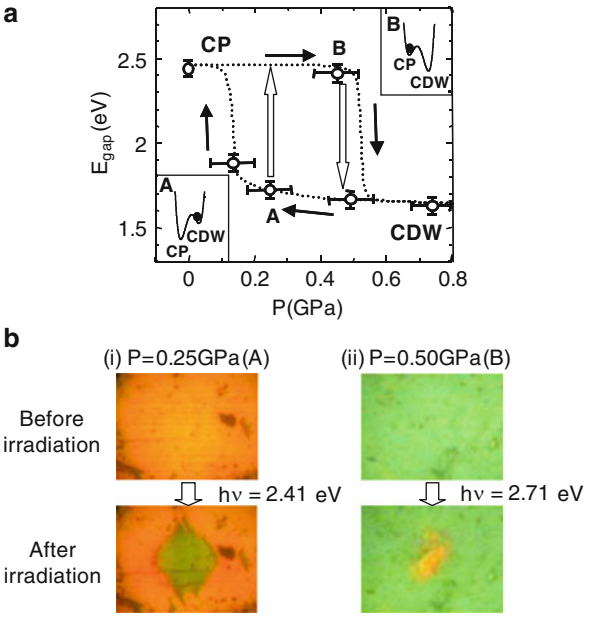

Fig. 11.7 (**a**) Pressure dependence of E_{gap}. The insets show the schematic energy potential curves. (**b**) Photographic images at the points (i) *A* and (ii) *B* before and after photoexcitation. Polarization of the excitation light is parallel to the chain axis *c*

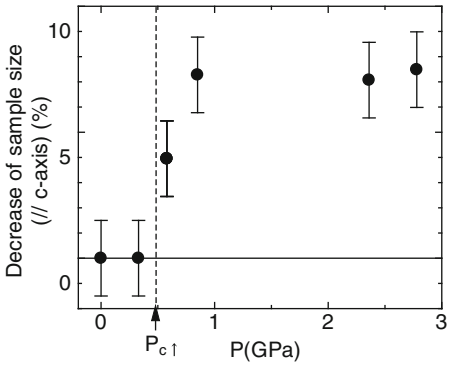

Fig. 11.8 Pressure dependence of the magnitudes of decreases of sample size along the chain axis *c* in $[(C_2H_5)_2NH_2]_4[Pt_2(pop)_4I]$ in the pressure-applying run

from the meta-stable state to the ground state at the points *A* and *B* were investigated. Figure 11.7b(i) represents the images of the sample at *A* before and after the photoexcitation with 2.41-eV light for 8 ms, which is obtained from a CW Ar-ion laser. As can be seen, the crystal exhibits a permanent color change from brown to green in the irradiated region. The Raman signal in the irradiated region is almost identical to that of the low-pressure phase, indicating that the PIPT from CDW to CP state occurs.

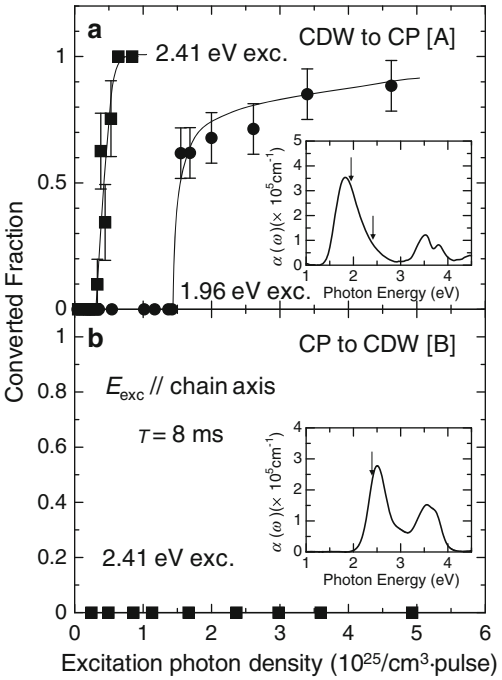

Fig. 11.9 Excitation-photon-density dependence of the conversion efficiency from CDW to CP at the point *A* (**a**) and from CP to CDW at the point *B* (**b**). The insets show the absorption spectra obtained from the polarized reflectivity spectra. The *arrows* indicate the energy positions of the excitation lights

To clarify whether this PIPT is induced by an optical process or a laser heating, the dependence of the photoconversion efficiency on the excitation photon density N was investigated for two excitation energies E_{ex} of 1.96 and 2.41 eV. A He–Ne laser is used for the 1.96-eV light. The result is presented in Fig.11.9a. In the measurements, the excitation photon density N (photon density per pulse) was calculated considering the absorption coefficient and the reflection loss of the excitation light, both of which are obtained from the polarized reflection spectra. The converted fractions were estimated from the photoinduced changes in the integrated intensity of the Pt–Pt stretching Raman bands. The photoconversion efficiency shows a clear threshold N_{th}, the values of which are strongly dependent on E_{ex}; $N_{th} \sim 1.4 \times 10^{25}$ cm^{-3}/pulse at 1.96 eV and $\sim 3 \times 10^{24}$ cm^{-3}/pulse at 2.41 eV. The absolute values of N_{th} seem to be large. However, the irradiated power of the lights is very small. Note that N_{th} is calculated for one pulse with a long duration of 8 ms. This characteristic excitation energy dependence of N_{th} demonstrates that the observed PIPT is driven not by a laser heating but by an optical process. At the point *B*, PIPT could not be driven by the irradiation of 1.96-eV or 2.41-eV light (Fig. 11.9b), even if the intensity and duration of the light was changed. However, irradiation with 2.71-eV light for 30 s did result in a PIPT, as

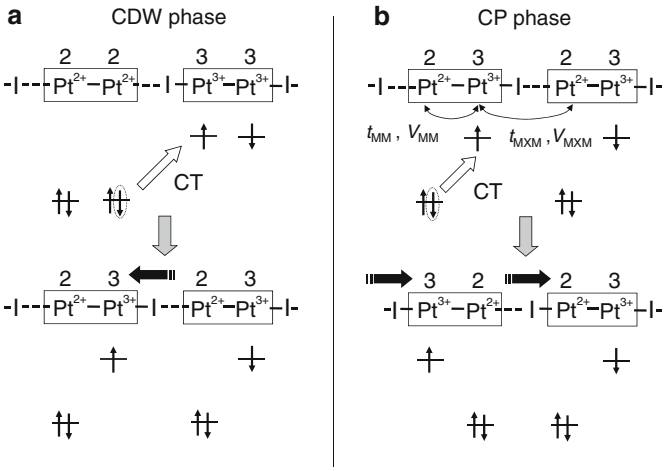

Fig. 11.10 Schematic illustration of the lowest-energy optical transitions in the CDW phase (the high-pressure phase) (**a**) and in the CP phase (the low-pressure phase) (**b**)

shown in Fig. 11.7b(ii). As this process appears to be strongly dependent on the excitation energy, the PIPT from CP to CDW state is also attributable to an optical process, although the efficiency of the PIPT from CP to CDW state is much lower than that from CDW to CP state.

Finally, let us briefly discuss the difference of the photoconversion efficiency between the CDW to CP and the CP to CDW transitions [18, 19]. In Fig. 11.10, the optical transitions of the MMX-chain compound in the CDW and CP ground states are schematically illustrated. The lowest optical transition in CDW state is the interdimer CT excitation from [–I–Pt^{2+}–Pt^{2+}–I–Pt^{3+}–Pt^{3+}–I–] to [–I–Pt^{2+}–Pt^{3+}–I–Pt^{2+}–Pt^{3+}–I–]. By taking into account the lattice relaxations due to the halogen displacements, the 2+3+2+3+ valence state will be stabilized in a photoexcited state as shown in Fig.11.10a. Namely, in the CDW state, an optical excitation will produce locally a CP state. This is the reason why the transition from CDW to CP state is easily induced by lights. In the CP state, it has been established that the intradimer CT transition from [–I–Pt^{2+}–Pt^{3+}–I–Pt^{2+}–Pt^{3+}–I–] to [–I–Pt^{3+}–Pt^{2+}–I–Pt^{2+}–Pt^{3+}–I–] shown in Fig. 11.10b is the dominant optical excitation corresponding to the optical gap transition. The intensity of the interdimer transition is smaller than that of the intradimer one. In this intradimer transition process, the CDW state is never produced, even as a local excited state, as shown in Fig. 11.10b. As a result, the CP to CDW transition is difficult to be achieved by the photoirradiation with the energy of 2.41 eV nearly equal to E_{gap}. As observed in the experiments, the 2.71-eV excitation drives the PIPT from CP to CDW state, although the transition efficiency is very low. Such a higher-energy excitation will induce the interdimer CT transition from [–I–Pt^{2+}–Pt^{3+}–I–Pt^{2+}–Pt^{3+}–I–] to [–I–Pt^{2+}–Pt^{2+}–I–Pt^{3+}–Pt^{3+}–I–], which may be relevant to the PIPT to CDW state.

11.4 Summary

In this chapter, we have reviewed the studies of photoinduced phase transition (PIPT) in the MMX-chain compound. The PIPT of the iodine-bridged binuclear Pt compound, $[(C_2H_5)_2NH_2]_4[Pt_2(pop)_4I]$, between the charge-density-wave (CDW) state and the charge polarization (CP) state has been discussed on the basis of the results obtained by several kinds of optical spectroscopies. This transition is an exceptional example of PIPT, demonstrating that it is possible to achieve fundamental changes in optical and magnetic properties in both directions from CDW to CP and CP to CDW through photoirradiation alone. In this compound, the investigations of the dynamics using the pump–probe spectroscopy has not been performed yet, which will clarify more detailed pictures of its PIPT. The finding of PIPT presented here indicates that MMX-chain compound can be candidates of future optical switching and memory devices.

Acknowledgment The studied reported here were done in collaboration with many researchers; Mr. T. Matsuoka, Prof. M. Yamashita, and Prof. S. Takaishi (Tohoku University), Prof. H. Kishida (Nagoya University). We thank all of these collaborators. We also thank Dr. K. Iwano and Prof. K. Nasu (KEK), Prof. K. Yonemitsu and Dr. M. Kuwabara (IMS), and Prof. S. Yamamoto (Hokkaido University) for valuable discussions.

References

1. Matsuzaki H, Matsuoka T, Kishida H, Takizawa K, Miyasaka H, Sugiura K, Yamashita M, Okamoto H (2003) Phys Rev Lett 90:046401
2. Robin MB, Day P (1967) Adv Inorg Radiochem 10:247
3. Kumoo M, Clark R (1985) Inorg Chem 24:4320
4. Butler LG, Zietlow MH, Che CM, Schaefer WP, Sridhar S, Grunthaner PJ, Swanson BI, Clark RJH, Gray HB (1988) J Am Chem Soc 110:1155
5. Yamashita M, Miya S, Kawashima T, Manabe T, Sonoyama T, Kitagawa H, Miya T, Okamoto H, Ikeda R (1999) J Am Chem Soc 121:2321
6. Kuwabara M, Yonemitsu K (2001) J Phys Chem Solids 62:453
7. Yamamoto S (2001) Phys Rev B 63:125124
8. Yamamoto S (2001) J Phys Soc Jpn 70:1198
9. Yamamoto S (2001) Phys Rev B 64:140402
10. Kimura N, Ohki H, Ikeda R, Yamashita M (1994) Chem Phys Lett 220:40
11. Bellitto C, Flamini A, Gastaldi L, Scaramuzza L (1983) Inorg Chem 22:4–34
12. Kitagawa H, Onodera N, Sonoyama T, Yamamoto M, Fukawa T, Mitani T, Seto M, Maeda Y (1999) J Am Chem Soc 121:10068
13. Takizawa K, Ishii T, Miyasaka H, Matsuzaka H, Yamashita M, Kawashima T, Matsuzaki H, Kishida H, Okamoto H (2002) Mol Cryst Liq Cryst 376:159
14. Baeriswyl D, Bishop AR (1988) J Phys C 21:339
15. Hemley RJ, Ashcroft NW (1998) Phys Today 51:26
16. Bonner JC, Fisher ME (1964) Phys Rev 135:A640
17. Kuwabara M, Yonemitsu K (2001) J Mater Chem 11:2163
18. Yonemitsu K, Miyashita N, Kuwabara M (2003) Synth Met 135:521
19. Yonemitsu K, Miyashita N (2003) Phys Rev B 68:75113

Chapter 12
Theory of MMX-Chain Compounds

Kenji Yonemitsu

12.1 Introduction

MMX-chain compounds have a variety of electronic phases owing to their low-dimensional electronic structures and their strong electron–lattice and electron–electron interactions. Some of these interactions compete with each other, while some of them collaborate. To understand the interplay, theoretical studies based on Peierls–Hubbard models are useful. The electronic properties depend on transition metal (M) ions, halogen (X) ions, ligands, and counterions. Observed and suggested electronic phases for MMX-chain compounds are schematically shown in Fig. 12.1 and classified into an averaged-valence (AV) phase, a charge-density-wave (CDW) phase, a charge-polarization (CP) phase, and an alternate-charge-polarization (ACP) phase. From the valences of the metal ions, the CDW, CP, and ACP phases are also called the 2233, 2323, and 2332 phases, respectively. Because electrons are not completely localized, the formal valences 2 and 3 mean valences $2.5 - \delta$ and $2.5 + \delta$, in reality, with $0 < \delta < 0.5$. The AV and CP phases are paramagnetic, while the CDW and ACP phases are nonmagnetic. In the CDW phase, the spin gap is expected to be comparable with the charge gap. Meanwhile, in the ACP phase, the spin gap is generally much smaller than the charge gap. In principle, all of the four phases are insulating because of the finite charge gap.

In this chapter, we consider compounds with M = Pt, where competition between different interactions is manifest. Two classes of MMX compounds exist. (1) In $R_4[Pt_2(pop)_4X]nH_2O$ with monovalent cations R, four ligands of pop $= P_2O_5H_2^{2-}$ surround the binuclear MM unit. The ground states of $K_4[Pt_2(pop)_4X]$

K. Yonemitsu (✉)
Department of Physics, Chuo University, 1-13-27 Kasuga, Bunkyo-ku, Tokyo 112-8551, Japan

JST, CREST, Tokyo 102-0076, Japan
e-mail: kxy@phys.chuo-u.ac.jp

M. Yamashita and H. Okamoto (eds.), *Material Designs and New Physical Properties in MX- and MMX-Chain Compounds*, DOI 10.1007/978-3-7091-1317-2_12,

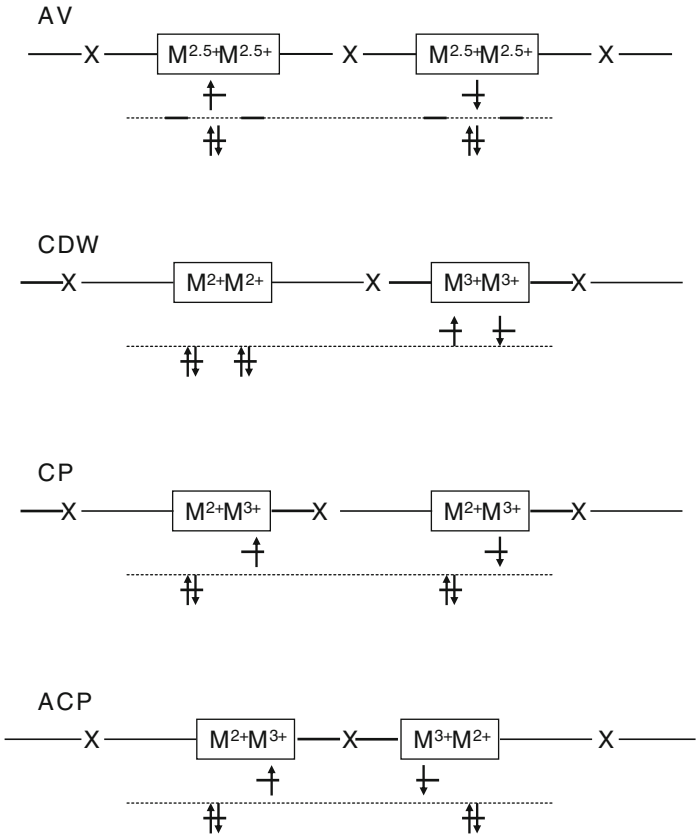

Fig. 12.1 Schematic electronic and lattice structures of MMX compounds

$n$$H_2O$ with X = Cl and Br are known to be in the CDW phase [1–4]. Meanwhile, the compounds with X = I have been studied extensively and show different electronic phases [5–7]. The mechanism of the variation of the electronic phases is clarified here. (2) In $Pt_2(RCS_2)_4I$, the ligands surrounding the binuclear MM unit are RCS_2 with R = CH_3, C_2H_5, n-C_4H_9, etc. Among them, the compound with R = CH_3 (the ligand is then dta = CH_3CS_2) has been studied for many years [8] and has been found to show the AV phase with "metallic" conductivity above room temperature [9, 10]. The compound with R = n-C_4H_9 clearly shows the ACP phase [11]. The difference between the pop and dta systems is discussed here from the theoretical viewpoint.

The more degrees of freedom, compared with those in the MX compounds, are responsible for the greater variety of electronic phases in the MMX compounds. Furthermore, the smaller charge gap enhances the controllability of relative stability among the four phases above. Indeed, electrons are more delocalized than in the MX compounds. Among the theoretical studies into the origins of the charge and

lattice orders in the MMX compounds, extended Hückel band structure calculations were first performed [12–14]. The Hartree–Fock approximation is applied to one-dimensional, three-band [15, 16] and two-band [17, 18] extended Peierls–Hubbard models. The Hartree–Fock calculations are extended to finite-temperature systems [19]. These calculations miss quantum fluctuations that are inherent in one-dimensional electron systems. Then, the quantum fluctuations originating from electron correlation in these models have been quantitatively taken into account by using the exact diagonalization method [20, 21] and the quantum Monte Carlo method [22]. In this chapter, we quantitatively treat the electron correlation in the ground and excited states by using the exact diagonalization method and analyze the numerical results with second- and fourth-order perturbation theories from the strong coupling limit [23]. We discuss in detail the relevance of our theoretical results to the experimentally observed variation of the ground and photoexcited states. Dynamical processes during photoinduced transitions between the CDW phase and the CP phase are also studied within the time-dependent Hartree–Fock approximation [24, 25].

12.2 Extended Peierls–Hubbard Model

To describe the ground- and excited-state properties, we adopt an extended Peierls–Hubbard model, which is schematically shown in Fig. 12.2. For simplicity, it takes only M d_{z^2} orbitals into account. Their energy levels and transfer integrals depend on the positions of the X ions,

$$\begin{aligned} H = & -\sum_{i,\sigma} t_{\mathrm{MM}}(c^{+}_{a,i,\sigma}c_{b,i,\sigma} + \mathrm{h.c.}) - \sum_{i,\sigma}[t_{\mathrm{MXM}} - \alpha(y_{b,i} + y_{a,i+1})](c^{+}_{b,i,\sigma}c_{a,i+1,\sigma} + \mathrm{h.c.}) \\ & - \beta\sum_{i}(y_{a,i}n_{a,i} + y_{b,i}n_{b,i}) + U_{\mathrm{M}}\sum_{i}(n_{a,i,\uparrow}n_{a,i,\downarrow} + n_{b,i,\uparrow}n_{b,i,\downarrow}) \\ & + \sum_{i}(V_{\mathrm{MM}}n_{a,i}n_{b,i} + V_{\mathrm{MXM}}n_{b,i}n_{a,i+1}) + V_2\sum_{i}(n_{a,i}n_{a,i+1} + n_{b,i}n_{b,i+1}) \\ & + (K_{\mathrm{MX}}/2)\sum_{i}(y^2_{a,i} + y^2_{b,i}) + (K_{\mathrm{MXM}}/2)\sum_{i}(y_{b,i} + y_{a,i+1})^2, \end{aligned} \tag{12.1}$$

where $c^{+}_{a,i,\sigma}(c^{+}_{b,i,\sigma})$ creates an electron with spin σ at site a (b) in the ith binuclear MM unit, h.c. denotes hermitian conjugate, $n_{a,i,\sigma} = c^{+}_{a,i,\sigma}c_{a,i,\sigma}(n_{b,i,\sigma} = c^{+}_{b,i,\sigma}c_{b,i,\sigma})$ is the number operator, and $n_{a,i} = \Sigma_\sigma n_{a,i,\sigma}(n_{b,i} = \Sigma_\sigma n_{b,i,\sigma})$. The unit cell contains two M sites a and b and an X site. The distance between the M site a (b) in the ith unit and its neighboring X site, relative to that in the undistorted structure, is denoted by $y_{a,i}$ ($y_{b,i}$). Thus, the change in the distance between the ith and (i + 1)th units is given by $y_{b,i} + y_{a,i+1}$. The nearest-neighbor transfer integral within the unit is fixed at t_{MM}. Meanwhile, the nearest-neighbor transfer integral through the X p_z orbital,

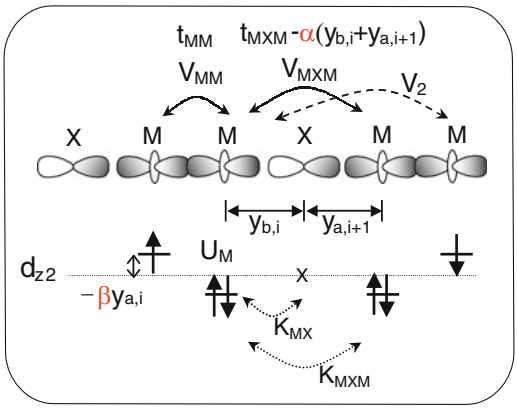

Fig. 12.2 Extended Peierls–Hubbard model for MMX compounds

t_{MXM}, is assumed to be linearly modified by the length change $y_{b,i} + y_{a,i+1}$ with coefficient α. The energy level of the M d_{z^2} orbital is assumed to depend linearly on the change in the MX bond length with coefficient β. The repulsion strengths are denoted by U_{M} for the on-site pair of electrons with opposite spins, V_{MM} for the nearest-neighbor pairs within the unit, V_{MXM} for the nearest-neighbor pairs accompanied with an X site in-between, and V_2 for the next-nearest-neighbor pairs. They are not assumed to depend on the positions of the X ions for simplicity. The elastic constants are denoted by K_{MX} for the MX bond length and K_{MXM} for the distance between the neighboring binuclear MM units. The latter constant is needed when counterions hinder the MM units from being displaced.

Here, the periodic boundary condition is imposed. The electronic ground state is determined by the exact diagonalization method except for the photoinduced dynamics in the last part. The lattice displacements y_a and y_b are treated as classical variables and determined in a self-consistent manner with the electronic ground state, unless otherwise stated, so that the system is in the lowest energy configuration, except for the photoinduced dynamics in the last part.

12.3 Kinetic Versus Interaction Terms

Electronic phases of $R_4[Pt_2(pop)_4I]nH_2O$ [R = Na, K, NH_4, $(CH_3(CH_2)_7)_2NH_2$, etc., pop = $P_2O_5H_2^{2-}$] are suggested to be classified according to the distance between the nearest-neighbor M ions accompanied with an X ion in-between, d_{MXM} [7]. In order to study the effects of changing d_{MXM}, we first obtain ground-state phase diagrams by varying t_{MXM}. Considering these pop systems containing charged MMX chains and counterions, we set K_{MXM} to be infinitely large, prohibiting displacements of M ions and allowing displacements of X ions only. The site-off-diagonal electron–lattice coupling α is then irrelevant. As a consequence, the ACP phase is not realized here. In addition, leaving detailed studies of

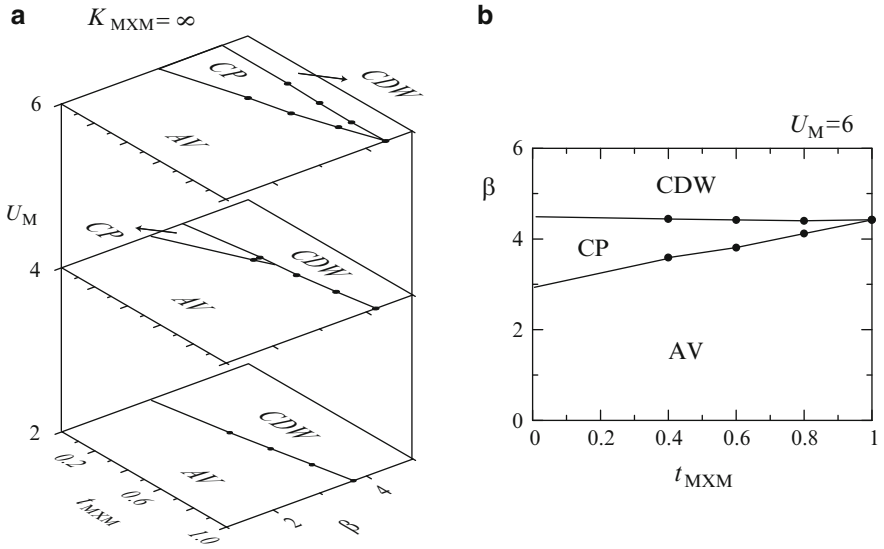

Fig. 12.3 Ground-state phase diagram of the 12-site model for infinitely large K_{MXM} (**a**) in the t_{MXM}–β–U_M space and (**b**) its cross section at $U_M = 6$. The parameters are $t_{MM} = 1$, $\alpha = 0$, $K_{MX} = 6$, $V_{MM} = 0$, $V_{MXM} = 0$, and $V_2 = 0$ [23]

competition among the charge-ordered phases until later, we simply ignore the long-range interactions. Exactly diagonalizing the present model, we show a phase diagram in the space spanned by t_{MXM}, β, and U_M in Fig. 12.3, where t_{MM} is set to be unity. Because the parameter sets (α, β, K_{MX}, K_{MXM}) and ($\lambda\alpha$, $\lambda\beta$, $\lambda^2 K_{MX}$, $\lambda^2 K_{MXM}$) are related by the scaling of y_a, and y_b and thus equivalent, the specific value of K_{MX} is insignificant. First of all, t_{MXM} is found to stabilize the AV phase. In $R_4[Pt_2(pop)_4I]nH_2O$, where electrons are the most delocalized among X = Cl, Br, and I, the AV phase may appear for small d_{MXM} because t_{MXM} is expected to become large. Meanwhile t_{MXM} does not much affect the boundary between the CDW and CP phases.

12.4 Electron–Lattice Versus Electron–Electron Interactions

In Fig. 12.3, the CDW phase is stabilized by the site-diagonal electron–lattice coupling β, while the CP phase is stabilized by the on-site repulsion U_M. Thus, the competition between the electron–lattice and electron–electron interactions determines the relative stability of these two charge-ordered phases. This fact is easily understood with the help of the second-order perturbation theory from the strong-coupling limit $t_{MM} = t_{MXM} = \alpha = 0$. The energies of the CDW and CP phases are degenerate in this limit as long as the long-range interactions are absent. Namely, their energies are both given by $-\beta|y| + U_M + K_{MX}y^2$ per binuclear unit.

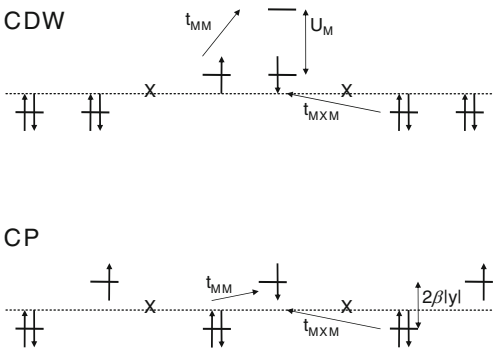

Fig. 12.4 Second-order processes with respect to t_{MM} and t_{MXM} in the CDW and CP phases

Though the effects of the long-range interactions are discussed later, it is here noted that V_{MM} increases the energy of the CDW phase and stabilizes the CP phase. The second-order processes with respect to t_{MM} shown in Fig. 12.4 lower the energy by $2{t_{MM}}^2/U_M$ in the CDW phase and by ${t_{MM}}^2/(2\beta|y|)$ in the CP phase. That is why the CDW phase is relatively stable for large β and the CP phase for large U_M. In a similar manner, the effect of t_{MXM} can be discussed from the second-order perturbation theory. It does not affect the relative stability between the CDW and CP phases. That is why the phase boundary is insensitive to t_{MXM}. It is noted that, if the long-range interactions are included, the second-order terms with respect to t_{MXM} for the CDW and CP phases become different. Even in such a case, the phase boundary is more sensitive to t_{MM}.

Experimentally, the ground states of $K_4[Pt_2(pop)_4X]nH_2O$ with X = Cl, Br and $n = 2, 3$ are shown to be in the CDW phase [1–4]. In general, when the halogen X ion is either Cl or Br, so far all the ground states are known to be in the CDW phase. For X = Cl and Br, the X p_z level is so deep that the effective nearest-neighbor transfer integral t_{MXM} mediated by charge transfers through the X p_z orbital is small. Meanwhile, the site-diagonal electron–lattice coupling β is large owing to the short distance between the neighboring M and X ions, d_{MX}. Thus, the CDW phase for X = Cl and Br is understood from the dominance of the electron–lattice coupling β over electron–electron interactions other than the on-site repulsion U_M, which is strong enough to suppress a phase with bipolarons discussed later.

In $R_4[Pt_2(pop)_4X]nH_2O$ with X = I, depending on the cation R and on the number of water molecules n, three electronic phases are suggested to appear: the AV phase, the CDW phase, and the CP phase in the order of increasing of d_{MXM} [7]. Though we have not obtained a phase diagram with the CDW phase between the other two, we believe that, for small d_{MXM}, the effect of t_{MXM} is larger than those of various interactions so that the larger t_{MXM} stabilizes the AV phase. Meanwhile, for intermediate to large d_{MXM}, the competition between the electron–lattice and electron–electron interactions discussed here and/or the competition between the short- and long-range electron–electron interactions discussed later determine the relative stability between the CDW and CP phases. As d_{MXM} increases, the site-diagonal electron–lattice coupling β becomes weak, while the on-site repulsion

U_M would not change so much. If the two phases compete with each other, then the effect of β dominates for intermediate d_{MXM} and that of U_M for large d_{MXM}. This partially explains why the CDW phase appears for intermediate d_{MXM} and the CP phase for large d_{MXM}. This variation of the charge-ordered phases can be explained also by the competition between the short- and long-range electron–electron interactions, as discussed below.

12.5 Short-Range Versus Long-Range Electron–Electron Interactions

Here, the long-range interactions V_{MM}, $V_{MXM,}$ and V_2 are included. The competition is easily understood in the strong-coupling limit, $t_{MM} = t_{MXM} = \alpha = 0$. The contribution from each interaction term to the total energy per binuclear unit is listed on the right-hand side of Fig. 12.5. The bond-charge-density-wave (BCDW) phase is introduced at the top here just to explain the competition, although it is never realized. Charge ordering is formally represented by $-M^{2+}M^{4+}-X-M^{2+}M^{2+}-X-$ there. Both the bond- and site-charge densities are modulated in this phase. If the site-diagonal electron–lattice coupling β were so strong that it dominated over the on-site repulsion U_M, the BCDW phase would be stable, forming a bipolaron lattice. The energy gain from the electron–lattice coupling β is the largest, approximately given by $3\beta|y|$ per unit, though the magnitudes of the lattice displacements are not uniform in the lowest-energy configuration. In any case, the BCDW phase is not experimentally observed because it is destabilized by the strong on-site repulsion U_M. The energy loss is also the largest, $(3/2)U_M$. For a fixed magnitude of the lattice displacements, all of the CDW, ACP, and CP phases gain energy by $\beta|y|$ and lose it by U_M. Then, the long-range interactions differentiate their energies. The CDW phase loses energy by $(5/2)V_{MM}$, the ACP phase by $(5/2)V_{MXM}$, and the CP phase by 5 V_2. Otherwise, the energy loss is given by $2V_{MM} + 2V_{MXM} + 4V_2$. When the nearest-neighbor repulsion within the unit V_{MM} is dominant, the CDW phase is unstable. Since we reasonably expect $U_M > V_{MM} > V_{MXM} > V_2$, the CP phase is the most stable in the strong-coupling limit if β is weak enough.

In $R_4[Pt_2(pop)_4I]nH_2O$, the CDW phase appears for intermediate d_{MXM}, and the CP phase appears for large d_{MXM} [7]. First of all, as long as K_{MXM} is infinitely large, the ACP phase was not realized in our calculations. As d_{MXM} increases, the next-nearest-neighbor repulsion V_2 would become weak. Meanwhile, the distance between the nearest-neighbor M ions within the unit is almost unchanged, so that the corresponding nearest-neighbor repulsion V_{MM} would not change so much in comparison with V_2. Then, as d_{MXM} increases, the CP phase becomes more stable relative to the CDW phase. This would be the other reason why the CDW phase is changed into the CP phase with increasing d_{MXM}. So far, we have limited the discussions to the case of infinitely large K_{MXM}, prohibiting displacements of M ions and keeping d_{MXM} constant.

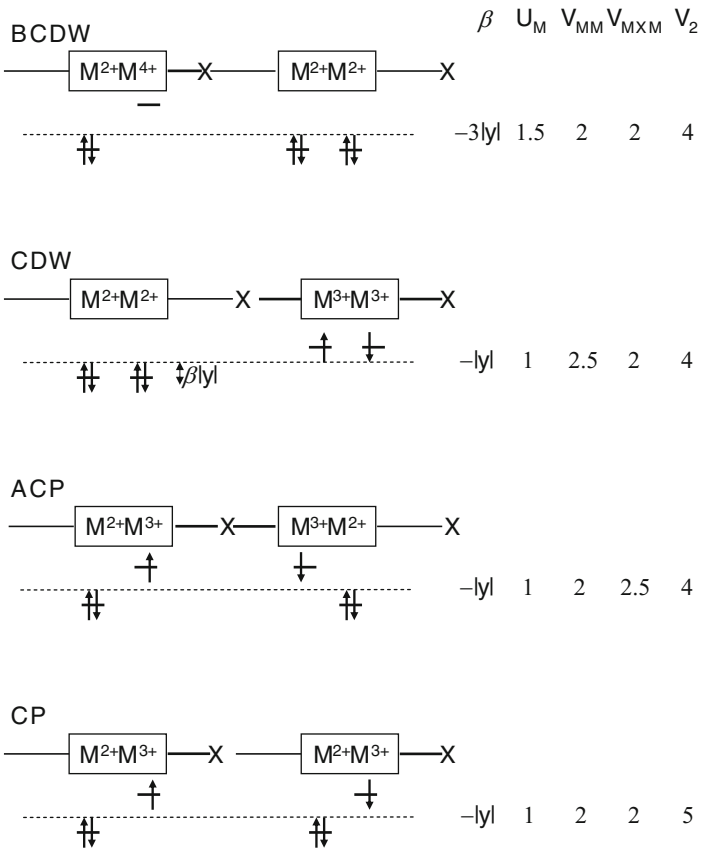

Fig. 12.5 Schematic structures of the electronic phases and the coefficients of their partial energies per binuclear unit with respect to site-diagonal electron–lattice coupling β, on-site repulsion U_M, nearest-neighbor repulsion V_{MM}, V_{MXM}, and next-nearest-neighbor repulsion V_2, in the strong-coupling limit

12.6 Site-Diagonal Versus Site-Off-Diagonal Electron–Lattice Interactions

The ACP phase is found at low temperatures in $Pt_2(RCS_2)_4I$ (R = CH_3, n-C_4H_9) [10, 11], where the MMX chains are neutral. There is no counterion that acts as an obstacle to displacements of M ions as in $R_4[Pt_2(pop)_4I]nH_2O$. Then, we set K_{MXM} to be zero. To start with, we simply ignore the long-range interactions and study the competition between the site-diagonal (β) and site-off-diagonal (α) electron–lattice couplings and the effect of the on-site repulsion U_M on it. The site-off-diagonal coupling α stabilizes the ACP phase, where the binuclear units are dimerized. It is regarded as a spin-Peierls state because a singlet is formed on the nearest-neighbor M sites accompanied with an X site in-between. Exactly diagonalizing the present

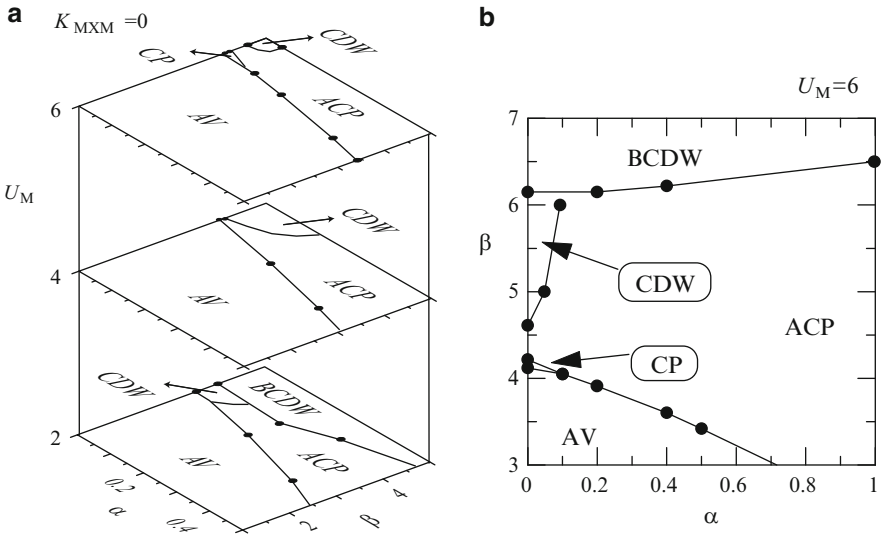

Fig. 12.6 Ground-state phase diagram of the 12-site model for $K_{MXM} = 0$ (**a**) in the α–β–U_M space and (**b**) its cross section at $U_M = 6$. The parameters are $t_{MM} = 1$, $t_{MXM} = 0.8$, $K_{MX} = 6$, $V_{MM} = 0$, $V_{MXM} = 0$, and $V_2 = 0$ [23]

model, we show how the on-site repulsion U_M modifies the competition between the α and β terms in Fig. 12.6. For small or moderate α and β, the AV phase appears. As U_M increases, all the phase boundaries are shifted to the large-β side, and consequently the region of the AV phase is widened. This is because the on-site repulsion U_M favors uniform charge densities, while the site-diagonal electron–lattice coupling β favors modulation of charge densities. Both terms compete with each other. Then, the BCDW phase is realized only when the β term is strong enough to dominate over the U_M term. This competition is easily understood in the unphysical limit of small ionic mass. In this limit, the lattice displacements instantaneously follow the motion of electrons so that the β term gives an attractive interaction to shift U_M to $U_{M\,eff} = U_M - \beta^2/K_{MX}$. This equation is derived from completing the squares with respect to variables $y_{a,i}$ and $y_{b,i}$. In the physical limit of large ionic mass, however, the lattice displacements are statically shifted to form a bipolaron lattice, i.e., the BCDW phase when β is large enough. The situation becomes different when the site-off-diagonal electron–lattice coupling α increases. It favors modulation of bond-charge densities. The U_M and α terms do not always compete with each other. In fact, they sometimes cooperate with each other when modulation of bond-charge densities is not accompanied with large modulation of site-charge densities [26–28]. That is why the phase boundaries are not shifted to the large-α side, but to the large-β side, when U_M increases. When α is large enough, the ACP phase is realized by modulating the distances between the neighboring binuclear units.

12.7 Combined Effects of the Competitions Above

Here, we further include the long-range interactions V_{MM}, V_{MXM}, and V_2: $V_{\mathrm{MM}} = 3$ and $V_2 = 2$ in addition to the parameters in Fig. 12.6b, $U_{\mathrm{M}} = 6$. We show phase diagrams in Fig. 12.7a for $V_{\mathrm{MXM}} = 2$ and in Fig. 12.7b for $V_{\mathrm{MXM}} = 3$. The AV phase is destabilized by the long-range interactions, which favor modulation of charge densities in the purely electronic origin and compete with the on-site repulsion U_{M}. The ACP phase is realized in a wide parameter space. The nature of the ACP phase changes continuously from small-α to large-α ranges. For small α, electrons are more localized so that the singlet pair of electrons is well described in the Heitler–London picture. For large α, the neighboring M d_{z^2} orbitals through the X p_z orbital are strongly overlapped to form a doubly occupied bonding orbital so that the electrons are as in a covalent molecule. Comparing Fig. 12.7a with Fig.12.7b, one sees that the nearest-neighbor repulsion through an X site, V_{MXM}, suppresses the ACP phase and stabilizes the other phases relative to the ACP phase, as already discussed through the aid of Fig. 12.5.

The ACP phase is clearly observed in $Pt_2(n\text{-}C_4H_9CS_2)_4I$ below 200 K [11]. It is, indeed, nonmagnetic as expected. The electronic structure of $Pt_2(CH_3CS_2)_4I$ is also suggested to be the ACP phase below 80 K, though the magnetic susceptibility does not drop at low temperatures [10]. Since the lattice displacements are very small in the latter case, this electronic state would be close to a paramagnetic phase such as the AV or CP phase. The CP phase is actually proposed above 80 K [10]. Because the spin excitation spectrum is gapless in the CP phase, it can generally gain more free energy than the ACP phase from the entropy term at high temperatures so that it is possible from the theoretical viewpoint. The X p_z orbitals ignored in this section are expected to be quantitatively important for the "metallic" (i.e., the resistivity increases with temperature) conductivity above 300 K (note that a small but finite gap is observed in the optical conductivity spectrum) and the small lattice displacements in the ACP phase.

We show phase diagrams containing all of the AV, ACP, CP, and CDW phases in Fig. 12.8. Note that K_{MXM} is not set to be zero or infinity here. These phase diagrams may become useful when experimental data are accumulated. The long-range interactions are weaker than those in Fig. 12.7. In Fig. 12.8a, we use $t_{\mathrm{MM}} = 1$, $t_{\mathrm{MXM}} = 0.8$, $K_{\mathrm{MX}} = 6$, and $U_{\mathrm{M}} = 6$ as before. For small α, as β increases, the ground state changes from the AV phase, the CP phase, to the CDW phase, as in the case of infinitely large K_{MXM}. It finally becomes the BCDW phase for very large β (not shown). For large enough α, the ACP phase appears as usual. The critical strength of α for the ACP phase is the smallest at the boundary between the AV and CP phases. In Fig. 12.8b, we change only K_{MX} from the parameters of Fig. 12.8a: $K_{\mathrm{MX}} = 4$. The MX bonds are more easily distorted by the smaller K_{MX}, while the distances between the neighboring binuclear units are almost unaffected because K_{MXM} is not changed. Consequently, the CP and CDW phases are stabilized to shift the phase boundaries to the small-β side, while the ACP phase is destabilized relative to these phases and invaded by them. In other words, some of the ACP

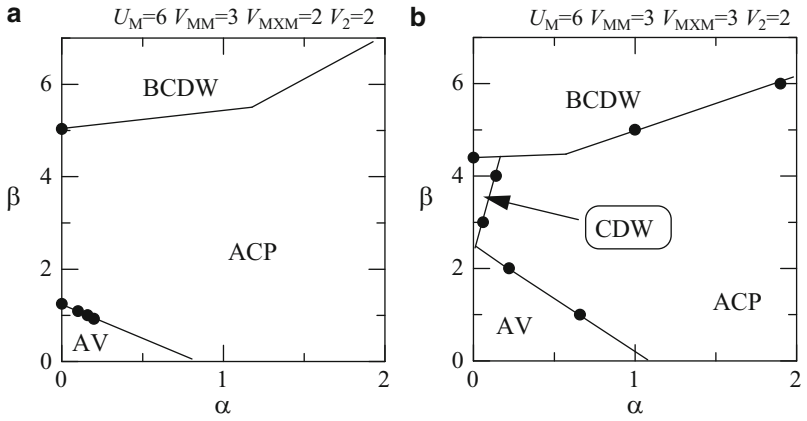

Fig. 12.7 Ground-state phase diagrams of the 12-site model for $K_{MXM} = 0$, on the α–β plane for (**a**) $V_{MXM} = 2$ and (**b**) $V_{MXM} = 3$. The parameters are $t_{MM} = 1$, $t_{MXM} = 0.8$, $K_{MX} = 6$, $U_M = 6$, $V_{MM} = 3$, and $V_2 = 2$ [23]

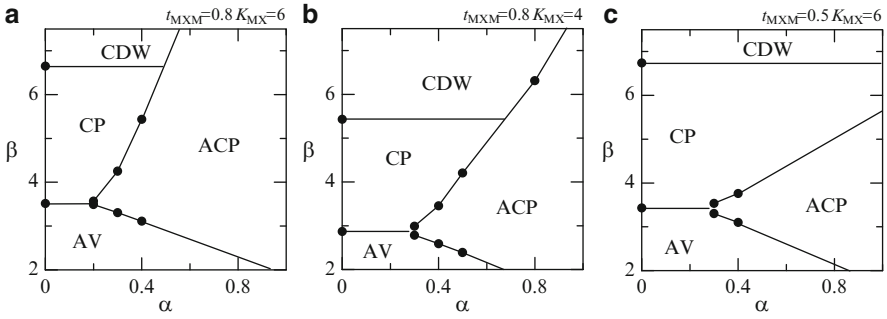

Fig. 12.8 Ground-state phase diagrams of the 8-site model for $K_{MXM} = 1$, on the α–β plane, for (**a**) $t_{MXM} = 0.8$, $K_{MX} = 6$, (**b**) $t_{MXM} = 0.8$, $K_{MX} = 4$, and (**c**) $t_{MXM} = 0.5$, $K_{MX} = 6$. The parameters are $t_{MM} = 1$, $U_M = 6$, $V_{MM} = 1.5$, $V_{MXM} = 1$, and $V_2 = 0.5$ [23]

states are replaced by the CDW states for the smaller K_{MX}. If we want to explain the difference between the pop and dta systems simply by the difference in K_{MX} (not in K_{MXM} as we do in this paper), we need larger K_{MX} for the dta systems, contrary to the intuition. In Fig. 12.8c, we change only t_{MXM} from the parameters of Fig. 12.8a: $t_{MXM} = 0.5$. The ACP phase is the most affected by this change and destabilized by the reduction of t_{MXM}. This is because the energy gain from forming a singlet pair of electrons (on the nearest-neighbor M sites accompanied with an X site in-between) is proportional to ${t_{MXM}}^2$. Meanwhile, the boundaries between the AV and CP phases and those between the CP and CDW phases are not much affected by the change of t_{MXM}. It is not regarded as a main mechanism for the variation of the electronic phases in $R_4[Pt_2(pop)_4I]nH_2O$.

12.8 Optical Conductivities in Different Electronic Phases

Here, we calculate the optical conductivity spectra, having $R_4[Pt_2(pop)_4I]nH_2O$ in mind. We focus on the differences among the spectra in the AV, CDW, and CP phases. We do not calculate the lattice displacements self-consistently but fix them to be a constant, $|y| = y_0$, although we change the distortion pattern according to the electronic phase. The elastic constants are then meaningless. The lattice displacements are $y_{a,i} = y_{b,i} = 0$ in the AV phase, $y_{a,i} = y_{b,i} = (-1)^i y_0$ in the CDW phase, and $y_{a,i} = -y_{b,i} = y_0$ in the CP phase. The optical excitation processes are schematically represented in Fig. 12.9 for the CDW and CP phases. The illustration becomes realistic only near the strong-coupling limit. In this limit, the excitation energies in the CDW phase are given by

$$E_{\mathrm{MM}}^{\mathrm{CDW}} = U_{\mathrm{M}} - V_{\mathrm{MM}}, \quad E_{\mathrm{MXM}}^{\mathrm{CDW}} = 2\beta|y| - V_{\mathrm{MM}} + 2V_2,$$

while those in the CP phase are given by

$$E_{\mathrm{MM}}^{\mathrm{CP}} = 2\beta|y| + V_{\mathrm{MXM}} - 2V_2, \quad E_{\mathrm{MXM}}^{\mathrm{CP}} = 2\beta|y| + V_{\mathrm{MM}} - 2V_2.$$

Among the four energies, $E_{\mathrm{MM}}{}^{\mathrm{CDW}}$ is much larger than the others because of the strong on-site repulsion U_{M}.

From the exact diagonalization of the present model, we show optical conductivity spectra in the three phases for $U_{\mathrm{M}} = 2$ in Fig. 12.10a, for $U_{\mathrm{M}} = 4$ in Fig. 12.10b, and for $U_{\mathrm{M}} = 6$ in Fig. 12.10c, with varying V_{MM} and V_{MXM} according to the relations, $V_{\mathrm{MM}} = U_{\mathrm{M}}/2$ and $V_{\mathrm{MXM}} = U_{\mathrm{M}}/4$. As the electron–electron interactions are not so weak, a single peak appears at a similar position in both of the AV and CDW phases, while two peaks generally appear in the CP phase in the energy range of the figures. The difference in the number of peaks between the CDW and CP phases is due to the strong on-site repulsion U_{M}, as discussed above. We then focus on the CP phase and show the dependence of the energies and intensities of the two excitations on the long-range interactions V_{MM} and V_{MXM} in Fig. 12.11. The lower energy $E_{\mathrm{MM}}{}^{\mathrm{CP}}$ increases with V_{MXM}, while the higher energy $E_{\mathrm{MXM}}{}^{\mathrm{CP}}$ increases with V_{MM}, as expected from the strong-coupling analysis. The excitation intensities are comparable when the energy difference is small. Meanwhile, the low-energy excitation is much stronger when the energy difference is large.

In the optical experiments, so far all $R_4[Pt_2(pop)_4I]nH_2O$ compounds have a single peak below 3 eV [7]. Observation of a single peak is reasonable in the AV and CDW phases because of the strong on-site repulsion U_{M}. Meanwhile, observation of a single peak in the CP phase indicates that the nearest-neighbor repulsion through an X site V_{MXM} is substantially weaker than the nearest-neighbor repulsion within the unit V_{MM}. At least, the repulsion V_{MM} is so strong as to stabilize the CP phase.

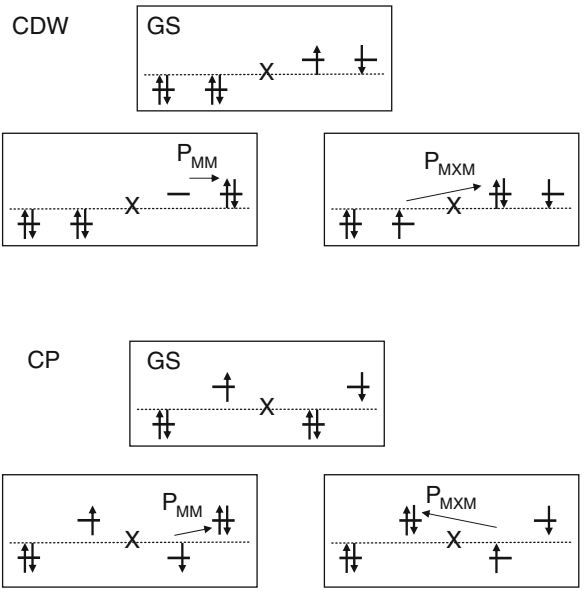

Fig. 12.9 Schematic electronic structures and charge-transfer excitations in the CDW and CP phases

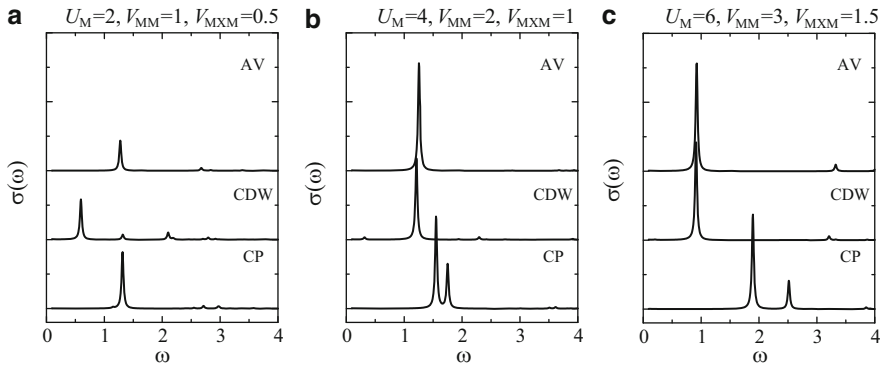

Fig. 12.10 Optical conductivity in the AV, CDW, and CP phases of the 12-site model for (**a**) $U_M = 2$, $V_{MM} = 1$, and $V_{MXM} = 0.5$, (**b**) $U_M = 4$, $V_{MM} = 2$, and $V_{MXM} = 1$, and (**c**) $U_M = 6$, $V_{MM} = 3$, and $V_{MXM} = 1.5$. The other parameters are $t_{MM} = 1$, $t_{MXM} = 0.8$, $\alpha = 0.2$, $\beta = 4$, $y_0 = 0.1$, and $V_2 = 0$ [23]

Among the energies of the experimentally observed peaks, that in the CDW phase is lower than those in the CP phase. The energy difference between the CDW and CP phases is reproduced in Fig. 12.10 for each parameter set. This is easily understood in the strong-coupling limit. The low-energy charge-transfer excitation takes place at $E_{MXM}^{CDW} = 2\beta|y| - V_{MM} + 2V_2$ in the CDW phase and at $E_{MM}^{CP} = 2\beta|y| + V_{MXM} - 2V_2$ in the CP phase. We concluded above that the nearest-neighbor repulsion through an X site V_{MXM} is substantially weaker, at least for the

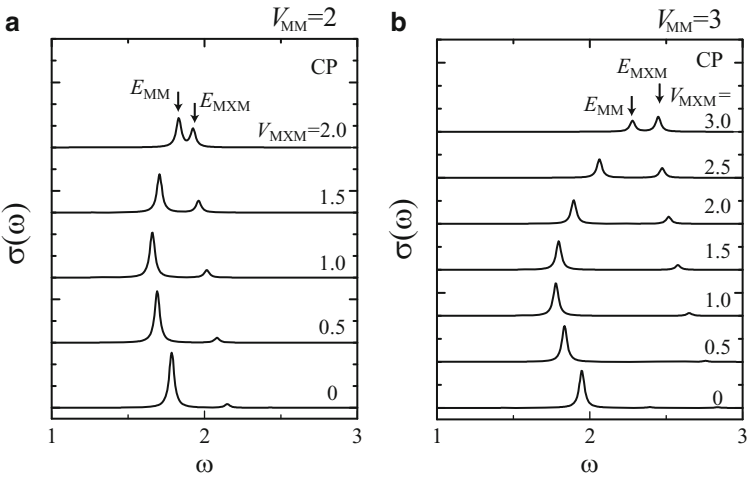

Fig. 12.11 Optical conductivity in the CP phase of the 12-site model, as a function of V_{MXM} for (**a**) $V_{MM} = 2$ and (**b**) $V_{MM} = 3$. The parameters are $t_{MM} = 1$, $t_{MXM} = 0.8$, $\alpha = 0.2$, $\beta = 4$, $y_0 = 0.1$, $U_M = 6$, and $V_2 = 0$ [23]

CDW and CP phases, than the nearest-neighbor repulsion within the unit V_{MM}. Furthermore, we reasonably expect that the next-nearest-neighbor repulsion V_2 is smaller than V_{MXM}. Therefore, we can derive the relation $E^{CDW}_{MXM} < E^{CP}_{MM}$, which is consistent with the observed energy difference between the CDW and CP phases. This relation is intuitively understood in the following way. In the CDW phase, holes reside at M^{3+} M^{3+} units. By any charge-transfer process, the hole pair in a unit is so separated that an electron and a hole attract each other by the amount of V_{MM}. In the CP phase, however, holes are so located that the distance between the neighboring holes is the largest among the possible electronic configurations. By any charge-transfer process, some holes approach each other, so that it costs repulsive energy.

12.9 Summary of Ground-State Properties

Different electronic phases appear in $R_4[Pt_2(pop)_4I]nH_2O$, depending on the counterion and on the number of water molecules. It is suggested from experiments that the electronic phases are classified according to the distance between the neighboring binuclear units d_{MXM} [7]. The CP phase is suggested to appear for large d_{MXM}, while the CDW phase is realized for small d_{MXM}. The relative stability between the two phases is determined by a combined effect of competition between electron–lattice and electron–electron interactions and competition between short- and long-range electron–electron interactions. As d_{MXM} decreases, the site-diagonal electron–lattice interaction and long-range electron–electron interactions become larger, and their effects become dominant over the effect of the short-range

electron–electron interaction. Thus the CP phase is reasonably converted to the CDW phase. The optical conductivity spectrum changes accordingly.

In $Pt_2(RCS_2)_4I$, the electric conductivity is rather high [10]. The itinerant character of electrons is much stronger than the pop systems. The main difference between the two systems is that MMX chains in $R_4[Pt_2(pop)_4I]nH_2O$ are charged while those in $Pt_2(RCS_2)_4I$ are neutral. The former systems need to have counterions, which prohibit free modulation of the distances between the neighboring binuclear units. This strongly suppresses the appearance of the ACP phase. On the other hand, the latter systems do not have counterions so that the distances between the neighboring binuclear units are easily modulated by sufficiently strong site-off-diagonal electron–lattice coupling. As a consequence, the ACP phase appears. From the optical conductivity spectrum, it is evident that the transfer integrals are large and electrons are more delocalized than in the pop systems. A quantitative comparison between theoretical and experimental results is possible by using a three-band model [23], which explicitly takes X p_z orbitals into account, instead of the present two-band model. Though the electric conductivity shows "metallic" behavior in $Pt_2(CH_3CS_2)_4I$ above room temperature, where the lattice is not distorted, the optical conductivity spectrum shows a small but finite charge gap [10]. This AV phase is thus regarded as a Mott–Hubbard insulator phase.

12.10 Photoinduced Dynamics in a Pop System

Generally, photoinduced phase transitions have attracted much attention [25]. They are observed in a broad range of materials. Photoinduced phase transitions that are realized experimentally and simulated theoretically include transitions from Mott insulator to metal phases [29, 30], charge-ordered insulator to metal phases in quasi-one- [31, 32] and two-dimensional [33–35] systems, ferroelectric ionic to paraelectric neutral phases [36, 37], and nonmagnetic to paramagnetic phases [38–41]. Among MMX-chain compounds, a photoinduced transition from the CDW phase to the CP phase has been found in a pop system, $R_4[Pt_2(pop)_4I]nH_2O$ [pop = $P_2O_5H_2^{2-}$, R = $(C_2H_5)_2NH_2$] [7]. Its mechanism is studied by solving the time-dependent Hartree–Fock equation in this and remaining sections of this chapter. Above a threshold in the photoexcitation intensity, a transition indeed takes place from the CDW to CP phases. The threshold intensity depends on the relative stability of these phases, which can be explained qualitatively by their diabatic potentials. However, the transition from the CP to CDW phases is hardly realized for two reasons [24, 25]: (1) low-energy charge-transfer processes occur only within a binuclear unit in the CP phase; (2) it is difficult for the CDW order to become long-ranged owing to its weak coherence.

We employ the extended Peierls–Hubbard model (12.1) again. Here, we set $1/K_{\mathrm{MXM}} = 0$, which is appropriate for the pop system and makes α irrelevant as explained in the previous sections and ignore the long-range electron–electron interactions, $V_{\mathrm{MM}} = V_{\mathrm{MXM}} = V_2 = 0$, for simplicity. Relabeling the site indices

using $y_{b,i} = -y_{a,i+1} = u_i$ and adding the kinetic energy of X ions, we rewrite the model (12.1) as

$$H = -t_{\mathrm{MM}} \sum_{i,\sigma} (c^{+}_{2i-1,\sigma} c_{2i,\sigma} + \mathrm{h.c.}) - t_{\mathrm{MXM}} \sum_{i,\sigma} (c^{+}_{2i,\sigma} c_{2i+1,\sigma} + \mathrm{h.c.}) + \beta \sum_i u_i (n_{2i+1} - n_{2i}) + U_{\mathrm{M}} \sum_i n_{i,\uparrow} n_{i,\downarrow} + K_{\mathrm{MX}} \sum_i u_i^2 + (M/2) \sum_i \dot{u}_i^2, \tag{12.2}$$

where the ith binuclear unit contains two M (M = Pt) sites, $2i - 1$ and $2i$ and the mass of the X ion is denoted by M. We have obtained the stable and metastable, static states using $t_{\mathrm{MM}} = 1.0$, $t_{\mathrm{MXM}} = 0.8$, and $K_{\mathrm{MX}} = 6.0$ as a typical parameter set. The main results shown below are, however, not affected by the details of the chosen parameters. Indeed, they are supported by the perturbation theory from the strong-coupling limit as explained below. For $U_{\mathrm{M}} = 6.0$, the boundary between the two phases is located at $\beta_{\mathrm{c}} = 4.4$ when the 12-site lattice is exactly diagonalized [23] and at $\beta_{\mathrm{c}} = 6.0$ in the time-*independent* Hartree–Fock (HF) approximation. The stable (metastable) state is CP (CDW) for $\beta < \beta_{\mathrm{c}}$ and CDW (CP) for $\beta > \beta_{\mathrm{c}}$. Because the time-*independent* approximation does not include quantum fluctuations, the effect of the on-site repulsion U_{M} is overestimated. Here we use $U_{\mathrm{M}} = 4.0$ instead hereafter. The boundary is then located at $\beta_{\mathrm{c}} = 4.9$.

For the photoinduced dynamics, we initially add small random numbers to the lattice variables u and $\dot{u}$. They help nucleation of a local domain in the stable phase. The Boltzmann distribution is employed at a fictitious temperature, $T = 0.01$ so that they are weakly random. During the calculations, the system is isolated and its total energy is conserved. Unless otherwise stated, lowest energy photoexcitations are introduced by changing the occupation [42] of the highest occupied and the lowest unoccupied HF orbitals. When higher energy excitations are considered, we change the occupation of different sets of HF orbitals.

The evolution of the HF wave functions is obtained by solving the time-dependent Schrödinger equation. The checkerboard decomposition is used for the exponential operator so that it is accurate to the second order with respect to the time slice. The evolution of the lattice variables is obtained by solving the classical equation of motion. The leapfrog method is used and accurate to the second order with respect to the time slice. Self-consistency is imposed at each time on the spin density by iteration and on the lattice variables through the Hellmann–Feynman theorem. The bare optical phonon energy used here is $\omega = (2K_{\mathrm{MX}}/M)^{1/2} = 0.0354$, as a typical parameter. The results below are not modified by the details of the model parameters. In the strong-coupling limit, the CDW phase is characterized by the electron density, $(n_1, n_2, n_3, n_4) = (1, 1, 2, 2)$ or $(2, 2, 1, 1)$. The CDW order parameters is defined as $\rho_{\mathrm{CDW}}(2i - 1) = (-1)^i(-n_{2i-2} + 2n_{2i-1} + n_{2i} - 3)/4$ and $\rho_{\mathrm{CDW}}(2i) = (-1)^i(+n_{2i-1} + 2n_{2i} - n_{2i+1} - 3)/4$. In the same limit, the CP phase is characterized by $(n_1, n_2, n_3, n_4) = (1, 2, 1, 2)$ or $(2, 1, 2, 1)$. The CP order parameter is defined as $\rho_{\mathrm{CP}}(i) = (-1)^i(-n_{i-1} + 2n_i - n_{i+1})/4$. The order parameter $\rho_{\mathrm{A}}(i)$ is so defined that, in the strong-coupling limit of the A phase, it takes uniformly a positive value or uniformly a negative value.

12.11 CDW-to-CP Transition

Starting from the metastable CDW phase inside the hysteresis loop, we find a transition to the stable CP phase for $\beta = 4.5 < \beta_c$. Because the delocalization tendency is weak, the 48-site chain is enough to derive the present conclusions. When three electrons are excited, the CDW order is partially destroyed and the CP order appears instead, but most of the regions remain in the CDW phase. When four electrons are excited, microscopic CDW domains survive only for a while, and the CDW domain is almost completely destroyed. After they disappear, CP domains appear. On average, they grow and mostly cover the system at last. A threshold exists in the photoexcitation intensity roughly between three- and four-electron excitations for the 48-site chain. When more electrons are excited, the CDW domain quickly disappears, and CP domains appear and grow to be merged into a single CP domain covering the system. Whether the transition is completed or not actually depends on the choice of random numbers initially added to the lattice variables. The threshold should be understood in a statistical manner for finite-size systems.

The threshold intensity sensitively depends on the relative stability of the two phases. For $\beta = 4.0$, which is much below β_c, we find the CDW phase still metastable, and the energy difference from the stable CP phase is enlarged. The threshold intensity is greatly reduced: one-electron excitation in the 48-site chain is sufficient for the transition to the CP phase. For $\beta = 5.0$, where the CDW phase is almost degenerate with the CP phase, the transition is not easily realized. Intensive excitations only destroy the CDW order, and they do not produce any charge–lattice order.

This dependence of the threshold intensity can be understood by drawing diabatic potentials in the CDW and CP phases. After the photoexcitation, the excess energy is quickly distributed to the surroundings, and the coherence is lost under thermal fluctuations. For the proliferation of new domains, the processes after the coherence is lost are more important than the process just after the photoexcitation. Since the electronic states in the MMX compounds with ligand pop are well described from the strong-coupling viewpoint [23], spatially local pictures are helpful. Then, we consider the diabatic potentials in the CDW and CP phases for the 4-site system, in which the binuclear unit on sites 1 and 2 are coupled with the other on sites 3 and 4 (Fig. 12.12):

$$H_{4-\mathrm{site}} = -t_{\mathrm{MM}} \sum_{\sigma} (c^{+}_{1,\sigma} c_{2,\sigma} + \mathrm{h.c.} + c^{+}_{3,\sigma} c_{4,\sigma} + \mathrm{h.c.}) - t_{\mathrm{MXM}} \sum_{\sigma} (c^{+}_{2,\sigma} c_{3,\sigma} + \mathrm{h.c.})$$
$$+\beta u_1 (n_3 - n_2) + U_{\mathrm{M}} \sum_{i=1}^{4} n_{i,\uparrow} n_{i,\downarrow} + K_{\mathrm{MX}} u_1^2 + (M/2)\dot{u}_1^2. \tag{12.3}$$

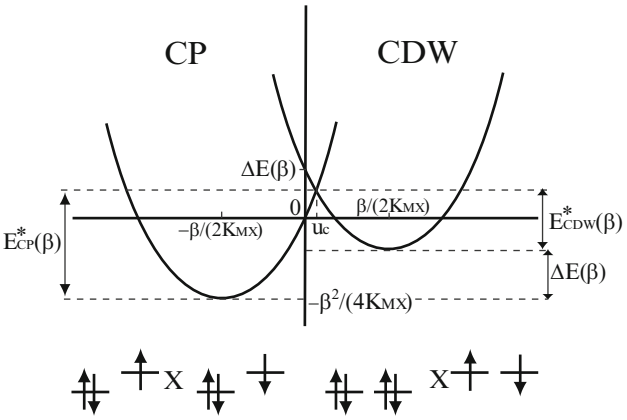

Fig. 12.12 Diabatic potentials and schematic electronic structures in the CP (*left*) and CDW (*right*) phases [24]

We consider the two electronic configurations shown at the bottom of Fig. 12.12, where $n_1 \approx 2$ and $n_4 \approx 1$. The total energies are given in the second-order perturbation theory with respect to t_{MM} and t_{MXM} [24]:

$$E_{\mathrm{CDW}}(u_1, \dot{u}_1) = K_{\mathrm{MX}}\left(u_1 - \frac{\beta}{2K_{\mathrm{MX}}}\right)^2 - \frac{\beta^2}{4K_{\mathrm{MX}}} + \Delta E(\beta) + \frac{M}{2}\dot{u}_1^2, \tag{12.4}$$

$$E_{\mathrm{CP}}(u_1, \dot{u}_1) = K_{\mathrm{MX}}\left(u_1 + \frac{\beta}{2K_{\mathrm{MX}}}\right)^2 - \frac{\beta^2}{4K_{\mathrm{MX}}} + \frac{M}{2}\dot{u}_1^2, \tag{12.5}$$

where the energies are equally shifted to have $E_{\mathrm{CP}}(0,0) = 0$ and the energy difference between the CDW and CP states $\Delta E(\beta)$ is given by

$$\Delta E(\beta) = \frac{2t_{\mathrm{MM}}^2 K_{\mathrm{MX}}}{\beta^2} - \frac{4t_{\mathrm{MM}}^2}{U_{\mathrm{M}}} \approx \frac{8\sqrt{2}t_{\mathrm{MM}}^2}{\sqrt{K_{\mathrm{MX}}U_{\mathrm{M}}^3}}(\beta_{\mathrm{c}} - \beta), \tag{12.6}$$

with $\beta_{\mathrm{c}} = (K_{\mathrm{MX}}U_{\mathrm{M}}/2)^{1/2}$, as a function of β. The diabatic potentials, $E_{\mathrm{CDW}}(u_1,0)$ and $E_{\mathrm{CP}}(u_1,0)$, are plotted in Fig. 12.12. The CDW and CP states become degenerate at $\beta = \beta_{\mathrm{c}}$ and $\Delta E(\beta_{\mathrm{c}}) = 0$. The crossing point u_{c} is defined by the relation $E_{\mathrm{CDW}}(u_{\mathrm{c}}, 0) = E_{\mathrm{CP}}(u_{\mathrm{c}}, 0)$ and given by $u_c = \Delta E(\beta)/(2\beta)$. The barrier heights are given by

$$E_{\mathrm{CDW}}^*(\beta) = E_{\mathrm{CDW}}(u_{\mathrm{c}}, 0) - E_{\mathrm{CDW}}\left(\frac{\beta}{2K_{\mathrm{MX}}}, 0\right) = \frac{K_{\mathrm{MX}}}{4\beta^2}\left(\Delta E(\beta) - \frac{\beta^2}{K_{\mathrm{MX}}}\right)^2, \tag{12.7}$$

$$E_{\mathrm{CP}}^*(\beta) = E_{\mathrm{CP}}(u_{\mathrm{c}}, 0) - E_{\mathrm{CP}}\left(-\frac{\beta}{2K_{\mathrm{MX}}}, 0\right) = \frac{K_{\mathrm{MX}}}{4\beta^2}\left(\Delta E(\beta) + \frac{\beta^2}{K_{\mathrm{MX}}}\right)^2. \tag{12.8}$$

Equations (12.6) and (12.7) show that, as the electron–lattice coupling β decreases, the energy difference $\Delta E(\beta)$ increases, and the barrier height $E^*_{\mathrm{CDW}}(\beta)$ decreases in the CDW phase. Finally, when the crossing point u_c reaches $\beta/(2K_{\mathrm{MX}})$, the CDW phase becomes unstable and the transition to the CP phase is realized by infinitesimal perturbations.

12.12 CP-to-CDW Transition

Starting from the metastable CP phase inside the hysteresis loop, we calculate the time evolution for $\beta = 5.5 > \beta_c$. Here, the CDW phase is thermodynamically stable. Nonetheless, the CDW phase is hardly photoinduced. When four electrons are excited, the initial CP domain acquires a few local defects. But the defects do not proliferate. In them, one of the four orders (i.e., positive ρ_{CDW}, negative ρ_{CDW}, positive ρ_{CP}, and negative ρ_{CP}) is locally developed, but they just stay there. In the defect-free CP regions, the CP order is slightly weakened initially, but it is almost completely recovered. The CP phase is dynamically stable. Even when more electrons are excited, this situation is not altered.

The difference between the dynamics from the CDW phase and that from the CP phase is at first understood on the basis of how charge is transferred by photoirradiation. In the CDW phase, charge transfer shown in Fig. 12.9 among the binuclear units needs a lower energy than that within the unit because the latter costs on-site repulsion U_{M}. In the CP phase, the situation is opposite, as long as t_{MM} is larger than t_{MXM}. This fact holds even if long-range electron–electron interactions are present. Recall that $E^{\mathrm{CDW}}_{\mathrm{MXM}} < E^{\mathrm{CDW}}_{\mathrm{MM}}$ and $E^{\mathrm{CP}}_{\mathrm{MXM}} > E^{\mathrm{CP}}_{\mathrm{MM}}$ in the strong-coupling limit. Therefore, by lower energy photoirradiation of the CP phase, charge is transferred only within each binuclear unit, so that the charge density does not become disproportioned among the binuclear units. Thus the path to the CDW phase is closed in the low-energy excitation channel.

Thus, we become interested in what happens if the CP phase is irradiated by higher energy photons? Again starting from the CP phase at $\beta = 5.5 > \beta_c$, we excite four electrons now from the lowest occupied orbitals to find that the initial CP domain is quickly destroyed. There appear CDW domains with positive and negative ρ_{CDW}. They occupy most of the areas, but none of the CDW domains dominates over the others. The boundaries between different CDW domains survive. Charge transfer among the binuclear units takes place incoherently. Since the interunit charge transfer is energetically unfavorable, the CDW domains do not proliferate.

Next, we artificially added interunit repulsion V_{MXM} between the nearest-neighbor sites bridged by a halogen site, without introducing intraunit nearest-neighbor repulsion V_{MM}. In real materials V_{MM} is larger than V_{MXM}. Since V_{MXM} increases the energy of the intraunit charge-transfer excitation only, the energy of the interunit charge-transfer excitation becomes relatively lower in the CP phase also. Now the path to the CDW phase appears open in the low-energy excitation

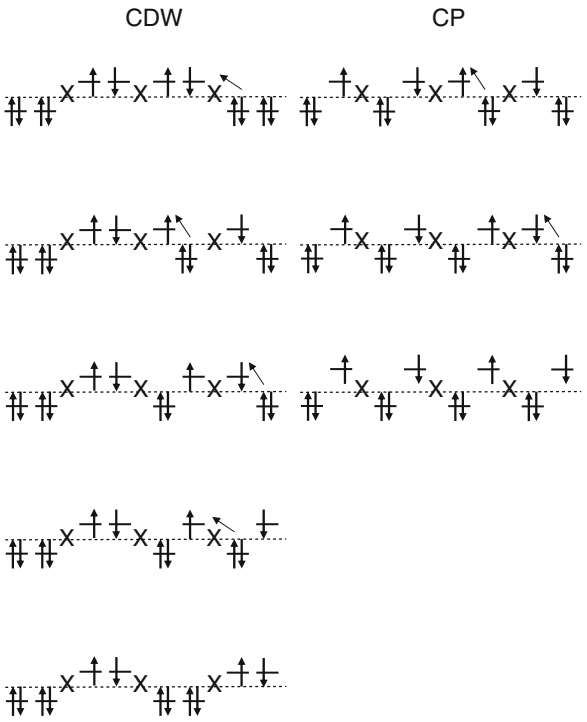

Fig. 12.13 Schematic processes that recover the coherence of the respective orders. To convert $\rho_{\mathrm{CDW}} < 0$ into $\rho_{\mathrm{CDW}} > 0$, two electrons need to be transferred to the next-nearest-neighbor site, which is beyond the halogen site. To convert $\rho_{\mathrm{CP}} < 0$ into $\rho_{\mathrm{CP}} > 0$, only one electron needs to be transferred to the nearest-neighbor site within the binuclear unit [24]

channel because proliferation of CDW domains is no longer energetically hindered. In spite of this favorable fact, the transition to the CDW phase is still hardly realized.

Suppose CP (CDW) domains with positive and negative ρ_{CP} (ρ_{CDW}) neighbor with each other. A unit of the CP domain consists of one binuclear unit. To convert $\rho_{\mathrm{CP}} < 0$ into $\rho_{\mathrm{CP}} > 0$, only one electron needs to be transferred to the nearest-neighbor site within the binuclear unit, as shown in Fig. 12.13. Meanwhile, a unit of the CDW domain consists of two binuclear units. To convert $\rho_{\mathrm{CDW}} < 0$ into $\rho_{\mathrm{CDW}} > 0$, two electrons need to be transferred to the next-nearest neighbor site beyond the halogen site. Therefore, a wrong phase is easily corrected in the CP phase, helping the growth of a single-phase CP domain. The coherence of the charge–lattice order is easily recovered in the CP phase. In other words, it is much easier for the CP order to become long ranged than for the CDW order. Here, the tunneling amplitude connecting the anti-phase domains is important. The barrier between the CP domains is much lower than that between the CDW domains. The tunneling process is assisted by large transfer integrals. In fact, when we reduce the interunit transfer integral t_{MXM}, we can easily suppress the transition from the CDW to CP phases also.

12.13 Comparison with Experimental Results

In summary, the transition from the metastable CDW phase to the stable CP phase, which is experimentally realized by photoirradiation under pressure, is reproduced by exciting a sufficient density of electrons. The threshold increases as the energy difference between the two phases becomes small. This is explained by drawing their diabatic potentials. On the other hand, a reverse transition from the CP phase to the CDW phase is hardly realized. Here are two key factors (1) the characters of the low-energy charge-transfer excitations in the respective phases and (2) how easily the respective order becomes long ranged. The difficulty of the CP-to-CDW transition is due to the fact that the low-energy charge transfer occurs within the binuclear unit in the CP phase and the fact that the coherence length of the CDW order is very short.

In iodine-bridged binuclear platinum complexes, $R_4[Pt_2(pop)_4I]nH_2O$ with cation R, phase transitions are indeed observed after the photoirradiation for a long time, 8 ms (for CDW-to-CP) and 30 s (for CP-to-CDW) [7]. To clarify whether the transitions are induced by an optical process or a laser heating, the dependence of the converted fraction on the excitation photon density is investigated for two excitation energies E_{ex} of 1.96 eV and 2.41 eV [43].

At 0.25 GPa where the CDW phase is metastable, the CDW-to-CP transition efficiency exhibits a clear threshold in the photon density per pulse N_{th}, which strongly depends on E_{ex}: $N_{th} \sim 1.4 \times 10^{25}$ cm^{-3} at $E_{ex} = 1.96$ eV and $\sim 3 \times 10^{24}$ cm^{-3} at 2.41 eV. The magnitude of N_{th} is large, but the irradiated power of the lights is very small and the pulse duration is very long. The threshold behavior demonstrates that the observed transitions are driven not by a laser heating but by an optical process. At 0.45 GPa where the CP phase is metastable, the CP-to-CDW transition could not be driven by the irradiation of 1.96-eV or 2.41-eV (nearly equal to the optical gap energy) light, even if the intensity and duration of the light were changed. However, irradiation with 2.71-eV light for 30 s did result in a CP-to-CDW transition. Therefore, the efficiency of the photoinduced CP-to-CDW transition is much lower than that of the CDW-to-CP transition. The former is observed near the edge of the hysteresis loop [43]. Thus, all these experimental facts are consistent with the present theoretical findings and arguments.

Acknowledgments This work was supported by Grants-in-Aid from the Ministry of Education, Culture, Sports, Science and Technology of Japan.

References

1. Kurmoo M, Clark RJH (1985) Inorg Chem 24:4420
2. Butler LG, Zietlow MH, Che C-M, Schaefer WP, Sridhar S, Grunthaner PJ, Swanson BI, Clark RJH, Gray HB (1988) J Am Chem Soc 110:1155
3. Yamashita M, Toriumi K (1990) Inorg Chim Acta 178:143

4. Weinrach JB, Hawley M, Sattelberger AP, Swanson BI (1991) Solid State Commun 77:853
5. Kimura N, Ohki H, Ikeda R, Yamashita M (1994) Chem Phys Lett 220:40
6. Yamashita M, Miya S, Kawashima T, Manabe T, Sonoyama T, Kitagawa H, Mitani T, Okamoto H, Ikeda R (1999) J Am Chem Soc 121:2321
7. Matsuzaki H, Matsuoka T, Kishida H, Takizawa K, Miyasaka H, Sugiura K, Yamashita M, Okamoto H (2003) Phys Rev Lett 90:046401
8. Bellitto C, Flamini A, Gastaldi L, Scaramunzza L (1983) Inorg Chem 22:444
9. Kitagawa H, Onodera N, Ahn J-S, Mitani T, Toriumi K, Yamashita M (1931) Synth Met 1997:86
10. Kitagawa H, Onodera N, Sonoyama T, Yamamoto M, Fukawa T, Mitani T, Seto M, Maeda Y (1999) J Am Chem Soc 121:10068
11. Mitsumi M, Kitamura K, Morinaga A, Ozawa Y, Kobayashi M, Toriumi K, Iso Y, Kitagawa H, Mitani T (2002) Angew Chem Int Ed 41:2767
12. Whangbo M-H, Canadell E (1986) Inorg Chem 25:1726
13. Borshch SA, Prassides K, Robert V, Solonenko AO (1998) J Chem Phys 109:4562
14. Robert V, Petit S, Borshch SA (1999) Inorg Chem 38:1573
15. S. Yamamoto (1999) Phys Lett A 258: 183; 261: 125(E)
16. Yamamoto S (2000) J Phys Soc Jpn 69:13
17. Kuwabara M, Yonemitsu K (2000) Mol Cryst Liq Cryst 341:533
18. Kuwabara M, Yonemitsu K (2000) Physica B 284–288:1545
19. Yamamoto S (2001) J Phys Soc Jpn 70:1198
20. Kuwabara M, Yonemitsu K (2000) Mol Cryst Liq Cryst 343:47
21. Kuwabara M, Yonemitsu K (2001) J Phys Chem Solids 62:435
22. Yamamoto S (2001) Phys Rev B 63:125124
23. Kuwabara M, Yonemitsu K (2001) J Mater Chem 11:2163
24. Yonemitsu K, Miyashita N (2003) Phys Rev B 68:075113
25. Yonemitsu K, Nasu K (2006) Phys Rep 465:1
26. Yonemitsu K, Bishop AR, Lorenzana J (1992) Phys Rev Lett 69:965
27. Yonemitsu K, Bishop AR, Lorenzana J (1993) Phys Rev B 47:8065
28. Yonemitsu K, Bishop AR, Lorenzana J (1993) Phys Rev B 47:12059
29. Iwai S, Ono M, Maeda A, Matsuzaki H, Kishida H, Okamoto H, Tokura Y (2003) Phys Rev Lett 91:057401
30. Maeshima N, Yonemitsu K (2005) J Phys Soc Jpn 74:2671
31. Chollet M, Guerin L, Uchida N, Fukaya S, Shimoda H, Ishikawa T, Matsuda K, Hasegawa T, Ota A, Yamochi H, Saito G, Tazaki R, Adachi S, Koshihara S (2005) Science 307:86
32. Onda K, Ogihara S, Yonemitsu K, Maeshima N, Ishikawa T, Okimoto Y, Shao X, Nakano Y, Yamochi H, Saito G, Koshihara S (2008) Phys Rev Lett 101:067403
33. Iwai S, Yamamoto K, Kashiwazaki A, Hiramatsu F, Nakaya H, Kawakami Y, Yakushi K, Okamoto H, Mori H, Nishio Y (2007) Phys Rev Lett 98:097402
34. Tanaka Y, Yonemitsu K (2010) J Phys Soc Jpn 79:024712
35. Miyashita S, Tanaka Y, Iwai S, Yonemitsu K (2010) J Phys Soc Jpn 79:034708
36. Iwai S, Tanaka S, Fujinuma K, Kishida H, Okamoto H, Tokura Y (2002) Phys Rev Lett 88:057402
37. Yonemitsu K (2006) Phys Rev B 73:155120
38. Okamoto H, Ikegami K, Wakabayashi T, Ishige Y, Togo J, Kishida H, Matsuzaki H (2006) Phys Rev Lett 96:037405
39. Maeshima N, Yonemitsu K (2006) Phys Rev B 74:155105
40. Maeshima N, Yonemitsu K (2007) J Phys Soc Jpn 76:074713
41. Maeshima N, Yonemitsu K (2008) J Phys Soc Jpn 77:074713
42. Iwano K (2002) Phys Rev B 66:060302
43. Okamoto H, Iwai S, Matsuzaki H (2004) In: Nasu K (ed) Photoinduced phase transitions. World Scientific, New Jersey, p 239

Index

M. Yamashita and H. Okamoto (eds.), *Material Designs and New Physical Properties in MX- and MMX-Chain Compounds*, DOI 10.1007/978-3-7091-1317-2,